ROYAL HOLLOWAY UNIVERSITY OF LONDON

DOCTORAL THESIS

Numerical modelling of the craton destruction process, with a type-example from the North China Craton

---

Author:
Liang Liu

Supervisors:
Prof. Jason P. Morgan
Prof. Martin A. Menzies
Prof. Yigang Xu

A thesis submitted in fulfilment of the requirements
for the degree of Doctor of Philosophy
April 10, 2018

Department of Earth Sciences
Royal Holloway University of London
Egham, United Kingdom

Declaration of Authorship

I, Liang Liu hereby declare that this thesis and the work presented in it is entirely my own. Where I have consulted the work of others, this is always clearly stated.

Signed: 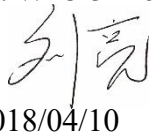

Date: 2018/04/10

Learning without thought is labor lost; thought without learning is perilous.

------ *Confucius*

Abstract:

The phenomenon of cratonic destruction has attracted attentions among numerical modelers. However, existing modelling work appears to lack enough constraints from geological and geophysical observations. To better combine the observations with the modelling approach, and to further understand the destruction of the North China Craton (NCC), I firstly reviewed current knowledge about the evolution of the North China Craton, and then outlined the strength and weakness associated with classic delamination and convective erosion models. By integrating new observational data and 2-D numerical modeling results, I put forward a two-stage model to account for the destruction of the NCC, that is, cratonic keel delamination followed by localized convective erosion and lithospheric extension.

As revealed in the evolution of the NCC, its destruction appears to be accompanied by the inversion of a pre-existing North China Cratonic Basin (NCCB), which is partly preserved in southeastern Ordos. This >300 Myr subsidence of the NCCB can most probably be explained by assuming a pre-existing dense keel for the eastern NCC (ENCC), consistent with the petrological and geochemical observations from mantle xenoliths/xenocrysts hosted in kimberlite/basalt in the ENCC.

As the bottom was dense, cratonic keel stability would have only been sustained by the buoyancy of the overlying lithospheric portion. Hereafter, if some weak intra-cratonic regions had existed above the dense bottom and were reactivated, intra-cratonic decoupling may finally occur, leading to keel delamination.

Coincidentally, some seismically visible Mid-Lithospheric Discontinuity Layers (MLDLs) exist at depths of ~80-100 km within modern cratons, including the remaining portions of the NCC and the Wyoming Craton (WC),. Interestingly, these depths are also where the relic lithospheric bottom appears to remain beneath

the keelless sub-regions of the eastern NCC and the WC. Because the MLDLs are suggested to be regions of preferential accumulation of metasomatic minerals and/or anomalously wet (>1000 ppm) peridotites (both of which would lead to a relatively weak rheology), we accordingly propose that the weak MLDLs may have been the intra-cratonic weak zone, which allowed delamination of the dense cratonic keels of the NCC and the WC.

This delamination model is studied in detail using 2-D analytical and numerical modelling, and the modelling results may help constrain the MLDL rheology needed for explaining the keel delamination rate estimated on the NCC and the WC. One can speculate that the delaminated cratonic keels may still exist or stagnate within the upper mantle. This suggestion may explain some, if not all, of the high velocity bodies beneath North China and Iowa, USA (which was the location caped by the Wyoming Craton before the Laramide Orogeny).

After keel delamination along the MLDLs, a protracted (*ca.* 50-100 Myr) period of small-scale convective erosion and/or lithospheric extension thinned the remaining ~90 km thick lithosphere and continuously reworked the former cratonic lithospheric mantle beneath the Moho. As indicated in the modeling results, this second stage evolution may explain the episodic magmatism and crustal deformation associated with the destruction of the NCC.

Acknowledgements

This thesis was supported by the joint PhD program between the Guangzhou Institute of Geochemistry, Chinese Academy of Sciences (GIGCAS) and Royal Holloway University of London (RHUL), and CAS Priority B Strategic project (XDB-18000000).

First, I would like to acknowledge my lead supervisor Prof. Jason P. Morgan. Prof. Morgan proposed the ideas for my Ph.D. researches and formats of publications. Jason is always patient in explaining the basic grammars and structures on scientific writing and helped me to modify my drafts many… many… times. He was willing to discuss with me about my numerical results and helped me to dig out the geophysical meanings of my experiments.

Second, I would like to acknowledge my second supervisor Prof. Martin Menzies and his wife Les. Prof. Menzies is one of the pioneer geologists studying craton destruction. He spent lots of time helping me to correct my writings and to think about geology. To have the chance to study his outlooks on life, career and values is one of my most significant achievements during the 3.5-year Ph.D. study in the U.K. I deeply appreciate the happy time in their house, and their kindly company during the Chinese Spring New Year.

I would definitely like to acknowledge my supervisor Prof. Yigang Xu and his wife Lin Lin. Prof. Xu is also one of the earliest geologists studying craton destruction. He provided me with the chance to study in the RHUL, to know geodynamics modeling, and to think about better modeling strategy. He and his wife encouraged me to bestir myself during the most difficult time I ever encountered, and they helped me to re-gain my confidence to continue my research.

Thanks to Miguel and Albert. Thank you both on helping me to learn the prototype code and sharing coding strategy.

I also like to say thank you to Bin Sheng, Yajun Li, Wanpeng Li, Shuo Zhang, Zhi Wang, Xiao Zhang, Xiangming Tao, Hanbing Li, Yizhuo Sun, Ning An, and

Hong Chen. Thank you for your company in abroad. I always remember the time we spent in the Sports Center, Great Winsor Park and Magic Wok.

Finally, but equally importantly, I would like to acknowledge my parents Liu Xianhou & Lv Li and my wife Zhu Ming. I know I spent <40 days with you in the past 3.5 yrs. Thank you for your supporting and understanding. You are always my power source!

Contents

List of Figures

List of Tables

To my family

Chapter 1: Introduction

1. Destruction of the North China Craton.

The North China Craton (NCC) is a well-studied Archean (ca. 2.5 Ga) craton (see Fig. 1-1 and 1-2) (Menzies et al., 2007; Zhao and Zhai, 2013), which had retained a ca. 40 wM/m^2 surface heat flow and a ca. 180-200 km thick lithospheric keel at least before ca. 460 Ma (Griffin et al., 1998). For the past 25 years, this craton has attracted lots of attention, because the Archean crust of its eastern part (Eastern North China Craton, ENCC) is identified to be underlain by less refractory lithospheric mantle with of the bottom at ca. 80km deep (Hong et al., 2012; Menzies et al., 1993; Xu, 2001). This feature contradicts with the conventional speculation that the ancient cratonic crust is always protected against active mantle convection by a refractory, buoyant and comparably ancient underlying lithospheric mantle (cf. Sleep, 2003).

The NCC firstly attracted the attention of geologists about 80 years ago, because unlike most inert Archean cratons, the ENCC juxtaposes both ancient (>ca. 2.5 Ga) basement rocks (see Fig. 1-2) and Mesozoic (ca. 180-100 Ma) igneous rocks (see Fig. 1-1) (see review in (Chen, 1989)). The on-craton magmatism was contemporary with abnormally active crustal deformation and widespread gold mineralization (Yang et al., 2003) (see details in Chapters 4-5). Both features appear to be unique among the Archean comparatives. Later, with the improvement of geophysical techniques, the ENCC was found to have a significantly higher surface heat flow (ca. 64 mW/m^2) and a much thinner (ca. 80 km) thermal and seismic lithosphere (see Fig. 1-1) than stable comparatives (Chen et al., 2008; Chen et al., 2001; He, 2015; Menzies et al., 2007; Xu et al., 1996). Menzies et al. (1993) hence pointed out that the ENCC had experienced a lithospheric thinning process and lost its cratonic keel, implying that Archean craton can also be reworked and destroyed.

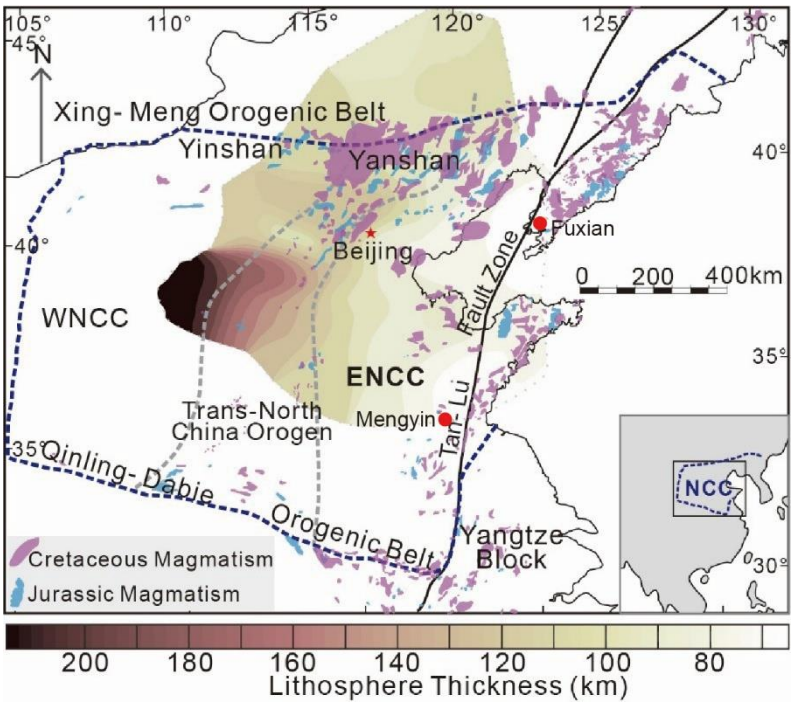

Fig. 1.1. Post-Paleozoic magmatism within the North China Craton (NCC)

Jurassic magmatism (blue) (ca. 180 Ma to 160 Ma) is relatively minor. Cretaceous (ca.145 Ma to 110 Ma) magmatism (purple) is focused near the craton margins and lithospheric weak zones (e.g. the Tan-Lu fault zone). Yinshan, Yanshan refer to mountain ranges. Xing-Meng and Qinling-Dabie refer to Orogenic Belts. The Yangtze Block is a neighboring lithospheric block. The Tan-Lu Fault Zone is a deep fault system, thought to have been reactivated during the collision event (ca. 210 Ma) between the NCC and the Yangtze blocks. Mengyin and Fuxian are locations for the ca. 460 Ma kimberlite intrusions. The arrow marked "N" indicates north. Colors show the present-day lithospheric thickness (in km) inferred from seismic measurement (Zhu et al., 2011). Abbreviations: ENCC- Eastern North China Craton, WNCC- Western North China Craton.

Benefiting from increasing inputs of petrologists and geochemists, the general evolution of the NCC is now generally established: 1) micro blocks of the NCC were formed at >ca. 2.5 Ga and were finally stabilized at ca. 1.8 Ga (see Fig. 1-2) (Zhao and Zhai, 2013); 2) the NCC remained intact until ca. 180Ma; 3) during ca. 180-110 Ma, the ENCC lost most of its ancient mantle and its lithosphere was thinned to be locally < 60 km (Menzies et al., 2007; Menzies and Xu, 1998; Zhu

et al., 2012); 4) the lithosphere beneath the ENCC grew to its present-day thickness of ca. 80-100 km (see Fig. 1-1), with the lowermost part of the lithosphere being mainly composed of newly accreted asthenospheric material (Hong et al., 2012; Xu, 2001); and 5) since ca. 1.8 Ga, the western NCC (e.g. Ordos, see Fig. 1-1) has generally remained stable. To highlight the special evolution of the ENCC, stages 2 to 3 have been categorized as one single geologic event, being referred to as the craton destruction phenomenon (Xu, 2001; Zhu et al., 2012).

The evolution of the ENCC comprises cratonic keel removal and lithospheric accretion. Both processes appear to be fundamental in studying the Earth's solid lid. Although some cratonic destruction cases may also have occurred (e.g. the Sahara Metacraton (cf. (Liégeois et al., 2013))), most footprints of the older cases could have been 'erased' by later events. In this sense, the ENCC, which was destroyed in the late Mesozoic, represents a particularly important type-example in studying the craton destruction processes.

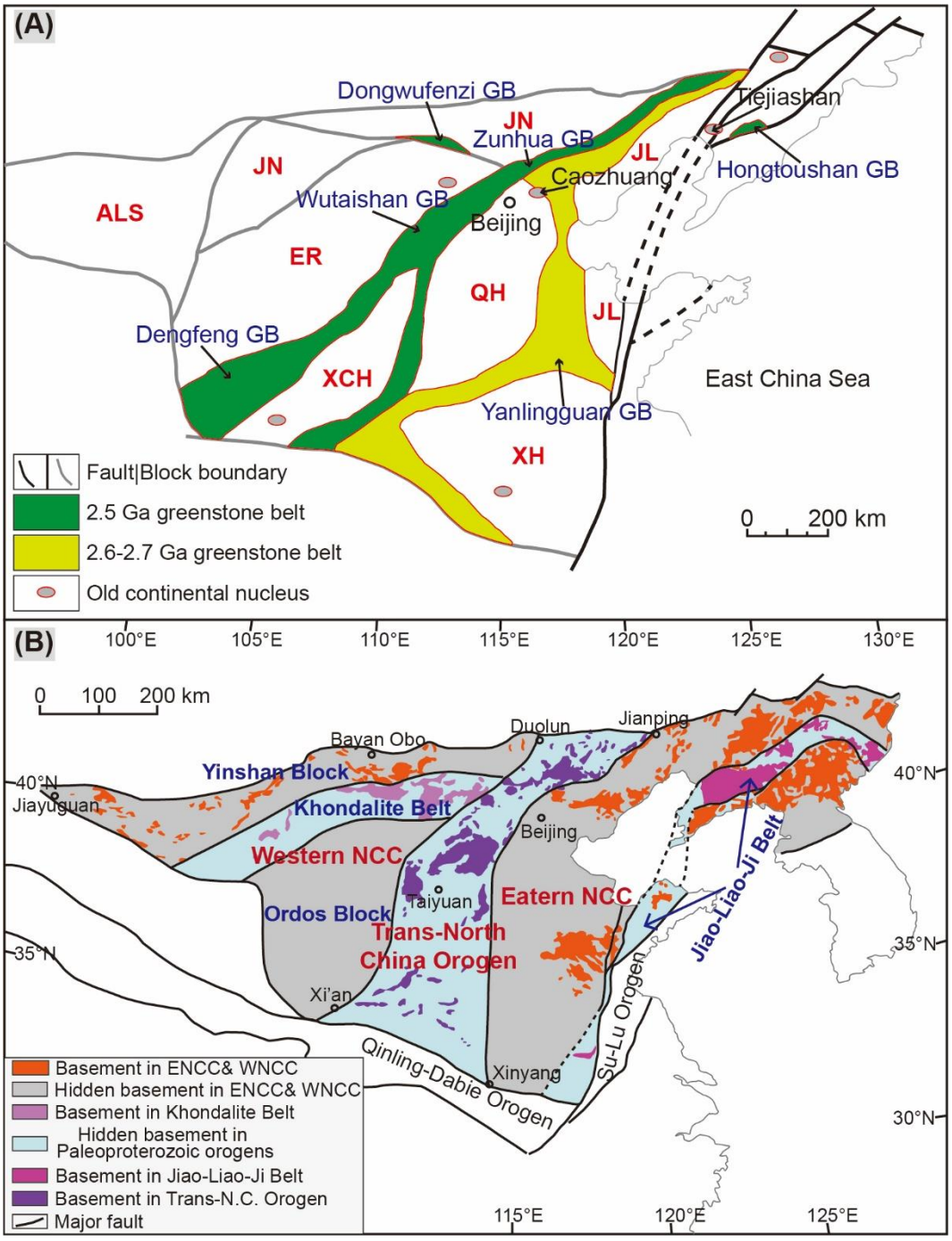

Fig. 1.2. Distribution of cratonic nuclei and Paleoproterozoic orogenic belts on the NCC

(A) Distribution of cratonic nuclei, Archean micro blocks and greenstone belts on the NCC. The ancient (ca. 3.0-3.8 Ga) nuclei are mainly composed of orthogneiss and metamorphosed sedimentary rocks. The Archean micro blocks are ca. 2.7Ga old, and the greenstone belts are ca. 2.54-2.6Ga old (Zhai and Santosh, 2011). Abbreviations: JL- Jiaoliao, QH- Qianhuai, OR- Ordos, JN- Jining, XCH- Xuchang, XH- Xuhuai, ALS- Alashan. GB- Greenstone Belt. (B) Distribution of the Paleoproterozoic (ca. 2.5-1.8Ga)

orogenic belts on the NCC (Zhao et al., 2005; Zhao and Zhai, 2013).

2. Existing problems and objectives of this study

Despite significant advances of the study of the destruction of the NCC, the mechanism of cratonic destruction remains contentious. Two types of conceptual models have been proposed: 1) 'bottom-up' models, which emphasize that the keel is gradually eroded during the upwelling of abnormally hot and/or water-enriched material (He, 2014; Xu, 2001; Zhang et al., 2008; Zheng et al., 2007); and 2) 'top-down' models, which highlight a rapid foundering process of the dense keel bottom (Gao et al., 2004; Gao et al., 2009; Xu et al., 2008). Both models can be self-consistent in explaining parts of observations on the ENCC (see more specific discussion in Chapters 3-5).

The traditional study approach may have limitations. The established models would be more convincing only if the suggested process can be verified by lab-analogue- or numerical experiments. Assessment of analogue experiments is beyond the scope of this thesis. As far as we know, the method of forward numerical modeling appears to be irreplaceable in linking observations and testing the physical feasibility of geological models.

The existing numerical models appear to focus more on verifying the feasibility of geological models, while neglecting the important constraints from geological and geophysical observations. Numerical models should be loyal to geological observations before any assumption can be made on parameters and/or the initial and boundary conditions. In this thesis, the author reviewed the available evidence regarding the destruction of the NCC before doing any numerical calculation. Several key observations are outlined and are considered as inputs to numerical modeling. It is anticipated that such a practice could greatly improve the study of cratonic destruction.

3. Outline of the thesis

This thesis is written in the 'Paper format' based on the rules of the Royal Holloway, University of London. Chapter 2 will be modified into a format of *Lithos*. Chapters 3 and 4 have been submitted to *JGR: Solid Earth* and are now under review. Chapters 5 has been submitted to *Terra Nova*.

Chapter 2 reviews the pre-Cambrian geological evolution of the North China Craton. In particular, the sedimentation pattern in the NCC is believed to provide evidence that the ENCC possessed a dense lithospheric keel and in a meta-stable state before destruction.

Chapter 3. The role of the seismically visible Mid-Lithospheric Discontinuity Layers (MLDLs) is emphasized in cratonic destruction. MLDLs are suggested to be regions of preferential accumulation of metasomatic minerals and/or anomalously wet (>1000 ppm) peridotites, both of which would lead to a relatively weak rheology. In this chapter, we propose that the cratonic keels of the eastern North China Craton (ENCC) and the western Wyoming Craton (WWC) were delaminated from overlying lithosphere along MLDLs. According to the modelling results: a) dense keels beneath a MLDL bearing cratons can persist for billions of years as long as the MLDL's edge abut relatively cold and strong lithosphere; b) failure of the MLDL's edge can induce rapid intra-mantle keel delamination; and c) the predicted rates of keel delamination along a ~10km thick MLDL with a hydrous olivine or metasomatic mineral-dominated rheology are consistent with observations for the removal speeds of the WWC and the ENCC.

Chapter 4.

In this chapter we propose a two-stage evolutionary process to explain the destruction of the ENCC. First, *ca.* 100 km of cratonic "keel" underlying a weak mid-lithospheric discontinuity layer (*ca.* 80 km to 100 km) was rapidly removed in <10-20 Myr. This was followed by a protracted (*ca.* 50-100 Myr) period of small-scale convective erosion and/or lithospheric extension that thinned the

remaining lithosphere and continuously reworked the former cratonic lithospheric mantle beneath the Moho.

Then, we designed numerical experiments to study the second stage of the ENCC's lithospheric evolution. We find: 1) lithospheric mantle capped by thick and/or high-heat-production crust can be locally replaced by deep mantle material in 100 Myr due to small-scale convective erosion; 2) asthenospheric upwelling & related extension can replace lithospheric mantle over horizontal length-scales of ~50-150km, and account for observed "mushroom-shaped" low-seismic-wavespeed structures; 3) modelling shows conditions that could lead to the observed multiple ENCC magmatic pulses *ca*. 180-100Ma associated with temporal and spatial changes in magma source petrology and a magmatic hiatus; 4) a "wet" mid-lithospheric discontinuity layer provides a potential source material for on-craton magmatism.

Chapter 5. In at least two places, beneath former locations of the eastern North China Craton and western Wyoming Craton, the mantle transition zone has high seismic wavespeed anomalies which lack a direct correlation with recently subducted slabs. The conventional interpretation for these seismic anomalies has been that they are due to stagnant slabs introduced by subduction. In this chapter we show further seismic evidence that supports the recent hypothesis (Xu and Zhao 2009) that these high wavespeed anomalies may be due to the presence of delaminated cratonic "keel" fragments.

Chapter 6 summarizes the main conclusions of the thesis.

References:

Chen, G., 1989. Tectonics of China. International Academic Publishers. 258pp.

Chen, L., Tao, W., Zhao, L., Zheng, T., 2008. Distinct lateral variation of lithospheric thickness in the Northeastern North China Craton. Earth and Planetary Science Letters 267, 56-68.

Chen, S., O'Reilly, S.Y., Zhou, X., Griffin, W.L., Zhang, G., Sun, M., Feng, J., Zhang, M., 2001. Thermal and petrological structure of the lithosphere beneath Hannuoba, Sino-Korean Craton, China: evidence from xenoliths. Lithos 56, 267-301.

Gao, S., Rudnick, R.L., Yuan, H.L., Liu, X.M., Liu, Y.S., Xu, W.L., Ling, W.L., Ayers, J., Wang, X.C., Wang, Q.H., 2004. Recycling lower continental crust in the North China craton. Nature 432, 892-897.

Gao, S., Zhang, J.F., Xu, W.L., Liu, Y.S., 2009. Delamination and destruction of the North China Craton. Chinese Science Bulletin 54, 3367-3378.

Griffin, W.L., Andi, Z., O'Reilly, S.Y., Ryan, C.G., 1998. Phanerozoic evolution of the lithosphere beneath the Sino-Korean Craton. Mantle Dynamics and Plate Interactions in East Asia 27, 107-126.

He, L.J., 2014. Numerical modeling of convective erosion and peridotite-melt interaction in big mantle wedge: Implications for the destruction of the North China Craton. Journal of Geophysical Research-Solid Earth 119, 3662-3677.

He, L.J., 2015. Thermal regime of the North China Craton: Implications for craton destruction. Earth-Science Reviews 140, 14-26.

Hong, L.-B., Xu, Y.-G., Ren, Z.-Y., Kuang, Y.-S., Zhang, Y.-L., Li, J., Wang, F.-Y., Zhang, H., 2012. Petrology, geochemistry and Re–Os isotopes of peridotite xenoliths from Yantai, Shandong Province: Evidence for Phanerozoic lithospheric mantle beneath eastern North China Craton. Lithos 155, 256-271.

Liégeois, J.-P., Abdelsalam, M.G., Ennih, N., Ouabadi, A., 2013. Metacraton: nature, genesis and behavior. Gondwana Research 23, 220-237.

Menzies, Fan, W., Zhang, M., 1993. Palaeozoic and Cenozoic lithoprobes and the loss of> 120 km of Archaean lithosphere, Sino-Korean craton, China. Geological Society, London, Special Publications 76, 71-81.

Menzies, M., Xu, Y.G., Zhang, H.F., Fan, W.M., 2007. Integration of geology, geophysics and geochemistry: A key to understanding the North China Craton. Lithos 96, 1-21.

Menzies, M.A., Xu, Y., 1998. Geodynamics of the North China craton. Mantle Dynamics and Plate Interactions in East Asia, 155-165.

Sleep, N.H., 2003. Survival of Archean cratonal lithosphere. Journal of Geophysical Research-Solid Earth 108 (B6), p. 2302, 10.1029/2001JB000169.

Xu, W., Hergt, J.M., Gao, S., Pei, F., Wang, W., Yang, D., 2008. Interaction of adakitic melt-peridotite: implications for the high-Mg# signature of Mesozoic adakitic rocks in the eastern North China Craton. Earth and Planetary Science Letters 265, 123-137.

Xu, Y., Menzies, M., Mattey, D., Lowry, D., Harte, B., Hinton, R., 1996. The nature of the lithospheric mantle near the Tancheng-Lujiang fault, China: an integration of texture, chemistry and O-isotopes. Chemical Geology 134, 67-81.

Xu, Y.G., 2001. Thermo-tectonic destruction of the archaean lithospheric keel beneath the Sino-Korean Craton in China: Evidence, timing and mechanism. Physics and Chemistry of the Earth Part A-Solid Earth and Geodesy 26, 747-757.

Xu, Y.G., Li, H.Y., Pang, C.J., He, B., 2009. On the timing and duration of the destruction of the North China Craton. Chinese Science Bulletin 54, 3379-3396.

Yang, J.-H., Wu, F.-Y., Wilde, S.A., 2003. A review of the geodynamic setting of large-scale Late Mesozoic gold mineralization in the North China Craton: an association with lithospheric thinning. Ore Geology Reviews 23, 125-152.

Zhai, M.-G., Santosh, M., 2011. The early Precambrian odyssey of the North China Craton: a synoptic overview. Gondwana Research 20, 6-25.

Zhang, H.F., Goldstein, S.L., Zhou, X.H., Sun, M., Zheng, J.P., Cai, Y., 2008. Evolution of subcontinental lithospheric mantle beneath eastern China: Re-Os isotopic evidence from mantle xenoliths in Paleozoic kimberlites and Mesozoic basalts. Contributions to Mineralogy and Petrology 155, 271-293.

Zhao, G., Sun, M., Wilde, S.A., Sanzhong, L., 2005. Late Archean to Paleoproterozoic evolution of the North China Craton: key issues revisited. Precambrian Research 136, 177-202.

Zhao, G., Zhai, M., 2013. Lithotectonic elements of Precambrian basement in the North China Craton: review and tectonic implications. Gondwana Research 23, 1207-1240.

Zheng, J., Griffin, W., O'Reilly, S.Y., Yu, C., Zhang, H., Pearson, N., Zhang, M., 2007. Mechanism and timing of lithospheric modification and replacement beneath the eastern North China Craton: peridotitic xenoliths from the 100 Ma Fuxin basalts and a regional synthesis. Geochimica et Cosmochimica Acta 71, 5203-5225.

Zhu, Xu, Y., Zhu, G., Zhang, H., Xia, Q., Zheng, T., 2012. Destruction of the north China Craton. Science China Earth Sciences 55, 1565-1587.

Zhu, R., Chen, L., Wu, F., Liu, J., 2011. Timing, scale and mechanism of the destruction of the North China Craton. Science China Earth Sciences 54, 789-797.

Chapter 2: Sedimentary evidence for a pre-destruction dense keel beneath the Eastern North China Craton

Liang Liu, Yigang Xu, Martin Menzies and Jason P. Morgan. This manuscript will be submitted to *Lithos*.

Authors contribution

Liang Liu proposed the idea for this review-type paper. L. Liu. collected the geological, geochemical and geophysical observations in this paper. L. Liu. suggested the geological implication with discussion with Yigang Xu. L. Liu wrote the manuscript in collaboration with Y-G Xu, M. Menzies and J. P. Morgan.

Abstract:

The North China Craton (NCC) is a well-studied Archean carton, whose keel beneath the eastern part has been permanently lost during the Mesozoic (ca. 180-110 Ma) *cratonic destruction* process. Numerical modeling studies always indicate that to allow craton destruction to happen, the pre-existing cratonic keel needs to be denser than estimated. This proposition is mainly based on observations from stable cratons, while still lacks direct supports from the records on the NCC.

In this chapter, we review the pre-destruction evolution of the NCC, which indicates that the eastern NCC may have been underlain by a dense keel before destruction. Based on the sedimentary records, a cratonic-basin-like structure had developed on the NCC for ca. 300 Ma, which was partially inverted right above the eastern NCC during the early stage ca. 180-160 Ma of the craton destruction. Such a basin evolution can be best explained by the presence of a dense keel underneath the eastern NCC, supported by the simple 2-D numerical experiments here. If this is correct, it presents for the first-time solid evidence for the dense cratonic keel as a precondition for cratonic destruction.

1. Introduction

The North China Craton (NCC) is a well-studied Archean (ca. 2.5Ga) craton (see Fig. 1-2) (Menzies et al., 2007; Zhao and Zhai, 2013). Its ca. 180-200 km thick lithospheric keel beneath the eastern part (Eastern North China Craton, ENCC) has been partly removed and replaced during the Mesozoic (ca. 180-110 Ma) craton destruction event (Hong et al., 2012; Menzies et al., 1993; Xu, 2001). To explain this rather unusual phenomenon, two types of conceptual models have been proposed: 1) 'bottom-up' models, in which the keel is gradually eroded during the upwelling of abnormally hot and/or water-enriched material (He, 2014; Xu, 2001; Zhang et al., 2008; Zheng et al., 2007); and 2) 'top-down' models, which emphasize a rapid foundering process of dense keels (Gao et al., 2004; Gao et al., 2009; Xu et al., 2008). Based on these models, many groups of modelers have developed a series of numerical models to further explore the specific conditions which controlled the removal of a cratonic keel (Gorczyk et al., 2012; He, 2014; Liao et al., 2017; Lin et al., 2005; Wang et al., 2016; Wenker and Beaumont, 2017; Yang et al., 2017) (also see the author's work in Chapters 3-5).

The existing numerical models commonly indicate that: to allow for effective removal of the cratonic keel bottom within ca. 100 Ma, the pre-existing cratonic keel needs to be dense, i.e. its net density (compositional+ thermal) is higher than that of adjacent and/underlying asthenosphere (Gorczyk et al., 2012; He, 2014; Krystopowicz and Currie, 2013; Liao et al., 2017; Lin et al., 2005; Morency and Doin, 2004; Wang et al., 2016; Wenker and Beaumont, 2017; Yang et al., 2017) (see Chapters 3-4). This assumption apparently contrasts with the isopycnic theory that suggests a balanced density structure between lithosphere and its surroundings at every depth level (Jordan, 1988), and also contrasts with the buoyant keel as suggested by xenolith and gravity studies (Boyd, 1989; Djomani et al., 2001; Sleep, 2003).

This proposition of a dense pre-existing cratonic keel is mainly based on the

observations on stable cratons:

1) Mantle metasomatism may modify the mineral assemblage of mantle rocks, e.g. introducing Fe-rich pyroxene through consuming Mg-rich olivine. This is apparent in the layered structure of some kimberlite profiles – e.g. depth- Mg# (mole ratio of Mg/[Fe^{2+}+Mg] in whole rock) and/or Fo (mole ratio of Mg/[Fe^{2+}+Mg] in olivine). For example, the Fo changes to <92 beneath ~140 km in some North American cratons; and this change occurs beneath ~170 km in some portions of the Kaapvaal Craton (Griffin et al., 2004; Griffin et al., 2003). Because Fe-rich mantle rocks can be 0.5-1.9% denser than highly refractory cratonic mantle rocks (Djomani et al., 2001; Lee et al., 2011), cratonic keels bearing higher proportions of these rocks would have a dense bottom.

2) A layered keel structure also appears to be supported by the distinctive anisotropy directions within cratonic lithosphere, e.g. in the North American cratons and the Kaapvaal Craton (Hu et al., 2018; Yuan and Romanowicz, 2010). This also promotes the development of the stacking mechanism for craton formation, which suggests that some Archean cratons grow in an arc environment through slab accretions (Griffin et al., 2004; Lee et al., 2011), supported by recent numerical modelling work (Eaton and Perry, 2013). Because oceanic slabs commonly experienced less melt-extraction (10-25%) than cratonic lithosphere (>35%) (cf. (Niu, 2005)), some cratonic keel bottom can be originally denser than estimated (Lee et al., 2011).

3) Important evidence may come from the long-term subsidence of cratonic basins. As their subsidence is always weakly related to adjacent tectonics, it has been proposed that their formation was caused by the relative denser underlying cratonic keel, formed through extension-related mantle rejuvenation (Artemieva, 2003; Downey and Gurnis, 2009; Foley, 2008; Nikishin et al., 1996).

However, to directly apply the implication of dense cratonic keel to destroyed

cratons can be problematic, after all, the observed cratons nevertheless maintain stable. Instead, the immediate method to test this application is to study the pre-existing keel of the destroyed ENCC. Although the keel is permanently lost, if it was dense, it could have affected the pre-destruction evolution of the ENCC, e.g. the gravity-induced differential down-warping of the surface (Artemieva, 2003; Downey and Gurnis, 2009; Nikishin et al., 1996). Therefore, a review of the ENCC's pre-destruction evolution is necessary.

In this chapter, we show that, (1) a cratonic-basin-like structure appears to have developed on the NCC from at least ca. 530 Ma to ~200 Ma; (2) the eastern part of this basin is reversed in the Mesozoic times (ca. 180-160 Ma); (3) the >300 Ma basin evolution might reflect the presence of a dense keel underneath the ENCC; and (4) the simple 2-D numerical experiments support the assumption that a dense cratonic keel can lead to long-term (ca. >200 Ma) subsidence of the craton surface, and thus supports the dense-keel-proposition usually assumed in numerical models

2. Review of the NCC's evolution before destruction

2.1. ca. 200 km thick lithosphere beneath the ENCC before the craton destruction

Cratons are conventionally referred to as regions that capped by Archean (> 2.5Ga) crust, underlain by comparably old lithospheric mantle with bottom at >150 km deep. These regions generally lack tectonic or volcanic events, and their surface heat flow remains low (ca. 45mW/m^2) (Menzies et al. 2007). Based on the studies of mantle xenoliths entrained into kimberlites, cratonic mantle is found to be extremely depleted in water and rich in magnesium (i.e. Mg# >92) (Boyd, 1989; Lee, 2003), and thus to be strong and buoyant that leading to craton stability (Sleep, 2003; 2009). So, the ages of the crust and mantle, the tectonic and volcanic state, and the depth distribution and petrology of mantle xenoliths can give the first-order constraints on judging whether the ENCC had a cratonic state (i.e. a ~200

km thick lithosphere) (Menzies et al. 2007):

1) On the ENCC, ca. 80% of the crustal rocks are estimated to have Archean ages (> 2.5 Ga). The basement rocks are dated to be 2.5-3.8 Ga old, focusing between 2.5- 2.9 Ga (Zhai, 2011; 2014). Based on the studies of the lower crustal xenoliths, the oldest lower crust is ca. 3.6 Ga (Zheng et al., 2004). Before ca. 180 Ma, the crust of the central craton did not experience tectonic or volcanic events (Xu et al. 2009).

2) Mantle xenoliths before the ENCC destruction (ca. 180 Ma) are mainly found in two kimberlite intrusions ((ca. 460 Ma, locations in Fig. 1.1) (Zheng et al., 2006). The Re-depletion ages (T_{RD}) of the kimberlite-borne mantle xenoliths on the ENCC had a wide range between ca. 1.6-2.7 Ga (Gao et al., 2002).

3) The kimberlite-borne mantle xenoliths are mainly garnet facies (> 80 km deep), and the appearance of diamond megacrysts suggests that the ENCC lithosphere was at least 150 km thick (Menzies et al., 2007). According to the studies on the trace elements of the garnet concentrates, Griffins et al. established the p-T path of the ENCC lithosphere, which suggests that the surface heat flow was ~40 mW/m^2 and the lithospheric bottom lied at ca. 180-220 km depths (Griffin et al., 1992, 1998, 1999) (Fig. 2.1).

4) The solid inclusions in the kimberlite-borne diamonds are mainly peridotitic minerals. The ENCC mantle is suggested to be composed of Mg-peridotite or harzburgite at 180-200 m depths, which indicates the melt-depleted feature of the lithospheric bottom (Meyer, 1987).

The above observations on the ENCC are consistent with the ‘general’ definition for cratons. Therefore, we believe that the ENCC kept its thick keel and remained a stable cratonic state, at least before the explosion of the Paleozoic (ca. 460 Ma) kimberlites.

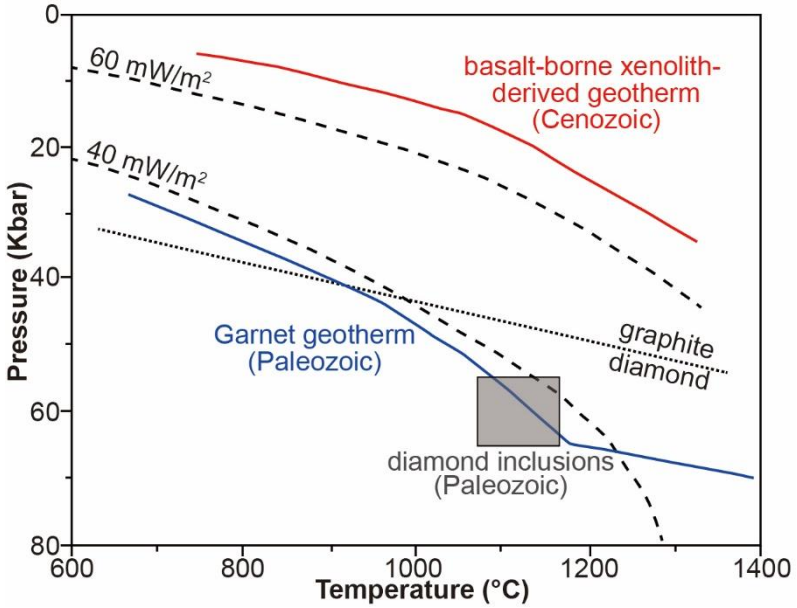

Fig. 2.1. Geotherm estimated for the ENCC lithosphere (after Menzies et al., 2001). The Paleozoic geotherm best fits the thermo-barometric data from the kimberlite borne garnet concentrates (after Griffin et al., 1998; Xu, 2001). The Cenozoic geotherm best fits thermo-barometric data from basalt-borne mantle xenoliths (Xu et al., 1998; Chen et al., 2001; Xu, 2001).

2.2. Assembly and cratonization of the North China Block

Like most Archean cratons, the NCC may have originally belonged to a large supercraton (Bleeker, 2003; Li et al., 2008; Zhang et al., 2012b) and itself is composed of several ca. >2.5 Ga micro blocks (see Fig. 1-2A) (Zhai and Santosh, 2011; Zhang et al., 2012a). After the ENCC and the western NCC merged through the Trans-North China Orogeny (TNCO) at ca. 1.8 Ga, the NCC generally reached a stable cratonic state with almost no crustal melting and deformation; only its margin witnessed rifting-related ca. 1.6-1.2 Ga extension and magmatism and ca. 650 Ma seismites (limited), which may indicate the response of the NCC to the dispersal of the 'Nuna' and the Rodinia supercontinent (Qiao and Gao, 2000; Zhang et al., 2012b; Zhao and Guo, 2012).

2.3. Paleogeography

According to several authors (e.g., Li et al., 2008; Lu et al., 2002; Zhang et al.,

2012b), the NCC appears to have been located in an environment resembling the margin of a large continental plate (e.g. a supercontinent) between ca. 1800- 600 Ma (or until ca. 500 Ma (Metcalfe, 2013)). During this time, the NCC may have been episodically close to extensional centers, e.g. a passive margin (Allen et al., 2015; Lu et al., 2002; Ying et al., 2012); while major plume activities may not have directly affected the NCC (Li et al., 2008) (see Fig. A2.1A-C).

When it came to Phanerozoic times (< ca. 540 Ma), the NCC was isolated and wandered within the middle latitude regions (see Fig. A2.1 D-H). It started to be directly affected by subduction/collision events since ca. 300 Ma (see Fig. A2.1 F) (Liu et al., 2004; Wan et al., 2005; Zhang et al., 2009). During ca. 210-140 Ma, the NCC was predominantly in a convergent state; occasionally, it may have been close to extensional centers caused by paleo-Pacific subduction, as evidenced in the early Jurassic (ca. 180 Ma) pro-type basins in the northern ENCC (see Fig. A2.1H) (Li et al., 2012; Maruyama et al., 1997; Meng, 2003; Ritts et al., 2001; Wu et al., 2005).

2.4. Lithospheric mantle beneath the NCC

The characteristics of the pre-destruction NCC mantle are mainly revealed in the studies of the kimberlite-bearing mantle xenoliths which were erupted at ~460 Ma (see Fig. 1.1 for locations). Although mantle xenoliths are sparse and limited information is available, important observations are forthcoming: 1) parts of the mantle beneath the ENCC appear to have a Proterozoic age (ca. 1.5 Ga) (Gao et al., 2002), much younger than the overlying crust (ca. >2.5 Ga); 2) these mantle xenoliths show similar Zr/TiO_2 and Zr/Y trends like some stable cratons, which may indicate the effects of mantle metasomatism (see Fig. 2.2); 3) the Mg# and Fo found in these xenoliths have a much wider range (from <88 to >93), unlike those of stable cratons that focus around 92 (see Fig. 2.3C-D); and 4) parts of the ENCC mantle appear to have a higher proportion (>50%) of Ca-rich harzburgite compared to stable cratons (~20%) (Griffin et al., 1998).

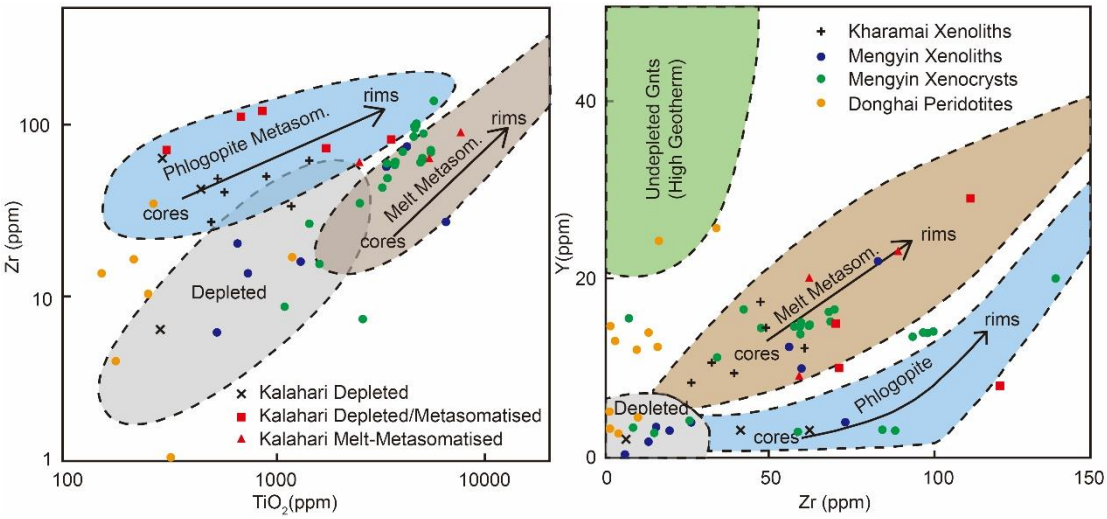

Fig. 2.2. Trace element geochemistry of mantle xenoliths and xenocrysts on several Archean cratons.

Before the on-ENCC magmatism (ca. 180), the mantle composition of the central ENCC (Mengyin kimberlite, ca. 460 Ma) (Chu et al., 2009; Lu, 2010; Zheng et al., 2006; Zheng et al., 2005) was modified by metasomatism processes similar to those in the Kalahari and Kharamai cratons (Griffin et al., 2005; Griffin et al., 2003). Footprints of metasomatism processes are much weaker in the southern edge of the ENCC, as reflected in the composition of CCSD-PP1 peridotites (Zheng et al., 2006; Zheng et al., 2005). Because these peridotites were brought to a shallow crustal depth between ca. 240 and 220 Ma (Zheng et al., 2006), their composition may resemble that of lithospheric mantle before the ENCC destruction.

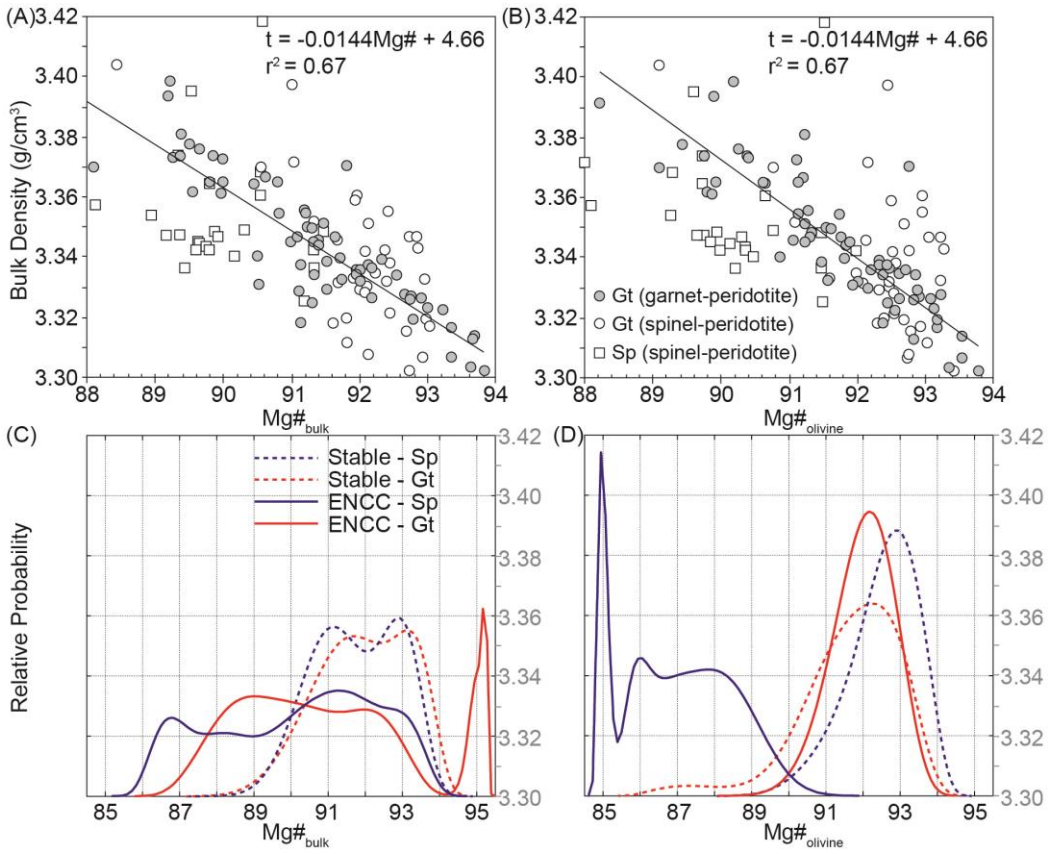

Fig. 2.3. Mg# and Fo of the pre-destruction mantle xenoliths on the NCC.

Panels A-B: Relationship between Mg# atomic (100×Mg/ (Mg+ Fe_T)) and STP bulk density of mantle xenoliths. Mg# is expressed in the bulk (Panel A) or in olivine (Panel B) (Lee, 2003). Thick solid lines represent regression through all the data. STP conditions: standard temperature and pressure: 25°C and 1 atm. GT- Garnet facies, SP- Spinel facies. **Panels C-D**: Mg# of mantle xenoliths from stable cratons (marked by 'stable') (Bernstein et al., 2006; Beyer et al., 2006; Boyd et al., 1997; Griffin et al., 1996; Griffin et al., 2005; Griffin et al., 2003; Hanghøj et al., 2001; MacKenzie and Canil, 1999; Schmidberger and Francis, 1999) and the ENCC (>180Ma) (Chu et al., 2009; Gao et al., 2002; Lu et al., 2004; Lu et al., 1991; Zhang et al., 2008; Zheng et al., 2005). Compared with stable cratons, the ENCC mantle xenoliths have a wider Mg# range. Grey solid lines are from the regression lines in Panels A and B.

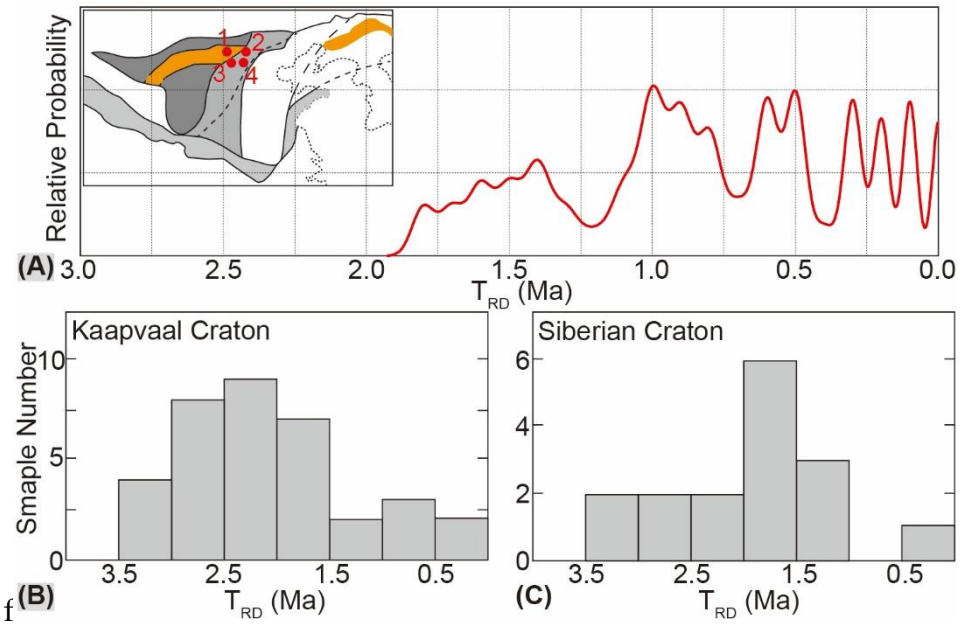

Fig. 2.4. The Re-depletion model age (T_{RD}) of basalt-bearing mantle xenoliths.

(A) Re-depletion model age (T_{RD}) of basalt-bearing mantle xenoliths from the North China Craton (Liu et al., 2011). Sampling locations: 1- Hannuoba, 2- Yangyuan, 3- Jinling, 4- Datong, 5- Fushan, 6- Hebi. Most of the above basaltic magmatism occurred <<120 Ma (except Fushan, ca. 125 Ma (Xu et al., 2010)); the T_{RD} of entrained mantle xenoliths may record major mantle events since its formation (or replacement). **Panels B-D**: T_{RD} of peridotites from the Kaapvaal and Siberian cratons. In both cratons, a higher proportion of the T_{RD} clusters in the pre-Cambrian times (> ca. 540 Ma).

More information about the pre-destruction NCC mantle can be collected through studying basalt-bearing mantle xenoliths (Liu et al., 2011). Although these basalts were erupted after cratonic destruction (ca. <150 Ma), the relatively old (ca. 1.8 Ga) T_{RD} of the entrained xenoliths suggest that they record parts of pre-destruction mantle evolution (see Fig. 2.4 A). As shown in Fig. 2.4A, these mantle xenoliths also reveal the presence of young mantle (< ca. 1.8 Ga) beneath parts of the NCC. Fig. 2.4A also reflects an increased number of age peaks in ca. <500 Ma Phanerozoic times (see Fig and Gao et al. 2002), in contrast with the Kaapvaal and Siberian Cratons where less Phanerozoic age peaks are found in T_{RD} (see Fig. 2.4). This T_{RD} pattern may indicate that the material interchange between parts of the

NCC keel and underlying asthenosphere became more vigorous in Phanerozoic times (cf. (Pearson et al., 1995)).

3. Sedimentary cover on the NCC

A unique feature of the NCC's pre-destruction evolution comes from the on-craton sedimentary record. The NCC appears to be the only Archean craton where >30% was covered by sea water (Algeo and Wilkinson, 1991). More specifically, its eastern parts ENCC and TNCO were submerged by an epeiric sea at least three times before craton destruction (see Fig. 2.5) (Lu et al., 2002; Watson et al., 1987; Ying et al., 2012; Yuan, 1996).

This special sedimentary evolution of the NCC is illustrated in Fig. 2.5. In the Mesoproterozoic (ca. 1.6-1.2 Ga) rifting episode, the NCC locally recorded >8 km sedimentation (see Fig. 2.5A) (Lu et al., 2004; Ying et al., 2012). This syn-rift sedimentation was terminated by the Qinyu Uplift at ca. 1.0 Ga (Allen et al., 2015; Lu et al., 2002; Ying et al., 2012), coeval with the assembling of the Rodinia Supercontinent (Condie, 2015; Li et al., 2008). Since then, the NCC partly came into an intra-continental basin stage, accepting epeirogenic sedimentation and episodic basin inversions. The sedimentation was centered on the ENCC, where a ~500 m thick sequence can still be locally identified (Liu et al., 1996; Lu et al., 2002; Lu et al., 2008; Ying et al., 2012). This pre-Cambrian sedimentation continued to ca. 570 Ma to the east of the Tan- Lu Fault zone (see Fig. 2.5B); while in the west, it was separated from younger strata by a sedimentary hiatus at ca. 800- 530 Ma, roughly coeval with the assembling process of the Gondwana Supercontinent (Condie, 2015; Lu et al., 2002; Yuan, 1996).

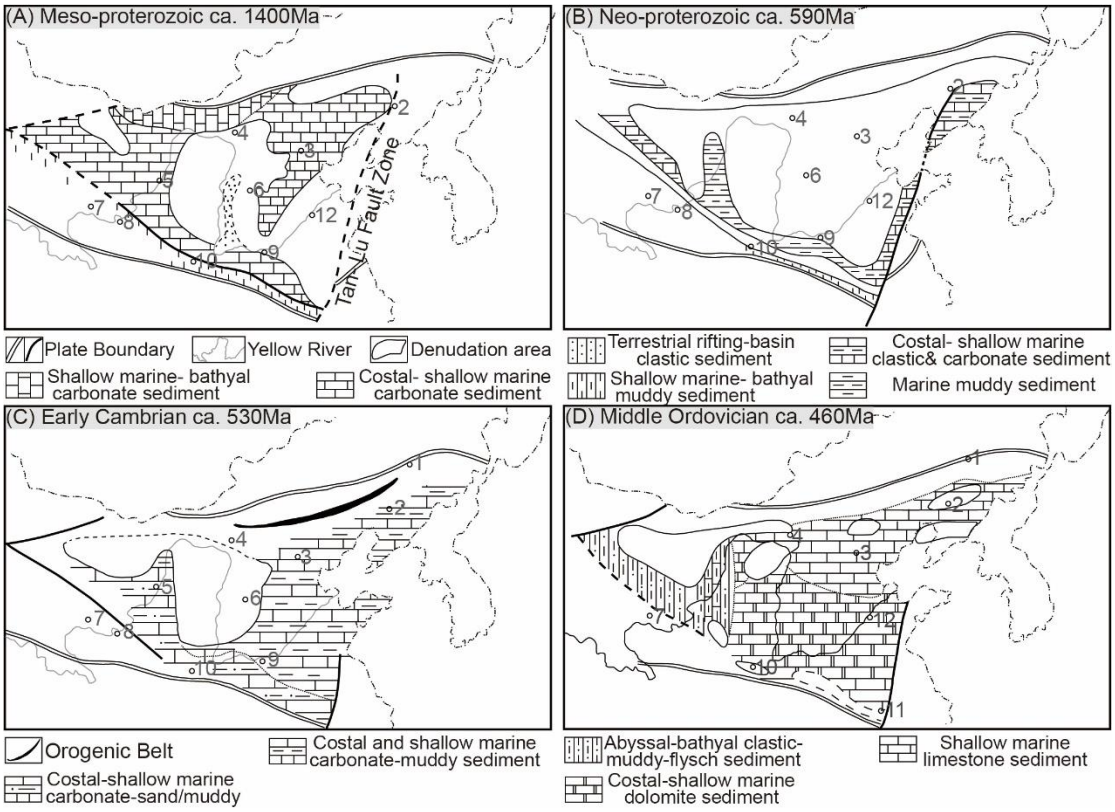

Fig. 2.5. The sedimentary evolution of the North China Craton.

Modified after (Liu et al., 1996; Watson et al., 1987).

(A) Syn-rifting marine-facies sedimentation during ca. 1.6-1.2 Ga.

(B) After the rifting episode, sediments mainly disturbed in regions to the east of the Tan-Lu fault zone.

(C-D) A flare-up of marine-facies sedimentation occurred on the NCC in the Cambrian times, which continued into the Ordovician times. The isopach of the sediments has a saucer-like shape (see Fig. 2.6).

(E-F) The first basin inversion episode in the Phanerozoic times.

(G) The NCC was covered by sea water again, indicating a second subsidence stage (also see Lines 5 and 7 in Fig. 2.6).

(H) The NCC mostly left the marine sedimentary environment.

(I) The Jurassic sedimentation is sparsely found on the ENCC.

(J) Since ca. 140 Ma, the ENCC came into a rifting episode, revealed in widely-spread syn-rifting basins. City name: 1- Changchun, 2 Shenyang, 3- Beijing, 4- Huhehaote, 5- Yinchuan, 6- Taiyuan, 7-Xining, 8- Lanzhou, 9- Zhengzhou, 10- Xi'an, 11- Hefei, 12 Jinan.

During Phanerozoic times (since ca. 530 Ma), the NCC experienced another two episodes of basin subsidence and inversion, which appear to be not clearly related to any rifting event (see Fig. 2.5C-J) (Xie, 2007; Zhu et al., 2012a). The subsidence still centered on the ENCC between ca. 530-450 Ma, and the basin remained a saucer-shape (see Fig. 2.6B-C), accumulating >1.5 km thickness of marine-facies sediments (Li, 2007; Lv, 2009; Watson et al., 1987; Xie, 2007; Yuan, 1996). Its first inversion occurred at ca. 450-360 Ma (see Fig. 2.5E) (Liu et al., 1996; Meng et al., 1997; Watson et al., 1987), coeval with the Caledonian-time orogeny (ca. 490-390 Ma) recorded along the margin (Condie, 2015; Song et al., 2014; Xiao et al., 2003).

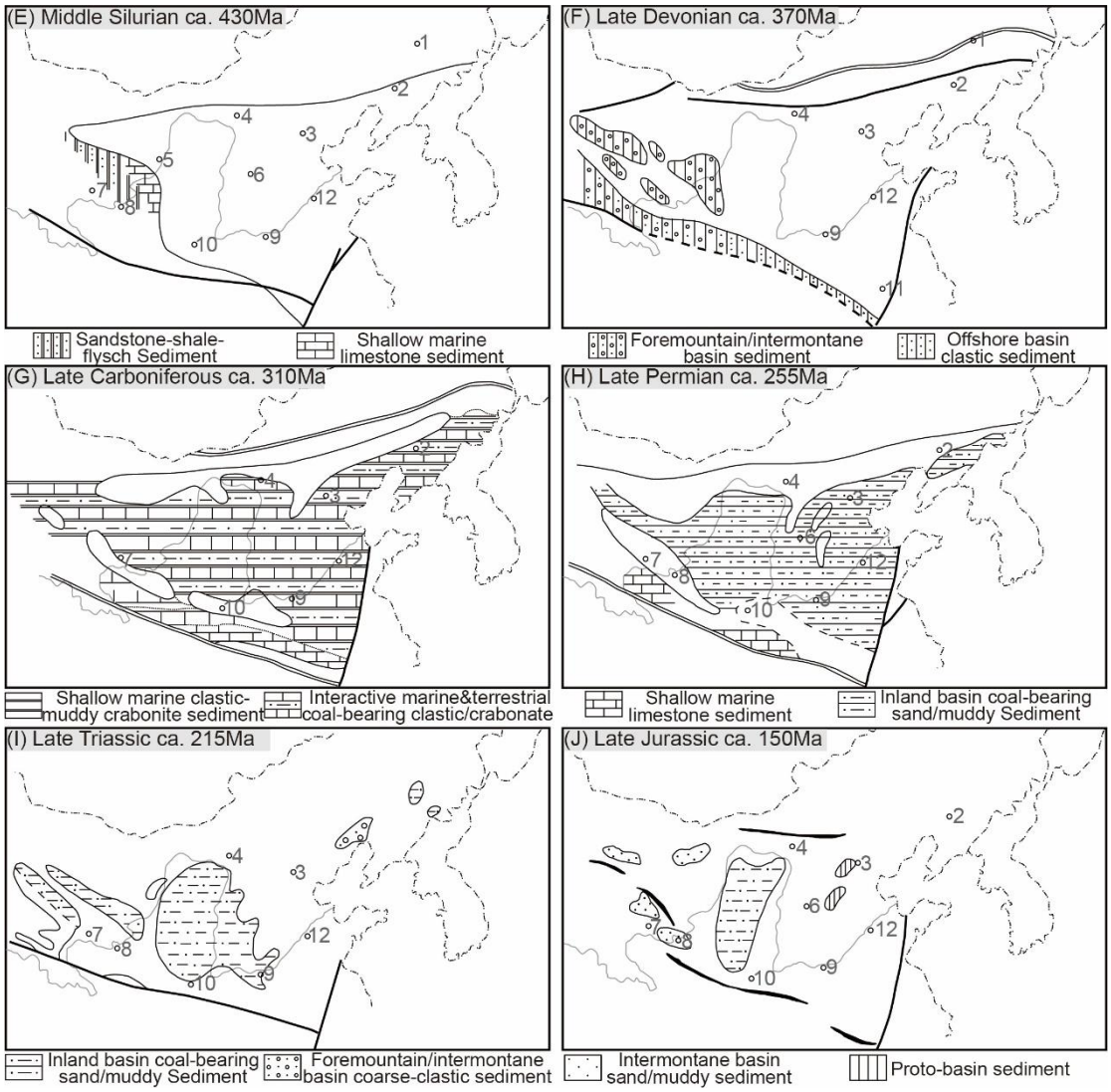

Fig. 2.5. (continued)

Since ca. 360 Ma, along with the ending of the former convergent state, the southern margin of the ENCC started to accept offshore & marine-terrestrial facies sediments (e.g. in north Dabie region) (Yuan, 1996). In the meanwhile, the rest of the craton was nearly flat lowland (with the elevation <200 m). Later in the late Carboniferous times (ca. 320 Ma), transgressive episodes happened, and sea water covered most of the NCC surface (see Fig. 2.5G) (Mueller et al., 1991).

Roughly contemporary with strengthened subduction/collision along the margin since ca. 300 Ma, the NCC gradually left the marine sedimentary environment (see Fig. 2.5H) (Xie, 2007; Yuan, 1996). Its Triassic (ca. 250-200 Ma) sequence is not preserved on the ENCC (see Fig. 2.6I), although the isopach map of the sequence on the western North China Craton (WNCC) still shows an eastward thickening trend (see Fig. 2.6D). In the early Jurassic (ca. 180 Ma), this trend is reversed, and the sequence on the WNCC appears to thin out towards the east (see Fig. 2.6F).

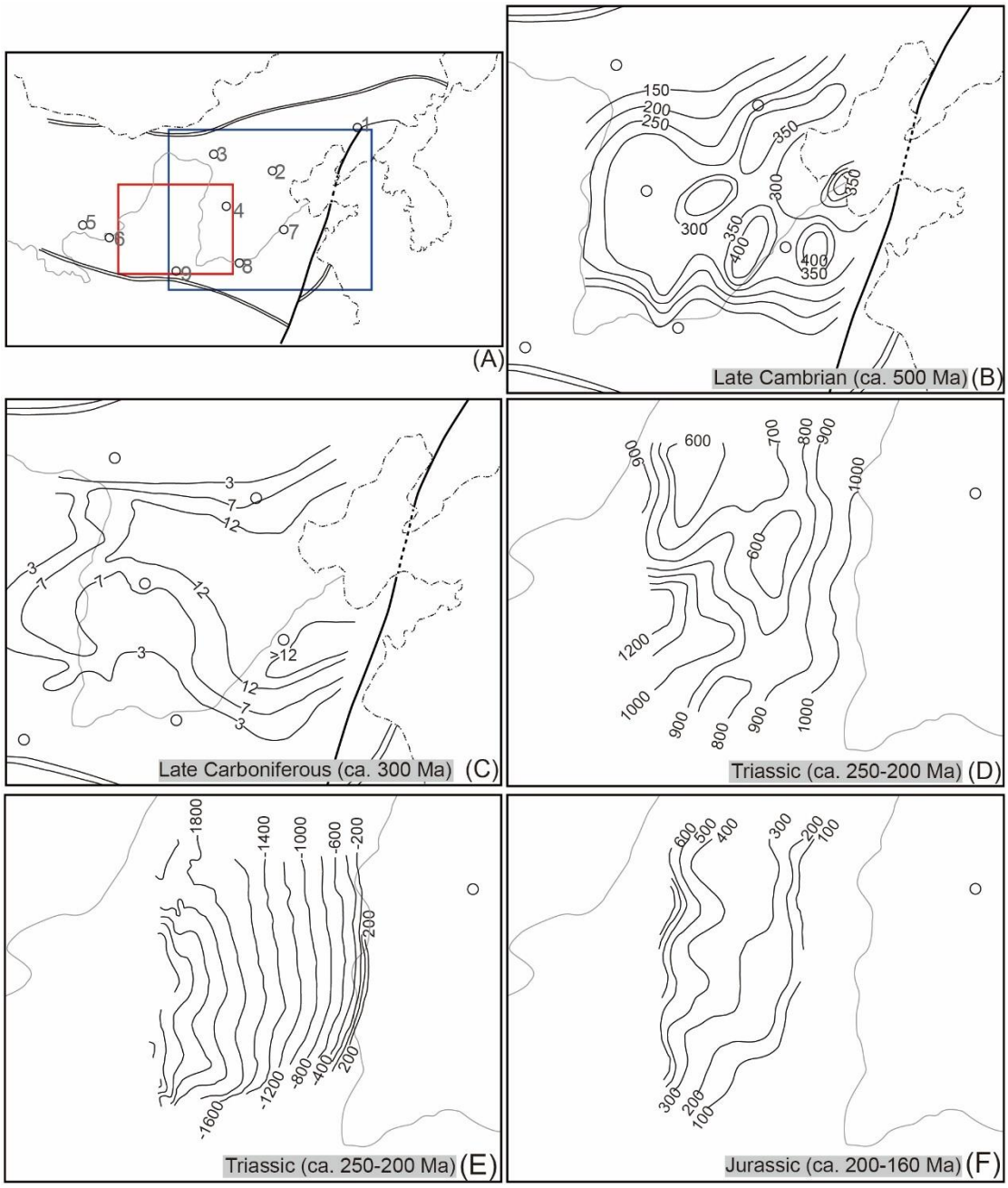

Fig. 2.6. Basin evolution on the NCC.

(A) Locations for the following Panels. Panels B-C are from the location of the blue box, Panels D-F are from the location of the red box. City Names: 1- Shenyang, 2- Beijing, 3- Huhehaote, 4- Taiyuan, 5-Xining, 6- Lanzhou, 7- Jinan, 8- Zhengzhou, 9- Xi'an. (B) Isopach map (in meter) of Late Cambrian (ca. 500 Ma) sequence (Li, 2007). (C) Isopach map (in meter) of the Late Carboniferous (ca. 300 Ma) sequence (Lv, 2009). (D) Isopach map (in meter) of the Triassic (ca. 250-200 Ma) sequence, the southern Ordos Basin (Xie, 2007) (E) Structure contour map of the base of the Triassic deposits, the southern Ordos

Basin (Xie, 2007). (F) Isopach map (in meter) of the Jurassic (ca. 200-160 Ma) sequence, the southern Ordos Basin (Xie, 2007)

4. A partly failed North China Cratonic Basin

Burgess (2008) divided cratonic regions into three categories based on the thickness of preserved strata: shield (no preserved strata), platform (~1 km thick strata) and cratonic basin (>1km thick strata). In this perspective, the surface of the ENCC and the eastern WNCC can be classified as a cratonic basin (i.e. before ca. 140 Ma); and its saucer-shape (see Fig. 2.7B-C) and relative long-term (>300 Myr) subsidence history share the common features of cratonic basins (see Fig. 2.7) (Allen and Armitage, 2009; Armitage and Allen, 2010; Crosby et al., 2010; Quinlan, 1987). For convenience, 'North China Cratonic basin (NCCB)' is referred to as the cratonic basin used to cover the NCC.

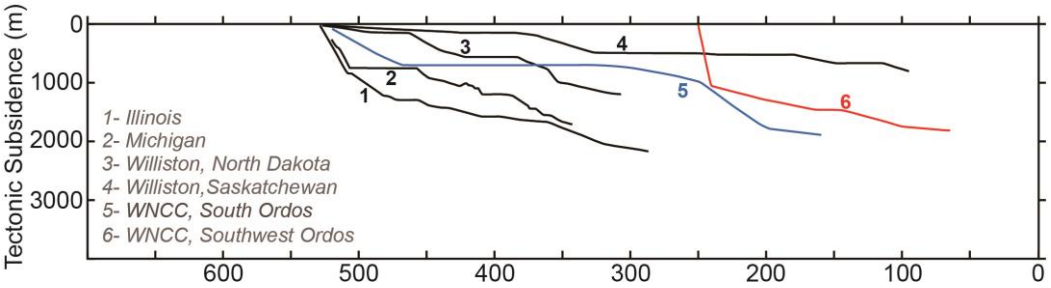

Fig. 2.7. Tectonic subsidence of some well-known cratonic basins.

Lines 5 and 6 are from western North China Craton, which still retained its cratonic keel. Modified after (Xie, 2007; Xie and Heller, 2009).

The preserved sequence indicates a major basin inversion event on the ENCC, which may have occurred between Late Triassic and Middle Jurassic times (ca. 200- 160 Ma). Although the Triassic sequence is not preserved on the ENCC, the eastward thickening trend of the isopach map on the WNCC (see Fig. 2.6D) precludes an obvious differential uplift of the ENCC during this time (ca. 250-200

Ma). On the other hand, because the base of the Triassic sequence on the WNCC has been differentially uplifted towards the east (see Fig. 2.6E), the absence of the Triassic sequence on the ENCC could have been due to later denudation. Given that the Jurassic sequence on the WNCC thins out towards the east, the ENCC had most likely uplifted at ca. 180-160 Ma, consistent with the previous conclusions (Yang et al., 2006).

In this way, the keel-intact WNCC appears to have survived the major basin inversion event in the Mesozoic time (ca. >160 Myr) (see Fig. 2.5I-J& 2.6) (Xie, 2007; Xie and Heller, 2009). Differently, the ENCC has not only experienced cratonic destruction, but also has lost its craton-type basin used to cap its surface for >ca. 300 Myr.

5. How did a cratonic basin form upon the NCC?

As we noted above, no later than ca. 1.0 Ga, the eastern NCCB has started to subside and to accept marine facies sedimentation. Intuitively, this feature looks 'normal' because almost all present cratons have platform portions, which are capped by Phanerozoic sedimentary covers (Burgess, 2008; Kovtun, 1976; Xie and Heller, 2009).

However, an isostatic craton is expected to be 'much higher than sea level'. If the keel density and crustal thickness of the NCC resemble averaged values of cratons (ca. 3310 kg/m^3, ca. 40-50 km thick crust) (Lee, 2003; Xia et al., 2017), the paleoaltimetry of the NCC would be, if not higher than, comparable to the present-day averaged value of global cratons (ca. > 500 m) (Vérard et al., 2015). Given that the estimated sea level at *ca.* 300-250 Ma was <100 m higher than the present-day (see Fig. 2.8A):

1) how could the NCC surface have been at least 400 m lower than the average elevation value of global cratons since ca. 1.0 Ga?

2) how had the NCCB sustained subsidence for >300 Myr and subsided

for >1.5 km? *i.e.* from ~500 to ~200 Ma.

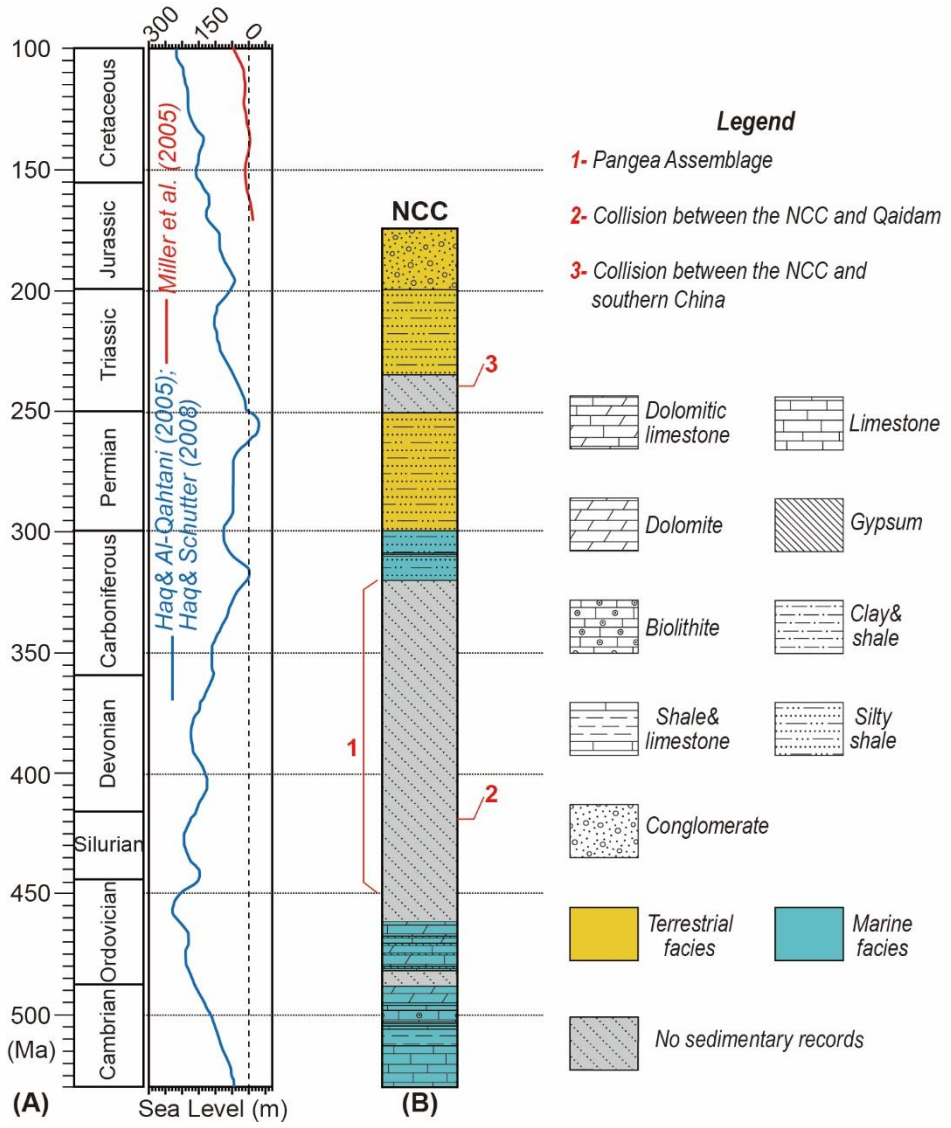

Fig. 2.8. Simplified sedimentary column on the NCC.

(A) Reconstruction of the Phanerozoic eustatic sea level (Conrad, 2013). (B) Simplified sedimentary column on the NCC (Liu et al., 1996; Watson et al., 1987).

Before attempting to answer both questions, we need to rule out the effect of the eustatic sea-level, which is variable (see Fig. 2.8A) due to fluctuations of climate, ridge-spreading rate, and magmatic production rate on sea floor (Bond, 1978; Conrad, 2013; Kominz, 1984). However, the sea-level change alone can be pale in explaining up-/ down- warping of cratonic basins (Bond, 1978; Gurnis, 1990; Müller et al., 2008). As shown in Fig. 2.5 & 2.8, the NCCB was flooded by

sea water even when the eustatic sea-level was low during ca. 320-300 Ma; while during some sea-level-high periods (ca. 390 Ma and 100 Ma), it experienced denudation and lacked sedimentary records.

5.1 Shallow-origin mechanisms leading to cratonic subsidence

Lithospheric extension

As previously introduced, no lithospheric extension has been identified to be coeval with NCCB subsidence. The lack of any extensional records might be due to the fact that the strong cratonic keel had effectively resisted stretching (cf. (Corti et al., 2013; Sleep, 2003)). In contrast such stretching would not have been resisted by relatively thin Proterozoic terrains (ca. 120-160 km) (or Mobile Belts) (see Fig. 1.2B). For example, lithospheric extension in the African continent led to focused rifting along the Proterozoic portion, which was accompanied by bimodal magmatism (Corti et al., 2013; Morley, 2010). Similar Proterozoic terranes also exist on the NCCB (see. Fig. 1.2B), but obvious lithospheric extension and related-magmatism only happened after ca. 180 Ma (cf. (Li et al., 2012; Zhu et al., 2012b)).

Lack of extensional records on Proterozoic terranes can also be due to the fact that paleo-extensional direction(s) sub-paralleled the trend of weak zones, especially when the extensional rate is low (e.g. ~10^{-16}/s) (Armitage and Allen, 2010). If this was the case, the process leading to surface subsidence should have also thinned the crystalline basement, especially the ductile middle crust by ca. 1.1-1.3 (e.g. the Russian Platform) (Armitage and Allen, 2010; Artemieva, 2003, 2007). However, the thickness of the crust and middle crust in the stable NCC portions seems ‘normal’ compared to the average value of global cratons (Xia et al., 2017).

Effects of subduction

The effects of an adjacent subduction process can be three-fold. The first is caused by loads of the oblique slab and wedge sediments. These loads can

elastically bend the continent >1 km to further accept marine sediments (Dávila and Lithgow-Bertelloni, 2015; Gurnis, 1992, 1993). The second effect is suggested to be caused by a flattened slab. Due to piling of a cold slab at the base of the continent, the compensated continental surface could remain low before heating-up or the foundering of the slab (Liu et al., 2010; Liu et al., 2008). At last, a long-term subduction process may create density anomalies within the deep mantle, and thus drive a downwelling mantle. A plate may experience plate-scale subsidence above downwelling mantle, (Bertelloni and Gurnis, 1997; Gurnis, 1990).

However, when adjacent to active subduction zones during ca. 300-200 Ma (see Fig. A2.1), the NCCB was partly inverted to experience denudation (see Fig. 2.5H-I and 2.8B); on the other hand, the dynamic subsidence related to subduction is estimated to be <150 ± 50m, which is too small to explain the >1.5 km down-warping of the NCCB surface.

Load of piedmont sediments

In regions close to the margins of an orogenic belt, supracrustal loads can push the wedge downwards and create a 'foreland basin' (Beaumont, 1981; Garcia-Castellanos et al., 1997). This scenario differs from the subduction scenario by assuming a weak effect of the bending-stress attached to the margin (Beaumont, 1981). However, because of both the 'Andean-type' orogeny at its northern margin (ca. 230 Ma) and the continental collision at its southern margin (ca. 210 Ma), the NCCB lacks marine-facies sedimentary records.

Load of glacial sediments

As shown in Fig. A2.1, the NCC was in mid-latitude regions in the Phanerozoic time. Glaciation should not have affected its elevation like the Kaapvaal, Eastern European and eastern Atlantic Cratons, which ever lingered in a polar region (Müller et al., 2008).

5.2 Deep-origin mechanisms leading to cratonic subsidence

As we noted above, the long-term subsidence of cratonic basins has also been suggested to be caused by the downward drag of the dense keel (Artemieva, 2003, 2007; Downey and Gurnis, 2009). Compared with the isopycnic theory (Jordan, 1988), mantle metasomatism, different craton origins and mantle rejuvenation may shift the density structure of craton towards less compensated, and therefore create a relatively denser keel than surroundings (see Introduction). Here, we summarize the available evidence on the NCC that may support these mechanisms.

Mantle Refertilization

Possible evidence supporting this mechanism is revealed in the geochemistry of the kimberlite-borne xenoliths/xenocrysts on the ENCC, whose 1) Zr/Ti and Y/Zr ratios follow the trend of mantle metasomatism indicating refertilization (see Fig. 2.2); and 2) Mg# and Fo have wider distribution range than stable cratons (see Fig. 2.3C-D). Although these may indicate that parts of the cratonic keel appears to dense (see Fig. 2.3A-B), the limited sample numbers make it hard to further constrain the general condition of the pre-existing ENCC keel.

Different cratonic origins

As we noted above, the oldest age of the mantle beneath the northern ENCC and TNCO is ca. 1.8 Ga (see Fig. 2.4A), ca. 0.7 Ga younger than that of the overlying crust (Zhao and Zhai, 2013). To explain this age decoupling shown in both old and young mantle xenoliths, it has been proposed that the former old mantle had been extruded away and have been replaced by a younger ca. 1.8 Ga mantle (Gao et al., 2002; Liu et al., 2011). Therefore, it is possible that the northern ENCC had started to bear a relatively denser keel base since as early as ca. 1.8 Ga, e.g. leading to the Proterozoic transgressions on the northern ENCC and TNCO.

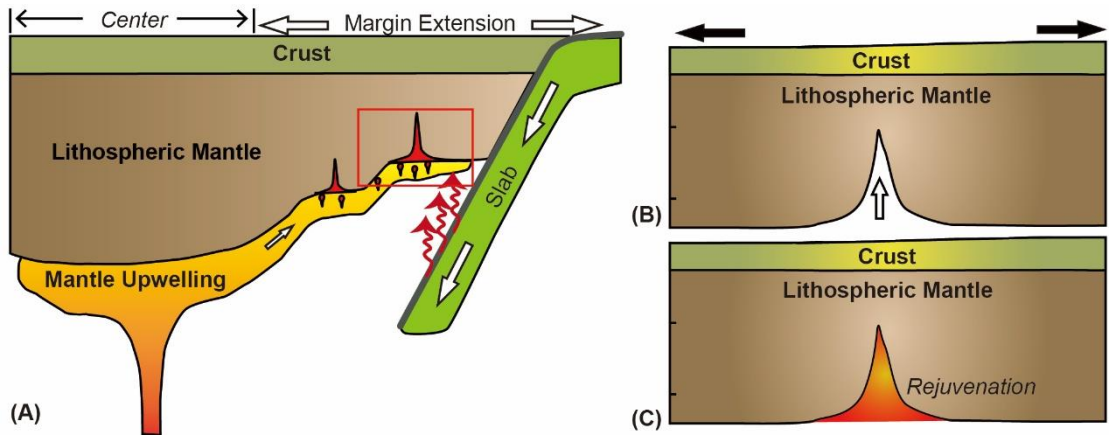

Fig. 2.9. Conceptual model of mantle rejuvenation.

(A) Mantle upwelling impacts on a cratonic keel with stepped basal topography. The low-viscous fusible components can be diverted towards thinner portions of the keel by buoyancy, e.g. the ENCC which distributed at continental edge (see Fig. A2.1). When reaching a shallow depth (ca. <200 km), the fusible components start to melt.

(B) Due to surrounding tectonics, e.g. subduction, mild lithospheric extension reactivates fractures within the keel, facilitating upward melt migration (see the red rectangle in Panel A for scale).

(C) . After cooling down, parts of the melt remain within the cratonic keel and may experience eclogite phase change, leading to mantle rejuvenation and keel-density increasing. Thereafter, the dense keel drives a prolonged cratonic subsidence.

Extension-related mantle rejuvenation

In an extensional setting, pre-existing lithospheric fractures within a craton can possibly be reactivated, which allows injection of the asthenosphere into cratonic keel and as a consequence cratonic mantle rejuvenates (see Fig. 2.9A-B) (Foley, 2008; Foley and Fischer, 2017). Due to a low extent of melt extraction (<<30%) (Lee et al., 2011), the newly accreted material can be dense (3390- >3340 kg/m^3) (Artemieva, 2003; Djomani et al., 2001), whose density can be further increased after basaltic composition experiences eclogitization phase change (Naimark and Ismail‐Zadeh, 1995; O'Reilly and Griffin, 2013). Possibly, the ca. 1.6-1.2 Ga rifting episode on the margin may have led to the partial rejuvenation

of the ENCC keel, and further mantle rejuvenation may occur rather implicitly due to far from extensional centers, e.g. in the < ca. 500 Ma Phanerozoic times (see Fig. 2.4A).

In summary, compared with shallow-origin mechanisms, a dense -keel-induced NCCB subsidence appears to be better supported by observations on the ENCC. The dense cratonic keel could have been originally created during the ca. 1.8 Ga craton amalgamation, partly rejuvenated during the 1.6-1.2 Ga rifting episode, and experienced enhanced rejuvenation and/or refertilization during subsequent >1 Ga mantle evolution (see Fig. 2.9).

Then, the question left would be, if a dense cratonic keel can lead to a long-term subsidence of cratonic basins as being suggested?

6. A simple numerical model of the NCCB subsidence

To test whether a dense cratonic keel can lead to a long-term subsidence of the NCCB, we deigned a group of simple 2-D numerical experiments. The numerical experiments are calculated with a modified version of “m2tri_trunk”, which has been successfully utilized to study the problems like the passive margin rifting, subduction and convective erosion (Hasenclever, 2010; Hasenclever et al., 2011; Ros et al., 2017) (also see Chapters 3-5). This method has a free surface boundary condition (Andres-Martinez et al., 2015). To study the tectonic subsidence of craton, the effects of sedimentation and erosion on topography are not included. Other details of the numerical method can be found in the Appendix.

6.1 Model set-up

The computational domain is a 2-D 3000 km wide × 600 km deep box (see Fig. 2.10). In solving the viscous flow evolution, we utilize a free surface boundary condition for the upper boundary segment and a free slip boundary condition for the result. For computational simplicity, temperature is treated as a potential

temperature. The heat flux across the left and right boundary segments is set to be 0. Potential temperature is set to be 0°C at the top boundary, and 1350°C at the base of the computational box.

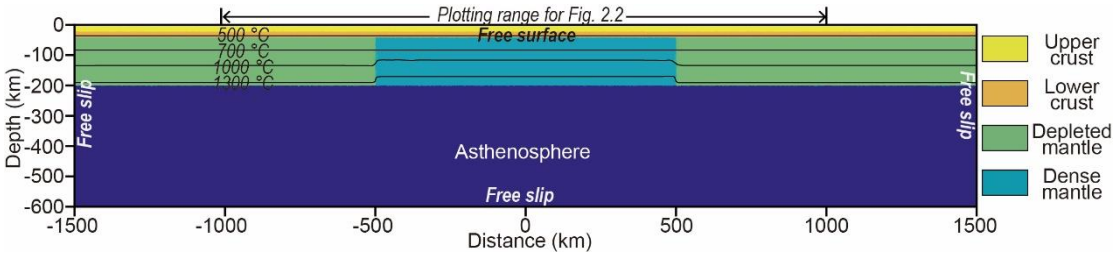

Fig. 2.10. The 2-D box for numerical experiments.

This computational domain is a mesh of triangular elements with small element sizes (~5 km) near internal boundaries between different materials. Element sizes are 10 times larger than this (~50 km) in regions far from internal material interfaces, at transitional distances element size is linearly interpolated between these two end-member values. The cratonic lithosphere is set to be 200 km thick, which contains a 20 km thick upper crust, a 20 km thick lower crust, and a 160 km thick lithospheric mantle. The initial temperature profile is given by a 1-D steady-state conductive thermal profile (Turcotte and Schubert, 2014) assuming the lithospheric bottom is at 200 km deep. The initial temperature of the >100 km deep portion of dense mantle is creased by 100-200 ˚C (see details in text).

We assume that before the initial NCCB subsidence and its following accelerated subsidence (see Fig. 2.7), some melts were added into the keel (see Fig. 2.9), which enhanced the keel bottom (>100 km deep) temperature by 100-200 ˚C (see the example for the initial temperature structure in Fig. 2.10 and see Tab. 1 for parameters in different runs). During cooling down, parts of the frozen melts may experience eclogitization phase change as suggested in (Naimark and Ismail‐Zadeh, 1995; O'Reilly and Griffin, 2013). This phase-change-induced dense increase is crudely implemented with the following equation (Naimark and Ismail‐Zadeh, 1995).

$$\overline{\rho}(t) = \overline{\rho}_0 + \overline{\Delta\rho}\left(1 - \exp(-\gamma t)\right) \quad (1)$$

$\overline{\rho}(t)$ is the averaged density of the cratonic mantle at time t. $\overline{\rho}_0$ is calculated density for the cratonic mantle (see Eq. 2). $\overline{\Delta\rho}$ is the assumed average dense change caused by phase change. γ is a time constant. To match the subsidence pattern for the NCCB, this parameter is varied in runs as recommended in Refs. See Tab. 1 for parameters.

The equation of state for density is:

$$\overline{\rho_0} = \rho_0 \exp\left[-\int_{T_0}^{T_F} \alpha\left(P = P_0, T\right) dT + \int_{P_0}^{P_F} \frac{dP}{k}\right] \quad (2)$$

$$\alpha = \alpha_0 + \alpha_1 T + \alpha_2 T^{-2} \quad (3)$$

where ρ_0 is the reference density, α is the temperature dependent thermal expansion coefficient at $T_0 = 20^{\circ}C$, P_0 is atmospheric pressure, k is the bulk modulus (assumed to be constant), and T_F and P_F are the temperature (in Kelvin) and pressure.

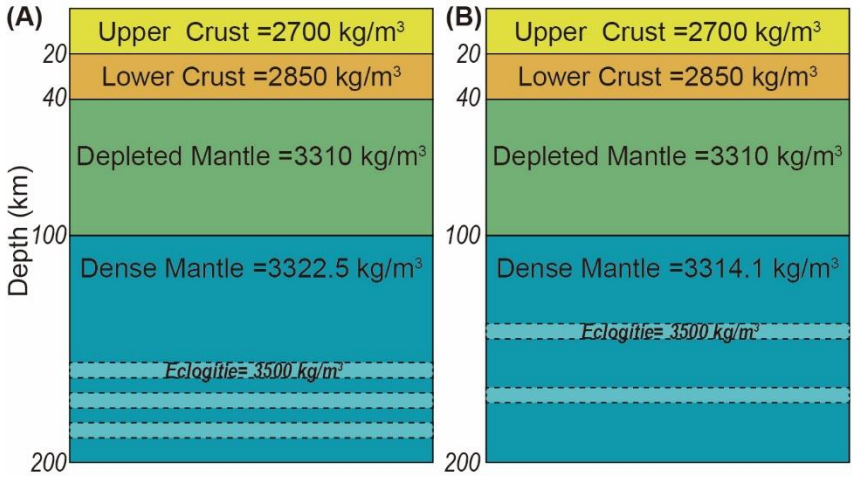

Fig. 2.11. Density structure assumed for lithospheric portion containing dense mantle. (A) in Runs 1-4, after a complete phase change, the sparsely distributed eclogite layer is assumed to be 15 km thick in total. The average mantle density before phase change is ~3312.4 kg/m^3 and after is ~3330 kg/m^3. The assumed eclogitization would increase the mean mantle density by 17.6 kg/m^3. (B) in Runs 5-9, after a complete phase change, the sparsely distribute eclogite layer is assumed to be 20 km thick in total. The average mantle density before phase change is ~3317 kg/m^3 and after is ~3340 kg/m^3, consistent with the estimation range in Djomani et al., 2001. The assumed eclogitization would increase the mean mantle density by 23 kg/m^3.

	ΔT	**ρ_0**	**Δρ**	**γ**
Run 1	100 ˚C	3312.4 kg/m^3	17.6 kg/m^3	0.02
Run 2	100 ˚C	3312.4 kg/m^3	17.6 kg/m^3	0.03
Run 3	100 ˚C	3312.4 kg/m^3	17.6 kg/m^3	0.05
Run 4	200 ˚C	3312.4 kg/m^3	17.6 kg/m^3	0.05
Run 5	100 ˚C	3317 kg/m^3	23 kg/m^3	0.02
Run 6	100 ˚C	3317 kg/m^3	23 kg/m^3	0.05
Run 7	200 ˚C	3317 kg/m^3	23 kg/m^3	0.02
Run 8	200 ˚C	3317 kg/m^3	23 kg/m^3	0.03
Run 9	200 ˚C	3317 kg/m^3	23 kg/m^3	0.04

Tab. 2.1. Parameters used in different runs.

ΔT is the temperature increase assumed for the >100 km deep part of the dense cratonic mantle. ρ_0, Δρ and γ are used for calculating the density increment for the averaged density of the dense mantle after eclogite phase change (see Fig. 10 and more details in text).

We also assume that the cratonic mantle has a layered structure as found in some cratons (Hu et al., 2018; O'Reilly and Griffin, 2013; Yuan and Romanowicz, 2010), e.g. it has a depleted layer at 40-100 km deep, a less-depleted layer at >100 km deep and some eclogite layers scattered in the lower layer (see Fig. 2.11). For computational simplicity, these 'layers' are not represented as real layers in calculation (see Fig. 2.10) and the densities of different 'layers' are averaged to be to one equivalent density for the cratonic mantle (see Fig. 2.11).

6.2 Results

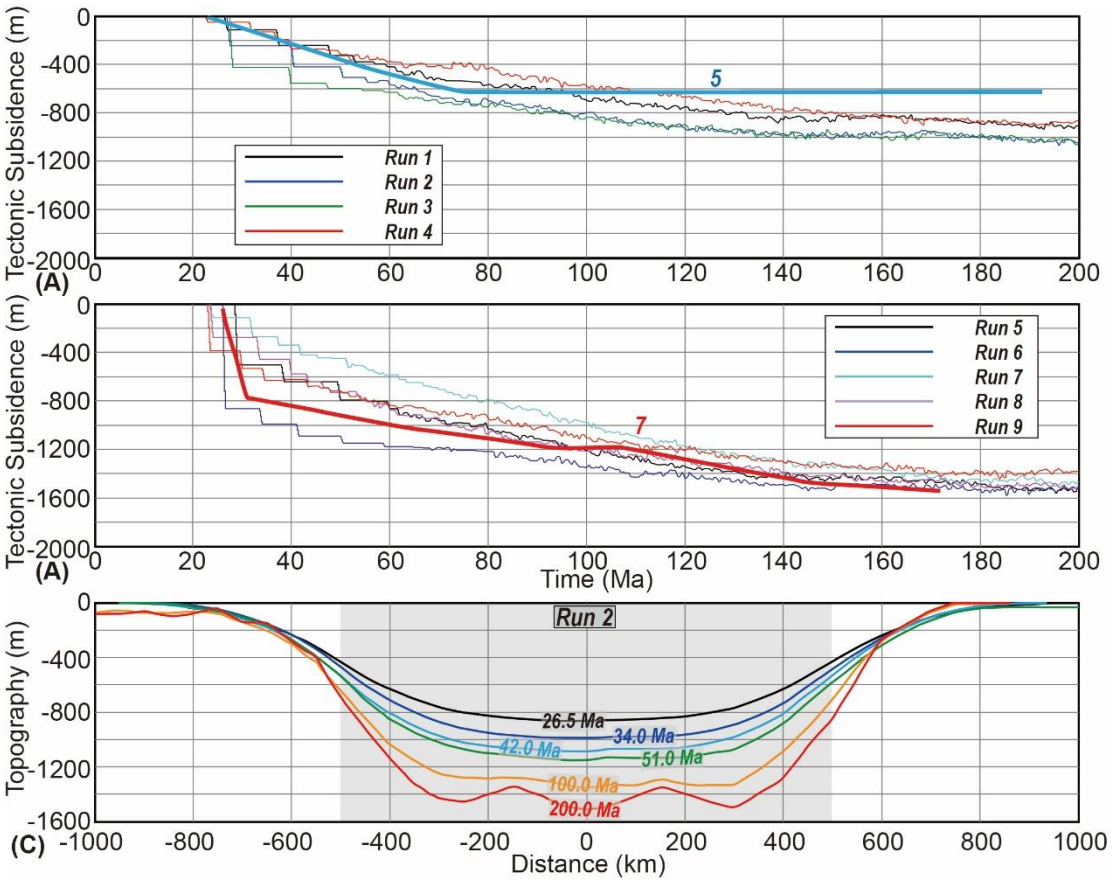

Fig. 2.12. Results for numerical experiments.

(A-B) evolution of the relative subsidence of the 'basin' bottom compared the edge. Blue thick line with 5 and red thick line with 7 are from Fig. 2.7. (C) evolution of the basin base topography in Run 6. The shadow area illustrates the range of lithosphere bearing dense keel (see Fig. 2.10).

Due to the combined effects of cooling down and eclogite phase change (see Eq. 1-3), the blue keel (see Fig. 2.10) becomes denser than the surrounding green ones. This dense different induces the differential subsidence of the surface, which centers above the blue keel. Through changing the assumed temperature change caused by mantle rejuvenation and the $\overline{\Delta\rho}$ caused by eclogite phase change, our numerical results (see Fig. 2.12) can crudely match the tectonic subsidence line of the NCCB (see Fig. 2.7). As shown in Fig. 2.12, to match the tectonic subsidence of the NCCB, the averaged mantle density after ca. 300 Ma needs to be ~10 kg/m^3

denser than that of the earlier subsidence stage (see Fig. 2.11).

7. Discussion

The experiment results support the proposition that a dense cratonic keel can lead to long-term subsidence of the cratonic surface. This dense keel also stretches parts of the adjacent surface downwards, although the adjacent keel(s) does(do) not need to be comparably dense. As we noticed above, the NCCB used to focus on the ENCC, where craton destruction occurred, and its sediments thin out towards the still-stable western NCC (see Fig. 2.5 and 2.6). This may indicate that the pre-existing ENCC keel was the major reason leading to the formation of the NCCB.

A pre-existing dense keel beneath the ENCC may also explain the inversion of the eastern NCCB at ca. 180-160 Ma. Note that, this is also the time when the earliest craton-destruction-related magmatism occurred on the ENCC (Li, 2013; Zhu et al., 2012a) (also see Chapter 4). As indicated in numerical modelling, the rebound subsequent to the removal of the dense keel is estimated to be 2-3 km to <1 km (Krystopowicz and Currie, 2013; Morency and Doin, 2004) (also see Chapter 3). Probably due to loss of the dense keel, the ENCC lost the NCCB used to cap it for >300 Ma.

As shown in Fig. 2.12, to explain the faster tectonic subsidence of the NCCB after ~300 Ma, the keel needs be ~10 kg/m^3 denser. This change can possibly be explained by the mantle rejuvenation model in Fig. 2.9. Due to the episodic mantle rejuvenation and related phase changes, the keel can gradually accumulate dense material, revealing in the increasing subsidence rate at the later evolution stage of a cratonic basin (see Lines 3-6 in Fig. 2.7).

Occasionally, the NCCB subsidence can have been inverted by surrounding orogenies (Condie, 2015; Nikishin et al., 1996), which resulted in sedimentary hiatus on the NCC (see Fig. 2.8).

8 Conclusions

1) A long-term >300 Ma subsidence is observed in the ENCC, which may suggest that a dense cratonic keel underlaid the ENCC before its destruction.

2) The results of our numerical modeling experiments support this suggestion. If correct, our work presents for the first-time solid evidence for the dense cratonic keel as a precondition for cratonic destruction.

3)The results also indicate that the increased subsidence rate observed on the NCCB after ca. 300 Ma may reflect a denser keel state in this time.

4) The dense cratonic keel beneath the ENCC can be firstly formed during the ca. 1.8 Ga Trans-North China Orogeny and was continued rejuvenated during the following evolution.

5) The destruction of the ENCC appears to be accompanied by a cratonic basin lost process in the Mesozoic times (ca. 180-160 Ma).

Appendix:

Method.

This appendix describes the algorithms that are used in this study. A modified version of 2-D Lagrangian finite element code, "m2tri_trunk" [*Hasenclever*, 2010] based on the approaches used in "MILAMIN" [*Dabrowski et al.*, 2008], is used. This thermomechanical code solves for heat transport and elastoviscoplastic deformation in crust and mantle rocks.

Temperature

For computational simplicity, temperature is treated as a potential temperature. The thermal calculation includes the effects of thermal diffusion, thermal convection, radioactive heating and shear heating (viscous dissipation) (Equation A1).

Temperature is determined from an equation governing energy conservation:

$$\rho C_p \frac{\partial T}{\partial t} = \frac{\partial}{\partial x}\left(K \frac{\partial T}{\partial x} \right) + \frac{\partial}{\partial z}\left(K \frac{\partial T}{\partial z} \right) + H \qquad \text{(A1)}$$

where ρ is density, C_p is heat capacity, t is time, K is thermal conductivity, and H is the volumetric heat production rate (including both radioactive heating and viscous dissipation).

Elastoviscoplastic Deformation

The different materials used in the model are treated as incompressible materials with use of the Boussinesq Approximation [*Turcotte et al.*, 2014]. Tracer particles are used to track seven different compositional materials (e.g. upper crust, asthenosphere, etc.). See Fig. 2.10 for the definitions of each possible material type. Each material type is associated with a specific rheology that is potentially p, T, strain-rate, accumulated strain, and plastic yield-stress dependent. Tab. S1 gives the values assumed for the experiment. The number of tracer particles within each element ranges between 7 and 25. Viscosity is calculated at every integration point

using the material phase determined by the nearest tracer particle within the element. Density is also uniform within each element with a value determined by the average of the density of each of the tracer particles within the element.

For each tracer particle, density is temperature and pressure dependent (Eq. 2-3) [*Djomani et al.*, 2001; *Schutt et al.*, 2006]. Each material rheology can include elastic, viscous, and plastic effects. Yielding and plastic flow behavior are calculated using the method described in Moresi et al., 2003 [*Moresi et al.*, 2003].

Elastoviscoplastic deformation is described using the equations for force equilibrium (A2-3) and mass conservation (A4):

$$\frac{\partial}{\partial x}\left(\eta_{VEP}\left(\frac{4}{3}\frac{\partial u}{\partial x}-\frac{2}{3}\frac{\partial v}{\partial z}\right)\right)+\frac{\partial}{\partial z}\left(\eta_{VEP}\left(\frac{\partial u}{\partial x}+\frac{\partial v}{\partial z}\right)\right)-\frac{\partial P}{\partial x}=f_x+F_x^{e,t} \quad \text{(A2)}$$

$$\frac{\partial}{\partial z}\left(\eta_{VEP}\left(\frac{4}{3}\frac{\partial v}{\partial z}-\frac{2}{3}\frac{\partial u}{\partial x}\right)\right)+\frac{\partial}{\partial z}\left(\eta_{VEP}\left(\frac{\partial u}{\partial x}+\frac{\partial v}{\partial z}\right)\right)-\frac{\partial P}{\partial y}=\rho g+f_y+F_y^{e,t} \quad \text{(A3)}$$

$$\frac{\partial u}{\partial x}+\frac{\partial v}{\partial z}=-\frac{P}{\kappa} \quad \text{(A4)}$$

In these equations u and v refer to horizontal and vertical velocity components, P is the dynamic pressure, g is the acceleration of gravity, and κ is the penalty term used for ensuring incompressibility with κ being 10^6 times the maximum effective viscosity (η_{VEP}) [*Hasenclever*, 2010]. $F_i^{e,t}$ is the internal elastic stress [*Moresi et al.*, 2003] that can be advected by material flow. This behavior is described as

$$F_i^{e,t}=-\left(\eta_{EVP}/\mu\Delta t\right)\left(\partial\tau_{ii}^{old\,J}/\partial x_i+\partial\tau_{ii}^{old\,J}/\partial x_j\right) \quad \text{(A5)}$$

where μ is elastic shear modulus, Δt is time step, and $\tau_{ii}^{old\,J}$ is the Jaumann-rotated stress of the previous time [*Kaus et al.*, 2010], given by:

$$\tau_{ij}^{old\,J}=\tau_{ij}^{old}-\omega_{ik}^{old}\tau_{ki}^{old}+\tau_{ik}^{old}\omega_{ki}^{old} \quad \text{(A6)}$$

where τ_{ij}^{old} is the is the deviatoric stress from the previous time step, and $\omega_{ij}=1/2\left(\partial u_i/\partial x_j-\partial u_j/\partial x_i\right)$.

	A.M.	D.M.	Den. M.	L.C.	U.C.
Flow Law Parameters[1-7]					
A_{dis} ($Pa^{-n}\cdot s^{-1}$)	$10^{-15.05}$	$10^{-15.56}$	$10^{-15.56}$	$10^{-21.05}$	10^{-28}
n_{dis}	3.5			4.2	4.0
E_{dis} (kJ/mol)	480	530	530	445	223
V_{dis} (cm^3/mol)	8			-	
A_{dif} ($Pa^{-n}\cdot s^{-1}$)	$10^{-8.65}$			$10^{-13.3}$	$10^{-8.4}$
n_{dif}	1				
E_{dif} (kJ/mol)	335	375	375	170	220
V_{dif} (cm^3/mol)	4			-	
Elasticity and Plasticity					
G (GPa)	74			40	36
C_0 (Mpa)	20				
Thermal Parameters					
k ($Wm^{-1}K^{-1}$)	3.3			2.5	2.1
H_r ($\mu W/m^3$)	0.033			0.25	1
c_p (J/(kg· K)	1200				
Density Parameters[6-7]					
ρ_0 ($g\cdot cm^{-3}$)	3.36	3.31	see Tab. 1	2.85	2.7
a_1(10^{-4})	0.2697	0.27165	0.27014	0.27014	
a_2(10^{-8} K^{-1})	1.0192	1.04971	1.05945	1.05945	
a_3 (K^2)	-0.1282	-0.15031	-0.1243	-0.1243	
K (Gpa^{-1})	134	129	130	63	

Tab. 2.A1. Parameters for the numerical experiments discussed in the paper.

V - activation volume. Subscript "dis" refers to parameters for dislocation creep, while "dif" is for diffusion creep. G- shear modulus, C_0- Cohesion, k- thermal conductivity, H_r- radioactive heat production, c_p-heat capacity, ρ_0- the reference density at room temperature (20℃) and pressure (0.1 Mpa), K- bulk modulus.

Abbreviations: A.M. - asthenosphere, D.M. - depleted cratonic mantle, Den. M. - dense cratonic mantle, L.C.- Lower Crust, U.C.- Upper Crust.

Parameter references: 1- [*Hirth and Kohlstedt*, 2004], 2- [*Wilks and Carter*, 1990], 3- [*Rybacki and Dresen*, 2004], 4- [*Gleason and Tullis*, 1995], 5- [*Rutter and Brodie*, 2004], 6- [*Djomani et al.*, 2001], 7- [*Schutt and Lesher*, 2006].

Figure.

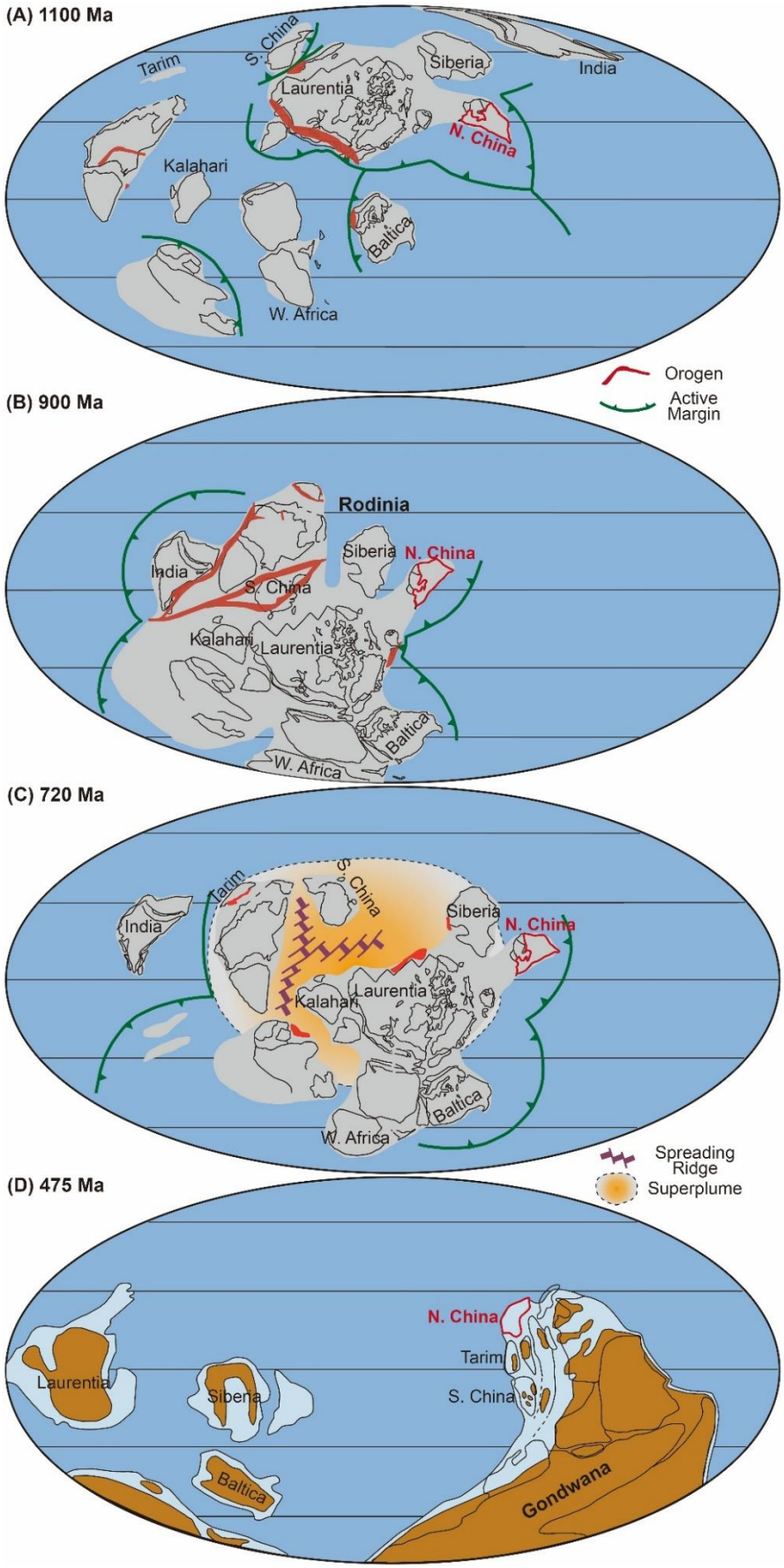
(A) 1100 Ma
Tarim
S. China
Siberia
India
Laurentia
N. China
Kalahari
Baltica
W. Africa
Orogen
Active Margin
(B) 900 Ma
Rodinia
Siberia
N. China
India
S. China
Kalahari
Laurentia
Baltica
W. Africa
(C) 720 Ma
Tarim
S. China
India
Siberia
N. China
Laurentia
Kalahari
Baltica
W. Africa
Spreading Ridge
Superplume
(D) 475 Ma
N. China
Tarim
Laurentia
Siberia
S. China
Baltica
Gondwana

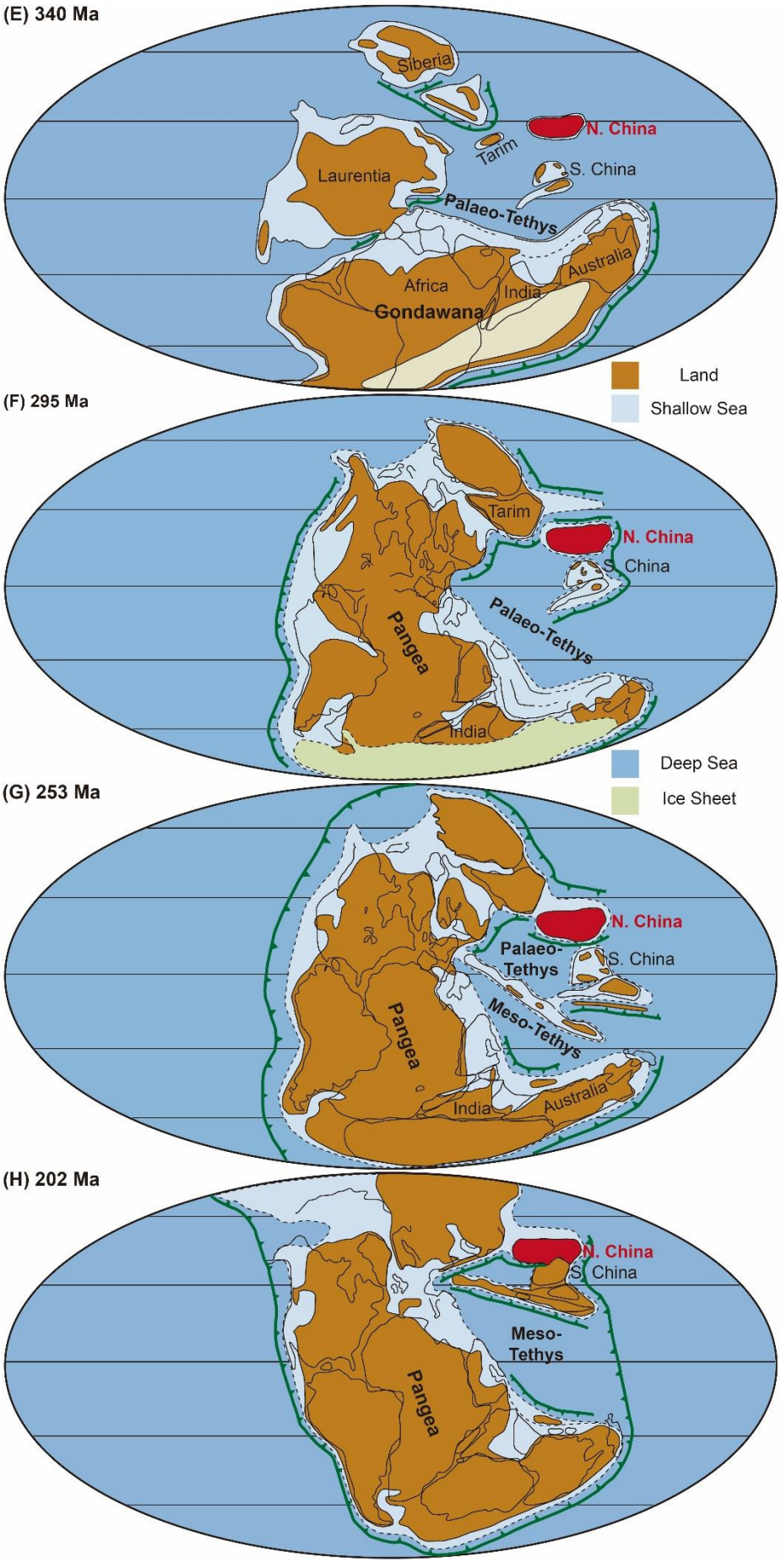
(E) 340 Ma
Siberia
N. China
Tarim
S. China
Laurentia
Palaeo-Tethys
Australia
Africa
India
Gondawana
Land
Shallow Sea
(F) 295 Ma
Tarim
N. China
S. China
Pangea
Palaeo-Tethys
India
Deep Sea
Ice Sheet
(G) 253 Ma
N. China
Palaeo-
Tethys
S. China
Meso-Tethys
Pangea
India
Australia
(H) 202 Ma
N. China
S. China
Meso-
Tethys
Pangea

Fig. A2.1. Tectonic and paleogeographic evolution of the North China Craton (ca. 1100-202 Ma).

Panels A-C: The NCC is suggested to be a part of pre-Cambrian supercontinent(s) since ca. >1100 Ma, e.g. the 'Rodinia' and 'Laurentia' supercontinent (Li et al., 2008). It was located in a continental margin environment and stayed close to active margins till ca. 600 Ma (Li et al., 2008) (or ca. 500Ma (Metcalfe, 2013)). **Panels D-H**: Between ca. 500-200Ma, the NCC appears to have kept a 'small' size, 'isolated' from other major Pre-Cambrian blocks (Li et al., 2008; Metcalfe, 2013).

References:

Algeo, T.J., Wilkinson, B.H., 1991. Modern and ancient continental hypsometries. Journal of the Geological Society 148, 643-653.

Allen, P., Armitage, J., 2009. Syntectonic basin development, active to ancient: recent advances.

Allen, P., Eriksson, P.G., Alkmim, F., Betts, P., Catuneanu, O., Mazumder, R., Meng, Q., Young, G., 2015. Classification of basins, with special reference to Proterozoic examples. Geological Society, London, Memoirs 43, 5-28.

Andres-Martinez, M., Morgan, J.P., Perez-Gussinye, M., Rupke, L., 2015. A new free-surface stabilization algorithm for geodynamical modelling: theory and numerical tests. Physics of the Earth and Planetary Interiors 246, 41-51.

Armitage, J.J., Allen, P.A., 2010. Cratonic basins and the long-term subsidence history of continental interiors. Journal of the Geological Society 167, 61-70.

Artemieva, I.M., 2003. Lithospheric structure, composition, and thermal regime of the East European Craton: implications for the subsidence of the Russian platform. Earth and Planetary Science Letters 213, 431-446.

Artemieva, I.M., 2007. Dynamic topography of the East European craton: shedding light upon lithospheric structure, composition and mantle dynamics. Global and Planetary Change 58, 411-434.

Beaumont, C., 1981. Foreland basins. Geophysical Journal International 65, 291-329.

Bernstein, S., Hanghøj, K., Kelemen, P.B., Brooks, C.K., 2006. Ultra-depleted, shallow cratonic mantle beneath West Greenland: dunitic xenoliths from Ubekendt Ejland. Contributions to Mineralogy and Petrology 152, 335.

Bertelloni, C.L., Gurnis, M., 1997. Cenozoic subsidence and uplift of continents from time-varying dynamic topography. Geology 25, 735-738.

Beyer, E.E., Griffin, W.L., O'reilly, S.Y., 2006. Transformation of Archaean lithospheric mantle by refertilization: evidence from exposed peridotites in the Western Gneiss Region, Norway. Journal of Petrology 47, 1611-1636.

Bleeker, W., 2003. The late Archean record: a puzzle in ca. 35 pieces. Lithos 71, 99-134.

Bond, G., 1978. Speculations on real sea-level changes and vertical motions of continents at selected times in the Cretaceous and Tertiary Periods. Geology 6, 247-250.

Boyd, F., 1989. Compositional distinction between oceanic and cratonic lithosphere. Earth and Planetary Science Letters 96, 15-26.

Boyd, F., Pokhilenko, N., Pearson, D., Mertzman, S., Sobolev, N., Finger, L., 1997. Composition of the Siberian cratonic mantle: evidence from Udachnaya peridotite xenoliths. Contributions to Mineralogy and Petrology 128, 228-246.

Burgess, P.M., 2008. Phanerozoic evolution of the sedimentary cover of the North

American craton. In: Miall, A.D. (ed.) The Sedimentary Basins of the United States and Canada. Elsevier, Amsterdam, 31–63.

Chen, S., O'Reilly, S.Y., Zhou, X., Griffin, W.L., Zhang, G., Sun, M.,Feng, J., Zhang, M., 2001. Thermal and petrological structure of the lithosphere beneath Hannuoba, Sino-Korean craton, China: Evidence From Xenoliths. Lithos 56, 267–301.

Chu, Z.-Y., Wu, F.-Y., Walker, R.J., Rudnick, R.L., Pitcher, L., Puchtel, I.S., Yang, Y.-H., Wilde, S.A., 2009. Temporal evolution of the lithospheric mantle beneath the eastern North China Craton. Journal of Petrology 50, 1857-1898.

Condie, K.C., 2015. Earth as an evolving planetary system. Elsevier, Academic Press. pp. 1–447.

Conrad, C.P., 2013. The solid Earth's influence on sea level. Bulletin , 125(7-8), 1027-1052.

Corti, G., Iandelli, I., Cerca, M., 2013. Experimental modeling of rifting at craton margins. Geosphere 9, 138-154.

Crosby, A., Fishwick, S., White, N., 2010. Structure and evolution of the intracratonic Congo Basin. Geochemistry, Geophysics, Geosystems 11 (6) , p. Q06010.

Dávila, F.M., Lithgow-Bertelloni, C., 2015. Dynamic uplift during slab flattening. Earth and Planetary Science Letters 425, 34-43.

Djomani, Y.H.P., O'Reilly, S.Y., Griffin, W.L., Morgan, P., 2001. The density structure of subcontinental lithosphere through time. Earth and Planetary Science Letters 184, 605-621.

Downey, N.J., Gurnis, M., 2009. Instantaneous dynamics of the cratonic Congo basin. Journal of Geophysical Research: Solid Earth 114, p. B06401, 10.1029/2008JB006066.

Eaton, D.W., Perry, H.C., 2013. Ephemeral isopycnicity of cratonic mantle keels. Nature Geoscience 6, pp. 967-970.

Foley, S.F., 2008. Rejuvenation and erosion of the cratonic lithosphere. Nature Geoscience 1, 503-510.

Foley, S.F., Fischer, T.P., 2017. An essential role for continental rifts and lithosphere in the deep carbon cycle. Nature Geoscience 10, 897.

Gao, S., Rudnick, R.L., Carlson, R.W., McDonough, W.F., Liu, Y.S., 2002. Re-Os evidence for replacement of ancient mantle lithosphere beneath the North China craton. Earth and Planetary Science Letters 198, 307-322.

Gao, S., Rudnick, R.L., Yuan, H.L., Liu, X.M., Liu, Y.S., Xu, W.L., Ling, W.L., Ayers, J., Wang, X.C., Wang, Q.H., 2004. Recycling lower continental crust in the North ChinaCraton. Nature 432, 892-897.

Gao, S., Zhang, J.F., Xu, W.L., Liu, Y.S., 2009. Delamination and destruction of the North

China Craton. Chinese Science Bulletin 54, 3367-3378.

Garcia-Castellanos, D., Fernàndez, M., Torne, M., 1997. Numerical modeling of foreland basin formation: a program relating thrusting, flexure, sediment geometry and lithosphere rheology. Computers & Geosciences 23, 993-1003.

Gorczyk, W., Hobbs, B., Gerya, T., 2012. Initiation of Rayleigh-Taylor instabilities in intra-cratonic settings. Tectonophysics 514, 146-155.

Griffin, W.L., O'Reilly, S.Y., Ryan, C.G., 1992. Composition and thermal structure of the lithosphere beneath South Africa, Siberia and China : proton microprobe studies. International Symposium on Cenozoic Volcanic rocks and deep-seated xenoliths of China and its Environs, Beijing, vol. 20.

Griffin, W., Kaminsky, F., Ryan, C., O'Reilly, S., Win, T., Ilupin, I., 1996. Thermal state and composition of the lithospheric mantle beneath the Daldyn kimberlite field, Yakutia. Tectonophysics 262, 19-33.

Griffin, W., Natapov, L., O'Reilly, S., van Achterbergh, E., Cherenkova, A., Cherenkov, V., 2005. The Kharamai kimberlite field, Siberia: modification of the lithospheric mantle by the Siberian Trap event. Lithos 81, 167-187.

Griffin, W.L., Andi, Z., O'Reilly, S.Y., Ryan, C.G., 1998. Phanerozoic evolution of the lithosphere beneath the Sino-Korean Craton. Mantle Dynamics and Plate Interactions in East Asia 27, 107-126.

Griffin,W.L., Fisher, N.I., Friedman, J., Ryan, C.G., O'Reilly, S.Y., 1999. Cr-pyrope garnets in the lithospheric mantle I Compositional systematics and relations to tectonic setting. J. Petrol. 40, 679 – 704.

Griffin, W.L., O'Reilly, S.Y., Doyle, B.J., Pearson, N.J., Coopersmith, H., Kivi, K., Malkovets, V., Pokhilenko, N., 2004. Lithosphere mapping beneath the north American plate. Lithos 77, 873-922.

Griffin, W.L., O'Reilly, S.Y., Natapov, L.M., Ryan, C.G., 2003. The evolution of lithospheric mantle beneath the Kalahari Craton and its margins. Lithos 71, 215-241.

Gurnis, M., 1990. Bounds on global dynamic topography from Phanerozoic flooding of continental platforms. Nature 344, 754.

Gurnis, M., 1992. Rapid continental subsidence following the initiation and evolution of subduction. Science 255, 1556-1558.

Gurnis, M., 1993. Phanerozoic marine inundation of continents driven by dynamic topography above subducting slabs. Nature 364, 589.

Hanghøj, K., Kelemen, P., Bernstein, S., Blusztajn, J., Frei, R., 2001. Osmium isotopes in the Wiedemann Fjord mantle xenoliths: a unique record of cratonic mantle formation by melt depletion in the Archaean. Geochemistry, Geophysics, Geosystems 2.

Hasenclever, J., 2010. Modeling Mantle Flow and Melting Processes at Mid-Ocean

Ridges and Subduction Zones — Development and Application of Numerical Models Dirssertation. *Ph.D. Dissertation*, Hamburg University. URL: http://ediss.sub.uni-hamburg.de/volltexte/2010/4873/.

Hasenclever, J., Morgan, J.P., Hort, M., Rupke, L.H., 2011. 2D and 3D numerical models on compositionally buoyant diapirs in the mantle wedge. Earth and Planetary Science Letters 311, 53-68.

He, L.J., 2014. Numerical modeling of convective erosion and peridotite-melt interaction in big mantle wedge: implications for the destruction of the North China Craton. Journal of Geophysical Research-Solid Earth 119, 3662-3677.

Hong, L.-B., Xu, Y.-G., Ren, Z.-Y., Kuang, Y.-S., Zhang, Y.-L., Li, J., Wang, F.-Y., Zhang, H., 2012. Petrology, geochemistry and Re–Os isotopes of peridotite xenoliths from Yantai, Shandong Province: evidence for Phanerozoic lithospheric mantle beneath eastern North China Craton. Lithos 155, 256-271.

Hu, J., Liu, L., Faccenda, M., Zhou, Q., Fischer, K.M., Marshak, S., Lundstrom, C., 2018. Modification of the Western Gondwana craton by plume–lithosphere interaction. Nature Geoscience, 1, 203-210.

Jordan, T.H., 1988. Structure and formation of the continental tectosphere. Journal of Petrology, 11-37.

Kominz, M.A., 1984. Oceanic ridge volumes and sea-level change-an error analysis. Interregional Unconformaties and Hydrocarbon Accumulation (3rd ed.) Schlee (Ed.), p. 36

Kovtun, A., 1976. Induction studies in stable shield and platform areas. Acta Geod. Geophys. Mont., Acad. Sci. Hung 11, 333-346.

Krystopowicz, N.J., Currie, C.A., 2013. Crustal eclogitization and lithosphere delamination in orogens. Earth and Planetary Science Letters 361, 195-207.

Lee, C.-T.A., Luffi, P., Chin, E.J., 2011. Building and destroying continental mantle. Annual Review of Earth and Planetary Sciences 39, 59-90.

Lee, C.T.A., 2003. Compositional variation of density and seismic velocities in natural peridotites at STP conditions: implications for seismic imaging of compositional heterogeneities in the upper mantle. Journal of Geophysical Research-Solid Earth 108.

Li, H., 2013. Destruction of North China Craton: Insights from temporal and spatial evolution of the proto-basins and magmatism. Science China Earth Sciences 56, 464-478.

Li, S., Zhao, G., Dai, L., Liu, X., Zhou, L., Santosh, M., Suo, Y., 2012. Mesozoic basins in eastern China and their bearing on the deconstruction of the North China Craton. Journal of Asian Earth Sciences 47, 64-79.

Li, W., 2007. The characteristic and evolution of sequence-lithofacies paleogeography of lower Paleozoic and around Bohai Gulf area. *Ph.D. Dissertation*, Chengdu University of Technology, p. 143.

Li, Z.-X., Bogdanova, S., Collins, A., Davidson, A., De Waele, B., Ernst, R., Fitzsimons, I., Fuck, R., Gladkochub, D., Jacobs, J., 2008. Assembly, configuration and break-up history of Rodinia: a synthesis. Precambrian research 160, 179-210.

Liao, J., Wang, Q., Gerya, T., Ballmer, M.D., 2017. Modeling craton destruction by hydration‐induced weakening of the upper mantle. Journal of Geophysical Research: Solid Earth 122, 7449-7466.

Lin, G., Zhang, Y., Guo, F., Wang, Y.J., Fan, W.M., 2005. Numerical modelling of lithosphere evolution in the North China Block: thermal versus tectonic thinning. Journal of Geodynamics 40, 92-103.

Liu, B., Quan, Q., Feng, Q., Zhao, X., Zhou, Z., 1996. Historical Geology. Geological Press, Beijing : 1-277.

Liu, F., Xu, Z., Liou, J., Song, B., 2004. SHRIMP U–Pb ages of ultrahigh‐pressure and retrograde metamorphism of gneisses, south‐western Sulu terrane, eastern China. Journal of Metamorphic Geology 22, 315-326.

Liu, J., Rudnick, R.L., Walker, R.J., Gao, S., Wu, F.-y., Piccoli, P.M., Yuan, H., Xu, W.-l., Xu, Y.-G., 2011. Mapping lithospheric boundaries using Os isotopes of mantle xenoliths: an example from the North China Craton. Geochimica et Cosmochimica Acta 75, 3881-3902.

Liu, L., Gurnis, M., Seton, M., Saleeby, J., Müller, R.D., Jackson, J.M., 2010. The role of oceanic plateau subduction in the Laramide orogeny. Nature Geoscience 3, 353.

Liu, L., Spasojević, S., Gurnis, M., 2008. Reconstructing Farallon plate subduction beneath North America back to the Late Cretaceous. Science 322, 934-938.

Lu, F., 2010. Multiple-geological events of ancient lithospheric mantle beneath North China Craton as inferred from peridotite kenoliths in kimberlite. Acta Petrologica Sinica 26, 3177-3188.

Lu, F., Chunyang, W., Jianping, Z., 2004. Lithospheric composition and structure beneath the northern margin of the Qinling orogenic belt. Science in China Series D: Earth Sciences 47, 13-22.

Lu, F., Han, Z., Zheng, J., Ren, Y., 1991. Characteristics of Paleozoic mantle-lithosphere in Fuxian, Liaoning province. Geological Science and Technology Information 10, 2-19.

Lu, S., Yang, C., Li, H., Li, H., 2002. A Group of Rifting Events in the Terminal Paleoproterozoic in the North China Craton. Gondwana Research 5, 123-131.

Lu, S., Zhao, G., Wang, H., Hao, G., 2008. Precambrian metamorphic basement and

sedimentary cover of the North China Craton: a review. Precambrian research 160, 77-93.

Lv, D., 2009. Study of the transgressive event deposition and paleogeography characteristics of Neopaleozoic in North China Area. Shandong University of Science and Technology, pp. 192.

MacKenzie, J., Canil, D., 1999. Composition and thermal evolution of cratonic mantle beneath the central Archean Slave Province, NWT, Canada. Contributions to Mineralogy and Petrology 134, 313-324.

Maruyama, S., Isozaki, Y., Kimura, G., Terabayashi, M., 1997. Paleogeographic maps of the Japanese Islands: plate tectonic synthesis from 750 Ma to the present. Island Arc 6, 121-142.

Meng, Q.-R., 2003. What drove late Mesozoic extension of the northern China–Mongolia tract? Tectonophysics 369, 155-174.

Meng, X., Ge, M., Tucker, M.E., 1997. Sequence stratigraphy, sea-level changes and depositional systems in the Cambro-Ordovician of the North China carbonate platform. Sedimentary Geology 114, 189-222.

Menzies M A, Fan, W., Zhang, M., 1993. Palaeozoic and Cenozoic lithoprobes and the loss of> 120 km of Archaean lithosphere, Sino-Korean craton, China. Geological Society, London, Special Publications 76, 71-81.

Menzies, M., Xu, Y.G., Zhang, H.F., Fan, W.M., 2007. Integration of geology, geophysics and geochemistry: A key to understanding the North China Craton. Lithos 96, 1-21.

Metcalfe, I., 2013. Gondwana dispersion and Asian accretion: tectonic and palaeogeographic evolution of eastern Tethys. Journal of Asian Earth Sciences 66, 1-33.

Meyer, H.O.A., 1987. Inclusions in diamonds. In: Nixon, P.H. (Ed.), Mantle Xenoliths. John Wiley and Sons, Chichester, England, pp. 501 – 522.

Morency, C., Doin, M.P., 2004. Numerical simulations of the mantle lithosphere delamination. Journal of Geophysical Research-Solid Earth 109.

Morley, C., 2010. Stress re-orientation along zones of weak fabrics in rifts: an explanation for pure extension in 'oblique' rift segments? Earth and Planetary Science Letters 297, 667-673.

Mueller, J.F., Rogers, J.J., Yu-Gan, J., Huayu, W., Wenguo, L., Chronic, J., Mueller, J.F., 1991. Late Carboniferous to Permian sedimentation in Inner Mongolia, China and tectonic relationships between north China and Siberia. The Journal of Geology 99, 251-263.

Müller, R.D., Sdrolias, M., Gaina, C., Steinberger, B., Heine, C., 2008. Long-term sea-level fluctuations driven by ocean basin dynamics. Science 319, 1357-1362.

Naimark, B.M., Ismail‐Zadeh, A.T., 1995. Numerical models of a subsidence mechanism in intracratonic basins: application to North American basins. Geophysical Journal International 123, 149-160.

Nikishin, A., Ziegler, P., Stephenson, R., Cloetingh, S., Furne, A., Fokin, P., Ershov, A., Bolotov, S., Korotaev, M., Alekseev, A., 1996. Late Precambrian to Triassic history of the East European Craton: dynamics of sedimentary basin evolution. Tectonophysics 268, 23-63.

Niu, Y., 2005. Generation and evolution of basaltic magmas: some basic concepts and a new view on the origin of Mesozoic–Cenozoic basaltic volcanism in eastern China. Geological Journal of China Universities 11, 9-46.

O'Reilly S Y, Griffin, W L., 2013. Mantle metasomatism, Metasomatism and the chemical transformation of rock. Springer, pp. 471-533.

Pearson, D., Carlson, R., Shirey, S., Boyd, F., Nixon, P., 1995. Stabilisation of Archaean lithospheric mantle: a Re Os isotope study of peridotite xenoliths from the Kaapvaal craton. Earth and Planetary Science Letters 134, 341-357.

Qiao, X., Gao, L., 2000. Earthquake events in Neoproterozoic and Early Paleozoic and its relationship with supercontinental Rodinia in North China. Science Bulletin 45, 931-935.

Quinlan, G., 1987. Models of subsidence mechanisms in intracratonic basins and their applicability to North American examples. C. Beaumont, A.J. Tankard (Eds.), Sedimentary Basins and Basin-Forming Mechanisms. Mem. 12, Canadian Society of Petroleum Geologists, Calgary, AB, Canada (1987), pp. 463-481

Ritts, B.D., Darby, B.J., Cope, T., 2001. Early Jurassic extensional basin formation in the Daqing Shan segment of the Yinshan belt, northern North China Block, Inner Mongolia. Tectonophysics 339, 239-258.

Ros, E., Pérez‐Gussinyé, M., Araújo, M., Thoaldo Romeiro, M., Andrés‐Martínez, M., Morgan, J.P., 2017. Lower crustal strength controls on melting and serpentinization at magma‐poor margins: potential implications for the South Atlantic. Geochemistry, Geophysics, Geosystems. 18, 4538–4557. https://doi.org/10.1002/2017GC007212.

Schmidberger, S., Francis, D., 1999. Nature of the mantle roots beneath the North American Craton: mantle xenolith evidence from Somerset Island kimberlites. Lithos 48, 195-216.

Sleep, N. H. (2009), Stagnant lid convection and carbonate metasomatism of the deep continental lithosphere, *Geochemistry, Geophysics, Geosystems*, *10*(11).

Sleep, N.H., 2003. Survival of Archean cratonal lithosphere. Journal of Geophysical Research-Solid Earth 108 (B6), p. 2302, 10.1029/2001JB000169.

Song, S., Niu, Y., Su, L., Zhang, C., Zhang, L., 2014. Continental orogenesis from ocean subduction, continent collision/subduction, to orogen collapse, and orogen recycling: The example of the North Qaidam UHPM belt, NW China. Earth-Science Reviews 129, 59-84.

Vérard, C., Hochard, C., Baumgartner, P.O., Stampfli, G.M., Liu, M., 2015. 3D palaeogeographic reconstructions of the Phanerozoic versus sea-level and Sr-ratio variations. Journal of Palaeogeography 4, 64-84.

Wan, Y., Li, R., Wilde, S.A., Liu, D., Chen, Z., Yan, L., Song, T., Yin, X., 2005. UHP metamorphism and exhumation of the Dabie Orogen, China: evidence from SHRIMP dating of zircon and monazite from a UHP granitic gneiss cobble from the Hefei Basin. Geochimica et Cosmochimica Acta 69, 4333-4348.

Wang, Z.S., Kusky, T.M., Capitanio, F.A., 2016. Lithosphere thinning induced by slab penetration into a hydrous mantle transition zone. Geophysical Research Letters 43, 11567-11577.

Watson, M., Hayward, A., Parkinson, D., Zhang, Z.M., 1987. Plate tectonic history, basin development and petroleum source rock deposition onshore China. Marine and Petroleum Geology 4, 205-225.

Wenker, S., Beaumont, C., 2017. Can metasomatic weakening result in the rifting of cratons? Tectonophysics. 10.1016/j.tecto.2017.06.013.

Wu, F.Y., Lin, J.Q., Wilde, S.A., Zhang, X.O., Yang, J.H., 2005. Nature and significance of the Early Cretaceous giant igneous event in eastern China. Earth and Planetary Science Letters 233, 103-119.

Xia, B., Thybo, H., Artemieva, I.M., 2017. Seismic crustal structure of the North China Craton and surrounding area: synthesis and analysis. Journal of Geophysical Research-Solid Earth 122, 5181-5207.

Xiao, W., Windley, B.F., Hao, J., Zhai, M., 2003. Accretion leading to collision and the Permian Solonker suture, Inner Mongolia, China: termination of the central Asian orogenic belt. Tectonics 22. p. 1069, 10.1029/2002TC001484.

Xie, X., 2007. Sedimentary record of Mesozoic intracontinental deformation in the south Ordos Basin, China. *Ph.D.* Dissertation. Laramie: University of Wyoming. 280 p.

Xie, X., Heller, P.L., 2009. Plate tectonics and basin subsidence history. Geological Society of America Bulletin 121, 55-64.

Xu, W., Hergt, J.M., Gao, S., Pei, F., Wang, W., Yang, D., 2008. Interaction of adakitic melt-peridotite: implications for the high-Mg# signature of Mesozoic adakitic rocks in the eastern North China Craton. Earth and Planetary Science Letters 265, 123-137.

Xu, W., Yang, D., Gao, S., Pei, F., Yu, Y., 2010. Geochemistry of peridotite xenoliths in Early Cretaceous high-Mg# diorites from the Central Orogenic Block of the North

China Craton: the nature of Mesozoic lithospheric mantle and constraints on lithospheric thinning. Chemical Geology 270, 257-273.

Xu, X.S., O'Reilly, S.Y., Griffin, W.L., Zhou, X.M., 1998. The nature of the Cenozoic lithosphere at Hushan, central eastern China. In: Flower, M., Ching, S.L., Lo, C.H., Lee, T.Y. (Eds.), Mantle Dynamics and Plate Interactions in East Asia. AGU Geodynamics Series, vol. 27, pp. 167–196.

Xu, Y. G., H. Y. Li, C. J. Pang, and B. He (2009), On the timing and duration of the destruction of the North China Craton, *Chinese Science Bulletin*, *54*(19), 3379-3396, doi:10.1007/s11434-009-0346-5.

Xu, Y.G., 2001. Thermo-tectonic destruction of the Archaean lithospheric keel beneath the Sino-Korean Craton in China: Evidence, timing and mechanism. Physics and Chemistry of the Earth Part A-Solid Earth and Geodesy 26, 747-757.

Yang, J., Zhao, L., Kaus, B.J., Lu, G., Wang, K., Zhu, R., 2017. Slab-triggered wet upwellings produce large volumes of melt: insights into the destruction of the North China Craton. Tectonophysics (2017).

Yang, J.H., Wu, F.Y., Shao, J.A., Wilde, S.A., Xie, L.W., Liu, X.M., 2006. Constraints on the timing of uplift of the Yanshan Fold and Thrust Belt, North China. Earth and Planetary Science Letters 246, 336-352.

Ying, J.F., Zhou, X.H., Su, B.X., Tang, Y.J., 2012. Continental growth and secular evolution: Constraints from U-Pb ages and Hf isotope of detrital zircons in Proterozoic Jixian sedimentary section (1.8-0.8 Ga), North China Craton, *Ph.D.* Dissertation. Institute of Geology and Geophysis, CAS.

Yuan, 1996. Velocity structure of the Qinling lithosphere and mushroom cloud model. Science in China (Series D), 39 (1996), pp. 236-244.

Yuan, H., Romanowicz, B., 2010. Lithospheric layering in the North American Craton. Nature 466, 1063.

Zhai, M., 2014. Multi-stage crustal growth and cratonization of the North China Craton. Geoscience Frontiers 5, 457-469.

Zhai, M.-G., Santosh, M., 2011. The early Precambrian odyssey of the North China Craton: a synoptic overview. Gondwana Research 20, 6-25.

Zhang, H.-F., Ying, J.-F., Santosh, M., Zhao, G.-C., 2012a. Episodic growth of Precambrian lower crust beneath the North China Craton: a synthesis. Precambrian Research 222, 255-264.

Zhang, H.F., Goldstein, S.L., Zhou, X.H., Sun, M., Zheng, J.P., Cai, Y., 2008. Evolution of subcontinental lithospheric mantle beneath eastern China: Re-Os isotopic evidence from mantle xenoliths in Paleozoic kimberlites and Mesozoic basalts.

Contributions to Mineralogy and Petrology 155, 271-293.

Zhang, S.-H., Zhao, Y., Song, B., Hu, J.-M., Liu, S.-W., Yang, Y.-H., Chen, F.-K., Liu, X.-M., Liu, J., 2009. Contrasting Late Carboniferous and Late Permian–Middle Triassic intrusive suites from the northern margin of the North China Craton: Geochronology, petrogenesis and tectonic implications. Geological Society of America Bulletin 121, 181-200.

Zhang, S., Li, Z.X., Evans, D.A.D., Wu, H., Li, H., Dong, J., 2012b. Pre-Rodinia supercontinent Nuna shaping up: a global synthesis with new paleomagnetic results from North China. Earth & Planetary Science Letters, 353–354, 145-155.

Zhao, G., Guo, J., 2012. Precambrian geology of China: Preface. Precambrian research 222-223, 1-12.

Zhao, G., Zhai, M., 2013. Lithotectonic elements of Precambrian basement in the North China Craton: review and tectonic implications. Gondwana Research 23, 1207-1240.

Zheng, J., Griffin, W L., O'Reilly, S.Y., Yu, C., Zhang, H., Pearson, N., Zhang, M., 2007. Mechanism and timing of lithospheric modification and replacement beneath the eastern North China Craton: peridotitic xenoliths from the 100 Ma Fuxin basalts and a regional synthesis. Geochimica et Cosmochimica Acta 71, 5203-5225.

Zheng, J., Griffin, W.L., O'Reilly, S.Y., Yang, J., Li, T., Zhang, M., Zhang, R.Y., Liou, J.G., 2006. Mineral chemistry of peridotites from Paleozoic, Mesozoic and Cenozoic lithosphere: constraints on mantle evolution beneath eastern China. Journal of Petrology 47, 2233-2256.

Zheng, J., Zhang, R.Y., Griffin, W L., Liou, J., O'Reilly, S.Y., 2005. Heterogeneous and metasomatized mantle recorded by trace elements in minerals of the Donghai garnet peridotites, Sulu UHP terrane, China. Chemical Geology 221, 243-259.

Zheng, J., Griffin, W., O'Reilly, S.Y., Lu, F., Wang, C., Zhang, M., Wang, F., Li, H., 2004. 3.6 Ga lower crust in central China: new evidence on the assembly of the North China Craton. Geology 32, 229-232.

Zhu, Xu, Y., Zhu, G., Zhang, H., Xia, Q., Zheng, T., 2012a. Destruction of the North China Craton. Science China Earth Sciences 55, 1565-1587.

Zhu, G., Jiang, D.Z., Zhang, B.L., Chen, Y., 2012b. Destruction of the eastern North China Craton in a backarc setting: Evidence from crustal deformation kinematics. Gondwana Research 22, 86-103.

Chapter 3. Craton Destruction Part I: Cratonic Keel Delamination a weak Mid-Lithospheric Discontinuity layer

Liang Liu, Jason P. Morgan, Yigang Xu and Martin Menzies. This manuscript has been published in *JGR: Solid Earth*.

Authors contribution

J. P. Morgan Proposed the idea for this work. L. Liu performed this work under the primary supervision of J. P. Morgan. L. Liu and J. P. Morgan collected the geological, geochemical and geophysical observations in this paper. L. Liu modified the existed code for 2-D triangle mesh generation into the adaptive version. L. Liu designed the algorithm for subduction geometry and finished the subduction bench mark test. L. Liu and J. P. Morgan designed the temperature-dependent strain weakening algorithm in the computational code. L. Liu and J. P. Morgan designed the numerical experiments. L. Liu, J. P. Morgan and Y-G Xu discussed the implications from numerical experiments. L. Liu wrote the manuscript in collaboration with J. P. Morgan, M. Menzies and Y-G Xu.

Craton Destruction Part I: Cratonic Keel Delamination a weak Mid-Lithospheric Discontinuity layer

Liang Liu[1, 2, 3], Jason P. Morgan[2, 4], Yigang Xu[1] and Martin Menzies[1, 2]

[1] *State Key Laboratory of Isotope Geochemistry, Guangzhou Institute of Geochemistry, Chinese Academy of Sciences, Guangzhou 510640, China*

[2] *Department of Earth Sciences, Royal Holloway University of London, Egham, TW200EX, United Kingdom.*

[3] *College of Earth Sciences, University of Chinese Academy of Sciences, Beijing, 100049, China.*

[4] *Department of Earth & Planetary Sciences, Harvard University, Cambridge, MA, USA.*

Key Points:

- New conceptual model for cratonic keel delamination—refertilized keel delaminates along a weak mid-lithospheric discontinuity layer (MLDL).
- Keel stability is closely related to the stability of the craton's surrounding lithosphere in the depth range of the MLDL.
- Keel delamination appears to be supported by seismic observations beneath northern China and North America.

Corresponding author: L. Liu, liangliu@gig.ac.cn

Corresponding author: J. Morgan, Jason.Morgan@rhul.ac.uk

Corresponding author: Y.G. Xu, yigangxu@gig.ac.cn

Abstract

Cratons are generally observed to retain thick (>180 km) conductive keels for billions of years. However, some cratons have undergone keel removal, with well-documented examples being the eastern North China Craton (NCC) and the Wyoming Craton (WC). These keelless sub-regions appear to have kept a lithospheric bottom at ~80-100 km depths. This is also the depth range where modern cratons, including the remaining portions of the NCC and the WC, have seismically visible Mid-Lithospheric Discontinuity Layers (MLDLs). MLDLs are proposed to be regions of preferential accumulation of metasomatic minerals and/or anomalously wet (>1000 ppm) peridotites, both of which would lead to a relatively weak rheology. We propose that the cratonic keels of the eastern North China Craton (ENCC) and the western Wyoming Craton (WWC) utilized this weak MLDL layer to delaminate from overlying lithosphere. We first explore this hypothesis with a lubrication-theory based analytical model. This model suggests a close relationship between a cratonic keel's long-term stability and the strength of the MLDL's edge. We further test this prediction with less idealized 2-D numerical experiments which reveal that: a) dense lower keels beneath MLDL-bearing cratons can persist for billions of years as long as the MLDL's edges abut relatively cold and strong lithosphere; b) MLDL edge failure can induce rapid intra-mantle lower keel delamination; and c) the predicted rates of keel delamination along a ~10 km thick MLDL with a hydrous olivine or metasomatic mineral-dominated rheology are consistent with observations for the removal speeds of the WWC and the ENCC.

1. Introduction

Cratons are extremely long-lived and extremely stable continental regions. Their tectonic quiescence has been attributed to their 150-220 km thick lithosphere that contains a compositionally highly viscous and buoyant cratonic mantle keel [*Jordan*, 1988; *Lenardic and Moresi*, 1999; *Menzies et al.*, 2007; *Sleep*, 2003]. However, cratonic keel-removal events have been well documented for the Eastern North China Craton (ENCC) [*Griffin et al.*, 1998; *Menzies et al.*, 1993; *Xu*, 2001; *Xu et al.*, 2009; *Zhu et al.*, 2012] and the Western Wyoming Craton (WWC) [*Eggler and Furlong*, 1991; *Wu et al.*, 2014]. Both events appear to be associated with subsequent large-scale crustal deformation [*Feeley et al.*, 2002; *Zhu et al.*, 2012] and magmatic flare-ups within 20 Myr (see Fig. 1). Other more speculative examples of known keel removal events may include the Dharwar Craton and the Brazilian Craton (cf. [*Griffin et al.*, 2009a; *Read et al.*, 2004; *Wu et al.*, 2014]). After keel removal events, former cratonic regions appear to retain relic lithospheric mantle to depths of ~80-100 km (see Fig. 1 and 2B) (cf. [*Hansen et al.*, 2015; *Hopper et al.*, 2014; *Wu et al.*, 2014; *Zhang et al.*, 2008; *Zheng et al.*, 2001; *Zhu et al.*, 2012]). This is directly documented by the presence of shallow (<~80 km), but not deep (>~80 km), Archaean mantle xenoliths in later magmatism [*Menzies et al.*, 1993; *Xu*, 2001; *Zheng et al.*, 2001].

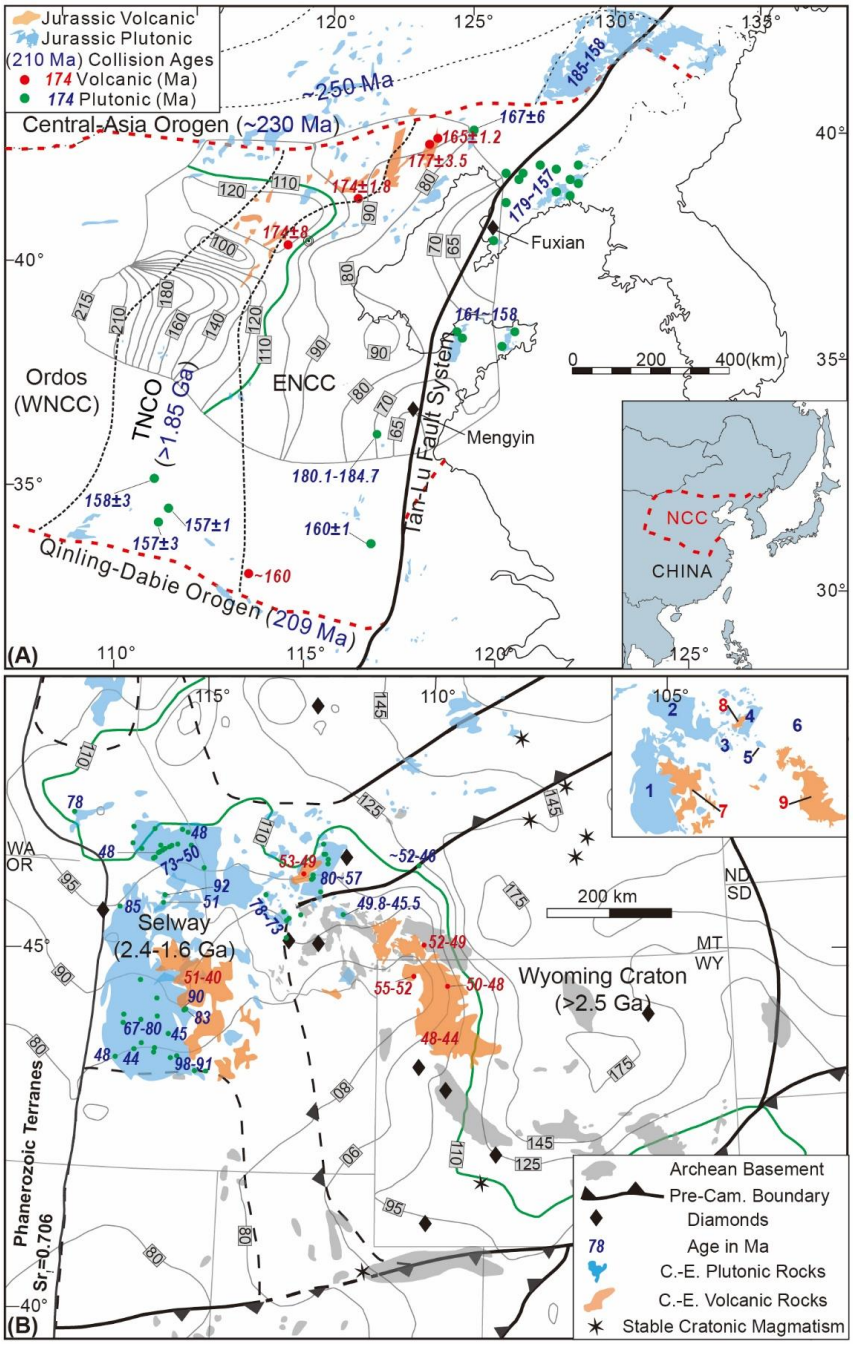

Fig. 1. Geological and geophysical maps of the ENCC and the WWC.

(A) Eastern North China Craton (ENCC): Lithospheric thickness contours (in km) are from Zhu et al. (2012). *Abbreviations:* Western Northern China Carton (WNCC). *Magmatism*: 1-Tongshi [*Lan et al.*, 2012], 2-Southern Hanjialing [*Wu et al.*, 2005], 3-Xinglonggou [*Yang and Li*, 2008], 4-Tiaojishan [*Davis et al.*, 2001], 5-Heigou [*Wu et al.*, 2005], 6-Nandaling [*Zhao et al.*, 2006], 7-Lanqi [*Yang and Li*, 2008], 8-Xinyang [*Zheng et al.*, 2008], 9-Jiaodong [*Yang et al.*, 2012].

(B) Western Wyoming Craton (WWC): post-keel-removal magmatism is located on the

Paleoproterozoic Selway terrane in its west [*Foster et al.*, 2006]. Because this terrane is known to contain Archean basement and diamond mines, the western limit to the proto-Wyoming Craton is thought to include this terrane [*Foster et al.*, 2006]. Lithospheric thicknesses are converted from temperature contours at ~82 km depth [*Hansen et al.*, 2015], under the assumption that the local geotherm is steady state (see Supplement). *Abbreviation:* C.-E. - Cretaceous to Eocene times. *Labelled Magmatism (numbers in inset figure)*: 1-Atlanta [*Gaschnig et al.*, 2010], 2-Bitterroot [*Gaschnig et al.*, 2010], 3-Pioneer [*Foster et al.*, 2012], 4-Boulder [*Lund et al.*, 2002], 5-Tobacco [*Mueller et al.*, 1996], 6-Crazy Mountain [*Dudás*, 1991], 7-Challis [*Norman and Mertzman*, 1991], 8-Lowland Creek [*Dudás et al.*, 2010], 9-Absaroka [*Feeley and Cosca*, 2003].

During the long-term evolution of a craton, its overall mantle keel buoyancy can be affected by mantle refertilization processes [*Gao et al.*, 2002; *Griffin et al.*, 1998; *Griffin et al.*, 2004; *O'Reilly and Griffin*, 2013; *Tang et al.*, 2013]. As refertilized keel bases (cf. [*Griffin et al.*, 2009b]) or relatively "young" Proterozoic keel bases (ca. 1.8Ga [*Djomani et al.*, 2001; *Gao et al.*, 2002]) contain compositionally denser peridotites, they can sometimes have a 0.5-1.9% average compositional density decrease compared to the primitive mantle [*Artemieva and Vinnik*, 2016; *Kaban et al.*, 2003; *Kaban et al.*, 2016; *Lee*, 2003; *Lee et al.*, 2011; *Mooney and Kaban*, 2010]. For cratons containing a fertile/refertilized keel base, the negative thermal buoyancy associated with a thick mantle keel can be larger than that of the positive "floating" tendency due to the keel's average depletion being greater than that of the asthenosphere (see the numerical experiments in Section 5.2, and [*Kaban et al.*, 2003]). In this case, the factors that resist the tendency of the denser keel to sink will be the overall buoyancy of its overlying continental crust and the strong mechanical strength of the lithosphere. If crust-mantle or intra-mantle coupling is disturbed, then cratons could experience keel-removal event(s) through lithospheric delamination [*Bird*, 1979; *Kay and Kay*,

1993]. Continental delamination was originally proposed, with crust-mantle delamination, for the recent uplift of the Colorado Plateau [*Bird*, 1979]. Its geochemical implications were first explored systematically by Kay and Kay (1993), who further emphasized the possibility that a lower crustal transformation to denser eclogite could be the driving force for delamination. However, as noted, above, there is strong observation evidence that shallow lithospheric mantle relics persist after cratonic keel removal events.

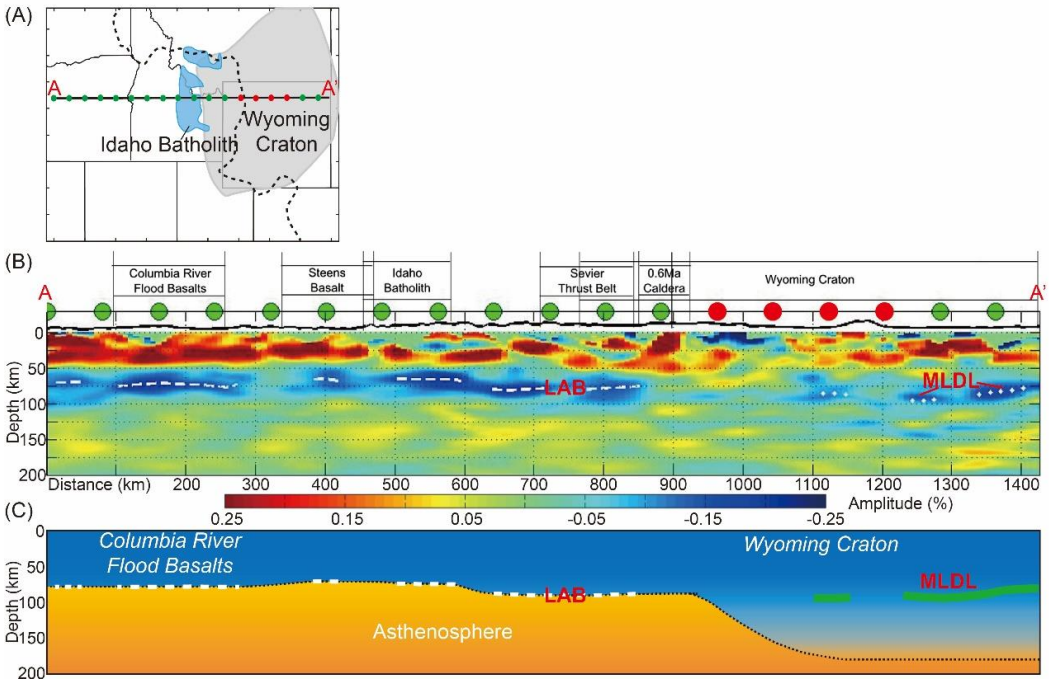

Fig. 2. The MLDL distribution within the Wyoming Craton.

(A) Cross-section locations for the seismic structure in panel B; the red dots mark the region of the Wyoming Craton beneath which the MLDL appears to be absent; the black dashed line marks the contour of the estimated ~95 km thick lithosphere in Fig. 1. (B) Seismic structure of the northwestern United States [*Hopper et al.*, 2014] along the profile shown in panel A. The proposed lithosphere-asthenosphere boundary (LAB) is marked with a white dashed line, while the MLDL is marked with white dots. The MLDL appears to be absent beneath the part of the WC where the region of significant lithospheric thinning terminates; (C) Interpretation of panel B. The present-day LAB beneath Selway Terrane and the WWC (see Fig. 1) shares a similar depth with the present-day MLDL in

the un-thinned eastern WC.

We propose that potential intra-cratonic decoupling occurs along a seismologically revealed intra-cratonic layer named the Mid-Lithospheric Discontinuity (MLD) that is seen at ~80-100 km [*Abt et al.*, 2010; *Aulbach et al.*, 2017; *Chen et al.*, 2014; *Hopper et al.*, 2014; *Nita et al.*, 2016; *Selway et al.*, 2015; *Sodoudi et al.*, 2013]. The MLD is a common but not ubiquitous seismic feature in cratonic regions. Here we suggest that the MLD is better viewed as a thin layer instead of a discontinuity, e.g. an MLD Layer (MLDL). Since the MLD was identified, its potential origin(s) have been widely discussed. Proposed mechanisms of formation include:

1) A transition to grain-boundary-sliding (GBS) due to the upper mantle under this region being richer in water (up to 1000 ppm) [*Karato et al.*, 2015]. Such high chemically bound water contents can also weaken its strength in dislocation and diffusion creep [*Hirth and Kohlstedt*, 2004; *Korenaga and Karato*, 2008]. As potential evidence supporting this mechanism, the Cretaceous (~120 Ma) ENCC mantle has been identified to locally contain >1000 ppm water [*Xia et al.*, 2013].

2) Tectonic-stacking. This can lead to an MLD if cratonic layers have sharp enough compositional differences [*Abt et al.*, 2010]. In this scenario, the interface between stacked layers would be rich in volatile-rich melts [*Griffin et al.*, 2004] whose rheology could be similar to that of metasomatised mantle.

3) Metasomatic layers [*Selway et al.*, 2015] deposited during multiple episodes of metasomatism [*O'Reilly and Griffin*, 2013]. MLDLs appear to exist at a similar depth (80-100 km) to that proposed for enhanced metasomatism of cratonic lithosphere (cf. [*Griffin et al.*, 2003; *Sodoudi et al.*, 2013]). Metasomatic minerals, e.g. mica and/amphibole, are found in mantle xenoliths in the ENCC, the WWC, Tanzanian Craton and South African craton [*Downes et al.*, 2004; *Dawson and Smith*, 1988; *Dudás*, 1991; *Gao et al.*, 2002; *Griffin et al.*, 2004; *Lu et al.*, 1991;

Tang et al., 2013]. These xenoliths are named MARID xenoliths, composed of **M**ica (>50 vol.%), **A**mphibole (~25 vol.%), **R**utile, **I**lmenite, and **D**iopside [*Dawson and Smith*, 1977]. At 80-100 km depths, amphibole [*Getsinger and Hirth*, 2014] and mica [*Kirby and Kronenberg*, 1987] appear to be weaker than wet olivine [*Hirth and Kohlstedt*, 2004].

In summary, MLDLs, if due to any of the above mechanisms, are likely to have a relatively weak rheology in comparison to their overlying and underlying lithospheric mantle. We currently favor the third (metasomatic layer) hypothesis.

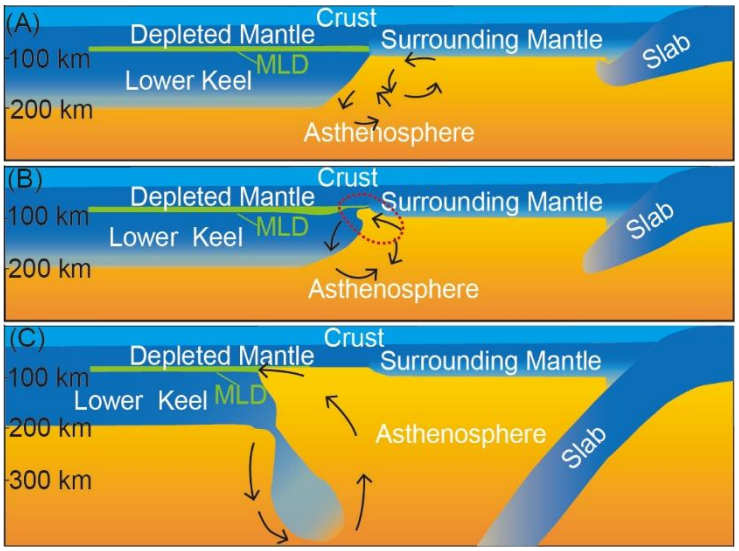

Fig. 3. Intra-mantle Keel Tearing and Delamination Model.

(A) Onset Stage. Configuration at the onset of tearing after potential mechanisms discussed in Section 6 have modified the craton's margin so that the MLDL is now 'close' to margin's edge. (B) Initial Tearing Stage. The keel is denser than its adjacent asthenosphere. Now materials adjacent to the MLDL's edge are soft enough so that the denser keel can start to sag away from the MLDL. The keel's sagging induces a low-pressure zone within the MLDL (see Fig. 4, 5 and 7), which acts to suck material within and along the MLDL towards the tip of the growing keel tear. This region of inward flow is marked by a red dashed circle. Induced inward flow can further weaken inflowing material due to enhanced power-law creep. This effect will accelerate the keel's tearing along the MLDL. (C) Mature Keel Tearing Stage. Once there is a good flow connection

between the MLDL and its adjacent asthenosphere then relatively ductile asthenosphere can readily compensate the void left by keel tearing. This is the stage of most rapid keel delamination.

We propose that dense cratonic lower keels can delaminate along a weak intra-mantle MLDL and sink into deeper mantle (see Fig. 2C and 3). Note that the exact thickness needed for a weak MLDL to have a significant dynamic impact is tightly linked to the viscosity reduction within this layer. Lubrication theory (see Section 3) indicates that the effective viscous strength of the layer will be proportional to its viscosity, but inversely proportional to the cube of its thickness, e.g. doubling the thickness of the MLDL would have the same effect as reducing its viscosity by a factor of 8. Top-side seismic reflection techniques suggest the topside wavespeed reduction in this layer is associated with a relatively sharp (<5 km thick) depth-interval, and a total layer thickness of ~10-25 km (Karen Fischer, personal communication, November 30, 2017). Receiver function and SS-precursor-inferred layer thicknesses are consistent with a ~10 km-thick MLDL, but have much cruder vertical resolution. For example, Sp receiver functions are consistent with inferred MLDL thickness in the western US of 15-30 km [*Lekić and Fischer*, 2014], while SS-precursor measurements only constrain the 'reflector' to be a 'sharp discontinuity with an average velocity contrast of 5±1.5% occurring over <14 km' [*Tharimena et al.*, 2017]. In what follows, we will usually assume that the main weak region of the MLDL is 10 km thick.

A consequence of this hypothesis is that the Lithosphere-Asthenosphere Boundary (LAB) in regions that have undergone a keel delamination event should have a depth similar to that of the MLD in preserved cratonic keels, as is seen in the western US (Fig. 1 and 2B) [*Hopper et al.*, 2014]. A similar depth relationship appears to also exist between the LAB in the keelless ENCC and the remaining

MLDL beneath the unthinned western NCC [*Chen et al.*, 2014].

Here we will further explore the dynamics of cratonic keel delamination along a ~80-100 km deep MLDL (see Fig. 3). We first review previous models for cratonic keel removal, which appear to have limitations in explaining some observations on the ENCC and WCC. Second, we discuss a lubrication-theory-based analytical analysis that provides insights into the mechanics of this keel delamination process. Third, we examine these predictions using less idealized 2-D numerical experiments.

2. Review of Previous Scenarios for Keel Removal

After it was recognized that the North China Craton had lost its cratonic keel [*Menzies et al.*, 1993], many conceptual and numerical models were proposed to thin a keel. Most are related to convective erosion. However, these previous models appear to have limitations to explain some observations on the ENCC and the WCC.

2.1. Convective Erosion Models

Many scenarios propose that cratonic lithospheric can thin by convective erosion [*Xu*, 2001] driven by a Rayleigh-Taylor type gravity instability (cf. [*Conrad and Molnar*, 1997]). These models share the assumption that the keel has lost its high strength before removal begins. Specific keel weakening mechanisms include:

1) Keel heating and/or yielding during orogenic events [*Conrad and Molnar*, 1997; *Gorczyk et al.*, 2012; *Houseman et al.*, 1981];

2) Long-term (>1 Gyr) keel refertilization [*Foley*, 2008; *O'Reilly and Griffin*, 2013; *Tang et al.*, 2013]; and

3) Relatively rapid (<200 Myr) weakening due to the incorporation of volatiles from nearby subducting slabs [*He*, 2014; *Niu*, 2005; *Wang et al.*, 2016; *Wenker and Beaumont*, 2017; *Zhao*, 2004].

These hypotheses all appear to conflict with some observations. Keel thinning driven by orogeny appears inconsistent with keel-removal events recorded in cratonic interiors (see Fig. 1). Keel weakening due to long-lived keel refertilization appears inconsistent with the presence of sudden craton-wide magmatic flare-ups (see Fig. 1). If keel thinning by long-term convective erosion were a general process, some modern cratons would be expected to exist in an intermediate state between stable and keelless, e.g. to have a blob-like lithospheric base like that described in models of the growth of a Rayleigh-Taylor gravity instability [*Conrad and Molnar*, 1997; *Houseman et al.*, 1981]. This does not appear to be the case.

Given that both the ENCC and the WWC appear to have been adjacent to long-term active subduction zones (cf. [*Engebretson et al.*, 1985; *Xu et al.*, 2009]), a further puzzle exists in scenarios for slab-volatilization-induced weakening to remove cratonic keels: Why did on-cratonic magmatism (see Fig. 1A) occur in the ENCC interior almost contemporaneously with the proposed initiation of subduction of the Pacific Plate (cf. 185 Ma [*Maruyama et al.*, 1997; *Wu et al.*, 2011]), while WWC delamination occurred at least ~70 Myr after the initiation of subduction of Farallon Plate at ca. 150 Ma [*Engebretson et al.*, 1985]? Why wouldn't similar weakening mechanisms proceed along similar time scales?

2.2. Flat Subduction

Magmatic flare-ups have previously been described as a frequent by-product of flat subduction. This concept was developed to explain the Laramide Orogenic event in western North America (cf. [*English and Johnston*, 2004; *Snyder et al.*, 1976]). In this scenario, spatially and temporally continuous magmatism would indicate transient slab positions during an episode of flat subduction.

However, the time-space patterns of on-craton Laramide magmatism appear inconsistent with predictions from simple scenarios for flat-subduction. For example, Challis and Lowland Creek Volcanism (see Magmatism 7 and 8 in Fig.1B) occurred later than the earliest events in the Absaroka Volcanism to the east [*Feeley*

and Cosca, 2003], but earlier than the latest Absaroka events (see Magmatism 9 Fig. 1B). This pattern cannot be easily explained by eastward migrating flat subduction followed by westward slab roll-back [*Dudás*, 1991]. Furthermore, the temporal contiguity of the earliest magmatism on the northern sub-region of the ENCC (see Fig. 1A) would indicate a southward flat subduction migration. This also conflicts with the proposition that contemporary paleo-Pacific subduction initialized at ~190-180 Ma, and was >800 km away from the sites of magmatism (cf. [*Maruyama et al.*, 1997; *Wu et al.*, 2011]).

Second, unlike subduction beneath thinner (e.g. 100 km) lithosphere, slab subduction beneath cratons (~200 km) is expected to be influenced by the thick keel (cf. [*Manea et al.*, 2012; *Sigloch et al.*, 2008]). Beneath a ~200-km-thick keel, a cold and volatile-stripped slab would not further dewater to generate large-scale on-craton magmatism [*Dudás*, 1991]. Indeed, the current flat subduction beneath South America is associated with an absence of magmatism, not enhanced magmatism [*Kay and Coira*, 2009]. Furthermore, if early on-craton mafic magmatism can document the transient lithospheric thickness during magmatism to be less than ~100 km ([*Dudás*, 1991; *Xu*, 2001]), then shouldn't these magmas have preferentially sourced more volatile-rich slab components, instead of the magma-composition-inferred enriched lithospheric mantle source [*Dudás*, 1991; *Feeley and Cosca*, 2003; *Menzies et al.*, 1993; *Norman et al.*, 1991; *Wu et al.*, 2005; *Xu*, 2001]? While flat subduction may be mechanically linked to episodes of cratonic keel thinning, thinning typically does not rapidly happen when a flat slab lies directly beneath a cratonic keel.

2.3. Lithospheric Delamination along a Weakened Moho

As noted above, lithospheric mantle delamination has frequently been proposed to be the primary mechanism for the destruction and recycling of continental lithosphere (cf. [*Bird*, 1979; *Gao et al.*, 2002; *Gao et al.*, 2009; *Kay and Kay*, 1993]). Based on this conceptual model, many authors have described

and studied scenarios in which a dense lithospheric root rapidly peels along the weak and/or deepened Moho [*Bao et al.*, 2014; *Bird*, 1979; *Gray and Pysklywec*, 2012; *Krystopowicz and Currie*, 2013; *Li et al.*, 2016; *Morency and Doin*, 2004]. Most of these studies highlight that the negative buoyancy of the lithospheric mantle is what triggers delamination, with possible additional contributions from an eclogitized lower crust. Some experiments [*Morency and Doin*, 2004] demonstrate that lower crustal eclogitization is not needed as long as the Moho is weak enough.

However, cratonic keel delamination from the Moho appears to conflict with several key observations on the ENCC and the WWC:

1) Relics of the ancient lithospheric mantle typically remain after a keel thinning event, as revealed by basalt-bearing xenoliths (cf. [*Dudás*, 1991; *Tang et al.*, 2013; *Zhang et al.*, 2008; *Zheng et al.*, 2001]). This would be a geometric impossibility if delamination occurred along/above the Moho. Instead this clearly suggests that at least a layer of former cratonic mantle survives after a keel delamination event. Similarly, a layer of relic shallow lithospheric mantle appears to survive after non-cratonic delamination events such as that proposed to have recently happened beneath the Canadian Cordillera [*Bao et al.*, 2014]. After keel delamination there, ~1 Ga 'old lithospheric mantle' mantle xenoliths were exhumed, carried in post-delamination asthenosphere-sourced magmas [*Francis et al.*, 2010; *Peslier et al.*, 2000].

2) Regional keel thinning appears to be independent of lower crustal eclogitization. Until late Cretaceous times, ancient lower crust still existed beneath the ENCC (cf. [*Zhu et al.*, 2012]), while contemporaneous large-scale mantle-melting suggests that the craton had already been thinned to ~ 80 km [*Xu et al.*, 2009].

In contrast to these previous models, keel delamination along an intra-cratonic MLDL (see Fig. 3) appears to be able to simultaneously explain 1) the flare-up of

magmatism on craton (see Fig. 1); 2) the presence of relic ancient crust and shallow mantle in post-destruction lithosphere; and 3) the similar depth distribution of the post-delamination LAB and pre-delamination MLDLs (see Fig. 3). To progress further in assessing this hypothesis, we explore this conceptual model with semi-analytical and numerical modelling approaches.

3. Theoretical Analysis

3.1. Lubrication-theory-based Model

The feasibility and factors influencing the proposed scenario here for cratonic keel delamination can be explored using a simple lubrication-theory-based analytical model. As illustrated in Fig. 4, the lower keel's decoupling from its overlying lithosphere is simplified to be a process of downward bending of denser keel root, with compensating material flowing into the delaminating region. This simplified model shares a lubrication-theory formulation with Bird's (1979) original delamination model. It primarily differs from Bird's model in that Bird imagined the weak channel to be hot, ductile, lower crust, while we propose that it takes place along a deeper weak MLDL. We also propose that the rate limiting factor is the ability of material to flow into the growing intra-lithospheric delamination channel. In contrast, Bird envisioned there was limitless easy supply of weak material by upwelling of asthenosphere through a vertical conduit within the lithosphere. Here the delaminating lower keel is assumed to be: a) overlain by a viscous conduit-like MLDL channel (see the yellow area in Fig. 4) into which the material inflows to allow keel separation; b) embedded at its distal end (the left end in Fig. 4), e.g. where the MLDL disappears laterally; c) subjected to a uniform body load (F) due to the average net density difference between the denser lower keel and its adjacent asthenosphere (see Equation 1).

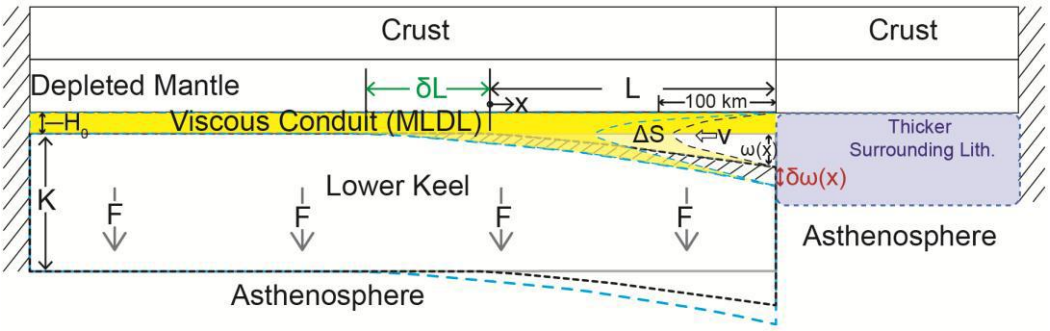

Fig. 4. Lubrication-theory based analytical model.

If the net density (compositional+ thermal) of the lower keel is higher than that of the adjacent asthenosphere (F>0), the lower keel will tend to sag downwards along the weak MLDL. Sagging of the lower keel cannot occur unless the material void (ΔS) is filled. If weak enough material can flow to fill this space, then rapid keel delamination can develop. Otherwise, the lower keel will not delaminate. Model Symbols: x – horizontal distance; F – body force favoring keel sinking; H_0 – initial thickness of the weak MLDL; L – Length of keel tearing along the MLDL. ∂L – new increment of MLDL tearing; V(x) – speed of lateral flow into and within the MLDL; w(x) additional opening of the MLDL as keel tearing develops. *Abbreviation*: Lith. - Lithosphere.

The body load F that drives delamination is given by:

$$F(x) = \overline{\Delta\rho} g K(x) \tag{1}$$

where K(x) is the lower keel thickness as a function of lateral distance x, Δρ is the average density difference between the lower keel and adjacent asthenosphere, and *g* is the gravitational acceleration.

As the lower keel flexes and delaminates (the lower keel is the black dashed line in Fig. 4), the vertical deflection of the plate ω from its initial position is given by Equation 2 [*Turcotte and Schubert*, 2014], where the flexural rigidity $D = Eh^3/12\left(1-\nu^2\right)$ and L is the lateral distance over which delamination has occurred:

$$\omega_1 = \frac{Fx^2}{D}\left(\frac{x^2}{24} + \frac{Lx}{6} + \frac{L^2}{4}\right) \tag{2}$$

For an increment δL of propagation of the delaminating region (the "plate" is the blue dashed line in Fig. 4), the new ω would be:

$$\omega_2 = \frac{F\left(x+\delta L\right)^2}{D}\left(\frac{\left(x+\delta L\right)^2}{24}+\frac{\left(L+\delta L\right)\left(x+\delta L\right)}{6}+\frac{\left(L+\delta L\right)^2}{4}\right) \tag{3}$$

With terms containing δL^2 and higher orders neglected, the incremental deflection $\delta\omega$ for an increment δL of delamination is given by:

$$\delta\omega = \omega_2 - \omega_1 = \delta L\left(\frac{F}{D}\right)\left(\frac{x^3}{3}+x^2L+\frac{xL^2}{2}\right) \tag{4}$$

This increment of keel bending would leave a material void (see Fig. 4), to be filled by lateral flow within the weak MLDL channel. The 'area' (e.g. 'volume per unit cross-section') of this material hole ΔS is given by:

$$\Delta S = \int_0^x \delta\omega\left(x\right)\,dx = \delta L\left(\frac{F}{D}\right)\left(\frac{x^4}{12}+\frac{x^3L}{3}+\frac{x^2L^2}{4}\right) \tag{5}$$

In order for the lower keel to sag further, material must flow into the MLDL to compensate the void space ΔS. This flow Q is:

$$Q\left(x\right) = v\left(\frac{F}{D}\right)\left(\frac{x^4}{12}+\frac{x^3L}{3}+\frac{x^2L^2}{4}\right) \tag{6}$$

where the speed of delamination $v = \delta L/\delta t$.

In the lubrication theory approximation (c.f. [*Batchelor*, 2000; *Bird*, 1979; *Parmentier et al.*, 1985]), the pressure gradient dP/dx is related to flow Q(x) by:

$$\frac{dP}{dx} = -\frac{12\mu(x)Q(x)}{h(x)^3} \tag{7}$$

where $\mu(x)$ is the MLDL channel viscosity at distance x. (This expression neglects buoyancy effects because the flow is assumed to be horizontal.)

In this case, the pressure reduction ΔP at a distance x is:

$$\Delta P\left(x\right) = -12\int_x^L \frac{\mu\left(x\right)Q\left(x\right)}{h\left(x\right)^3}\,dx \tag{8}$$

The negative sign implies a pressure drop towards the tip of the laterally

migrating region of delamination. If we assume that the total pressure drop dynamically balances the weight of the lower keel (F), then by equating Equation 8 with Equation 1, the growth rate of the delaminating region can be estimated from

$$\int_0^L \Delta P(x)\, dx = FL \tag{9}$$

As the left-hand side of the Equation 9 is difficult to integrate analytically, we numerically evaluate it in MATLAB, with a discrete sampling interval Δx=100m. If the MLDL viscosity $\mu(x)$ is assumed to be piecewise constant, $\int_0^L \Delta P(x)\, dx$ can be approximated by Equation 10.

$$\int_0^L \Delta P(x)\, dx \approx \sum_{k=1}^{n} \overline{\Delta P(x_k)} \cdot \Delta x \tag{10}$$

where $\overline{\Delta P(x_k)} = \left(\Delta P(x_{k-1}) + \Delta P(x_k)\right)/2$, n= L/$\Delta$x, x_k is the coordinate of the k^{th} grid-point and x_{k-1} is that of the previous grid point (for k=1, x_{k-1}= x_k).

3.2. Analytical Model Results

Once the conduit flow velocity (v) is calculated, the tearing speed of keel delamination can be determined. This speed is a function of the channel's thickness (H_0), length (L), and viscosity ($\mu(x)$), and of the negative buoyancy of the lower keel (F).

The effects of varying H_0, F and $\mu(x)$ are illustrated in Fig. 5. Here we consider two scenarios: 1) the conduit viscosity is a constant; 2) the outermost 100 km of the conduit is stronger than the rest of the channel, which resembles a scenario where the layer and its underlying lower keel are strongly coupled with stronger surrounding mantle (see Fig. 4). Here the stronger mantle should be treated as part of the tearing-linked conduit. In each plot, we only vary two variables, while keeping the others constant.

In Scenario 1 (see Fig. 5A), the pressure (ΔP) within the conduit decays gradually in the first 250-300 km close to the outside (right) edge, where is also

the range that the pressure gradient exists. In Scenario 2 with a sharper outer edge (see Fig. 5B), a significant pressure gradient only exists within the 100 km outermost edge of the conduit. In this scenario, conduit flow only occurs when the outermost region can deform enough to supply material into the weaker central portion of the MLDL's low viscosity channel.

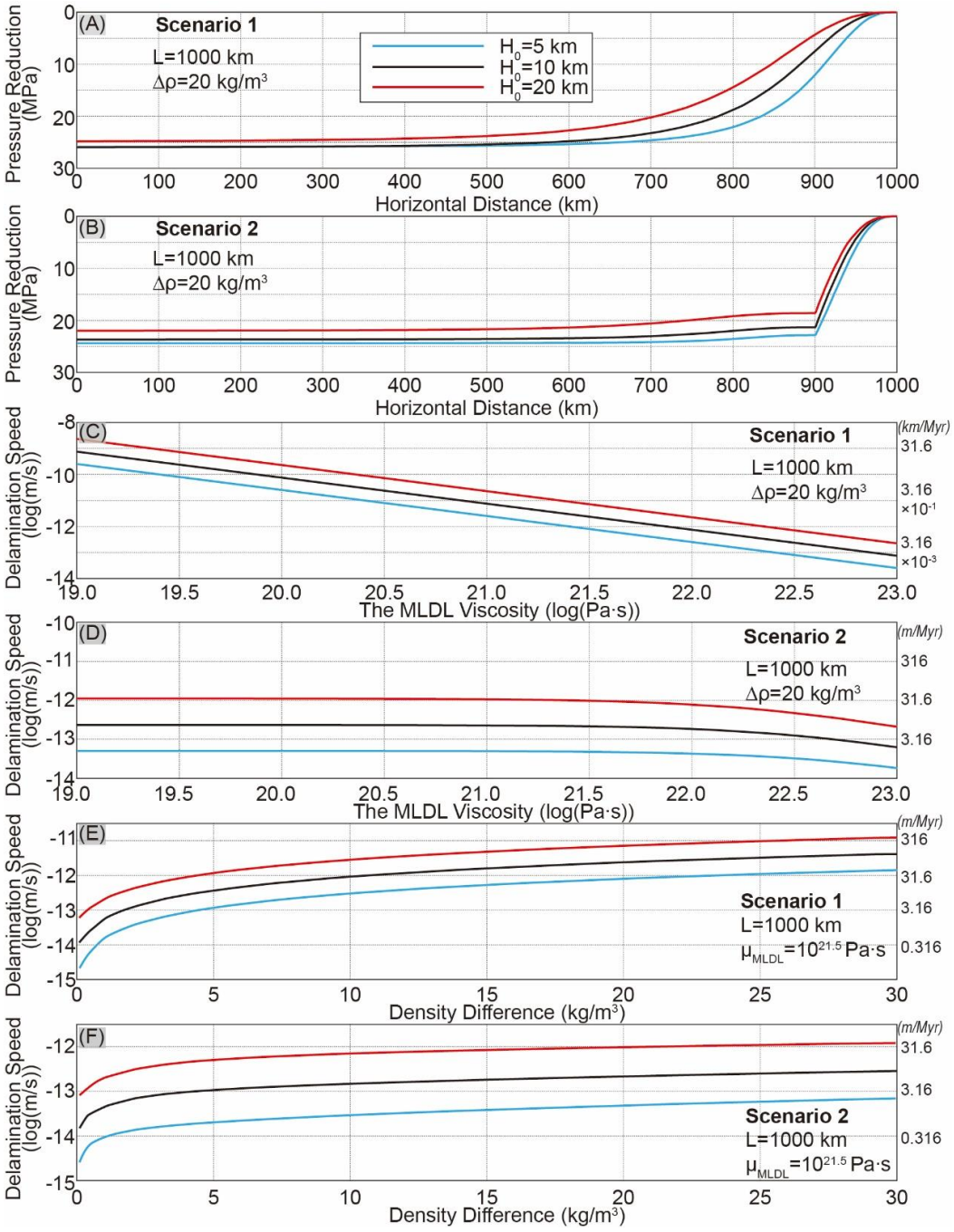

Fig. 5. Effects of MLDL viscosity and keel density on mean conduit flow velocity (=speed of keel delamination).

(A-F) The pressure-drop induced by keel sagging is plotted along the conduit (1000 km marks the right end, see Fig. 4). μ_{MLDL}- MLDL viscosity. $\Delta\rho$- average net density difference between the keel and its neighboring asthenosphere. Note that the units (km/Myr) for the right axis of Panel C differ from those (m/Myr) used for Panels D-F.

The speed at which the delamination tear migrates along the MLDL is controlled by the MLDL's viscosity in Scenario 1. In Scenario 2, it is controlled by the viscosity of the stronger "asthenosphere" and lithosphere that must also deform to supply material for the tear to propagate (see Fig. 5D). Faster conduit flow and tearing happen when the density difference $\Delta\rho$ between the lower keel and adjacent asthenosphere is larger (see Fig.5E-F), or when the conduit is thicker (see Fig. 5C-F).

3.3. Implications

Based on the above analysis, two end-member situations for keel evolution will naturally arise.

If a MLDL channel ends within strong (~10^{23} Pa·s) surrounding mantle, then delamination will not happen. For these parameters, the tearing speed is estimated to be <6 km/Gyr, e.g. be essentially stable (see Fig. 5D and 5F).

On the other hand, if the edges of a ~10 km thick weak MLDL are reactivated to have a ~10^{19} Pa·s viscosity (e.g. see Fig. 10F), and this layer is underlain by a lower keel possessing a large enough net density difference (e.g. ~20 kg/m^3, e.g. see the Density Panel in Fig. 7A), the tearing speed is predicted to be >30 km/Myr (see Fig. 5C). In this scenario, a >400 km regional keel-removal event would happen within 15 Myr.

The change in delamination speed due to variations in layer thickness can be crudely estimated from the results in Fig. 5C, which indicate that a 2 times

thicker/thinner layer can lead to ~3.2 times faster/slower delamination speeds. Finally, although this model is only 2-D, the basic mechanics are also only 2-D, e.g. flow along a weak intra-cratonic channel fed from the edge of the channel. Therefore, 3-D analysis is not needed to understand the basic speed and stresses/relief associated with this mode of intra-cratonic keel delamination.

4. 2-D Numerical Experiments

To further explore this scenario under less idealized conditions, we have also analyzed 2-D numerical experiments of this process.

4.1. Methods

The numerical experiments performed here use a modified version of 2-D incompressible elastoviscoplastic thermomechanical Lagrangian finite element code with diffusion and dislocation creep, "m2tri_trunk" [*Hasenclever*, 2010; *Hasenclever et al.*, 2011]. This version includes a free surface boundary condition [*Andrés-Martínez et al.*, 2015]. Melting is also included. Tracer particles are added for tracking different material properties. The 2-D experimental domain is subdivided using an adaptive triangle mesh generator that keeps high resolution across material boundaries and interfaces, e.g. slabs and keels (see Appendix B). More details on the numerical approach are given in Appendices, and in [*Andrés-Martínez et al.*, 2015; *Hasenclever*, 2010; *Hasenclever et al.*, 2011]. Table 1 shows the parameters used in numerical experiments.

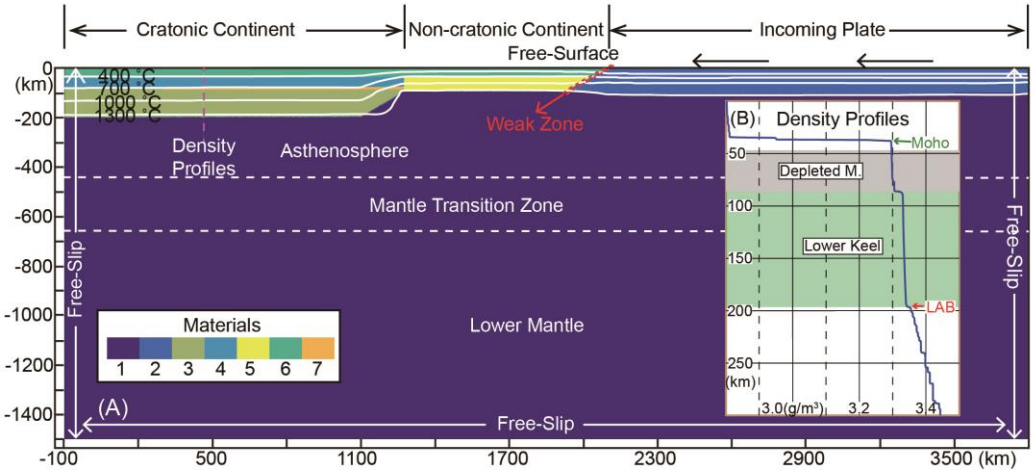

Fig. 6. Model set-up.

(A) The computational domain for Runs 2-7. The region is 3900 km wide × 1500 km deep. For Runs 1, 4*, and 7* it is 1900 km wide × 800 km deep. Mesh resolution for the MLDL phase boundaries is ~450m. Mesh resolution close to other phase boundaries (~4.5 km) is about 10 times finer than that (~45 km) in regions far away from these boundaries. Mesh resolutions within transitional distance range (~210 km) are linearly interpolated between these end-member values. To simulate the far-field effects of subduction in Runs 2-7, a leftwards 2×10^{-9} m/s (~6 cm/yr) velocity is applied to represent the incoming plate. A <10 km thick weak zone (10^{19} Pa·s) is added between the oceanic plate and the continental plate to promote decoupling. Material types: 1-asthenosphere, 2-oceanic plate, 3-cratonic keel, 4-depleted cratonic mantle, 5 non-cratonic mantle, 6-crust, 7-the MLDL metasome. (B) Initial density structures, data from the purple dashed line in (A). *Abbreviations*: M. - mantle, LAB - lithosphere-asthenosphere boundary.

4.2. Initial Density and Viscosity Structure and Boundary Conditions

We assume that mantle metasomatism (cf. [*O'Reilly et al.*, 2001; *Tang et al.*, 2013]) have increased the compositional keel density below the weak MLDL. This metasomatism would transform the keel from highly refractory peridotite (3310 kg/m^3 compositional density) to a compositional density of 3340 kg/m^3, a value still less dense than fertile asthenosphere (3360 kg/m^3) (cf. [*Djomani et al.*, 2001; *Griffin*, 1999]). These density parameters are crudely consistent with studies of kimberlite-borne mantle xenoliths (cf. [*Djomani et al.*, 2001; *Griffin*, 1999]) and

with craton gravity anomalies [*Kaban et al.*, 2003]. Intra-lithospheric MLDL material is prescribed to be even more buoyant, e.g. set to the 3320 kg/m^3 compositional density found in amphibole bearing mantle xenoliths [*Dawson and Smith*, 1988].

The side and lower boundaries of the box are set to be free-slip (see Fig. 6A). In Runs 2-7, stresses from a developing subduction slab are generated by imposing "plate subduction" geometry and velocities on the far edge beyond where the craton abuts a newly formed marginal rift basin (see Fig. 6A). In Run 1 (the case with a stable craton), the 200-350 km depth range of the right boundary segment is prescribed with a ~3cm/yr downward velocity for 10 Ma every other 100 Ma to simulate the effects of episodic subduction initialization.

	A.M.	D.M.	L. Keel	S.M.	Slab	Crust	MLDL
Flow Law Parameters[1-7]							
A_{dis} ($Pa^{-n}\cdot s^{-1}$)	$10^{-15.05}$	$4.85\cdot10^{-17}$			$3.0\cdot10^{-22}$	$1.4\cdot10^{-21.2}$	$10^{-15.4}$
n_{dis}	3.5					4.2	3
E_{dis} (kJ/mol)	480	535			540	445	356
V_{dis} (cm^3/mol)	8						
A_{dif} ($Pa^{-n}\cdot s^{-1}$)	$10^{-8.65}$					$10^{-13.3}$	$10^{-13.3}$
n_{dif}	1						
E_{dif} (kJ/mol)	335	375				170	170
V_{dif} (cm^3/mol)	4						
r	r_{dif}=1.93, r_{dis}=1.95					-	-
Thermal Parameters[8,11]							
G (GPa)	74					40	74
k ($Wm^{-1}K^{-1}$)	3.3					2.5	3.3
H_r ($\mu W/m^3$)	0.033					1	0.33
c_p (J/(kg· K)	1200						
T_0^m (°C)	1081	1136				-	1081
$\left(\partial T^m/\partial f\right)_p$	132					-	132
$\left(\partial T^m/\partial P\right)_f$	250					-	250

Q_L (kJ/kg)	400					-	400
Density Parameters[9, 10]							
ρ_0 ($g \cdot cm^{-3}$)	3.36	3.31	3.34	3.31	3.31	2.80	3.32
a_1 (10^{-4})	0.2697	0.27165	0.27165	0.27014	0.27768	0.27014	0.2697
a_2 (10^{-8} K^{-1})	1.0192	1.04971	1.04971	1.05945	0.95451	1.05945	1.0192
a_3 (K^2)	-0.1282	-0.15031	-0.15031	-0.1243	-0.12404	-0.1243	-0.1282
K (Gpa^{-1})	134	129	129	130	128	63	134

Tab. 1. Parameters for numerical experiments.

Rheology parameters for the MLDL are varied in different experiments (see Section 5 and Table 2). Parameters in this table are for a wet anorthite rheology (Reference 5), the parameters for wet olivine and mica rheologies are from References 1, 7 and 6 below. Dislocation and diffusion viscosities are calculated using $\eta = 1/2\, A^{-1/n} C_{OH}^{-r/n} \varepsilon_{II}^{1/n-1} \exp\left((E + P \cdot V)/nRT\right)$, where η is viscosity, ε is the second invariant of strain rate, A is a pre-exponential constant, E is the activation energy, C_{OH} is water content in ppm H/Si (for olivine Fo90: 1ppm (wt) H_2O= 16.35H/10^6Si;), r describes the exponential dependence of viscosity on water content, R is the universal gas constant, T is temperature, P is pressure, and V is activation volume. Subscript "dis" refers to parameters for dislocation creep, while "dif" refers to diffusion creep.

Parameter references: 1- [*Hirth and Kohlstedt*, 2004], 2- [*Hirth and Kohlstedt*, 1996], 3- [*Karato and Wu*, 1993], 4- [*Wilks and Carter*, 1990], 5- [*Rybacki and Dresen*, 2004], 6- [*Kirby and Kronenberg*, 1987], 7- [*Korenaga and Karato*, 2008], 8- [*Brune et al.*, 2014], 9- [*Djomani et al.*, 2001], 10- [*Schutt and Lesher*, 2006],11- [*Morgan*, 2001].

Other symbols: G- shear modulus, k- thermal conductivity, H_r- radioactive heat production, c_p-heat capacity, T_0^m - the solidus at room temperature and pressure, $\left(\partial T^m/\partial f\right)_p$ describes the solidus's dependence on degree of melting, and $\left(\partial T^m/\partial P\right)_f$ describes the solidus's dependence on pressure, Q_L- Latent heat, ρ_0- the reference density at room temperature (20℃) and pressure (0.1 Mpa), K- bulk modulus.

Abbreviations: A.M. - asthenosphere, D.M. - cratonic lithospheric mantle above the MLDL, L. Keel- lower keel, cratonic lithospheric mantle below the MLDL, S.M., non-cratonic continental lithospheric mantle.

As noted in the introduction, because poor seismic resolution may lead to overestimates of MLDL thicknesses, in each experiment the weak layer is assumed to be 10km thick. Keel delamination rate is found to depend on the density contrast of the lower keel, MLDL rheology, and MLDL thickness (see Fig. 5). Here, we usually choose to fix the MLDL thickness to be 10 km in order to focus on exploring the effects of its rheology. The change in delamination speed due to differences in MLDL layer thickness can be crudely estimated from the results in Fig. 5C, which indicate that a 2 times thicker/thinner layer can lead to ~3.2 times faster/slower delamination speeds.

4.3. Goals of the numerical experiments.

Run 1 (see Table 2) is designed to test the first implication in Section 3.3 that: a dense lower keel beneath a weak MLDL can remain stable for >1 Ga, as long as the lithosphere adjacent to the weak layer remains strong. In this experiment, the lithosphere near the MLDL is 140 km thick, in which case its cooler geotherm implies that the lithosphere adjacent to the MLDL has $>10^{22}$ Pa·s viscosity (see Fig. 7B). A gradual lithospheric thickness change close to cratonic edges is consistent with seismic observations (cf. [*Begg et al.*, 2009]).

Because the rheology for the MLDL is quite uncertain, the experiments explore the implications for a wide range of MLDL rheologies that include a MARID-like mineral assemblage (Run 2), wet olivine (Runs 4 and 4*), and the rheology of the mixture of MARID and wet olivine (Runs 1, 3, 5, 6, 7 and 7*).

To crudely study the effects of nearby subduction process, Runs 4 and 4 *, and Runs 7 and 7* are compared to study scenarios with/without the subduction stress field.

	Sub. F.	N.L.T.	MLDL rheology	Water on melting
Run 1	yes	140 km	80% Wet Ol (214) + 20% Wet An	no

Run 2	yes	100 km	Wet An	no
Run 3	yes	100 km	33.3% Wet An + 66.6 % Mica	no
Run 4	yes	100 km	Wet Ol (214)	no
Run 4*	no	100 km	Wet Ol (214)	no
Run 5	yes	100 km	90% Wet Ol (214) + 10% Wet An	no
Run 6	yes	100 km	80% Wet Ol (214) + 20% Wet An	no
Run 7	yes	100 km	80% Wet Ol (214) + 20% Wet An	yes
Run 7*	no	100 km	80% Wet Ol (214) + 20% Wet An	yes

Tab. 2. The numerical experiments discussed in this study.

Effect of water on melting: In experiments where the MLDL is assumed to be mainly composed of wet peridotite (1000 ppm water), water's extra effect on mantle melting is treated using Equation A15. (214) marks the water content in ppm (by weight) used for calculating the rheology of olivine (see captions below Table 1). 33.3% refers to the lithology's volume proportion used in Equation 11. *Abbreviations*: Sub. - subduction stress field, N.L.T. - non-cratonic lithospheric thickness, Ol. - olivine, An. - anorthite.

5. 2-D Numerical Results

The 2-D numerical experiments focus on exploring: 1) What parameters lead to the general "typical" situation of a stable long-lived keel; 2) What MLDL rheology is needed in order for a rapid delamination event to occur; 3) Which parameters lead to the "best-simulating" numerical results when compared to the observations for partial keel delamination beneath the ENCC and the WWC; 4) How do lateral variations in the MLDL and variations in far-field subduction potentially influence keel delamination?

The detailed keel delamination process will only be described for Run 2. Other experiments with delamination evolve in similar patterns with varying speeds of keel-tearing and delamination. Before discussing delamination experiments, we first examine the most common case in which a cratonic keel remains stable and does not delaminate over billions of years.

5.1. A Cratonic Keel will be Stable as long as the MLDL's edge Remains Stable

Cratonic keel-removal is a rare geological phenomenon. Any keel delamination mechanism that can explain how keel-removal happened in the ENCC and the WWC must first be able to explain the longevity of stable cratons.

The previous analysis suggests that stable cratonic keels should have margins where MLDLs abut relatively thick and strong surrounding lithosphere. If this geometry persists, the analytical analysis and numerical experiments both predict that a dense cratonic keel can stably exist over billions of years (see Section 3.3). In the numerical example shown in Run 1, the craton-edge lithospheric thickness (Table 2) is set to be 140 km, 40 km thicker than in the following experiments in which delamination happens. Other parameters and boundary conditions are similar to Run 6 (see Table 2 and Section 5.2), where the experiment has an ENCC-like keel delamination duration. After 1Gyr of model time, the shape of the keel margin has become smoother. But the MLDL's shape change is hardly distinguishable (see Fig. 7B), and the keel has remained stable.

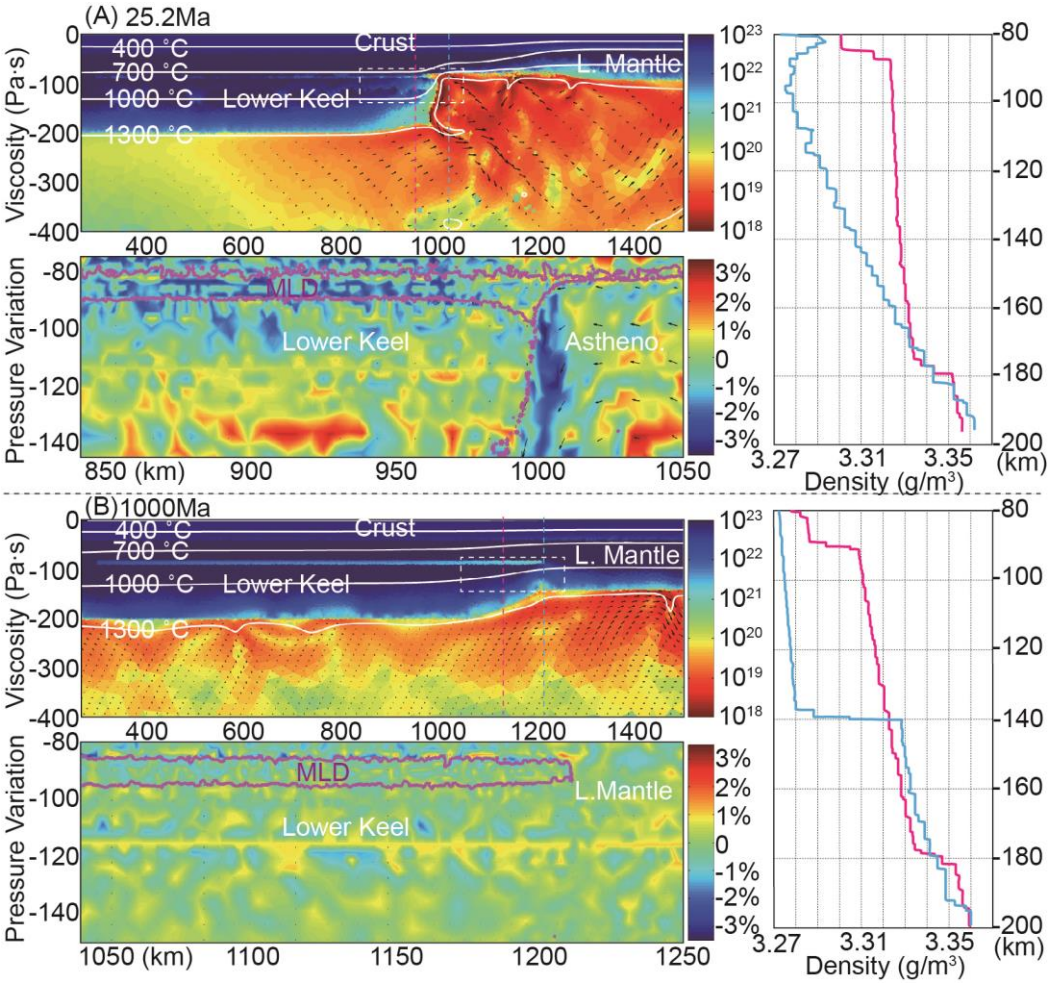

Fig. 7. The low-pressure zone induced by partial keel tearing.

(A) (lhs) *Viscosity Panel*: viscosity plot during Run 4. *Pressure Panel*: pressure variations (P_{var}) within the dashed box shown in the Viscosity Panel. Pressure variations are shown in percent, where $P_{\text{var}} = \left(P - P_{ref}\right) / P_{ref}$. The reference pressure profile P_{ref} is along the blue dashed line in the Viscosity Panel. (rhs) *Density Panel*: density profiles along the vertical purple and cyan dashed lines shown in the same color in the Viscosity Panel. (B) Results after 1Ga of evolution in Run 1. No keel tearing is observed. The same plot conventions are used as in panel A.

To better understand when keels are stable/unable to delaminate, in Fig 7, the pressure variations in Run 1 and Run 4 (see Section 5.2) are compared. Even though the keel delamination process in Run 4 is the slowest shown here (see Fig. 9), the theoretically predicted low pressure zone (see Fig. 5A) can still be seen

within the unreactivated portion of the MLDL (see Pressure Panel in Fig. 7A), suggesting that the channel-flow mode of keel tearing is taking place. Over time, the power law creep associated with channel flow (see Viscosity Pane in Fig. 7A) further weakens the surrounding mantle, which then more easily fills the void along the MLDL and accelerates keel tearing (see more details in Section 5.2). In contrast, in Run 1, because the MLDL edge is coupled to a stronger surrounding lithosphere, channel flow and its induced pressure drop do not appear within the MLDL (Fig. 7B). Therefore, MLDL edge failure by tearing and delamination also does not occur. The cratonic keel can remain stable for billions of years, even with a prominent MLDL within it, as long as the MLDL-containing portions abut against strong surrounding lithospheric mantle.

5.2. Keel Delamination Experiments

In the following numerical experiments, we assume that a MLDL has developed to extend close to the edge of a cratonic keel. This scenario may have existed, for the ENCC and WWC, just after the cratons amalgamated with a recently-formed "oceanic" plate, e.g. the north-eastern China blocks [*Wu et al.*, 2011] or accreted oceanic terranes to the west of the Salmon River suture zone [*Foster et al.*, 2006].

Delamination along a MLDL linked to Mantle Metasomatism

In Run 2, the MLDL is assumed to be related to persistent metasomatism events (see Introduction). Although the rheology of mica has not been studied under mantle conditions, limited experiments suggest that it has a weaker rheology than amphibole, which in turn resembles that of wet anorthite [*Getsinger and Hirth*, 2014]. We therefore use a wet anorthite rheology as the upper-limit strength for the rheology of a spatially discontinuous MARID-like MLDL.

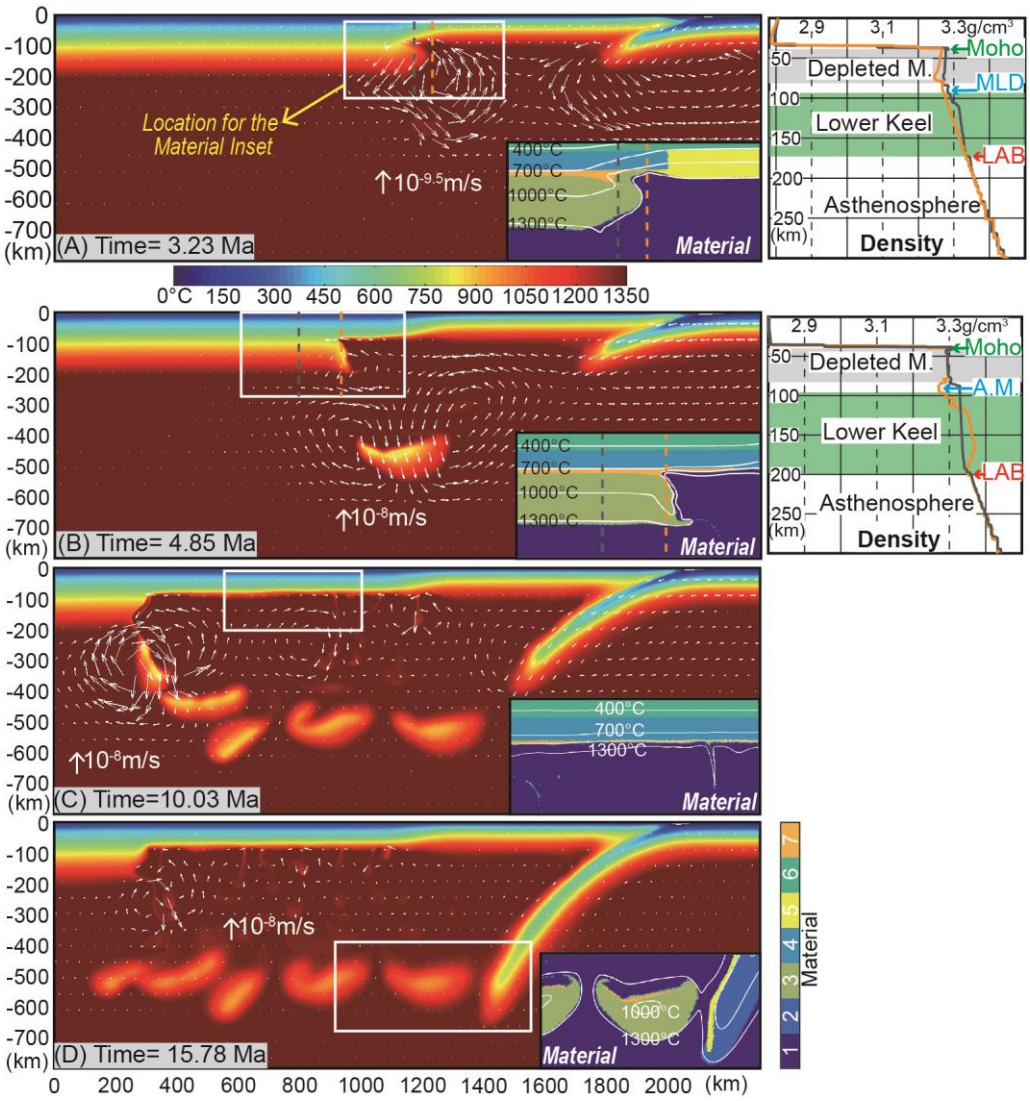

Fig. 8. Numerical realization of the keel delamination process (results of Run 2).

(A) Keel starts to decouple from the MLDL. *Material Panel Inset*: Material distribution within the white rectangle in panel A. Short white lines with arrow mark the direction of local convection. *Density Panel*: Density profiles along corresponding vertical dashed lines with the same orange and brown colors in panel A. (B) The delaminating keel triggers vigorous convection. (C) The last keel fragment separates. Post keel-delamination evolution, e.g. thermo-mechanical erosion, starts to develop in hotter relic regions. (D) Keel delamination stops where the MLDL terminates. Plot conventions are the same as in Fig. 6. Materials: 1-asthenosphere, 2-oceanic plate, 3-cratonic keel, 4-depleted cratonic mantle, 5 non-cratonic mantle, 6-crust, 7-the MLDL metasome.

Since horizontal temperature perturbations exist close to the keel, small-scale convection before delamination only occurs within the asthenosphere. The convection can further weaken the asthenosphere due to its power-law viscosity. But, a weak asthenosphere alone does not affect keel stability unless the asthenosphere can break a mechanical connection to the MLDL.

Because the keel margin is denser than the asthenosphere to its side (see Density Panel in Fig. 8A), according to the analytical analysis in Section 3, the lower keel should tend to sag downwards as long as material can flow laterally into the weak MLDL. When the surrounding lithosphere mantle is both thin (100 km) and weak, then this mode of deformation can occur. As the keel margin sags downwards, "intra-channel" material connecting the MLDL to the asthenosphere is pulled towards the MLDL (see Material Panel in Fig. 8A and also Fig.10B-D). The MLDL will have a direct horizontal connection with the asthenosphere once this stronger non-asthenospheric material is removed. When the direct connection forms, the rate of keel tearing increases (see Fig. 8B). As it tears away and delaminates, the lower keel itself tends to break into ~300 km wide blocks (see Fig. 8B-C), with keel fragmentation events associated with temporary pauses in keel tearing. The denser keel relics sink, with overall asthenosphere cooling around the descending keel fragments (see Material Panel in Fig. 8B). Some weak MLDL material is entrained into the deeper mantle during descent of delaminated keel fragments (see Material Panel in Fig. 8D) Due to its compositional buoyancy and weak rheology, most MLDL material either remains beneath the overlying relic lithosphere or is mixed into the asthenosphere (see Material Panel Fig. 8C). Note that small-scale convection and deformation of the now-exposed lithosphere above the MLDL following a delamination event [*Liu et al.*, 2016] (see Material Panel Fig. 8C), will be the focus of a companion paper (*Evolution of Cratonic Lithosphere after a Rapid Keel Delamination Event*, Liu et al., 2018, submitted, which we will hereafter refer to as Paper II). Keel delamination stops in places

where the intra-cratonic MLDL does not exist. In this scenario, the observed locally discontinuous nature of MLDLs [*Chen et al.*, 2014; *Hopper et al.*, 2014] is what limits the spatial scale of each regional keel delamination event. Note that inter-cratonic orogenesis and melting can also lead to melt-extraction-related removal of MLDL material.

Run 3 is a similar experiment to Run 2. In this case, a mica plus amphibole rheology, is considered as the weak-limit estimate to the strength of the MLDL. The MLDL's effective viscosity (μ_{MLDL}) is calculated assuming the bulk rheology given in Equation 11, where x_1 is the volume proportion of amphibole.

$$\mu_{MLDL} = \left(\frac{1 - x_1}{\mu_{amphibole}} + \frac{x_1}{\mu_{MARID}} \right)^{-1} \tag{11}$$

With a weaker MLDL rheology, delamination happens faster and finishes within ~3 Ma (see Fig. 9). In both experiments, the strength of the MARID layer (10 km thick, with a ~$10^{18.5}$ viscosity) is the factor controlling the speed of keel tearing during the delamination event is, not the viscosity of the surrounding mantle. This behavior is consistent with the analytical model. The implied duration for a 1000 km wide regional keel delamination event would be shorter than 10 Myr. These implied tearing rates (>100 km/Myr) are faster than the magmatism-indicated keel removal rates for the ENCC (~17 Myr for ~1000 km) or the WWC (~11 Myr for ~400 km) (see Fig. 1). Assuming the thickness of the MLDL layer is appropriate, then the MLDL should have a composition with a rheology stronger than that of a pure MARID component.

Delamination along a MLDL due to Chemically Bound Water

A MLDL has also been interpreted as a water-rich intra-cratonic layer (Origin 1 in the Section 1), with a rheology dominated by wet olivine. At 80-100 km depths within a 200 km craton (i.e., ~700-800℃, ~3Gpa), the chemically bound water content has been proposed to be >1000 ppm [*Karato et al.*, 2015]. If the MLDL contains are 60% olivine, 12% clinopyroxene and 28% orthopyroxene (cf.

[*Hirschmann et al.*, 2009]), the water content in olivine is estimated > 214 ppm. With 1.93 exponent factor [*Korenaga and Karato*, 2008] for the effect of water on diffusion creep, the MLDL is predicted to be >11 times weaker than a wet olivine (61 ppm) rheology.

In Run 4, the MLDL is assumed to have a wet (214 ppm) olivine rheology. In this case, lower keel delamination starts ~11 Myr after the onset of the experiment (see Fig. 9). A 1000 km wide regional keel delamination event ends at ~36 Myr, the delamination process taking ~25 Myr. This predicted delamination rate (~40 km/Myr) is consistent with evolution on the WWC, but somewhat slower than that (~60 km/Myr) of the ENCC (see Fig. 1).

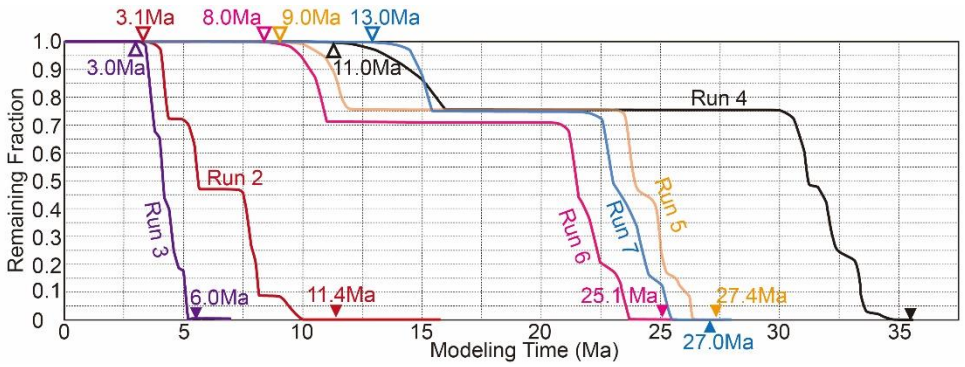

Fig. 9. The progress of keel tearing and delamination during Runs 2-7.

The remaining fraction of the lower keel is calculated by L_R / L_I, where L_I is the initial horizontal keel extent (1000 km) beneath the MLDL, and L_R is the remaining horizontal keel extent beneath the MLDL.

Keel Delamination along a MLDL with a Rheology Shaped by both Metasomatism and Chemically Bound Water

Geochemical observations on the ENCC can be interpreted to hint that both MARID-like metasomatic components and water-rich peridotites coexisted within the MLDL before the ENCC keel's destruction [*Menzies et al.*, 1993; *Xia et al.*, 2013; *Xu*, 2001; *Xu et al.*, 2009; *Zhu et al.*, 2012]. What if some MLDLs are rheologically weak because of both effects, e.g. they consist of a "wet" peridotite

layer that contains discrete interbedded MARID lamellae, with a composite rheology governed by an analog to equation 11?

In Runs 5 and 6, we assumed that the MLDL is composed of: a) 10% (volume percentage) MARID+ 90% wet peridotite, or b) 20% MARID + 80% wet peridotite. In both runs, the MLDL's effective viscosity (μ_{MLDL}) is calculated assuming the bulk rheology given in Equation 11, where x_1 is the volume proportion of the first component. Because the MLDL in Run 5 contains a lower proportion (10%) of the MARID component, its effective viscosity is higher. In this case, the keel delamination takes ~18.3 Myr, ~1.3 Myr longer than that of the Run 6 (see Fig. 9). In Run 6, the keel delamination starts at ~8Myr after the onset of the far-field subduction, and 1000 km wide regional keel delamination takes ~17.1 Myr. Both of these appear to be consistent with geological observations for the ENCC.

5.3. Other Factors Affecting Keel Delamination

Effects of MLDL Melting

If the MLDL is mainly due to chemically-bound water [*Karato et al.*, 2015], the high-water content will also lower the solidus of the layer (see Equation A15) (cf. [*Katz et al.*, 2003]). During partial melting, water in peridotite is thought to partition into melt roughly like Ce, with a ~0.009 peridotite/melt partition coefficient [*Aubaud et al.*, 2004]. In this case, the dehydration effect of potential melting process will tend to harden the residual MLDL. We have studied possible effects of MLDL melting on keel delamination with Run 7. This run is similar to the conditions in Run 6, except that it includes the effect of water (1000 ppm) on MLDL melting.

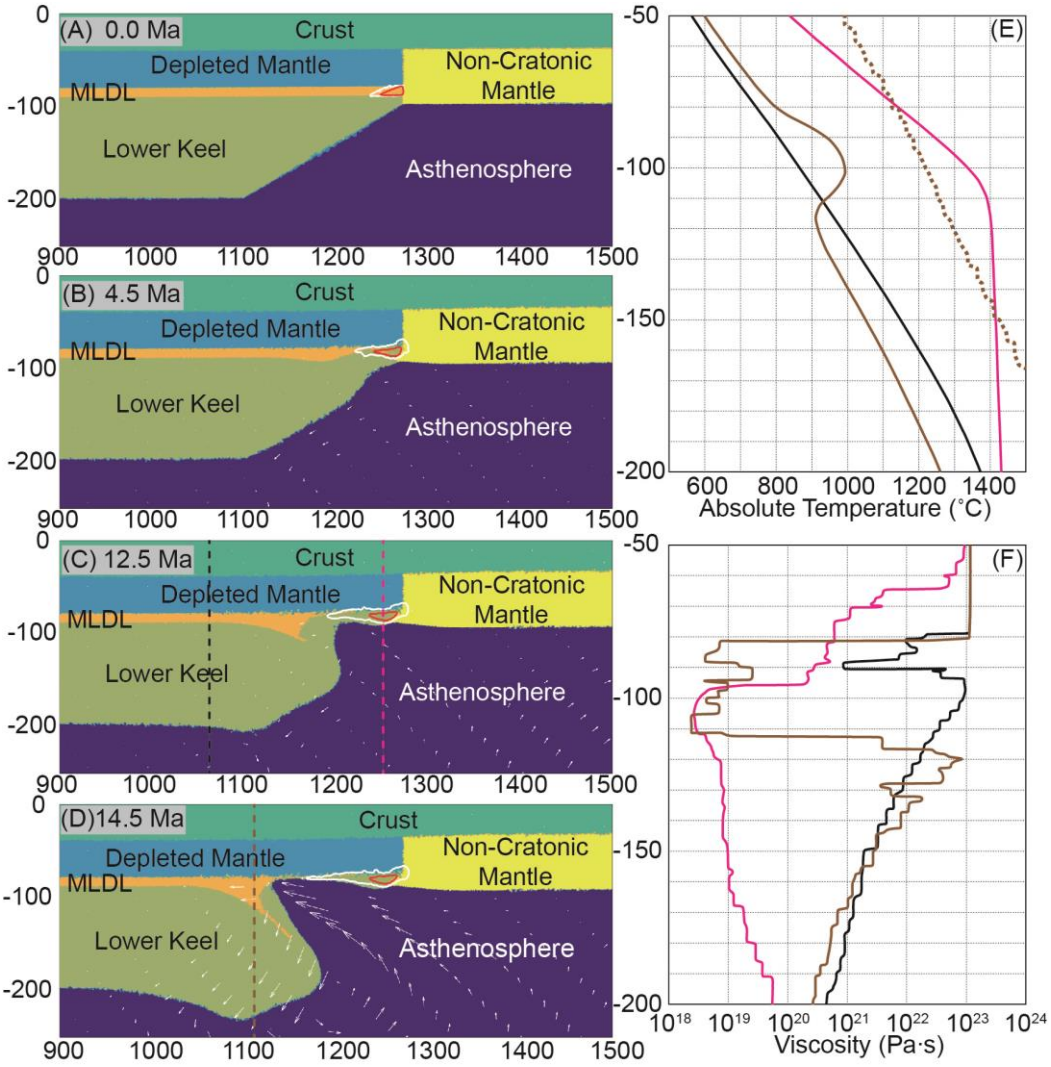

Fig. 10. Melting effects on keel delamination.

Panels A-D show results from Run 7. White lines mark regions where melting happens (with melting degree f > 0); red lines mark regions with melting degree >2%. Short while lines with arrow mark the direction of local convection. (E) Temperature profiles along the corresponding vertical dashed lines of the same color in Panels C and D. The Mantle Solidus (brown dashed line) is plotted along the dashed line in Panel D (see method in Appendix A). Note that: the MLDL remains its low temperature and does not melting during the delamination of the lower keel. (F) Viscosity profiles along the corresponding vertical dashed lines of the same color in Panels C and D.

In this run (Fig. 10), MLDL melting happens near the beginning of the experiment and is focused within a small and relatively hot region close to the

craton's margin. During subsequent keel tearing and delamination (Fig. 10B-D), the melting region does not expand. This happens because flow within the MLDL is horizontal flow of cool MLDL material (see Fig. 10E). Limited melting can dehydrate a small fraction of the MLDL, thereby transforming it into a drier and stronger residue (see Fig. 10B-D). This process is equivalent to supplying a mechanically different component at the end of the conduit (see Fig. 4). Since the dehydrated material is stronger, the keel's tearing rate slows. In this run, keel delamination starts at ~13 Ma, ~ 8 Ma later than that of Run 6 (see Fig. 9). However, because pervasive melting of MLDL does not happen during keel delamination, the evolution in this run is quite similar to Run 6 (see Fig. 9). This is also the reason that we do not view MLDL melting as a major factor when delamination happens. The paper II studies the melting processes that follow keel delamination.

Effects of Far-field Subduction

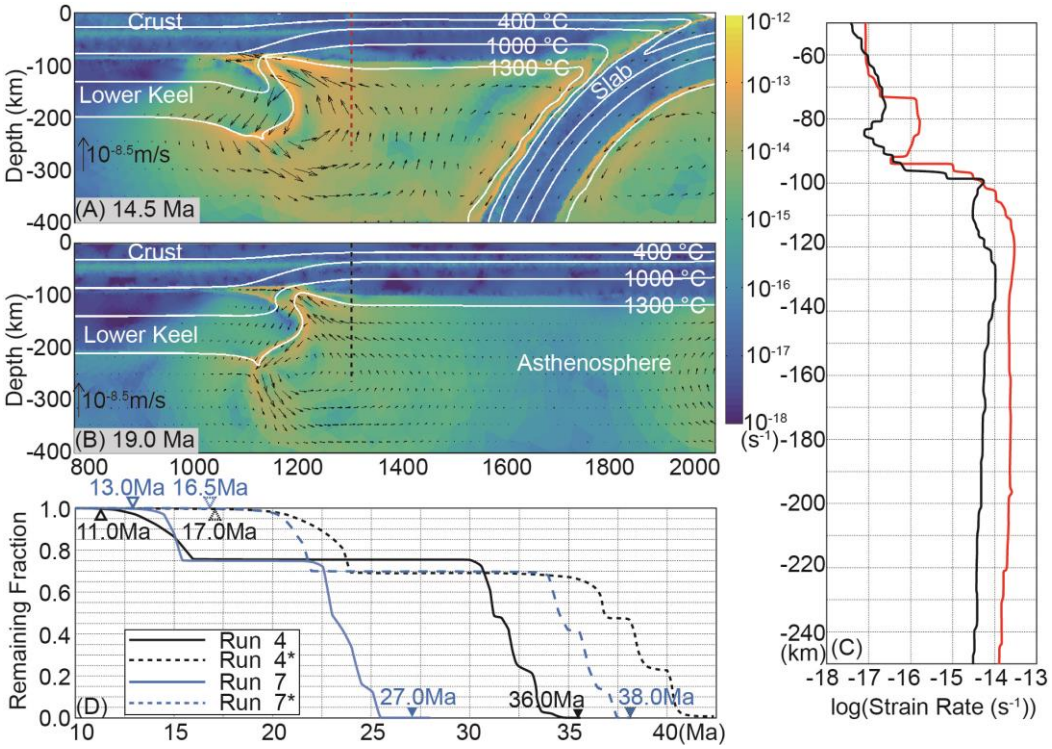

Fig. 11. Effects of far-field subduction on keel delamination.

Panels A - B are plots of second invariant of strain rate during Runs 7 and 7*. (C) The second invariant of strain rate along the corresponding vertical dashed lines of the same

color in Panels A and B. (D) The keel tearing and delamination progress during Runs 4, 7 (with subduction) and Runs 4*, 7*(without subduction). Plot conventions are the same as in Fig. 9.

Because the ENCC and the WWC keel-removal events may be related to subduction-craton interactions (cf. [*English and Johnston*, 2004; *Snyder et al.*, 1976; *Zhu et al.*, 2012]), we have also explored experiments that study the potential effects of subduction on the tearing mode of keel delamination.

The far-field subduction condition is removed in Runs 4* and 7*, which are otherwise similar to Runs 4 and 7. Without nearby regional subduction (see Fig 11), the onset of keel delamination is slower. This occurs because far-field subduction induces more vigorous flow in the asthenosphere near the keel's edge that weakens its power-law-creep-dependent viscosity (see Fig. 11 A-B). We see that strain rates in Runs 4 and 7 are generally higher than those of Runs 4* and 7* (see Fig. 11C), so that mantle material close to the MLDL in Run 4 and 7 is weaker than that in Run 4* and Run 7*. This weaker surrounding mantle can more easily flow into the MLDL to fill the void left by keel tearing and delamination (see Fig. 5C).

6. What controls the depth of the MLDL?

As noted above, the cause of the MLDL remains uncertain. Long-lived mantle metasomatism has been proposed to be the cause of the MARID layer observed in kimberlite xenoliths. The usual thermodynamic rationale for its location at ~80-100 km depths is that these are the p-T conditions at which MARID minerals exsolve and form in reactions between mantle and ascending volatile-rich CO_2-rich hydrous magmas [*Eggler*, 1978; *Dalton and Presnall*, 1998]. The melts that periodically infiltrate the lithosphere would be created by deeper upwellings at the craton base that generate fluid-rich hydrous magmas (kimberlites in crude sense, *cf.* [*Choukroun et al.*, 2005; *O'Reilly and Griffin*, 2013]). Episodic reheating of the

base of a craton could induce partial melting associated with repeated upward migrations of these magmas to MLDL depths of reaction/exsolution [see also *Griffin et al.*, 2014; *Malkovets et al.*, 2007]. Sleep (personal communication, 2018) has suggested the alternative mechanism that there may be a rheological control that leads to preferential ponding of CO_2-rich hydrous magmas at the MLDL depth, that they pond at the base of the lithosphere's brittle-ductile transition in its strength 'Christmas-tree' (Sleep, 2009). Finally, lithospheric 'stacking' during subduction has also been proposed as the origin for a craton and its MLDL, with the MLD reflecting the interval between the two lithospheric slices [*Lee et al.*, 2011].

Once formed within a craton, a MLDL can stably remain until the craton's edge is destroyed. For example, episodic and rapid back-arc extension during the evolution of subduction (cf. [*Faccenna et al.*, 2001]) could induce lithospheric extension close to the edge of the craton's MLDL (e.g. at ca. 180 Ma [*Maruyama et al.*, 1997]), and so create a geometry like the initial geometry assumed in Fig. 6.

7. Similarities and Differences Between Analytical and Numerical Results

In many respects the numerical experiments replicate basic aspects of the analytical lubrication-theory-based solutions. Keel delamination does not occur over an Archaean craton's lifetime when a 10s of km wide region at the edge of the MLDL has viscosities of order 10^{23} Pa·s. Geologically rapid delamination happens when a MLDL is 'exposed' to nearby low-viscosity ($<10^{21}$ Pa-s) asthenosphere. Other behavior is different. In numerical experiments, the delaminating keel breaks into ~200-300 km wide fragments as delamination progresses. While geologically rapid, the delamination process itself occurs in jerks, with pulses of rapid delamination ending as a keel fragment breaks away. This jerkiness in delamination is linked to lateral flow within the MLDL, with lateral flow allowing the MLDL to preferentially thicken in regions undergoing

slow delamination (see Fig. 12B) while also increasing lateral pressure gradients in regions adjacent to the delamination front. Tearing jerks are also linked to fragmentary keel breakoff, with breakoff associated with simultaneous local uplift (Fig. 12) and a reduction in the net negative buoyancy of the keel — the driving force for delamination.

Post-Delamination Uplift

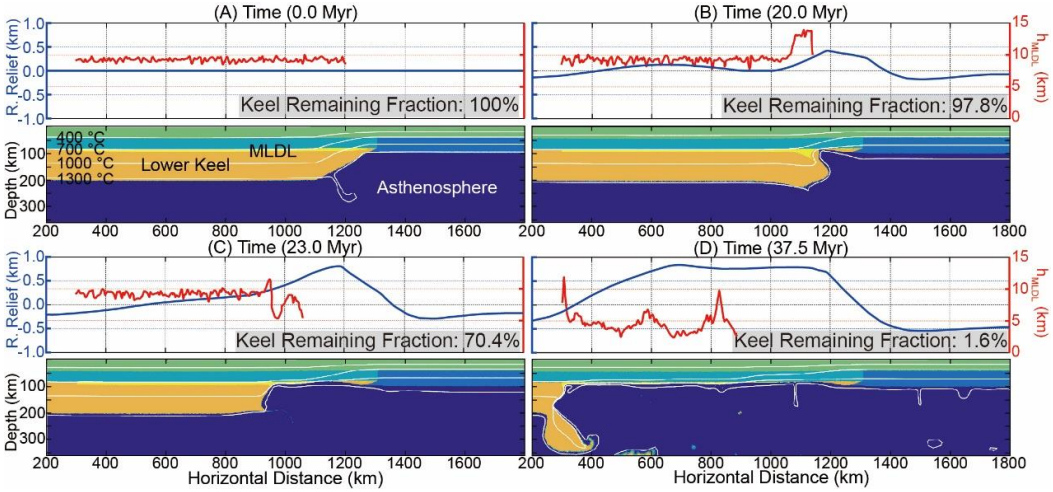

Fig. 12. The evolution of surface relief and MLDL thickness.

(A-D) Four snapshots of relative relief, MLDL thickness and material phase are plotted for Run 7* (see Table 2 and Fig. 9). Relative relief (R. Relief) is calculated by subtracting the surface relief from the 1st time step (see Panel A). Because the effects of erosion and sedimentation are not considered in the numerical experiments, relative relief can only crudely delimit delamination-induced variations in relief. See the Supplementary Videos for more insight into these time-dependent phenomena.

The 2-D numerical experiments indicate potential post-delamination uplift, which not apparent in 1-D experiments. After keel delamination, the surface expression is ~600 -900 m uplift (see Fig. 12 and Supplementary Videos 4), significantly less than the uplift of order ~3 km predicated in previous studies [*Krystopowicz et al.*, 2013]. (Total uplift will be related to the net density contrast between removed keel and infilled asthenosphere.) This suggests that delamination

may not be associated with the creation of a "high plateau" that reverses the source direction of local sediment transport. Therefore, the scenario here does not appear to contradict sedimentary records which suggest that during the Mesozoic (ca. 180-150 Ma) portions of the North China remained relatively low in elevation and still accepted sediments from its surrounding continental blocks [*Li et al.,* 2013]. Delamination is also likely to be associated with post-delamination extension that can create local depocenters.

8. Implications for Global Rates of Craton Destruction

Even with generous estimates for keel destruction beneath the ENCC and WWC, the implied recent rate of craton destruction is relatively small. For the ENCC, the surface area above the destroyed keel is estimated to be 5.7×10^5 km^2 [*He et al., 2015*]. For the WWC, the most conservative estimate for the surface area above the destroyed keel is the area to the west of 110 km thickness contour on the WCC (Fig. 1B), which is ~3.8×10^4 km^2 (38% of the total area [*Chamberlain et al.*, 2003]). If these two keel fragments were the only sites of keel delamination within the past 200 Myr, the implied destruction rate would be 6.1×10^5 km^2/200 Ma = 3.1×10^6 km^2/Gyr. The remaining cratonic fraction of continents is estimated to have a surface area of 3.7×10^7 km^2 [*Artemieva,* 2012], which would imply that modern rates of craton destruction would destroy 14 % of the original craton area over 2 Gyr, or 25% of the original craton area over 4 Gyr. Even assuming that paleo-destruction rates were likely to be faster during the Archean, modern rates of keel destruction are consistent with continents still retaining a large surviving craton area.

9. Lateral Variability in Cratonic Keel Removal

Although regional cratonic keel removal has been reported in the ENCC, the WWC, and possibly beneath parts of the Dharwar and the Brazilian Cratons, neighboring parts of these cratons still maintain their apparently stable thick

cratonic state. This suggests that keel delamination is both rare and piecewise. In our preferred scenario, this happens because:

1) MLDLs are laterally discontinuous and variable (see Fig. 2B) [*Chen et al.*, 2014; *Hopper et al.*, 2014]. In this case, cratonic parts without well-developed MLDLs survive due to their internal integrity (see Fig. 8D). Discontinuous MLDLs can be created by spatial and/or temporal variations during their formation. For example, intra-cratonic compositional layering in the Kalahari Craton may be linked to multiple kimberlite intrusion episodes in different epochs [*O'Reilly and Griffin*, 2013]. MLDL continuity can also be disturbed by episodic reheating and MLDL melting near cratonic edges, or where internal intra-cratonic boundaries are reheated by mantle plume-related processes [*Griffin et al.*, 2014]. Sharp vertical changes in adjacent MLDL depths could be created by strongly varying lateral temperature conditions at the time of metasomatism of each section of the discontinuous MLDL, e.g. due to the existence of thicker crust beneath ancient block boundaries [*Kinck et al., 1993; Youssof et al., 2013*]. This too would tend to increase the resistance of the craton to pervasive keel delamination.

2) The cratonic keel's fertility and compositional density may also be laterally inhomogeneous, which can be directly linked with heterogeneity in the MLDL (i.e. if both are due to metasomatic processes) [*Artemieva and Vinnik*, 2016; *Griffin et al.*, 2003; *Kaban et al.*, 2003; *Kaban et al.*, 2016; *Mooney and Kaban*, 2010]. Less fertile and more compositionally buoyant keel regions may better resist delamination (see Fig. 5). A more fertile keel state should naturally tend to appear at a craton's margin, due to the enhanced tendency for plume and/or asthenosphere melting beneath the thinner keel edges. The spatial scales for keel refertilization events can be limited, e.g. if some plume-related events have led to the keel refertilization in southwestern Kalahari Craton [*Griffin et al.*, 2003], keel refertilization may have been limited to the sizes of the plume tails (~100 km in diameter) or the lateral extent of drainage associated with lateral plume flow

[*Yamamoto et al.*, 2007].

10. Conclusions

1) We propose an intra-cratonic keel delamination model inspired by observations of geologically recent delamination events beneath the eastern North China Craton (ENCC) and western Wyoming Craton (WWC). This scenario is summarized in Fig. 3. The weak intra-lithospheric MLDL at ~80-100 km depths is the preferred site for keel tearing and delamination from overlying crust and lithosphere. Keel tearing can occur in situations when lateral flow within the MLDL 'tear' can connect to inflow from nearby weak asthenosphere. Delamination can be slightly sped up by ongoing far field subduction, or any mechanism that reduces the viscosity of the mantle at the craton's edge.

2) Keel delamination along a water rich or MARID bearing MLDL can explain the geologically implied keel removal speeds observed on the western Wyoming Craton in North America and the eastern North China Craton in China. However, if the craton's surrounding lithosphere stays thick, e.g. >140 km, and therefore relatively strong (e.g. $>10^{23}$ Pa·s), a fertile and negatively buoyant cratonic keel overlain by a weak MLDL will remain stable over billions of years.

3) Cratonic keel delamination appears to be independent of the weak intra-cratonic layer's density; delamination still occurs when the MLDL's net density is lower than that of keel and asthenosphere. Lateral variations in the distribution of the MLDL and/or in the fertility of its underlying keel are more important factors to lead to cratonic keel destruction.

Acknowledgements

This work was supported by the Chinese Academy of Sciences (Grant No. XDB18000000), the State Oceanography Bureau (Grant No. GASI -GEOGE-02) and the National Natural Science Foundation of China (Grant No. 41688103). We thank the Guangzhou Institute of Geochemistry, Chinese Academy of Sciences and Royal Holloway for supporting this PhD work. We thank the associate editor, and anonymous reviewer, and Norm Sleep for helpful suggestions to restructure and improve the submitted manuscript. We also thank Norm Sleep for his suggestions on the potential formation mechanism for the metasome/MLDL. There are no data sharing issues since all of the numerical information is provided in the figures& movies produced by solving the questions in the appendixes with initial& boundary conditions and parameters given in the paper.

Appendix A: Details of the Numerical Implementation for Thermomechanical Deformation and Melting

This appendix describes the algorithms that are used in this study. A modified version of 2-D Lagrangian finite element code, "m2tri_trunk" [*Hasenclever*, 2010] based on the approaches used in "MILAMIN" [*Dabrowski et al.*, 2008], is used. This thermomechanical code solves for heat transport and elastoviscoplastic deformation in crust and mantle rocks. The supplement shows a benchmark of this code against a recent subduction benchmark study [*Schmeling et al.*, 2008] (see Supplements).

Temperature

For computational simplicity, temperature is treated as a potential temperature. The thermal calculation includes the effects of thermal diffusion, thermal convection, radioactive heating and shear heating (viscous dissipation) (Equation A1).

Temperature is determined from an equation governing energy conservation:

$$\rho C_p \frac{\partial T}{\partial t} = \frac{\partial}{\partial x}\left(K \frac{\partial T}{\partial x} \right) + \frac{\partial}{\partial z}\left(K \frac{\partial T}{\partial z} \right) + H \qquad \text{(A1)}$$

where ρ is density, C_p is heat capacity, t is time, K is thermal conductivity, and H is the volumetric heat production rate (including both radioactive heating and viscous dissipation).

Elastoviscoplastic Deformation

The different materials used in the model are treated as incompressible materials with use of the Boussinesq Approximation [*Turcotte and Schubert*, 2014]. Tracer particles are used to track seven different compositional materials (e.g. upper crust, asthenosphere, etc.). See Fig. 6 for the definitions of each possible material type. Each material type is associated with a specific rheology that is potentially p, T, strain-rate, accumulated strain, and plastic yield-stress dependent.

Table 1 gives the values assumed for the experiment. The number of tracer particles within each element ranges between 7 and 25. Viscosity is calculated at every integration point using the material phase determined by the nearest tracer particle within the element. Density is also uniform within each element with a value determined by the average of the density of each of the tracer particles within the element.

For each tracer particle, density is temperature and pressure dependent (Equations A7-8) [*Djomani et al.*, 2001; *Schutt and Lesher*, 2006]. Each material rheology can include elastic, viscous, and plastic effects. Yielding and plastic flow behavior are calculated using the method described in Moresi et al., 2003 [*Moresi et al.*, 2003].

Elastoviscoplastic deformation is described using the equations for force equilibrium (A2-3) and mass conservation (A4):

$$\frac{\partial}{\partial x}\left(\eta_{VEP}\left(\frac{4}{3}\frac{\partial u}{\partial x}-\frac{2}{3}\frac{\partial v}{\partial z}\right)\right)+\frac{\partial}{\partial z}\left(\eta_{VEP}\left(\frac{\partial u}{\partial x}+\frac{\partial v}{\partial z}\right)\right)-\frac{\partial P}{\partial x}=f_x+F_x^{e,t} \qquad \text{(A2)}$$

$$\frac{\partial}{\partial z}\left(\eta_{VEP}\left(\frac{4}{3}\frac{\partial v}{\partial z}-\frac{2}{3}\frac{\partial u}{\partial x}\right)\right)+\frac{\partial}{\partial z}\left(\eta_{VEP}\left(\frac{\partial u}{\partial x}+\frac{\partial v}{\partial z}\right)\right)-\frac{\partial P}{\partial y}=\rho g+f_y+F_y^{e,t} \qquad \text{(A3)}$$

$$\frac{\partial u}{\partial x}+\frac{\partial v}{\partial z}=-\frac{P}{\kappa} \qquad \text{(A4)}$$

In these equations u and v refer to horizontal and vertical velocity components, P is the dynamic pressure, g is the acceleration of gravity, and κ is the penalty term used for ensuring incompressibility with κ being 10^6 times the maximum effective viscosity (η_{VEP}) [*Hasenclever*, 2010]. $F_i^{e,t}$ is the internal elastic stress [*Moresi et al.*, 2003] that can be advected by material flow. This behavior is described as

$$F_i^{e,t}=-\left(\eta_{EVP}/G\Delta t\right)\left(\partial\tau_{ii}^{old\,J}/\partial x_i+\partial\tau_{ii}^{old\,J}/\partial x_j\right) \qquad \text{(A5)}$$

where G is elastic shear modulus, Δt is time step, and $\tau_{ii}^{old\,J}$ is the Jaumann-

rotated stress of the previous time [*Kaus et al.*, 2010], given by:

$$\tau_{ij}^{old\,J} = \tau_{ij}^{old} - \omega_{ik}^{old}\tau_{ki}^{old} + \tau_{ik}^{old}\omega_{ki}^{old} \tag{A6}$$

where τ_{ij}^{old} is the is the deviatoric stress from the previous time step, and $\omega_{ij} = 1/2\left(\partial u_i/\partial x_j - \partial u_j/\partial x_i\right)$.

The equation of state for density is:

$$\rho = \rho_0 \, exp\left[-\int_{T_0}^{T_F} \alpha\left(P = P_0, T\right) dT + \int_{P_0}^{P_F} \frac{dP}{k}\right] \tag{A7}$$

$$\alpha = \alpha_0 + \alpha_1 T + \alpha_2 T^{-2} \tag{A8}$$

where ρ_0 is the reference density, α is the temperature dependent thermal expansion coefficient at $T_0 = 20^{\circ}C$, P_0 is atmospheric pressure, k is the bulk modulus (assumed to be constant), and T_F and P are the temperature (in Kelvin) and pressure.

A temperature dependent accumulated strain weakening effect is also included. This effect appears when large strains accumulate within a rock, inducing crystal lattice reorientation and recrystallization. Lattice reorientation can reduce the viscosity in dislocation creep [*Tommasi et al.*, 2009] as weaker slip systems become the preferred slip systems. Recrystallization can lead to a reduction in crystal grain size. In turn, the mean grain size *d* is thought to affect viscosity during diffusion creep by its dominant effect on grain boundary diffusion [*Hirth and Kohlstedt*, 1995]. This yields a power law dependence of ~-3 [*Dimanov et al.*, 2003; *Hirth and Kohlstedt*, 2003; *Xiao et al.*, 2002], e.g. the pre-exponent A is given by:

$$A(d) = A_0 d^{-3} \tag{A9}$$

where A_0 is a constant, and d is grain size.

These combined effects are commonly called “strain weakening”.

Strain weakening is temperature dependent since temperature shapes the ‘equilibrium’ grain size in a dynamically recrystallizing system. At ‘high-enough’ temperatures, crystals can more rapidly grow/recover to reach their preferred state of dynamic equilibrium. In this case, the preferred crystal size is relatively large

and strain weakening effects for diffusion creep are less significant. At 'lower' temperatures, Arrhenius-law-governed crystal growth rates are much slower. The resulting reduced grain-size in 'dynamic equilibrium' can lead to pronounced strain weakening during diffusion creep. The threshold temperature where this effect becomes significant is *ca.* 800 C [*Précigout et al.*, 2007] for natural subcontinental peridotites.

We parameterize temperature-dependent accumulated strain-weakening as a function of the second invariant of finite strain and the material-dependent temperature where viscous creep dominates plastic yielding effects (see Equations A10-12). Different maximum accumulated strain weakening coefficients are used for diffusion creep and dislocation creep (see Table A1).

$$S = S_{max} \cdot \min\left(1, \gamma/\gamma_0\right), \quad T < T_{lower} \tag{A10}$$

$$S = S_{max} \cdot \exp\left(A\frac{T - T_{upper}}{T_{upper}} \right) \cdot \min\left(1, \gamma/\gamma_0\right), \quad T_{lower} \le T \le T_{upper} \tag{A11}$$

$$S = 1, \quad T > T_{upper} \tag{A12}$$

In equations A10-12, S is the weakening factor, γ is the second invariant of finite strain (E_{KL}, see Equation A13), γ_0 =1.5 is the critical value for γ, A is given in Table A1, and T_{lower} and T_{upper} are the lower and upper temperatures of the temperature-range where accumulated strain-weakening can relax due to a larger grain-size at dynamic equilibrium. Finite strain is calculated using the form of Green-Lagrangian strain tensor (see Equation A13. cf. the method discussed in Chapter 4 of Malvern (1969) [*Malvern*, 1969]).

$$E_{KL} = \frac{1}{2}\left(\frac{\partial x_i}{\partial X_K}\frac{\partial x_i}{\partial X_L} - \delta_{KL}\right) \tag{A13}$$

where E_{KL} is the finite strain tensor, δ_{KL} is the Kronecker delta. The displacement gradient $\frac{\partial x_i}{\partial X_K}$ is described as:

$$\frac{\partial x_i}{\partial X_K} = \frac{\partial x_i}{\partial X_{K\ old}} + dt\left(\frac{\partial \mu_i}{\partial x_i}\frac{\partial x_i}{\partial X_{K\ old}} + \frac{\partial \mu_i}{\partial x_j}\frac{\partial x_j}{\partial X_{K\ old}}\right) \quad \text{(A14)}$$

where u_i is velocity vector, $\frac{\partial x_i}{\partial X_{K\ old}}$ is the displacement gradient of the previous time step.

Melting

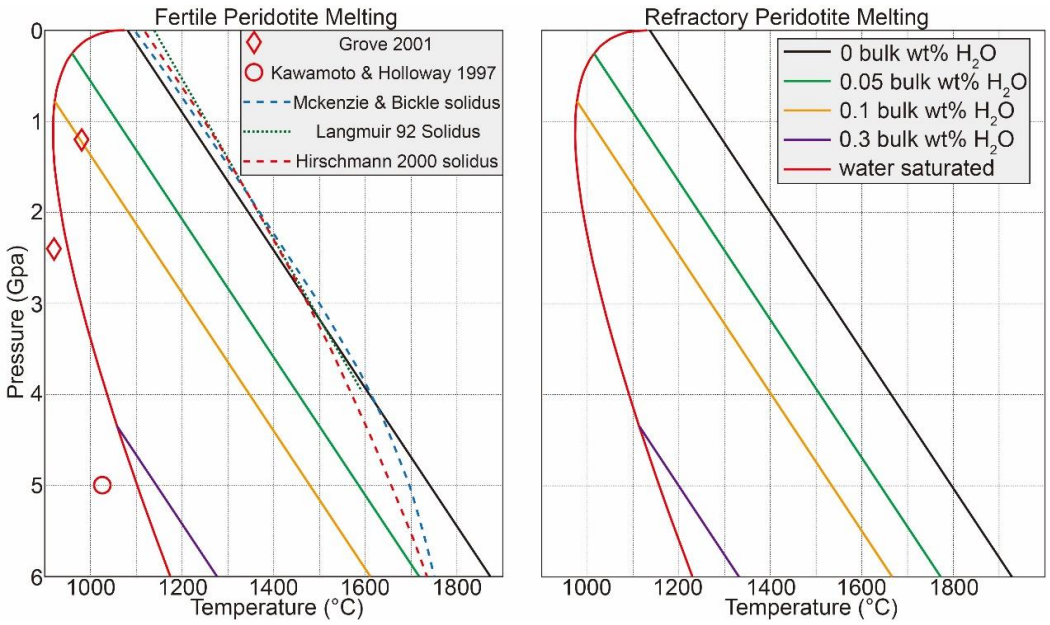

Fig. A1. The solidus for different bulk water contents of asthenosphere/MLDL material (Left Panel) and lithospheric mantle (Right Panel).

Following Katz et al. (2003), the dissolved water's effect on solidus is taken to be linear and bounded by the saturation of water in the melt. "0.05 bulk wt. %, etc." are labels for the water content used to determine the corresponding solidus.

Material melting is found using methods described in [*Hasenclever*, 2010; *Morgan*, 2001] with the mantle solidus T_m given by Equation A15 (see Fig. A1). We have also considered the effects of melting degree f and water content X_{H_2O} on the solidus [*Katz et al.*, 2003; *Morgan*, 2001]. For each time step, the melting process is modelled using the following recipe that is an extension of the approach developed in [*Morgan*, 2001]:

1) Heat-induced melting. If the temperature T_a (transformed from the potential

temperature T with a 0.33 K/km adiabatic gradient) lies above the solidus $dT= T_a - T_m>0$, then a heat-induced melting degree increment df_{heat} will occur. The amount is calculated with Equation A16. The temperature after melting is set to the solidus determined from the updated degree of melting and water content.

2) Pressure release melting. If upwelling leads to a pressure decrease dP, and the material is at its solidus, melting will also occur. In this case, the degree of melting and new solidus is updated according to the new pressure [*Morgan*, 2001]. The pressure-release-induced melting degree increment df is calculated using Equation A17 (see Equation 11 in [*Morgan*, 2001]). The temperature of the melting parcel is then updated to the new depletion-dependent solidus. For increased stability, the melting increment is calculated iteratively, if $df_{heat}>\delta f$ (e.g. $\delta f=0.01$) in the first or $dP>\delta P$ (e.g. $\delta P=0.001$Gpa) in the second.

$$T_m = T_0^m + \left(\frac{\partial T^m}{\partial P}\right)_f P + \left(\frac{\partial T^m}{\partial f}\right)_P f - 43 \cdot X_{H_2O}^{0.75} \tag{A15}$$

$$\left(\frac{df}{dT}\right)_{\text{heat}} = 1 \Big/ \left(\left(\frac{\partial T^m}{\partial f}\right)_p + \frac{Q_L}{c_p}\right) \tag{A16}$$

$$-\left(\frac{df}{dP}\right)_s = \left(\left(\frac{\partial T^m}{\partial P}\right)_f - \frac{\alpha T}{\rho c_p}\right) \Big/ \left(\frac{Q_L}{c_p} + \left(\frac{\partial T^m}{\partial f}\right)_P\right) \tag{A17}$$

where T_0^m is the solidus at room temperature and pressure, α is thermal expansion coefficient, Q_L is latent heat during melting, $\left(\partial T^m/\partial f\right)_p$ describes the solidus's dependence on degree of melting, and $\left(\partial T^m/\partial P\right)_f$ describes the solidus's dependence on pressure. Table 1 shows the parameters used in the numerical experiments.

	Mantle.	*Crust*
T_{lower}	1073.15 K	473.15 K
T_{upper}	1573.15 K	973.15 K
$A_{diffusion}$	-14.4892	-7.6140
$A_{dislocation}$	-7.2446	-3.1324
$S_{max\ dislocation}$	10	5

$S_{max\ diffusion}$	100	50

Tab. A1. Parameters for temperature-dependent strain weakening recovery.

Appendix B: Meshing and Re-meshing

The computational domain is a mesh of triangular elements that is built using an adaptive mesh generation algorithm that makes element sizes be relatively small (~4.5 km) when near internal boundaries between different materials (see Equations A19-21). Element sizes are made to be 10 times larger than this (~40 km) in regions far from internal material interfaces, while at transitional distances, element size is linearly interpolated between these two end-member values. This approach guarantees relatively high resolution along material interfaces and within thin material layers during a calculation. We find that material interfaces remain well-tracked even when high velocities occur due to the effects of slab subduction and keel tearing and sinking (see Fig. 8 and S3).

Because we use a Lagrangian approach in which straight-sided element vertices advect with material flow, some elements can become heavily distorted in regions of strong shear. A new equant-element mesh is regenerated by re-meshing whenever elements are deemed to be 'too-distorted' (This is defined to be when any interior angle of an element is larger than 170° or smaller than 7°, or any mesh quality factor Q is smaller than 0.2, see Equation A18). In Run 1, the Lagrangian approach is only used for the portion with temperature >1150 °C; a semi-Lagrangian approach [*Hasenclever*, 2010] is used for the remaining deeper portion (the more ductile asthenosphere) in order to minimize computational time. Equations 19-21 are used to define the preferred element size R as a function of distance r from an internal boundary interface.

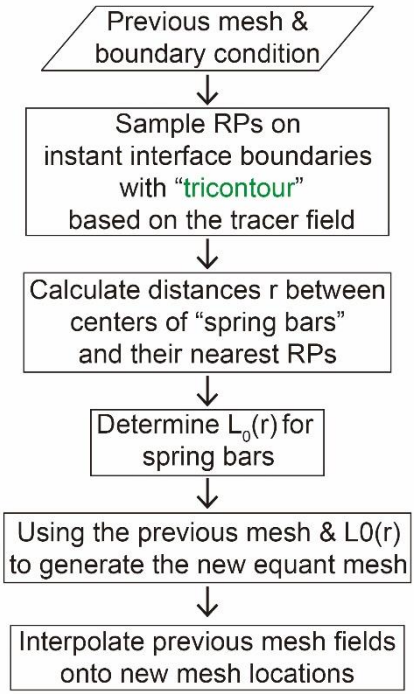

Fig. A2 Flowchart for the adaptive mesh resizing algorithm.

Reference points (RPs) are the points used to determine the characteristic element size as a function of spatial position (e.g. distance from nearest RP). The characteristic element size L_0 (or the characteristic bar length for "virtual spring" connecting element vertexes [*Persson and Strang*, 2004]) is determined based on Equations A19-21. 'Tricontour' is an open source MATLAB function developed by Darren Engwirda, (see https://uk.mathworks.com/matlabcentral/fileexchange/10408-contours-for-triangular-grids?focused=5068781&tab=function). It is used to resample RPs on the contoured interfaces between different materials within the unstructured triangular mesh. The sampling distance for RPs is determined by the number of tracer particles in nearby elements, which ranges from 7-25 per element.

$$Q = \left(L_2 + L_3 - L_1\right)(L_1 + L_3 - L_2)(L_1 + L_2 - L_3)\big/(L_1 L_2 L_3) \tag{A18}$$

where L_1, L_2 and L_3 are the side lengths of the triangular element.

$$L_0 = R_2 \ when \ r \ > 4.75 \cdot R_2 \tag{A19}$$

$$L_0 = \frac{r}{3.75 \cdot R_2}(R_2 - R_1) + R_1 \ when \ R_1 < r \le 4.75 \cdot R_2 \tag{A20}$$

$$L_0 = R_1 \ when \ r <= R_1 \tag{A21}$$

where L_0 is the characteristic element size used for a certain set of coordinates, r is distance between center of "spring bar" connecting element vertexes [*Persson and Strang*, 2004] to its closest reference point (RP) sampled along an interphase boundary. R_1 is the smallest element size (here 4.45 km), and R_2 is the largest size (44.32 km). The adaptive algorithm to determine the preferred element sizes over the computational domain is shown in Figure A2. It first samples reference points (RPs) on the interfaces between different material types using the MATLAB function 'tricontour'. It then determines how far the center of each spring bar is from its nearest RP, and assigns a preferred length size R to the center of each spring bar. This mesh-size information is used to generate a new relatively equant mesh of triangles using a finite-element-reformulated version of the DISTMESH algorithm [*Persson and Strang*, 2004] done by Taramón et al. (2017). The last step is to interpolate the current variable fields onto the new mesh.

References:

Abt, D. L., K. M. Fischer, S. W. French, H. A. Ford, H. Y. Yuan, and B. Romanowicz (2010), North American lithospheric discontinuity structure imaged by Ps and Sp receiver functions, *J Geophys Res-Sol Ea*, *115*(B9), doi: 10.1029/2009jb006914.

Aulbach, S., M. Massuyeau, and F. Gaillard (2017), Origins of cratonic mantle discontinuities: A view from petrology, geochemistry and thermodynamic models, *Lithos*, *268*, 364-382.

Andrés-Martínez, M., J. P. Morgan, M. Pérez-Gussinyé, and L. Rüpke (2015), A new free-surface stabilization algorithm for geodynamical modelling: Theory and numerical tests, *Physics of the Earth and Planetary Interiors*, *246*, 41-51.

Artemieva, I. M., and L. P. Vinnik (2016), Density structure of the cratonic mantle in southern Africa: 1. Implications for dynamic topography, *Gondwana Research*, *39*, 204-216, doi:10.1016/j.gr.2016.03.002.

Artemieva (2012), A lithospheric perspective on structure and evolution of Precambrian cratons, in Regional Geology and Tectonics: Principles of Geologic Analysis, edited, pp. 94-111, Elsevier.

Aubaud, C., E. H. Hauri, and M. M. Hirschmann (2004), Hydrogen partition coefficients between nominally anhydrous minerals and basaltic melts, *Geophysical Research Letters*, *31*(20), doi: 10.1029/2004gl021341.

Bao, X., D. W. Eaton, and B. Guest (2014), Plateau uplift in western Canada caused by lithospheric delamination along a craton edge, *Nat Geosci*, *7*(11), 830.

Batchelor, G. K. (2000), *An introduction to fluid dynamics*, Cambridge university press., 615pp. Cambridge, UK.

Bird, P. (1979), Continental Delamination and the Colorado Plateau, *J Geophys Res*, *84*(Nb13), 7561-7571.

Begg, G., W. Griffin, L. Natapov, S. Y. O'Reilly, S. Grand, C. O'Neill, J. Hronsky, Y. P. Djomani, C. Swain, and T. Deen (2009), The lithospheric architecture of Africa: Seismic tomography, mantle petrology, and tectonic evolution, *Geosphere*, *5*(1), 23-50.

Brune, S., C. Heine, M. Perez-Gussinye, and S. V. Sobolev (2014), Rift migration explains continental margin asymmetry and crustal hyper-extension, Nature communications, 5, 4014, doi:10.1038/ncomms5014.

Chamberlain, K. R., C. D. Frost, and B. R. Frost (2003), Early Archean to Mesoproterozoic evolution of the Wyoming Province: Archean origins to modern lithospheric architecture, *Can J Earth Sci*, *40*(10), 1357-1374.

Chen, L., M. M. Jiang, J. H. Yang, Z. G. Wei, C. Z. Liu, and Y. Ling (2014), Presence of an intralithospheric discontinuity in the central and western North China Craton: Implications for destruction of the craton, *Geology*, *42*(3), 223-226,

doi:10.1130/G35010.1.

Choukroun, M., S. Y. O'Reilly, W. L. Griffin, N. J. Pearson, and J. B. Dawson (2005), Hf isotopes of MARID (mica-amphibole-rutile-ilmenite-diopside) rutile trace metasomatic processes in the lithospheric mantle, *Geology*, *33*(1), 45-48.

Conrad, C. P., and P. Molnar (1997), The growth of Rayleigh-Taylor-type instabilities in the lithosphere for various rheological and density structures, *Geophysical Journal International*, *129*(1), 95-112, doi:10.1111/j.1365-246X.1997.tb00939.x.

Dabrowski, M., M. Krotkiewski, and D. W. Schmid (2008), MILAMIN: MATLAB-based finite element method solver for large problems, *Geochem Geophy Geosy*, *9*(4), doi:10.1029/2007gc001719.

Dalton, J. A., and D. C. Presnall (1998), Carbonatitic melts along the solidus of model lherzolite in the system CaO-MgO-Al 2 O 3-SiO 2-CO 2 from 3 to 7 GPa, *Contrib Mineral Petr*, *131*(2-3), 123-135.

Davis, G. A., Z. Yadong, W. Cong, B. J. Darby, Z. Changhou, and G. Gehrels (2001), Mesozoic tectonic evolution of the Yanshan fold and thrust belt, with emphasis on Hebei and Liaoning provinces, northern China, Memoirs-Geological Society of America, 171-198.

Dawson, and J. Smith (1988), Metasomatised and veined upper-mantle xenoliths from Pello Hill, T anzania: evidence for anomalously-light mantle beneath the Tanzanian sector of the East African Rift Valley, *Contributions to Mineralogy and Petrology*, *100*(4), 510-527.

Dawson, and J. V. Smith (1977), The MARID (mica-amphibole-rutile-ilmenite-diopside) suite of xenoliths in kimberlite, *Geochimica et Cosmochimica Acta*, *41*(2), 309IN9311-9310IN11323.

Dimanov, A., M. P. Lavie, G. Dresen, J. Ingrin, and O. Jaoul (2003), Creep of polycrystalline anorthite and diopside, *J Geophys Res-Sol Ea*, *108*(B1), doi: 10.1029/2002jb001815.

Djomani, Y. H. P., S. Y. O'Reilly, W. L. Griffin, and P. Morgan (2001), The density structure of subcontinental lithosphere through time, *Earth and Planetary Science Letters*, *184*(3-4), 605-621.

Downes, H., R. MacDonald, B. G. J. Upton, K. G. Cox, J. L. Bodinier, P. R. D. Mason, D. James, P. G. Hill, and B. C. Hearn (2004), Ultramafic xenoliths from the Bearpaw Mountains, Montana, USA: Evidence for multiple metasomatic events in the lithospheric mantle beneath the Wyoming craton, *Journal of Petrology*, *45*(8), 1631-1662, doi:10.1093/petrology/egh027.

Dudás, F. Ö. (1991), Geochemistry of igneous rocks from the Crazy Mountains, Montana, and tectonic models for the Montana alkalic province, *Journal of Geophysical Research:*

Solid Earth, *96*(B8), 13261-13277.

Dudás, F. Ö., V. O. Ispolatov, S. S. Harlan, and L. W. Snee (2010), 40Ar/39Ar geochronology and geochemical reconnaissance of the Eocene Lowland Creek volcanic field, west-central Montana, The Journal of Geology, 118(3), 295-304.

Eggler, D. H. (1978), The effect of CO< 2) upon partial melting of peridotite in the system Na< 2) O-CaO-Al< 2) O< 3)-MgO-SiO< 2)-CO< 2) to 35 kb, with an analysis of melting in a peridotite-H< 2) O-CO< 2) system, *American Journal of Science*, *278*(3), 305-343.

Eggler, D., and K. Furlong (1991), Destruction of subcratonic mantle keel: The Wyoming Province. Ext. Abstr. 5th Int. Kimb. Conf., CPRM Spec. Publ. 2/91, Brasilia (1991), 85-87

Engebretson, D. C., A. Cox, and R. G. Gordon (1985), Relative motions between oceanic and continental plates in the Pacific basin, *Geological Society of America Special Papers*, *206*, 1-60.

English, J. M., and S. T. Johnston (2004), The Laramide orogeny: what were the driving forces?, *International Geology Review*, *46*(9), 833-838.

Faccenna, C., F. Funiciello, D. Giardini, and P. Lucente (2001), Episodic back-arc extension during restricted mantle convection in the Central Mediterranean, *Earth and Planetary Science Letters*, *187*(1-2), 105-116, doi: 10.1016/S0012-821x(01)00280-1.

Feeley, T. C., and M. A. Cosca (2003), Time vs. composition trends of magmatism at Sunlight volcano, Absaroka volcanic province, Wyoming, *Geological Society of America Bulletin*, *115*(6), 714-728, doi: 10.1130/0016-7606(2003)115<0714:Tvctom>2.0.Co;2.

Feeley, T. C., M. A. Cosca, and C. R. Lindsay (2002), Petrogenesis and implications of calc-alkaline cryptic hybrid magmas from Washburn volcano, Absaroka Volcanic Province, USA, *Journal of Petrology*, *43*(4), 663-703, doi: 10.1093/petrology/43.4.663.

Foley, S. F. (2008), Rejuvenation and erosion of the cratonic lithosphere, *Nature Geoscience*, *1*(8), 503-510, doi:10.1038/ngeo261.

Foster, D. A., P. A. Mueller, A. Heatherington, J. N. Gifford, and T. J. Kalakay (2012), Lu-Hf systematics of magmatic zircons reveal a Proterozoic crustal boundary under the Cretaceous Pioneer batholith, Montana, *Lithos*, *142*, 216-225, doi:10.1016/j.lithos.2012.03.005.

Foster, D. A., P. A. Mueller, D. W. Mogk, J. L. Wooden, and J. J. Vogl (2006), Proterozoic evolution of the western margin of the Wyoming craton: implications for the tectonic and magmatic evolution of the northern Rocky Mountains, *Canadian Journal of Earth Sciences*, *43*(10), 1601-1619, doi:10.1139/E06-052.

Francis, D. F., W. M. Minarik, Y. P. Proenza, and L. S. Shi (2010), An overview of the

Canadian Cordilleran lithospheric mantleThis articl, *Can J Earth Sci*, *47*(4), 353-368.

Gao, S., R. L. Rudnick, R. W. Carlson, W. F. McDonough, and Y. S. Liu (2002), Re-Os evidence for replacement of ancient mantle lithosphere beneath the North China craton, *Earth and Planetary Science Letters*, *198*(3-4), 307-322, doi: 10.1016/S0012-821X(02)00489-2

Gao, S., J. F. Zhang, W. L. Xu, and Y. S. Liu (2009), Delamination and destruction of the North China Craton, *Chinese Science Bulletin*, *54*(19), 3367-3378, doi:10.1007/s11434-009-0395-9.

Gaschnig, R. M., J. D. Vervoort, R. S. Lewis, and W. C. McClelland (2010), Migrating magmatism in the northern US Cordillera: in situ U-Pb geochronology of the Idaho batholith, Contrib Mineral Petr, 159(6), 863-883, doi:10.1007/s00410-009-0459-5.

Getsinger, A. J., and G. Hirth (2014), Amphibole fabric formation during diffusion creep and the rheology of shear zones, *Geology*, *42*(6), 535-538, doi:10.1130/G35327.1.

Gorczyk, W., B. Hobbs, and T. Gerya (2012), Initiation of Rayleigh-Taylor instabilities in intra-cratonic settings, *Tectonophysics*, *514*, 146-155, doi:10.1016/j.tecto.2011.10.016.

Gray, R., and R. N. Pysklywec (2012), Geodynamic models of mature continental collision: Evolution of an orogen from lithospheric subduction to continental retreat/delamination, *J Geophys Res-Sol Ea*, *117*(B3), doi: 10.1029/2011jb008692.

Griffin (1999), The composition and origin of subcontinental lithospheric mantle, *Mantle Petrology: Field Observation and Highpressure Experimentation: A Tribute to Francis R.(Joe) Boyd*, 13-45.

Griffin, W. L., Z. Andi, S. Y. O'Reilly, and C. G. Ryan (1998), Phanerozoic evolution of the lithosphere beneath the Sino-Korean Craton, *Mantle Dynamics and Plate Interactions in East Asia*, *27*, 107-126.

Griffin, W. L., J. M. Batumike, Y. Greau, N. J. Pearson, S. R. Shee, and S. Y. O'Reilly (2014), Emplacement ages and sources of kimberlites and related rocks in southern Africa: U-Pb ages and Sr-Nd isotopes of groundmass perovskite, *Contributions to Mineralogy and Petrology*, *168*(1), 1-13, doi: 10.1007/S00410-014-1032-4.

Griffin, W. L., A. F. Kobussen, E. V. S. S. K. Babu, S. Y. O'Reilly, R. Norris, and P. Sengupta (2009a), A translithospheric suture in the vanished 1-Ga lithospheric root of South India: Evidence from contrasting lithosphere sections in the Dharwar Craton, *Lithos*, *112*, 1109-1119, doi:10.1016/j.lithos.2009.05.015.

Griffin, W. L., S. Y. O'Reilly, J. C. Afonso, and G. C. Begg (2009b), The Composition and Evolution of Lithospheric Mantle: a Re-evaluation and its Tectonic Implications, *Journal of Petrology*, *50*(7), 1185-1204, doi:10.1093/petrology/egn033.

Griffin, W. L., S. Y. O'Reilly, B. J. Doyle, N. J. Pearson, H. Coopersmith, K. Kivi, V. Malkovets, and N. Pokhilenko (2004), Lithosphere mapping beneath the north

American plate, *Lithos*, *77*(1-4), 873-922, doi:10.1016/j.lithos.2004.03.034.

Griffin, W. L., S. Y. O'Reilly, L. M. Natapov, and C. G. Ryan (2003), The evolution of lithospheric mantle beneath the Kalahari Craton and its margins, *Lithos*, *71*(2-4), 215-241, doi:10.1016/j.lithos.2003.07.006.

Hansen, S. M., K. Dueker, and B. Schmandt (2015), Thermal classification of lithospheric discontinuities beneath USArray, *Earth and Planetary Science Letters*, *431*, 36-47, doi:10.1016/j.epsl.2015.09.009.

Hasenclever, J. (2010), Modeling Mantle Flow and Melting Processes at Mid-Ocean Ridges and Subduction Zones — Development and Application of Numerical Models. *Ph.D. Dissertation*, Hamburg University.URL: http://ediss.sub.uni-hamburg.de/volltexte/2010/4873/.

Hasenclever, J., J. P. Morgan, M. Hort, and L. H. Rupke (2011), 2D and 3D numerical models on compositionally buoyant diapirs in the mantle wedge, *Earth and Planetary Science Letters*, *311*(1-2), 53-68, doi:10.1016/j.epsl.2011.08.043.

He, D., Santosh, Li, and Chen (2015), Destruction of the north China Craton: a perspective based on receiver function analysis, Geol J, 50(1), 93-103.

He, L. J. (2014), Numerical modeling of convective erosion and peridotite-melt interaction in big mantle wedge: Implications for the destruction of the North China Craton, *J Geophys Res-Sol Ea*, *119*(4), 3662- 3677, doi:10.1002/2013JB010657.

Hirschmann, M. M., T. Tenner, C. Aubaud, and A. C. Withers (2009), Dehydration melting of nominally anhydrous mantle: The primacy of partitioning, *Physics of the Earth and Planetary Interiors*, *176*(1-2), 54-68, doi:10.1016/j.pepi.2009.04.001.

Hirth, G. and Kohlstedt, D., (2004). Rheology of the Upper Mantle and the Mantle Wedge: A View from the Experimentalists, in Inside the Subduction Factory (ed J. Eiler) 138: 83-105, American Geophysical Union, Washington, D. C., doi: 10.1029/138GM06.

Hirth, G., and D. L. Kohlstedt (1995), Experimental Constraints on the Dynamics of the Partially Molten Upper-Mantle - Deformation in the Diffusion Creep Regime, *J Geophys Res-Sol Ea*, *100*(B2), 1981-2001, doi: 10.1029/94jb02128.

Hirth, G., and D. L. Kohlstedt (1996), Water in the oceanic upper mantle: Implications for rheology, melt extraction and the evolution of the lithosphere, Earth Planet Sc Lett, 144(1-2), 93-108, doi: 10.1016/0012-821x(96)00154-9.

Hopper, E., H. A. Ford, K. M. Fischer, V. Lekic, and M. J. Fouch (2014), The lithosphere-asthenosphere boundary and the tectonic and magmatic history of the northwestern United States, *Earth and Planetary Science Letters*, *402*, 69-81, doi:10.1016/j.epsl.2013.12.016.

Houseman, G. A., D. P. Mckenzie, and P. Molnar (1981), Convective Instability of a Thickened Boundary-Layer and Its Relevance for the Thermal Evolution of Continental

Convergent Belts, *J Geophys Res*, *86*(Nb7), 6115-6132, doi: 10.1029/Jb086ib07p06115.

Jordan, T. H. (1988), Structure and formation of the continental tectosphere, *Journal of Petrology*(1), 11-37.

Kaban, M. K., P. Schwintzer, I. M. Artemieva, and W. D. Mooney (2003), Density of the continental roots: compositional and thermal contributions, *Earth and Planetary Science Letters*, *209*(1-2), 53-69, doi:10.1016/S0012-821x(03)00072-4.

Kaban, M. K., W. Stolk, M. Tesauro, S. El Khrepy, N. Al-Arifi, F. Beekman, and S. A. P. L. Cloetingh (2016), 3D density model of the upper mantle of Asia based on inversion of gravity and seismic tomography data, *Geochem Geophy Geosy*, *17*(11), 4457-4477, doi:10.1002/2016GC006458.

Karato, S., and P. Wu (1993), Rheology of the upper mantle: a synthesis, Science, 260(5109), 771-778, doi:10.1126/science.260.5109.771.

Karato, S. I., T. Olugboji, and J. Park (2015), Mechanisms and geologic significance of the mid-lithosphere discontinuity in the continents, *Nature Geoscience*, *8*(7), 509-514, doi:10.1038/NGEO2462.

Katz, R. F., M. Spiegelman, and C. H. Langmuir (2003), A new parameterization of hydrous mantle melting, *Geochem Geophy Geosy*, *4*(9), doi: 10.1029/2002gc000433.

Kaus, B. J. P., H. Muhlhaus, and D. A. May (2010), A stabilization algorithm for geodynamic numerical simulations with a free surface, *Physics of the Earth and Planetary Interiors*, *181*(1-2), 12-20, doi:10.1016/j.pepi.2010.04.007.

Kay, R. W., and S. M. Kay (1993), Delamination and Delamination Magmatism, *Tectonophysics*, *219*(1-3), 177-189, doi: 10.1016/0040-1951(93)90295-U.

Kay, S. M., and B. L. Coira (2009), Shallowing and steepening subduction zones, continental lithospheric loss, magmatism, and crustal flow under the Central Andean Altiplano-Puna Plateau, *Geol Soc Am Mem*, *204*, 229-259, doi:10.1130/2009.1204(11).

Kinck, J. J., E. S. Husebye, and F. R. Larsson (1993), The Moho depth distribution in Fennoscandia and the regional tectonic evolution from Archean to Permian times, *Precambrian Research*, 64(1-4), 23-51.

Kirby, S. H., and A. K. Kronenberg (1987), Rheology of the Lithosphere - Selected Topics, *Reviews of Geophysics*, *25*(6), 1219-1244, doi: 10.1029/Rg025i006p01219.

Korenaga, J., and S. I. Karato (2008), A new analysis of experimental data on olivine rheology, *J Geophys Res-Sol Ea*, *113*(B2), doi: 10.1029/2007jb005100.

Krystopowicz, N. J., and C. A. Currie (2013), Crustal eclogitization and lithosphere delamination in orogens, *Earth and Planetary Science Letters*, *361*, 195-207, doi:10.1016/j.epsl.2012.09.056.

Lan, T. G., H. R. Fan, M. Santosh, F. F. Hu, K. F. Yang, Y. H. Yang, and Y. S. Liu (2012), Early Jurassic high-K calc-alkaline and shoshonitic rocks from the Tongshi intrusive

complex, eastern North China Craton: Implication for crust-mantle interaction and post-collisional magmatism, Lithos, 140, 183-199, doi:10.1016/j.lithos.2012.01.015.

Lee, C.-T. A., P. Luffi, and E. J. Chin (2011), Building and destroying continental mantle, *Annual Review of Earth and Planetary Sciences*, *39*, 59-90.

Lee, C. T. A. (2003), Compositional variation of density and seismic velocities in natural peridotites at STP conditions: Implications for seismic imaging of compositional heterogeneities in the upper mantle, *J Geophys Res-Sol Ea*, *108*(B9), doi: 10.1029/2003jb002413.

Lekić, V., and K. M. Fischer (2014), Contrasting lithospheric signatures across the western United States revealed by Sp receiver functions, *Earth Planet Sc Lett*, *402*, 90-98.

Lenardic, A., and L.- N. Moresi (1999), Some thoughts on the stability of cratonic lithosphere: Effects of buoyancy and viscosity, *Journal of Geophysical Research: Solid Earth*, 104(B6), 12747-12758.

Li, H.-Y., Y.-G. Xu, Y.-M. Liu, X.-L. Huang, and B. He (2013), Detrital zircons reveal no Jurassic plateau in the eastern North China Craton, *Gondwana Research*, 24(2), 622-634.

Li, Z. H., M. A. Liu, and T. Gerya (2016), Lithosphere delamination in continental collisional orogens: A systematic numerical study, *J Geophys Res-Sol Ea*, *121*(7), 5186-5211, doi:10.1002/2016JB013106.

Liu. L, J. Morgan, Y. Xu, and M. Menzies (2016), Numerical Modelling of the Destruction of the Eastern North China Craton, paper presented at AGU Fall Meeting Abstracts, abstract #T11B-2624.

Lu, F., Z. Han, J. Zheng, and Y. Ren (1991), Characteristics of Paleozoic mantle-lithosphere in Fuxian, Liaoning province, *Geological Science and Technology Information*, *10*, 2-19.

Lund, K., J. N. Aleinikoff, M. J. Kunk, D. M. Unruh, G. D. Zeihen, W. C. Hodges, E. A. du Bray, and J. M. O'Neill (2002), SHRIMP U-Pb and 40Ar/39Ar age constraints for relating plutonism and mineralization in the Boulder Batholith region, Montana, Economic Geology, 97(2), 241-267.

Malkovets, V. G., W. L. Griffin, S. Y. O'Reilly, and B. J. Wood (2007), Diamond, subcalcic garnet, and mantle metasomatism: Kimberlite sampling patterns define the link, *Geology*, *35*(4), 339.

Malvern, L. E. (1969), *Introduction to the Mechanics of a Continuous Medium*. Prentice-Hall, Inc., Englewood Cliffs, 713 pp.

Manea, V. C., M. Perez-Gussinye, and M. Manea (2012), Chilean flat slab subduction controlled by overriding plate thickness and trench rollback, *Geology*, *40*(1), 35-38, doi:10.1130/G32543.1.

Maruyama, S., Y. Isozaki, G. Kimura, and M. Terabayashi (1997), Paleogeographic maps of the Japanese Islands: Plate tectonic synthesis from 750 Ma to the present, *Island Arc*, *6*(1), 121-142, doi: 10.1111/j.1440-1738.1997.tb00043.x.

Menzies, W. Fan, and M. Zhang (1993), Palaeozoic and Cenozoic lithoprobes and the loss of> 120 km of Archaean lithosphere, Sino-Korean craton, China, *Geological Society, London, Special Publications*, *76*(1), 71-81.

Menzies, M., Y. G. Xu, H. F. Zhang, and W. M. Fan (2007), Integration of geology, geophysics and geochemistry: A key to understanding the North China Craton, *Lithos*, *96*(1-2), 1-21, doi:10.1016/j.lithos.2006.09.008.

Mooney, W. D., and M. K. Kaban (2010), The North American upper mantle: Density, composition, and evolution, *J Geophys Res-Sol Ea*, *115*(B12), doi: 10.1029/2010jb000866.

Morency, C., and M. P. Doin (2004), Numerical simulations of the mantle lithosphere delamination, *J Geophys Res-Sol Ea*, *109*(B3), doi: 10.1029/2003jb002414.

Moresi, L., F. Dufour, and H. B. Muhlhaus (2003), A Lagrangian integration point finite element method for large deformation modeling of viscoelastic geomaterials, *Journal of Computational Physics*, *184*(2), 476-497, doi: 10.1016/S0021-9991(02)00031-1.

Morgan, J. P. (2001), Thermodynamics of pressure release melting of a veined plum pudding mantle, *Geochem Geophy Geosy*, *2*(4), doi: 10.1029/2000GC000049.

Mueller, P., A. Heatherington, K. D'Arcy, J. Wooden, and A. Nutman (1996), Contrasts between Sm-Nd whole-rock and U-Pb zircon systematics in the Tobacco Root batholith, Montana: implications for the determination of crustal age provinces, Tectonophysics, 265(1-2), 169-179.

Nita, B., S. Maurya, and J. P. Montagner (2016), Anisotropic tomography of the European lithospheric structure from surface wave studies, *Geochem Geophy Geosy*, *17*(6), 2015-2033, doi:10.1002/2015GC006243.

Niu, Y. (2005), Generation and evolution of basaltic magmas: some basic concepts and a new view on the origin of Mesozoic–Cenozoic basaltic volcanism in eastern China, *Geological Journal of China Universities*, *11*(1), 9-46.

Norman, M. D., and S. A. Mertzman (1991), Petrogenesis of Challis Volcanics from Central and Southwestern Idaho - Trace-Element and Pb Isotopic Evidence, *J Geophys Res-Solid*, *96*(B8), 13279-13293, doi: 10.1029/91jb00285.

O'Reilly, and W. Griffin (2013), Mantle metasomatism, in *Metasomatism and the chemical transformation of rock*, edited, pp. 471-533, Springer.

O'Reilly, W. Griffin, Y. Poudjom Djomani, and P. Morgan (2001), Are lithospheres forever, *Tracking changes in subcontinental lithospheric mantle through time: GSA Today*, *11*(4), 4-10.

Parmentier, E., and D. Forsyth (1985), Three‐dimensional flow beneath a slow spreading ridge axis: A dynamic contribution to the deepening of the median valley toward fracture zones, *Journal of Geophysical Research: Solid Earth*, *90*(B1), 678-684.

Persson, P. O., and G. Strang (2004), A simple mesh generator in MATLAB, *Siam Review*, *46*(2), 329-345, doi:10.1137/S0036144503429121.

Peslier, A. H., L. Reisberg, J. Ludden, and D. Francis (2000), Os isotopic systematics in mantle xenoliths; age constraints on the Canadian Cordillera lithosphere, *Chem Geol*, *166*(1-2), 85-101.

Précigout, J., F. Gueydan, D. Gapais, C. Garrido, and A. Essaifi (2007), Strain localisation in the subcontinental mantle—a ductile alternative to the brittle mantle, *Tectonophysics*, *445*(3), 318-336.

Read, G., H. Grutter, S. Winter, N. Luckman, F. Gaunt, and F. Thomsen (2004), Stratigraphic relations, kimberlite emplacement and lithospheric thermal evolution, Quirico basin, Minas Gerais state, Brazil, *Lithos*, *77*(1-4), 803-818, doi:10.1016/j.lithos.2004.04.011.

Rybacki, E., and G. Dresen (2004), Deformation mechanism maps for feldspar rocks, Tectonophysics, 382(3-4), 173-187, doi:10.1016/j.tecto.2004.01.006.

Schmeling, H., A. Babeyko, A. Enns, C. Faccenna, F. Funiciello, T. Gerya, G. Golabek, S. Grigull, B. Kaus, and G. Morra (2008), A benchmark comparison of spontaneous subduction models—Towards a free surface, *Physics of the Earth and Planetary Interiors*, *171*(1), 198-223.

Schutt, D. L., and C. E. Lesher (2006), Effects of melt depletion on the density and seismic velocity of garnet and spinel lherzolite, *J Geophys Res-Sol Ea*, *111*(B5), doi: 10.1029/2003jb002950.

Selway, K., H. Ford, and P. Kelemen (2015), The seismic mid-lithosphere discontinuity, *Earth and Planetary Science Letters*, *414*, 45-57, doi:10.1016/j.epsl.2014.12.029.

Sigloch, K., N. Mcquarrie, and G. Nolet (2008), Two-stage subduction history under North America inferred from multiple-frequency tomography, *Nature Geoscience*, *1*(7), 458-462, doi:10.1038/ngeo231.

Sleep, N. H. (2009), Stagnant lid convection and carbonate metasomatism of the deep continental lithosphere, *Geochemistry, Geophysics, Geosystems*, *10*(11).

Sleep, N. H. (2003), Survival of Archean cratonal lithosphere, *J Geophys Res-Sol Ea*, *108*(B6), doi: 10.1029/2001jb000169.

Snyder, W., W. Dickinson, and M. Silberman (1976), Tectonic implications of space-time patterns of Cenozoic magmatism in the western United States, *Earth and Planetary Science Letters*, *32*(1), 91-106.

Sodoudi, F., X. H. Yuan, R. Kind, S. Lebedev, J. M. C. Adam, E. Kastle, and F. Tilmann

(2013), Seismic evidence for stratification in composition and anisotropic fabric within the thick lithosphere of Kalahari Craton, *Geochem Geophy Geosy*, *14*(12), 5393-5412, doi:10.1002/2013GC004955.

Tang, Y. J., H. F. Zhang, J. F. Ying, and B. X. Su (2013), Widespread refertilization of cratonic and circum-cratonic lithospheric mantle, *Earth-Science Reviews*, *118*, 45-68, doi:10.1016/j.earscirev.2013.01.004.

Taramón, J. M., J. P. Morgan, C. Shi, J. Hasenclever (2017), Generation of unstructured meshes in 2-D, 3-D, and spherical geometries with embedded high resolution sub-regions; arXiv: 1711.06333.

Tharimena, S., C. Rychert, and N. Harmon (2017), A unified continental thickness from seismology and diamonds suggests a melt-defined plate, *Science*, *357*(6351), 580-583.

Tommasi, A., M. Knoll, A. Vauchez, J. Signorelli, C. Thoraval, and R. Loge (2009), Structural reactivation in plate tectonics controlled by olivine crystal anisotropy, *Nature Geoscience*, *2*(6), 422-426, doi:10.1038/NGEO528.

Turcotte, D. L., and G. Schubert (2014), *Geodynamics*, Cambridge University Press, 623 pp.

Wang, Z. S., T. M. Kusky, and F. A. Capitanio (2016), Lithosphere thinning induced by slab penetration into a hydrous mantle transition zone, *Geophysical Research Letters*, *43*(22), 11567-11577, doi:10.1002/2016GL071186.

Wenker, S., and C. Beaumont (2017), Can metasomatic weakening result in the rifting of cratons?, *Tectonophysics*, 0040-1951, doi: 10.1016/j.tecto.2017.06.013.

Wilks, K. R., and N. L. Carter (1990), Rheology of Some Continental Lower Crustal Rocks, Tectonophysics, 182(1-2), 57-77, doi: 10.1016/0040-1951(90)90342-6.

Wu, F. Y., D. Y. Sun, W. C. Ge, Y. B. Zhang, M. L. Grant, S. A. Wilde, and B. M. Jahn (2011), Geochronology of the Phanerozoic granitoids in northeastern China, *Journal of Asian Earth Sciences*, *41*(1), 1-30, doi:10.1016/j.jseaes.2010.11.014.

Wu, F. Y., Y. G. Xu, R. X. Zhu, and G. W. Zhang (2014), Thinning and destruction of the cratonic lithosphere: A global perspective, *Sci China Earth Sci*, *57*(12), 2878-2890, doi:10.1007/s11430-014-4995-0.

Wu, F. Y., J. H. Yang, S. A. Wilde, and X. O. Zhang (2005), Geochronology, petrogenesis and tectonic implications of Jurassic granites in the Liaodong Peninsula, NE China, *Chemical Geology*, *221*(1-2), 127-156, doi:10.1016/j.chemgeo.2005.04.010.

Xia, Q. K., J. Liu, S. C. Liu, I. Kovacs, M. Feng, and L. Dang (2013), High water content in Mesozoic primitive basalts of the North China Craton and implications on the destruction of cratonic mantle lithosphere, *Earth and Planetary Science Letters*, *361*, 85-97, doi:10.1016/j.epsl.2012.11.024.

Xiao, X., R. Wirth, and G. Dresen (2002), Diffusion creep of anorthite-quartz aggregates,

J Geophys Res-Sol Ea, *107*(B11), doi: 10.1029/2001jb000789.

Xu, Y. G. (2001), Thermo-tectonic destruction of the archaean lithospheric keel beneath the Sino-Korean Craton in China: Evidence, timing and mechanism, *Phys Chem Earth Pt A*, *26*(9-10), 747-757, doi: 10.1016/S1464-1895(01)00124-7.

Xu, Y. G., H. Y. Li, C. J. Pang, and B. He (2009), On the timing and duration of the destruction of the North China Craton, *Chinese Science Bulletin*, *54*(19), 3379-3396, doi:10.1007/s11434-009-0346-5.

Yamamoto, M., J. P. Morgan, and W. J. Morgan (2007), Global plume-fed asthenosphere flow—I: Motivation and model development, *Geological Society of America Special Papers*, *430*, 165-188.

Yang, K. F., H. R. Fan, M. Santosh, F. F. Hu, S. A. Wilde, T. G. Lan, L. N. Lu, and Y. S. Liu (2012), Reactivation of the Archean lower crust: Implications for zircon geochronology, elemental and Sr-Nd-Hf isotopic geochemistry of late Mesozoic granitoids from northwestern Jiaodong Terrane, the North China Craton, Lithos, 146, 112-127, doi:10.1016/j.lithos.2012.04.035.

Yang, W., and S. G. Li (2008), Geochronology and geochemistry of the Mesozoic volcanic rocks in Western Liaoning: Implications for lithospheric thinning of the North China Craton, Lithos, 102(1-2), 88-117, doi:10.1016/j.lithos.2007.09.018.

Youssof, M., H. Thybo, I. M. Artemieva, and A. Levander (2013), Moho depth and crustal composition in Southern Africa, *Tectonophysics*, 609, 267-287.

Zhang, H. F., S. L. Goldstein, X. H. Zhou, M. Sun, J. P. Zheng, and Y. Cai (2008), Evolution of s ubcontinental lithospheric mantle beneath eastern China: Re-Os isotopic evidence from mantle xenoliths in Paleozoic kimberlites and Mesozoic basalts, *Contributions to Mineralogy and Petrology*, *155*(3), 271-293, doi:10.1007/s00410-007-0241-5.

Zhao, D. P. (2004), Global tomographic images of mantle plumes and subducting slabs: insight into deep Earth dynamics, *Physics of the Earth and Planetary Interiors*, *146*(1-2), 3-34, doi:10.1016/j.pepi.2003.07.032.

Zhao, Y., B. Song, and S. Zhang (2006), Geochronology of the inherited zircons from Jurassic Nandaling basalt of the Western Hills of Beijing, North China: its implications, Earth Science Frontiers, 13(2), 184-190.

Zheng, J. P., et al. (2008), Continental collision and accretion recorded in the deep lithosphere of central China, Earth Planet Sc Lett, 269(3-4), 496-506, doi:10.1016/j.epsl.2008.03.003.

Zheng, J. P., S. Y. O'Reilly, W. L. Griffin, F. X. Lu, M. Zhang, and N. J. Pearson (2001), Relict refractory mantle beneath the eastern North China block: significance for lithosphere evolution, *Lithos*, *57*(1), 43-66, doi: 10.1016/S0024-4937(00)00073-6.

Zhu, Y. Xu, G. Zhu, H. Zhang, Q. Xia, and T. Zheng (2012), Destruction of the north China Craton, *Science China Earth Sciences*, *55*(10), 1565-1587.

Supporting Information

Journal of Geophysical Research Solid Earth

Supporting Information for

Craton Destruction Part I: Cratonic Keel Delamination

Liang Liu[1, 2, 3], Jason P. Morgan[2,4], Yigang Xu[1], Martin Menzies[1, 2]

[1] *State Key Laboratory of Isotope Geochemistry, Guangzhou Institute of Geochemistry, Chinese Academy of Sciences, Guangzhou 510640, China.*

[2] *Department of Earth Sciences, Royal Holloway University of London, Egham, TW200EX, United Kingdom.*

[3] *College of Earth Sciences, University of Chinese Academy of Sciences, Beijing, 100049, China.*

[4] *Department of Earth & Planetary Sciences, Harvard University, Cambridge, MA, USA.*

Contents of this file

Additional Supporting Information (Files uploaded separately)

Captions for Movies SV1 to SV10

Introduction

This supporting information provides a general overview of:

- The method for converting temperature contours into contours of lithospheric thermal thickness (see Fig. S1 and Test S1).
- Subduction runs compared to the results of a subduction benchmark paper (see Fig. S2).

- The effects of the adaptive mesh generator (see Fig. S3).

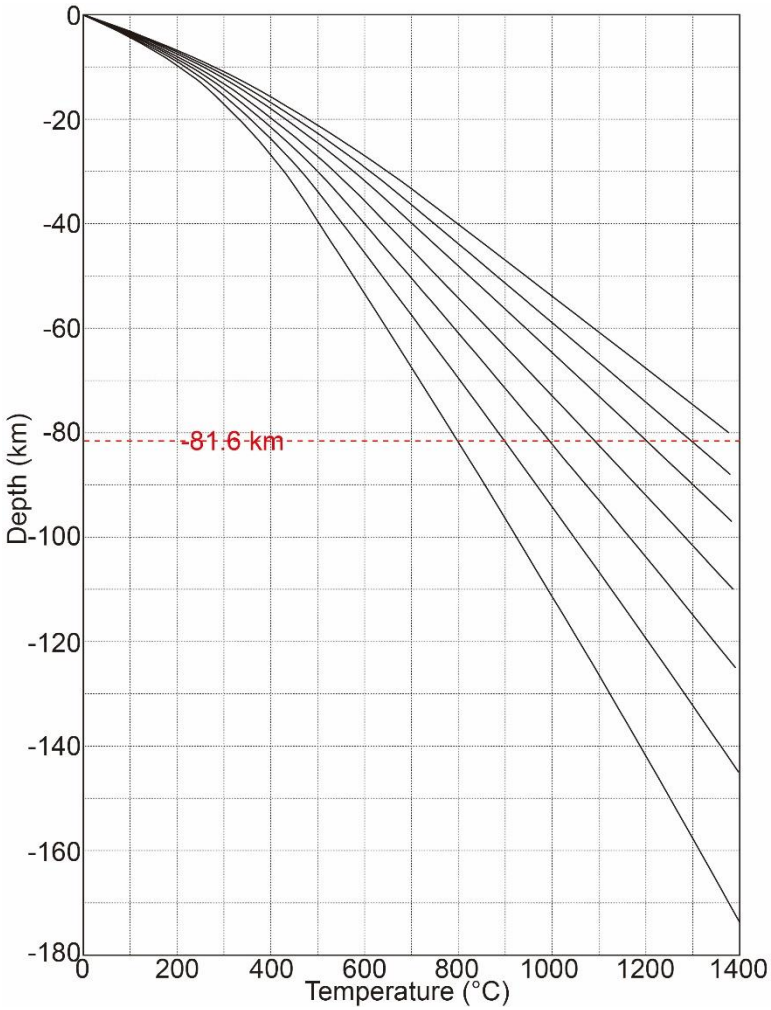

Figure S1. Steady state lithospheric geotherm for a lithospheric base at 80km, 88km, 97km, 110km, 125km, 145km, and 175km. The red dashed line marks the 81.6km depth where temperature contours are given in [Hansen et al., 2015].

Text S1.

Lithospheric thicknesses are converted from the temperature contours at 81.6km depth [*Hansen et al.*, 2015] under the assumption that the local geotherm has attained a steady state. A 1-D steady state geotherm is calculated by integrating Equation S1 (cf. [*Turcotte et al.*, 2014]) numerically using the finite difference method. The top temperature boundary condition is set to be 0˚C, and the bottom temperature boundary condition is set be a temperature transformed from asthenospheric potential temperature (1350˚C) with a 0.33K/km adiabatic gradient. See parameters in Table S1.

$$k\frac{d^2T}{dy^2}+\rho H_r=0 \tag{S1}$$

where k is thermal conductivity, T is temperature, y is depth, ρ is density, and H_r is radioactive heat productivity.

	Thickness	ρ (g/cm^3)	Hr (W/kg)	k (Wm^{-1}K^{-1})
Sediments	2 km	2.6	9.63×10^{-10}	3
Upper Crust	15 km	2.7	9.63×10^{-10}	3
Lower Crust	20 km	2.85	2.41×10^{-10}	3
Lith. Mantle	h-37km	3.34	7.32×10^{-12}	3

Table S1. Parameters for Equation S1. Symbol: h- lithospheric thickness. Abbreviation: Lith. Mantle- Lithospheric Mantle.

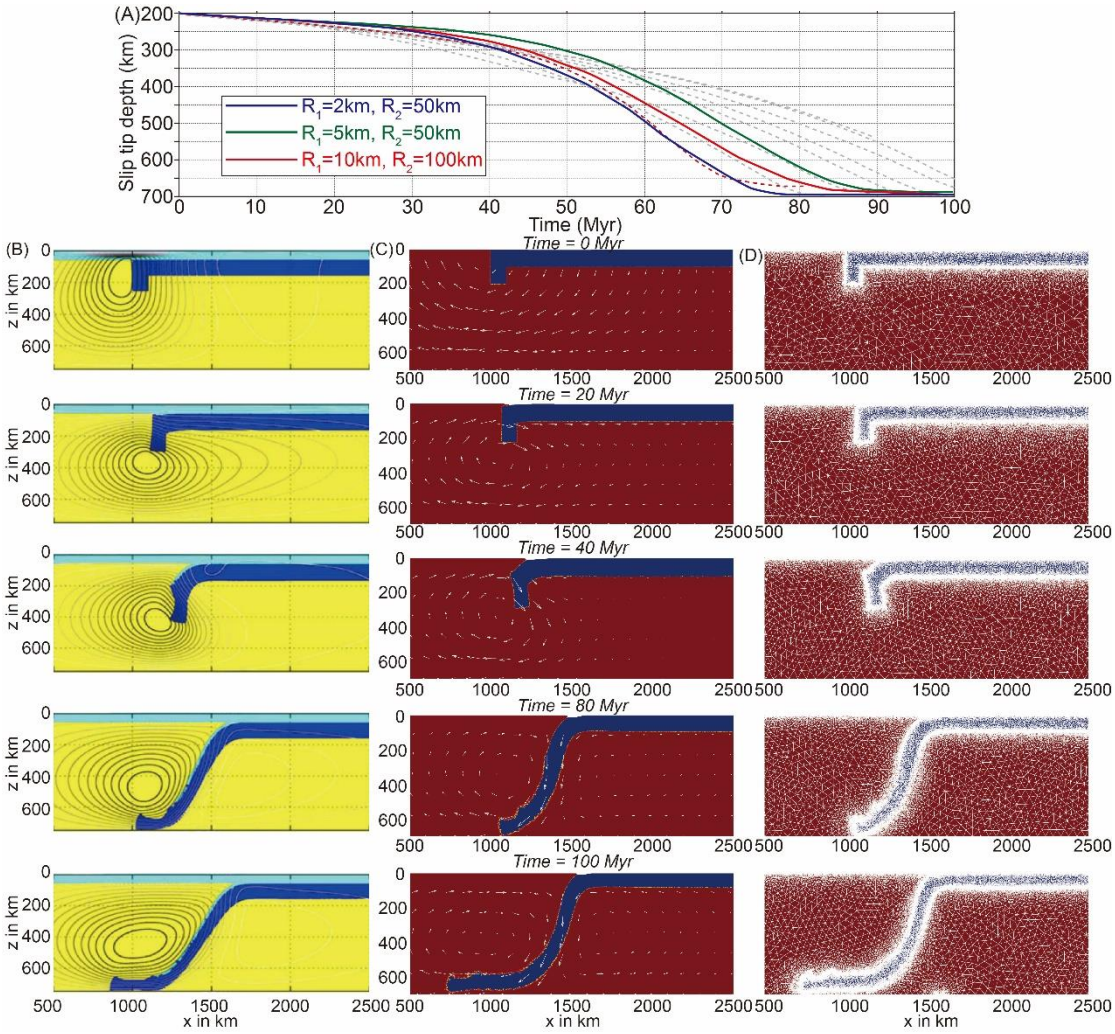

Figure S2. Subduction runs compared to the benchmarks in the subduction benchmark paper [Schmeling et al., 2008]. The same parameters and boundary conditions are used: The slab has ρ=3300 kg/m^3 and η=10^{23} Pa·s; the mantle has ρ=3200 kg/m^3 and η=10^{21} Pa·s; Free slip boundary condition are used for the left, right and bottom boundary segment; a free surface boundary condition [Andrés-Martínez et al., 2015] is used for the top boundary segment. The adaptive mesh generator (see Appendix B) is used for the numerical runs with 7 node (Crouzeix-Raviert) shape functions. The results closely match those in the subduction benchmarks. (A) Temporal evolution of the slab tip depth, using the same plotting convection as the benchmark paper. R1 and R2 are the best and worst mesh-resolutions used in numerical runs (see Appendix B). Gray dashed lines are taken from Fig. 13 of Schmeling et al. (2008); the red dashed line is from Fig. 10, with the name

“LaMEM 256×64 free surf” referring to Schmeling et al. (2008). (B) The typical behavior of this subduction model in Fig. 3 of Schmeling et al. (2008). (C) Temporal evolution of subduction in the run with R1 =2 km and R2 =50 km (see the red solid line in Panel A). White lines with an arrow mark the directions and speed of local flow. The maximum speed is 10-8 m/s. (D) The triangular mesh is added for snapshots in Panel B.

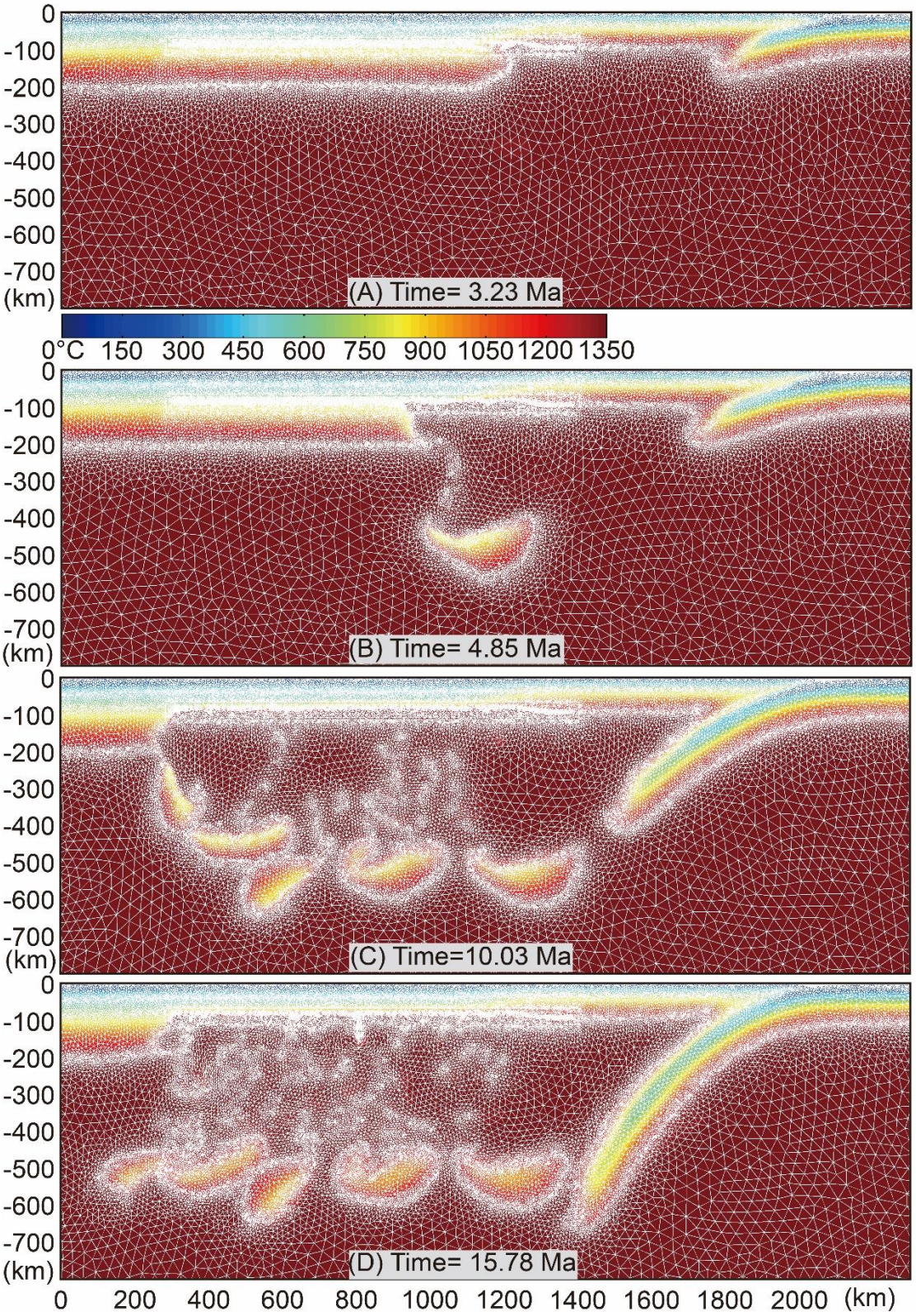

Figure S3. Material plot with meshes. The triangular meshes (in white) are plotted on the temperature field. Same plot convections as in Fig. 8.

Movie SV1. Records of Run 1 (see Table 2). Material Phase: 1- Asthenosphere; 2- non cratonic mantle; 3- depleted cratonic mantle; 4- crust; 5- cratonic keel; 6- the MLDL (also see captions on the first frame of this video).

Movie SV2. Records of Run 4 (see Table 2). Material Phase is same to Fig. 5. Plot conventions are same to Fig. 11.

Movie SV3. Records of Run 4* (see Table 2). Material Phase is same to SV1. Plot conventions are same to Fig. 11.

Movie SV4. Records of Run 7 (see Table 2). Material Phase is same to Fig. 5. Plot conventions are same to Fig. 11.

Movie SV5. Records of Run 7* (see Table 2). Material Phase is same to SV1. Plot conventions are same to Fig. 11.

Movie SV6. Temperature evolution of Run 1. White lines with an arrow mark the directions and speed of local flow. The maximum speed is 10-8.5 m/s. While contours are temperature contours (top-down): 400 ˚C, 700 ˚C, 1000 ˚C and 1300 ˚C.

Movie SV7. Temperature evolution of Run 4. Plot conventions are same to SV6.

Movie SV8. Temperature evolution of Run 4*. Plot conventions are same to SV6.

Movie SV9. Temperature evolution of Run 7. Plot conventions are same to SV6.

Movie SV10. Temperature evolution of Run 7*. Plot conventions are same to SV6.

Chapter 4. Craton Destruction Part II: Evolution of Cratonic Lithosphere after a Rapid Keel Delamination Event

Liang Liu, Jason P. Morgan, Yigang Xu and Martin Menzies. This manuscript has been published in *JGR: Solid Earth*.

Authors contribution

J. P. Morgan Proposed the idea for this work. L. Liu performed this work under the primary supervision of J. P. Morgan. L. L. collected the geological, geochemical and geophysical observations in this paper. L. L. modified the existed code for 2-D triangle mesh generation into the adaptive version. L. L. and J. P. Morgan designed the temperature-dependent strain weakening algorithm in the computational code. L. Liu and J. P. Morgan designed the numerical experiments. L. L., J. P. Morgan, Y-G Xu and M. Menzies discussed the implications from numerical experiments. L. L. wrote the manuscript in collaboration with J. P. Morgan, M. Menzies and Y-G Xu.

Craton Destruction Part II: Evolution of Cratonic Lithosphere after a Rapid Keel Delamination Event

Liang Liu[1, 2, 3], Jason P. Morgan[1,4], Yigang Xu[2], Martin Menzies[1, 2]

[1] *Department of Earth Sciences, Royal Holloway University of London, Egham, TW20 0EX, United Kingdom.*

[2] *State Key Laboratory of Isotope Geochemistry, Guangzhou Institute of Geochemistry, Chinese Academy of Sciences, Guangzhou 510640, China.*

[3] *College of Earth Sciences, University of Chinese Academy of Sciences, Beijing, 100049, China.*

[4] *Department of Earth & Planetary Sciences, Harvard University, Cambridge, MA, USA.*

Key Points:

- Keel delamination followed by convective erosion and lithospheric extension can explain the destruction of the eastern North China Craton.
- Reactivation of an enriched mantle layer is critical in leading to delamination of cratonic bottom and early post-delamination magmatism.
- The heterogeneous lithosphere beneath North China can be produced by post-delamination convective erosion and lithospheric extension.

Corresponding author: L. Liu, liangliu@gig.ac.cn

Corresponding author: J. Morgan, Jason.Morgan@rhul.ac.uk

Corresponding author: Y.G. Xu, yigangxu@gig.ac.cn

Abstract:

Cratonic lithosphere beneath the eastern North China Craton (ENCC) has undergone extensive destruction since early Jurassic times (*ca.* 190 Ma). This is recorded in its episodic tectonic and magmatic history. In this time, its lithosphere changed thickness from *ca.* 200 km to <60 km. This change was associated with a peak time (ca. 120 Ma) of lithospheric thinning and magmatism that was linked with high surface heat flow recorded in rift basins. We believe that these records are best explained by a two-stage evolutionary process. First, *ca.* 100 km of cratonic 'keel' underlying a weak mid-lithospheric discontinuity layer (*ca.* 80- 100 km) was rapidly removed in <10-20 Ma. This keel delamination stage was followed by a protracted (*ca.* 50-100 Ma) period of convective erosion and/or lithospheric extension that thinned the remaining lithosphere and continuously reworked the former cratonic lithospheric mantle.

This study focuses on numerical exploration of the well-recorded second stage of the ENCC's lithospheric evolution. We find: 1) lithospheric mantle capped by thick crust can be locally replaced by deeper mantle material in 100 Ma due to small-scale convective erosion; 2) asthenospheric upwelling & related extension can replace lithospheric mantle over horizontal length-scales of ~50-150 km, and account for observed 'mushroom-shaped' low-velocity structures; 3) modelling shows conditions that could lead to the multiple ENCC magmatic pulses between 190-115 Ma that are associated with temporal and spatial changes in magma source petrology and a magmatic hiatus; 4) a 'wet' mid-lithospheric discontinuity layer provides a potential source material for on-craton magmatism.

1. Introduction

Cratons are generally observed to retain tectonic and magmatic quiescence for billions of years. However, some cratonic regions do record extensive crustal deformation and on-cratonic magmatism that reflect craton destruction processes [*Griffin et al.*, 1998; *Menzies et al.*, 1993]. The eastern part of the North China Craton (ENCC) is the best-known Archaean craton to have experienced a recent destruction process [*Griffin et al.*, 1998; *Menzies et al.*, 1993; *Menzies et al.*, 2007; *Xu*, 2001; *Xu et al.*, 2009; *Zhu et al.*, 2012a]. Here cratonic lithosphere (*ca.* 180-220 km) [*Griffin et al.*, 1998; *Menzies et al.*, 1993]) was thinned to ~60-80 km between early Jurassic and early Cretaceous times (ca. ~190 -115 Ma [*Xu et al.*, 2009; *Zhu et al.*, 2012a]. The process of the ENCC thinning was mainly reflected in the ca. 190-155 Ma 'cold' and 135-115 Ma 'hot' on-cratonic magmas (Fig. 1) [*Wu et al.*, 2005; *Zhang et al.*, 2014]. Peak ENCC thinning occurred at *ca.* 120 Ma, and is apparent as wide-spread crustal melting and formation of metamorphic core complexes [*Xu et al.*, 2009; *Zhu et al.*, 2012a; *Zhu et al.*, 2012b] (Fig. 1B), rapid syn-rift surface subsidence, and high heat flow recorded in syn-rift basins [*Jiang et al.*, 2016; *Qiu et al.*, 2016]. The modern ENCC lithospheric mantle is a reworked product after craton destruction, and is mainly composed of young asthenosphere-derived lithospheric mantle [*Menzies et al.*, 2007; *Xu*, 2001; *Xu et al.*, 2009], that still contains pre-existing Archean "cratonic" relics [*Zhang et al.*, 2008; *Zheng et al.*, 2001].

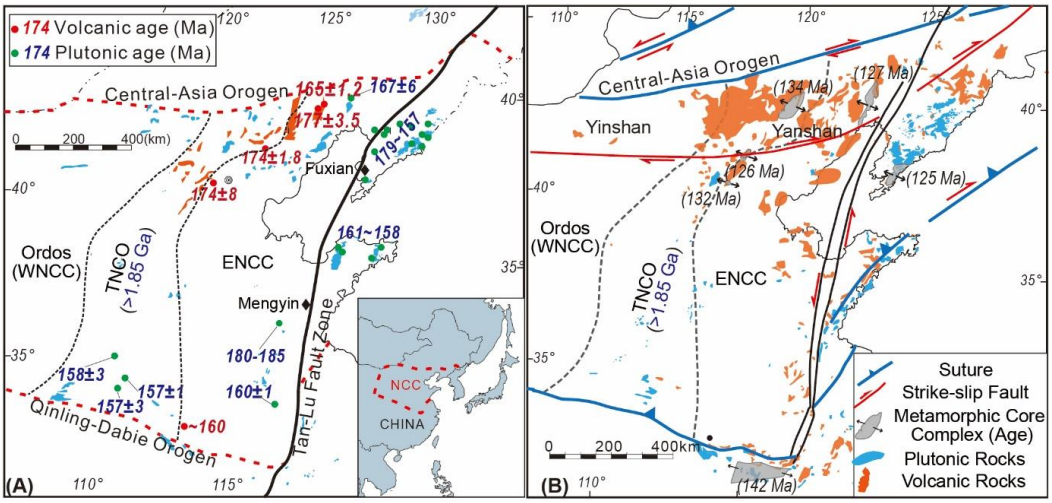

Fig. 1. Geological map of the Eastern North China Craton (ENCC).

(A) Distribution of Jurassic magmatism (ca. 190-160 Ma). (B) Distribution of Cretaceous magmatism (ca. 150-100 Ma) and major faults. See details for Cretaceous magma distribution in Fig. 11. *Abbreviations: TNCO- Trans- North China Orogen. WNCC- Western North China Craton.*

We think that this craton's thinning and reworking is best understood as a two-stage evolutionary process. First, *ca.* 100 km of cratonic keel underlying a weak mid-lithospheric discontinuity layer (*ca.* 80- 100 km) was rapidly removed in <10-20 Ma. This first stage of 'keel delamination' is the focus of a companion paper: *Craton Destruction Part I: Cratonic Keel Delamination; Liu et al., 2018; which we will hereafter refer to as Paper I*. A schematic cartoon of the proposed keel delamination process is shown in Fig. 2A-B, and a video of a numerical experiment illustrating this delamination stage is shown in supplementary video 9. The keel delamination stage was followed by a protracted (*ca.* 50-100 Ma) period of small-scale convective erosion and/or lithospheric extension that thinned the remaining lithosphere and continuously reworked the former cratonic lithospheric mantle beneath the Moho. The goal of the current study is to better understand this second stage of post-keel-delamination evolution of relic ENCC crust and uppermost lithospheric mantle. Our primary tool to do this will be to explore and compare the implications of a suite of numerical experiments with observed patterns of post-

Jurassic magmatism and deformation in the ENCC. Before diving into the numerical experiments and their ability to match the ENCC's well-documented post-delamination history, we first summarize the petrological, geochemical, geological, and geophysical observations that have been used to constrain the ENCC's recent evolution.

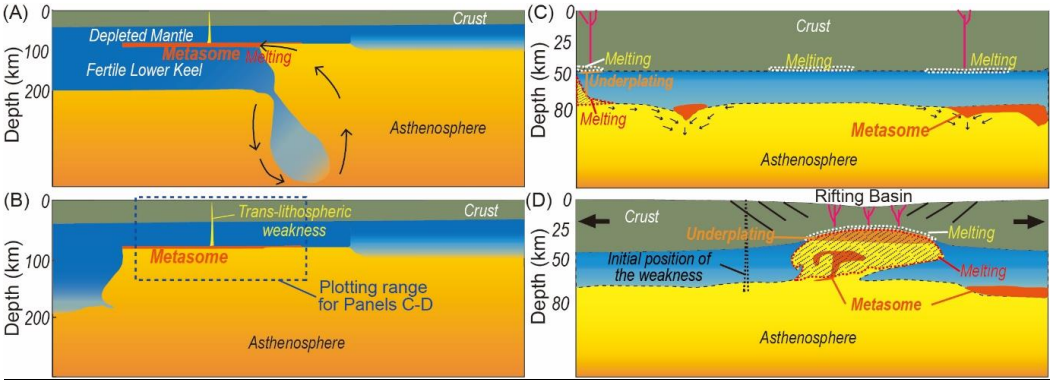

Fig. 2. Two-stage craton destruction model.

Panels A-B: Intra-mantle keel delamination model. (A) A ~10 km weak, partly discontinuous layer (e.g. the metasome Mid-Lithosphere Discontinuity Layer (MLDL)) exists between ~80-100 km depths in the craton lithosphere. Because the lower keel is denser than its adjacent asthenosphere and materials adjacent to the edge of metasome are soft enough, the denser lower keel starts to delaminate along the metasome. (The conditions for and evolution of this delamination process are the focus of Paper I.) (B) Delamination stops where the metasome MLDL disappears. After the delamination of the lower keel, pockets of metasome material locally survive at the base of the lithosphere. The overlying lithosphere initially retains its cool cratonic temperature and does not melt, leading to a magmatic hiatus after initial melting of the metasome warmed by contact with asthenosphere. **Panels C-D**: Post-delamination lithospheric evolution. (C) Cold remaining lithosphere can be locally denser than underlying hot asthenosphere. Therefore, dense lithosphere will tend to sag during convective erosion, leading to local thinning of lithosphere and intrusion of asthenosphere and metasome material into the relic cratonic lithosphere. During this process, the remaining lithosphere is slowly heated, and the lower crust can sometimes locally melt. (D) Later lithospheric extension (ca. 140 Ma) can lead

to focused magmatism and lithospheric replacement in regions close to pre-existing trans-lithospheric weak zone (e.g. the Tan-Lu fault zone).

2. Tectonic and Magmatic Evolution during ENCC Destruction.

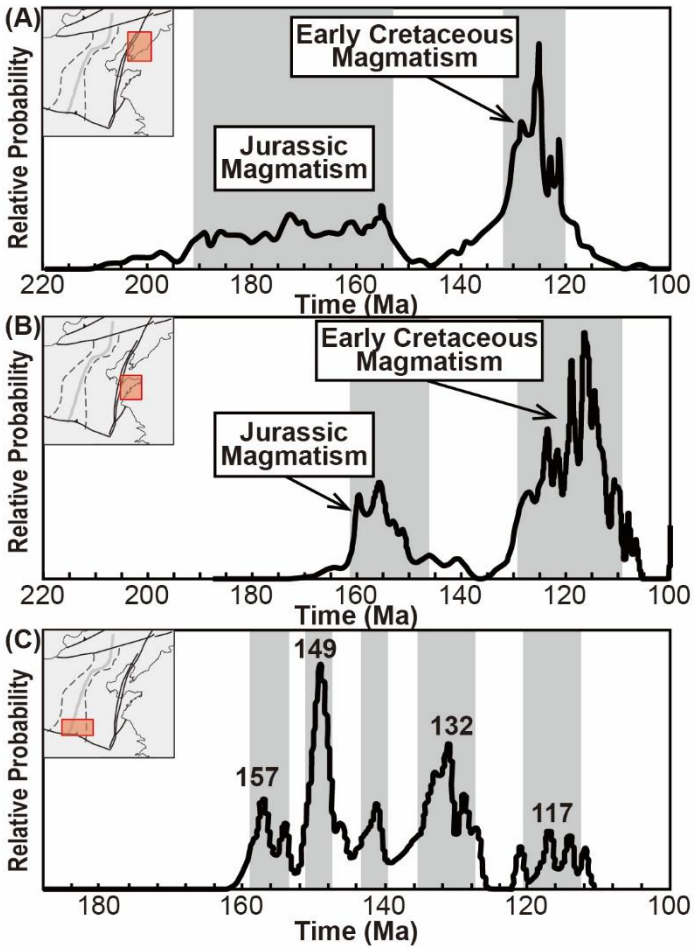

Fig. 3. Distribution of magmatic ages on the ENCC.

(A) Liaodong area [*Wu et al.*, 2005], (B) Jiaodong area [*Zhang et al.*, 2014] and (C) Xiaoqinling area [*Zhang et al.*, 2014]. On-craton magmatism occurred earlier in the northern ENCC (~190 Ma) than in the southern ENCC (~160 Ma). A ~10-20 Ma magmatic hiatus is always recorded on the ENCC after the Jurassic magmatic pulse, although magmatism can be locally continuous.

The ENCC destruction process is reflected in its episodic tectonic and magmatic (felsic-magma-dominated) record. Due to its location adjacent to active subduction-collision zones, a primarily compressional state of the ENCC appeared

no later than ca. 320 Ma [*Meng*, 2003; *Xu et al.*, 2009]. During this time, the crust along its margins is proposed to be locally thickened to *ca.*50 km (cf. [*Meng*, 2003]). (Alternatively, it is also possible that these crustal regions were initially thickened during the Archaean [*Kinck et al., 1993; Youssof et al., 2013; Zhai et al., 2011*].) Locally, lithospheric extension initiated at ca. 160-155 Ma, recorded in the subsidence of rift-basins [*He and Wang*, 2004; *Meng et al.*, 2003]. On the inner craton, the tectonic state generally transformed to be extensional at the Early Cretaceous times (ca. 140 Ma) (Fig. 1B) [*Meng et al.*, 2003], which is suggested to be related to the change in subduction directions of the paleo-Pacific plates [*Xu et al.*, 2009; *Zhu et al.*, 2012a].

Between ca. 190-160 Ma, magmatism moved from the margin to the interior (Fig. 1). By ca. 160 Ma, the ENCC keel appears to have been thinned to ca. 100-80 km, the depth-range of the commonly observed Mid-Lithosphere Discontinuity (MLD) [*Selway and Kelemen*, 2015]. Contact of the MLD layer (or MLDL) with hot, newly infilled asthenosphere triggered melting of this water-rich metasomatic layer known petrologically as the ‘metasome’, which is believed to be composed of mica-amphibole-rutile-ilmenite-diopside [*Menzies et al.*, 1993; *Xu*, 2001].

After a magmatic hiatus lasting 10-20 Ma, a second episode of magmatism occurred between ca. 150-115 Ma (Fig. 3, [*Xu et al.*, 2009; *Zhang et al.*, 2014; *Zhu et al.*, 2012a]). Locally, the pattern of magmatism can vary, i.e. multiple magmatic pulses are identified without any magmatic hiatus on the southwestern ENCC (Fig. 3C). Most of these magmas had stagnated close to the ENCC’s convergent margin (Fig. 1) that used to be capped by >50 km thick crust ([*Meng*, 2003; *Xu et al.*, 2009]) and the localized lithosphere-scale Tan-Lu fault zone [*Mercier et al.*, 2007; *Zhu et al.*, 2010]. In previous studies, this 190-115 Ma on-cratonic magmatism is proposed to reveal a long-lasting process of the craton destruction [*Menzies et al.*, 2007; *Xu*, 2001; *Xu et al.*, 2009; *Zhu et al.*, 2012a].

By the end of the second episode (ca. 110 Ma), the ENCC lithospheric mantle

had been replaced largely by asthenosphere-derived material with little xenolithic evidence for cratonic relics [*Menzies et al.*, 2007; *Xu*, 2001]. Mantle replacement beneath the Moho is supported by the high heat flow recorded in sedimentary basins (~90-100 W/m^2, [*Qiu et al.*, 2016]). The ENCC lithospheric thinning or mantle replacement rate appears to have been "slow", e.g. ~0.3 km/Ma, assuming ~80 km at 160 Ma changed to ~60 km at 100 Ma.

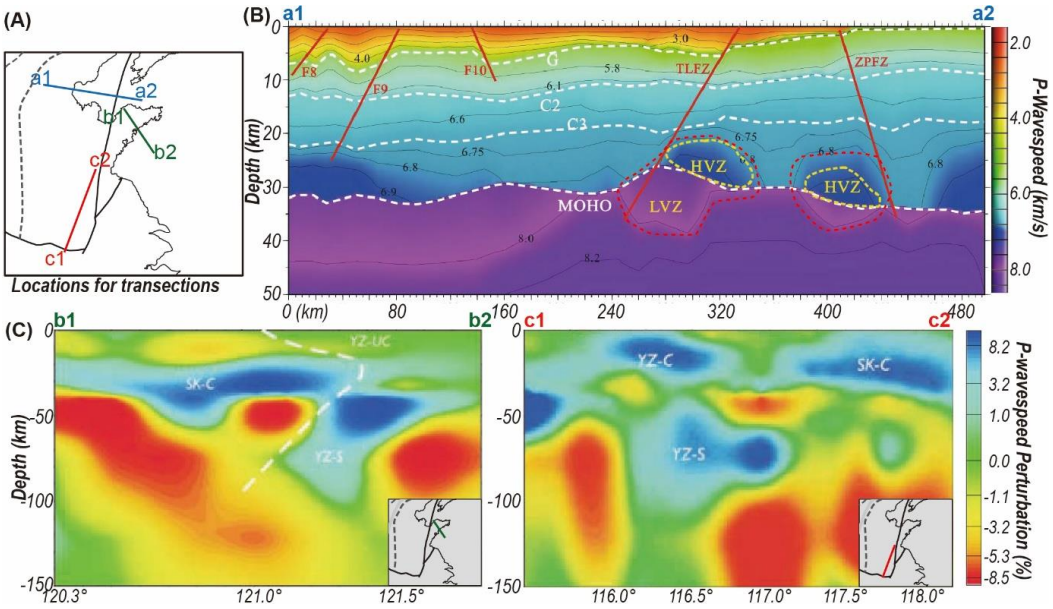

Fig. 4. The "mushroom" structures in the present-day ENCC lithosphere on both sides of the Tan-Lu fault.

(A) Locations for seismic transects in Panels B-D. (B) Refraction profile along the a1-a2 transect in Panel A [Hao et al., 2013]. Regions contoured by red dashed lines are the seismic wavespeed 'mushroom' structures that we think are associated with asthenosphere intruding into extending lithosphere (See text for more details). Abbreviations: TLFZ-Tan-Lu fault zone. ZPFZ- Zhangjiakou- Penglai fault zone. HVZ-high velocity zone, LVZ-low velocity zone. F8, F9 and F10 represent small-scale faults, see more details in Hao et al., 2013. (C-D) Seismic tomography structure along the b1-b2 and c1-c2 transects in Panel A [Xu et al. 2002].

The modern ENCC mantle appears to be heterogeneous in terms of its isotopic age and seismic velocity (Fig. 4). The mantle xenoliths entrained in < 80 Ma

basalts generally indicate a young and asthenospheric derived feature for the ENCC mantle [*Hong et al.,* 2012; *Xu* 2001; *Xu et al.*, 2009], but ancient mantle components do also locally exist [*Zhang* et al., 2008; *Zheng* et al., 2001]. Seismic tomography reveals a 50-150 km wide mushroom-like low-velocity anomalies within the lithospheric mantle, especially close to the Tan-Lu fault zone, and these 'mushrooms' are underlain by high-velocity anomalies within the crust [*Hao et al.*, 2013; *Xu et al.*, 2002; *Yuan*, 1996].

These features are taken as the most important basis by geologists for reconstructing the process of the ENCC destruction [*Menzies et al.*, 2007; *Xu*, 2001; *Xu et al.*, 2009; *Zhu et al.*, 2012a]. However, the requirement for both "fast" and "slow" aspects to the destruction of the craton, the origin and distribution of the on-cratonic magmas, and the origin of the heterogeneous modern ENCC mantle have not been addressed in previous numerical modelling studies:

(1) A "rapid" magmatic flare-up has been linked to many processes including lithospheric delamination along the weak and/or deep Moho [*Bird*, 1979; *Gao et al.*, 2004; *Kay et al.*, 1993], Rayleigh-Taylor type gravity instability [*Gorczyk et al.*, 2012; *Harig et al.*, 2010], and lithospheric rifting [*Liao et al.*, 2014; *Lin et al.*, 2005; *Wenker et al.*, 2017];

(2) Mechanisms used to explain on-craton magmatism include convective erosion (cf. [*Conrad et al.*, 1997]), assuming that cratonic keel lost its high strength before thinning, due to long-term (>1Ga) mantle refertilization, or short-term (<200 Ma) in situ metasomatism-related mantle transformation linked to dehydration in underlying (paleo-) Pacific slabs [*He*, 2014; *Liao et al.*, 2017; *Niu*, 2005; *Wang et al.*, 2016; *Xu*, 2001; *Yang et al.*, 2017; *Zhang et al.*, 2008].

We infer from the above observations that a two-stage process led to craton reworking in the ENCC [*Liu et al.*, 2016]. First, over a period of 10-20 Ma, *ca.* 100 km of the cratonic keel was rapidly removed along a weak Mid-Lithospheric

Discontinuity Layer (MLDL) that may have had a composition similar to the proposed metasome [*Karato et al.*, 2015; *Menzies et al.*, 1993; *Selway et al.*, 2015; *Xu*, 2001]. We propose this happened during a discrete keel delamination event -- see Fig. 2A-B, supplementary video 9, with a detailed investigation of this process in the companion *Paper I*. Second, the remaining cratonic lithospheric mantle was progressively replaced by asthenospheric mantle during convective erosion associated with widely-spread localized lithospheric extension along pre-existing fault(s).

This paper focusses on the post-delamination process (Stage 2). There have been many conceptual models for craton destruction, many with contradictory assumptions and conclusions. To guide our investigation, we aim to keep the following issues in mind:

(1) When (& why) does melting occur in the crust?

(2) Do trans-lithospheric weaknesses have an important role to play in craton failure?

(3) What is the role, if any, for 'in-situ' metasome-linked water?

3. 2-D Numerical Methods

3.1 Thermomechanical code

A 2-D incompressible Lagrangian finite element code with a free surface boundary condition is used for the numerical experiments [*Andrés-Martínez et al.*, 2015; *Hasenclever*, 2010; *Hasenclever et al.*, 2011]. Crust and mantle are assumed to be incompressible elastoviscoplastic materials that deform by both Newtonian and non-Newtonian creep. Material melting is found using methods described in [*Hasenclever*, 2010; *Morgan*, 2001]. Tracer particles are added for tracking different material properties. The 2-D experimental domain is subdivided using an adaptive triangle mesh generator that tracks material boundaries and interfaces, e.g. between asthenosphere and lithospheric mantle. A Drucker-Prager yield criterion is added to evaluate and formulate plasticity in extension experiments (cf. [*Moresi*

et al., 2003]). More details on the numerical approach are given in Andrés-Martínez et al. (2015), Hasenclever (2010), Hasenclever et al. (2011), the attached Appendixes, and those in Paper I)). Table 1 shows the parameters used in numerical experiments. Table 2 summarizes the major variables tested in numerical runs.

3.2. Model Setup

Initial Material Layering and Material Conditions

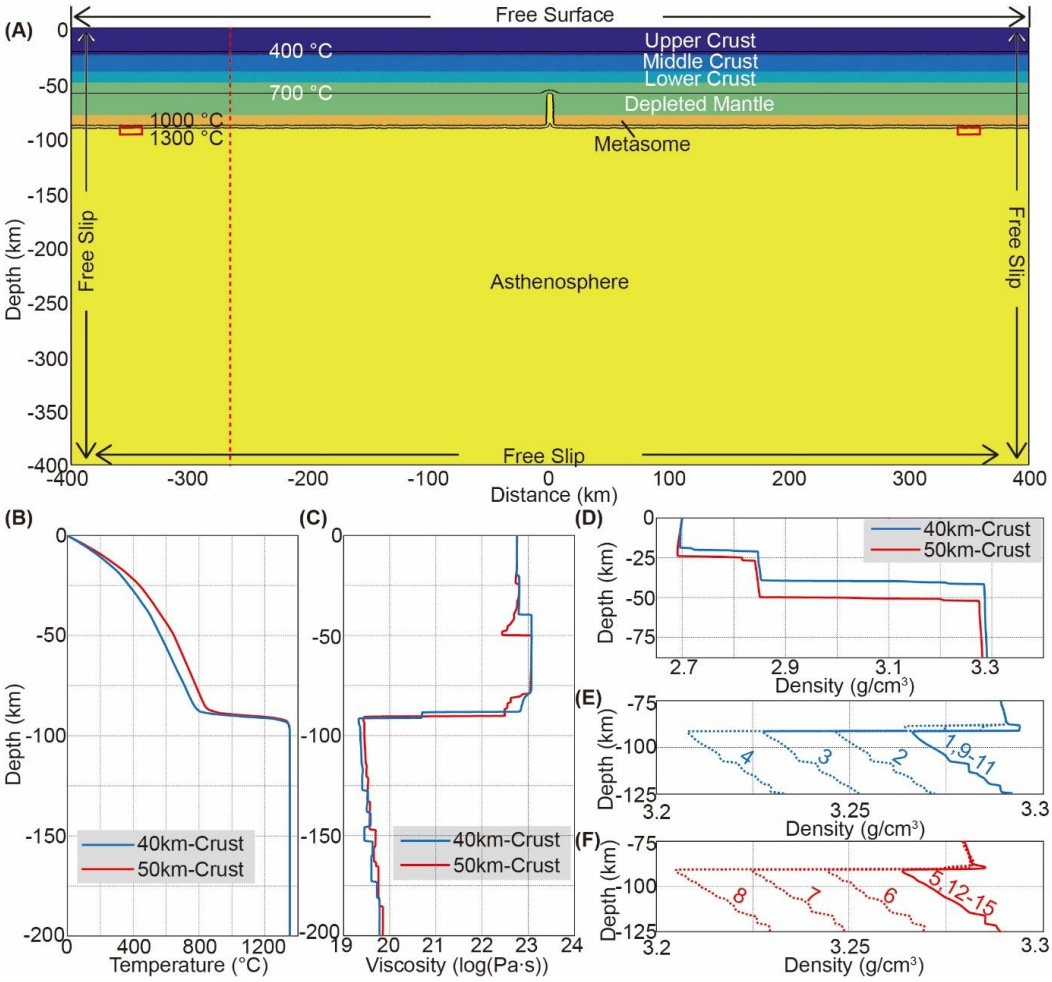

Fig. 5. Model setup.

(A) The post-delamination ENCC lithosphere is assumed to be 90 km thick, containing, from its top to bottom: 50 km thick (margin) or 40 km thick crust (interior), lithospheric mantle containing a basal metasome (10 km) within 40-50 km-thick relic cratonic (depleted) mantle that lies above the metasome layer. A ~5 km wide zone of asthenosphere-like material is added between 90-60 km depths at the center to simulate

an initial lithospheric weak zone. To trigger small scale mantle convection in Runs 1-8, two 20 km wide × 10 km thick dense (3.4 g/cm^3) blocks (see small red rectangles) are set at -350 km and 350 km, close to the left and right boundary segments. These two blocks sink to the bottom within 0.5 Ma and do not obviously affect the experiment following their initial sinking. The mesh resolution (~2 km) close to phase boundaries (~20 km) is *ca*. 10 times finer than in regions far away (~95 km) from phase boundaries. (B) The initial temperature profile of numerical experiments is the red dashed line in Panel A. 40 km-crust scenarios include Runs 1-4 and Runs 9-11; 50 km-crust scenarios include Runs 5-8 and Runs 12-15 (also see Table. 2). (C) Initial viscosity profile of numerical experiments，with data from the profile marked by the red dashed line in Panel A. (D) Initial density profile of numerical experiments above 80 km depth. (E) The 75-125 km depth range is zoomed up to demonstrate the initial density structure in Runs 1-4 and 9-11. (F) A similar amplification is also made for the initial density structure of Runs 5-8 and 12-15. In Panels (E-F), numbers beside the density profile represent the run-numbers of the numerical experiments considered here.

The initial lithosphere thickness is at 90 km, which contains a basal 10 km MLDL. This initial condition reflects the post-keel-delamination state of the ENCC lithosphere following a keel delamination event beneath a weak, buoyant metasoma-layer-like MLDL. The crustal thickness in Runs 1-4 and 9-11 is set at 40 km to be the initial value beneath inner cratonic areas (cf. [*Xia et al.*, 2017]). To investigate the effect of increased crustal thickness on magmatism in the ENCC's compressionally thickened margins (Fig. 1B), the crustal thickness chosen in Runs 5-8 and 12-15 is 50 km. A ~50 km crustal thickness appears to still remain beneath parts of the ENCC and the western North China Craton (e.g. beneath the southwestern ENCC and the western Ordos Basin [*Chen et al.*, 2014; *Xia et al.*, 2017]).

To study the potential effects of pre-existing lithospheric fault zones in controlling lithospheric evolution and magmatic distribution (cf. [*Deng et al.*, 2013;

Menzies et al., 2007; *Yuan*, 1996]), in runs 9-15 a 5 km wide zone of asthenospheric material is placed in the middle of the modeling box at ranges between 90 and 60 km, to act as an initial weak zone in the lithosphere. Vertical weak zones have been reported beneath some fault zones (cf. [*Pollitz et al.*, 2001]). In the case of the ENCC, they could possibly be created by long-term-active lithospheric shearing close to the Tan-Lu fault [*Zhu et al.*, 2010].

	A.M.	Metasome		D.M.	L.C.	M.C.	U.C.
Flow Law Parameters[1-7]							
A_{dis} ($Pa^{-n}\cdot s^{-1}$)	$10^{-15.05}$	$10^{-15.05}$		$10^{-15.56}$	$10^{-21.05}$	$10^{-15.4}$	10^{-28}
n_{dis}	3.5				4.2	3.0	4.0
E_{dis} (kJ/mol)	480	480		530	445	356	223
V_{dis} (cm^3/mol)	8				-		
A_{dif} ($Pa^{-n}\cdot s^{-1}$)	$10^{-8.65}$				$10^{-13.3}$	$10^{-13.3}$	$10^{-8.4}$
n_{dif}	1						
E_{dif} (kJ/mol)	335	335		375	170	170	220
V_{dif} (cm^3/mol)	4				-		
r	r_{dif}=1.93, r_{dis}=1.95				-		
Elasticity and Plasticity[7]							
G (GPa)	74				40	40	36
C_0 (Mpa)	20						
Φ (º)	30 (γ = 0) →15 (γ > 1.5)						
Thermal Parameters[7-9]							
k ($Wm^{-1}K^{-1}$)	3.3				2.5	2.5	2.1
H_r (μW/m^3)	0.033				0.25	0.25	1
c_p (J/(kg· K)	1200						
T_0^m (℃)	1081	1081		1136	-		
$\left(\partial T^m/\partial f\right)_p$	132				-		
$\left(\partial T^m/\partial P\right)_f$	250				-		
Q_L (kJ/kg)	400				-		
Density Parameters[10-11]							
ρ_0 ($g\cdot cm^{-3}$)	-	3.32		3.31	2.85	2.85	2.7
$a_1(10^{-4})$	0.2697	0.2697		0.27165	0.27014		
$a_2(10^{-8}\ K^{-1})$	1.0192	1.0192		1.04971	1.05945		
$a_3\ (K^2)$	-0.1282	-0.1282		-0.15031	-0.1243		

K (Gpa^{-1})	134	134	129	63

Tab. 1. Parameters for the numerical experiments discussed in the paper.

Dislocation and diffusion viscosities are determined as $\eta = 1/2\, A^{-1/n} C_{OH}^{-r/n} \varepsilon_{II}^{1/n-1} \exp\left((E + P \cdot V)/nRT\right)$, where η is viscosity, ε is second invariant of strain rate, A is a pre-exponential constant, E is activation energy, C_{OH} is water content in ppm H/Si (for olivine Fo90: 1ppm (wt) H_2O= 16.35H/10^6Si;), r describes the exponential dependency on water, R is the universal gas constant, T is temperature, P is pressure, and V is activation volume. Subscript "dis" refers to parameters for dislocation creep, while "dif" is for diffusion creep.

Parameter references: 1- [*Hirth and Kohlstedt*, 2004], 2- [*Wilks and Carter*, 1990], 3- [*Rybacki and Dresen*, 2004], 4- [*Gleason and Tullis*, 1995], 5- [*Rutter and Brodie*, 2004], 7- [*Brune et al.*, 2014], 8- [*Morgan*, 2001], 9- [*Korenaga and Karato*, 2008], 10- [*Djomani et al.*, 2001], 11- [*Schutt and Lesher*, 2006].

Other symbols: G- shear modulus, C_0- Cohesion, Φ- Friction Angle, k- thermal conductivity, H_r- radioactive heat production, c_p-heat capacity, T_0^m is the solidus at room temperature and pressure, $\left(\partial T^m/\partial f\right)_p$ describes the solidus's dependence on degree of melt extraction, and $\left(\partial T^m/\partial P\right)_f$ describes the solidus's dependence on pressure, Q_L- Latent heat, ρ_0- the reference density at room temperature (20℃) and pressure (0.1 Mpa), K- bulk modulus.

Abbreviations: A.M. - asthenosphere, D.M. - Depleted mantle, L.C.- Lower Crust, M.C.- Middle Crust, U.C.- Upper Crust.

Material Densities

The MLDL material is assumed to have a compositional density identical to that of MARID mantle xenoliths [*Dawson et al.,* 1977]. Given that 'margin processes' might reduce the compositional density ρ_{co} of the mantle wedge [*Gerya et al.*, 2006], while Fe-rich mafic melts could also increase the ρ_{co} of the overlying lithospheric mantle [*Griffin et al.*, 2009; *Zhang et al.*, 2008]: the ρ_{co} difference

between lithospheric mantle material and asthenosphere is varied in Runs 1-8 (Fig. 5D-F). These experiments will allow us to study the potential effects of more or less compositionally buoyant asthenosphere on convective erosion of the lithosphere.

Melting Parameters

Bi-modal patterns of magmatism are an important feature of the post-delamination history of the ENCC. These models also allow us to explore potential magmatism associated with metasome heating by newly infilled asthenosphere, melting associated with asthenospheric infilling and reworking of the relic ENCC lithosphere and crust, and crustal melting associated with its potential reheating. In these experiments, the asthenosphere is assumed to contain 100 ppm water as has been estimated for oceanic basalt sources (cf. [*Hirschmann et al.*, 2005]), In contrast, MLDL material is assumed to contain 1000 ppm water (cf. [*Karato et al.*, 2015]). No initial depletion is assumed for upper and middle crust, and we treat their melting behavior to be that of amphibolite (cf. [*López et al.*, 2001], Fig. A1A). A 20% initial depletion is used for lower crustal material to simulate the preexistence of granulite-facies rocks [*Gao et al.*, 1998], whose petrology can be treated as the residue after ~20% melt extraction from an amphibolite (cf. [*Rapp et al.*, 1995]). See the Appendix for the mantle and crustal solidi used in the numerical experiments.

Initial and Boundary Conditions

For the initial temperature field, a 1-D steady-state conductive thermal profile [*Turcotte et al.*, 2014] for ‘stable’ 200 km lithosphere (with various initial crustal thicknesses, Fig. 5B and Tab. 2) is used for the uppermost lithospheric layers. Below the MLDL, the starting temperature of asthenosphere is set to be 1350℃ to simulate the situation just after the rapid influx of warm asthenosphere during a

rapid delamination event. The surface boundary is fixed at 0℃. The bottom boundary is fixed to be that of the asthenospheric potential temperature (1350℃).

The following experiments will be presented in two groups. In Runs 1-8, no effects of extension are considered; while the effects of extension are studied in Runs 9-15. For runs without extension (Runs 1-8), a free slip boundary condition is used for the left, right and bottom boundaries. For runs with extension (Runs 9-15), an outward speed (Table. 2) is imposed along the righthand side of the computational region for 50 Ma, to simulate the maximum extension duration on the ENCC as discussed above; while the lower boundary of the region has an upward velocity taken to ensure overall material balance,

$$v_{vertical} = v_{right} L_{bottom} / L_{right} \quad (1)$$

where v_{right} is the speed prescribed along the right boundary (ranging from 1-4 mm/yr), $v_{vertical}$ is the speed prescribed along the bottom boundary; L_{right} is the evolving length of the right boundary, and L_{bottom} is the evolving length of the bottom boundary.

4. Results

For comparison with the above geological and geophysical observations on the ENCC (Section 2), the following experimental results will be discussed in terms of their melting behavior and lithospheric reworking/replacement. A summary of results will be presented before describing the specific processes of convective erosion or lithospheric extension. Experiments without lithospheric extension will be presented before those with extension.

Goal and variables studied with extension-free experiments

Prior to lithospheric extension, on-cratonic magmatism appears to have been focused close to the ENCC's margins. This may have happened because these

regions had initially thicker crust and/or a special subduction margin density structure discussed in previous studies (e.g. [*Gerya et al.*, 2003; *Hasenclever et al.*, 2011*; Meng et al.,* 2003*; Xu et al.,* 2009*;*]). In Runs 1-8, both factors are variables to be explored.

To study potential effects of thicker crust, a 50 km thick crust is set in Runs 5-8, which have a hotter initial geotherm (Fig. 5B); for comparison, the crustal thickness is set at 40 km in Runs 1-4, possible as a pre-destruction value for the inner craton (cf. [*Xia et al.*, 2017]).

Given that 'margin processes' might reduce the compositional density ρ_{co} of the mantle wedge [*Gerya et al.*, 2003], while associated Fe-rich mafic melts could also enhance the ρ_{co} of the overlying depleted lithospheric mantle [*Griffin et al., 2009; Zhang et al., 2008*]: the ρ_{co} difference ($\Delta\rho_{co}$) between lithospheric mantle (ρ_{co}^{L}) and asthenosphere (ρ_{co}^{A}) is varied in Runs 1-8 (Fig. 5D-F and Tab. 2).

Goals and variables studied in experiments with net lithospheric extension

In regions close the Tan-Lu fault zone, presently far from convergent margins, the observed enhanced magmatism and mantle heterogeneity may have been shaped by variable extension and/or crustal thickness (40 km thick for Runs 9-11 and 50 km thick for Runs 12-15, Table. 2). In Runs 9-15, the crustal thickness and the rate of lithospheric extension are considered as variables in each experiment.

Convective Erosion Modelling (Extension Speed = 0**)**				
40km-crust Scenario				
Run No.	*Run 1*	*Run 2*	*Run 3*	*Run 4*
$\rho_{A.M.}\|\rho_{L.M.}$ *(kg/m^3)*	3360|3310	3340|3310	3320|3310	3300|3310
50km-crust Scenario				
Run No	*Run 5*	*Run 6*	*Run 7*	*Run 8*
$\rho_{A.M.}\|\rho_{L.M.}$ *(kg/m^3)*	3360|3310	3340|3310	3320|3310	3300|3310
Lithospheric Extension Modelling ($\rho_{A.M.}\|\rho_{L.M}$ = 3360|3310(kg/m^3)**)**				
40 km-crust Scenario				
Run No.	Run 9		Run 10	Run 11

Extension Speed	1 mm/yr	2 mm/yr	3mm/yr	
50 km-crust Scenario				
Run No.	Run 12	Run 13	Run 14	Run 15
Extension Speed	1 mm/yr	2 mm/yr	3 mm/yr	4 mm/yr

Tab. 2. Variables in each run.

$\rho_{A.M.}$- compositional density of asthenosphere; $\rho_{L.M.}$- compositional density of lithospheric mantle.

4.1. Experiments without lithospheric extension

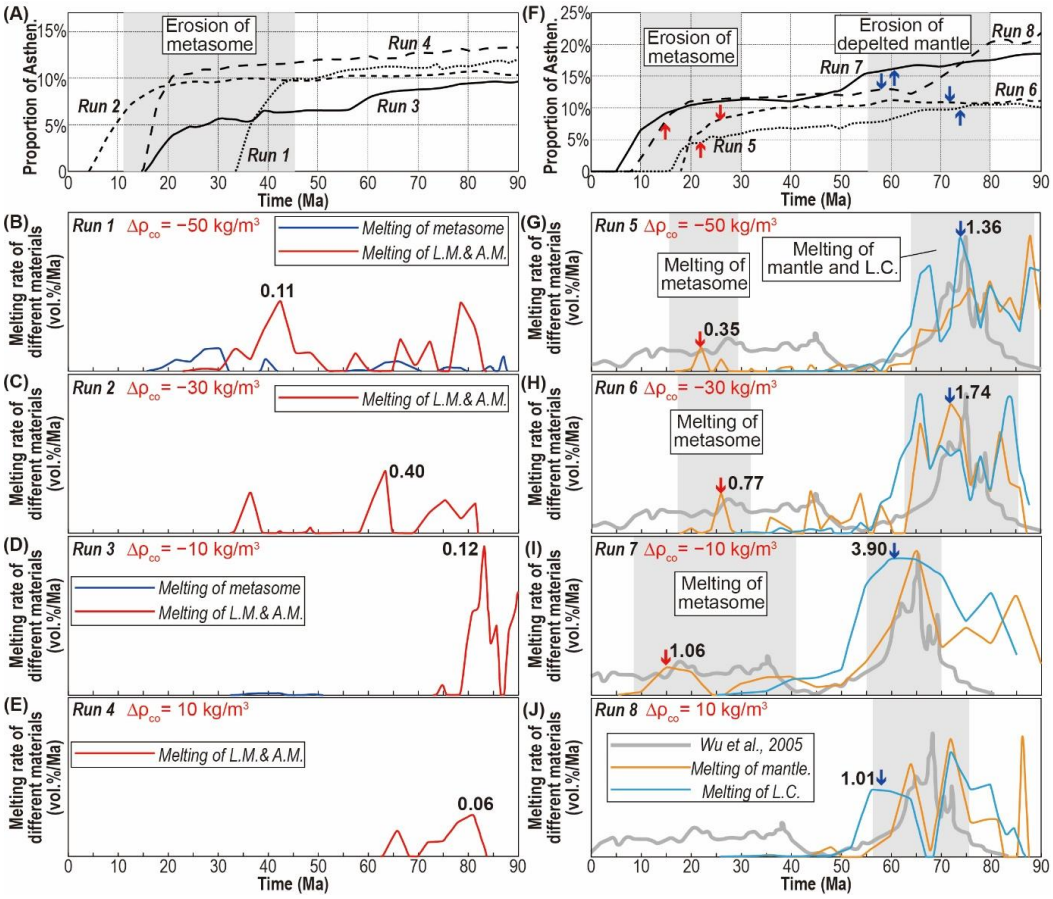

Fig. 6. Results of experimental runs without lithospheric extension.

Panels A-E: Runs 1-4 with 40 km thick crust. (A) Fraction of asthenosphere material within reworked lithosphere above 90 km depths. By the end of these experiments, asthenosphere material has replaced ~10-15% of the original relic cratonic lithosphere. Asthenosphere replacement of this initial metasoma layer accounts for ~10% of the intruded material, while replacement of depleted cratonic mantle accounts for <5%. (B-E) Melting rates of different materials (in volume proportion per million years) above 100 km depths. **Panels F-J**: Runs 5-8 with 50 km thick crust. (F) Fraction of asthenosphere

material within reworked lithosphere above 90 km depths. By the end of these experiments, asthenosphere has replaced ~10-25 % of the relic cratonic lithosphere. Replacement of initial metasome MLDL material accounts for ~10% and replacement of relic cratonic mantle accounts for <15 %. (G-J) Melting rates of different materials (in volume proportion per million years) at depths shallower than 100 km. The thick grey line is from Fig. 3A. Labels for lines in Panels G-I are same as those in Panel J. The horizontal range is between -400 km and 0 km (Fig. 5A). *L.C.- lower crust. L.M.- lithospheric mantle, A.M.- asthenospheric mantle.* $\Delta\rho_{co}$*- the compositional density difference between lithospheric mantle and asthenosphere.*

Runs 1-8 are designed to investigate the evolution of the relic keel without regional post-delamination extension. In these runs, convective erosion leads to lithospheric reworking/replacement and introduces ~10- >20 % asthenosphere into the reworked lithosphere (Fig. 6A and F). Minor melting occurs in the runs with 40 km thick crust (Fig. 6B-E); and two melting pulses are generally observed in those with 50 km thick crust (Fig. 6F-J).

In Runs 1-4 with 40 km thick crust, ~10 % lithosphere is replaced by asthenosphere after 100 Ma and minor melting of mantle occurs at ~20 Ma after the lithospheric is heated up (Fig. 6A-E). In these runs, increasing the compositional density difference ($\Delta\rho_{co}=\rho_{co}^{L}-\rho_{co}^{A}$) does not affect the results.

In Runs 5-8 with 50 km thick crust, two pulses of melting are observed (Fig. 6G-J). The first pulse is minor, caused by metasome melting. The second pulse features both mantle and lower crustal melting, dominated by crustal melting. The rate of lithosphere replacement increases to >20 % only when $\Delta\rho_{co}$ <-10 kg/m^3 (Fig. 6B). Runs 4 and 8 consider a less likely scenario, as the compositional density (3.31 g/cm^3 at STP condition) of depleted mantle is generally thought to be less than that of the asthenosphere (3.36-3.39 g/cm^3 at STP condition) (*cf.* [*Djomani* et al., 2001]).

Convective-erosion-dominated lithospheric reworking

Run 7 is taken as a type-example to describe convective erosion of the lithosphere in absence of extension.

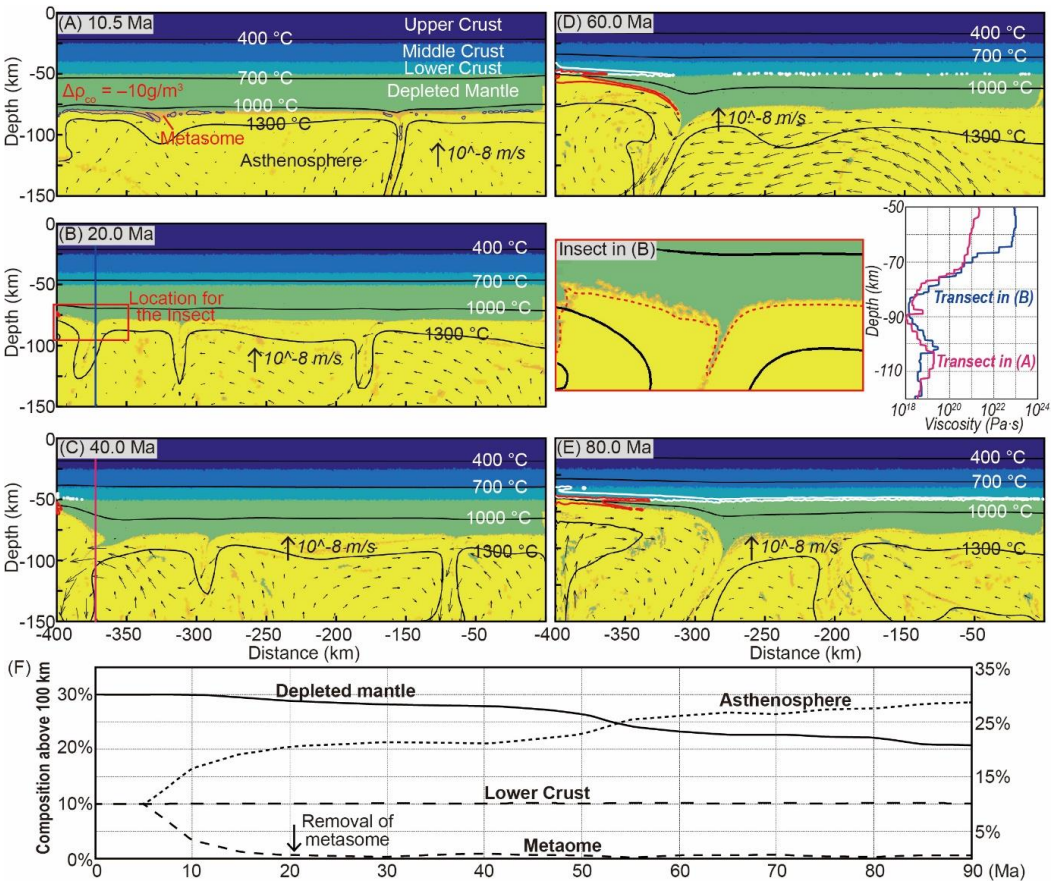

Fig. 7. Convective erosion of relic lithosphere (Run 7).

(A) Due to the weak rheology of the metasome MLDL material, it joins into small-scale convection after being heated. Metasome melting marks the first melting pulse at ~10-20 Ma. (B) Due to its higher net density (Fig. 5F), during small scale convection the depleted mantle entrains into the downwelling asthenosphere in the form of small-drops. These sinking drops pull adjacent materials towards the locus of sinking. The overall process leads to local lithospheric thinning (or asthenospheric diapirs, see the insect). A small melting region appears within the asthenospheric diapir. (C) The continuous growth of cratonic lithospheric drops results in a larger horizontal temperature variation and accelerates the small-scale convection. When an asthenospheric diapir impends near the crust, lower crust melting occurs. (D) Asthenosphere contacts with lower crust, as the

mantle melting depth range expands continuously. (E) ~30 % of reworked old lithosphere has been replaced by asthenosphere. (F) Volume fractions of different materials above 100 km depth. *In panels A-E:* white lines mark contours of crustal melt-extraction, red lines mark contours of mantle melt-extraction (with depletion >5%) and blue contours in Panel A show metasome melt-extraction. $\Delta\rho_{co}$- the compositional density difference between lithospheric mantle and asthenosphere.

Most of the metasome material enters small-scale mantle convection in the form of small drops and mix with asthenosphere after the start of experiment (i.e. 20 Ma) (Fig. 7A and 7F). This is due to the fact that the metasome has a weak rheology and a locally greater density (Table. 1). Its high-water content (~1000 ppm) is associated with a low solidus, which means that metasome melting dominates the early melting pattern (i.e. 20-10 Ma, Fig. 6I).

Thereafter, depleted cratonic mantle is in direct contact with the hotter underlying asthenosphere. Lithospheric downwelling stretches the surrounding materials so that lithosphere close to the sinking center thins and small asthenospheric diapirs begin to form (Fig. 7B). The initial diapirs are small (<15 km) and occur close to the ends/edges of the stretching depleted mantle region. Lower crustal melting begins above the asthenospheric diapirs, and initial pressure-release mantle melting occurs in the top of the asthenospheric diapirs (Fig. 7C).

Asthenospheric diapirs and melting regions gradually grow wider as the sinking center moves towards the inner lithosphere. In this way, ~15 % lithosphere is replaced by asthenosphere (i.e. 80 Ma, Fig. 7E-F). The newly accreted materials (asthenospheric+ metasome+ lithosphere) cool to a stage where the 1300℃ potential contour appears at > 80 km depth (Fig. 7E).

4.2. Experiments with lithospheric extension

Runs 9-15 are designed to investigate the evolution of relic keel under an extensional scenario. Lithospheric extension leads to ~50-150 km wide lithosphere to be replaced by 'mushroom'-like upwelling materials. Two pulses of melting occur in the runs with 40 km thick crust (Fig. 8B-C and 9B-D), while the melting behavior in the runs with 50 km thick crust appears to be continuous without obvious hiatuses (Fig. 8G-H and 9 F-H). In comparison to scenarios without extension, crustal melting is rare and is not observed in regions away from the center of extension (Fig. 9).

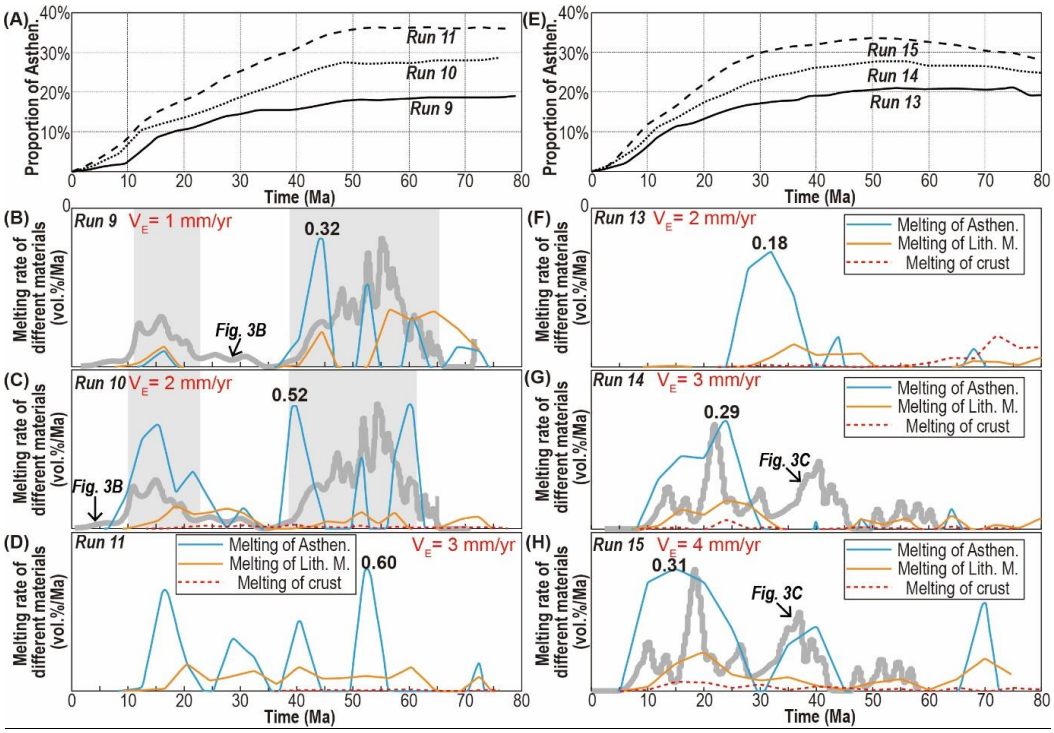

Fig. 8. Results of experimental runs with lithospheric extension.

Panels A-E: Runs 9-11 with 40 km thick crust. (A) Fraction of asthenosphere above 90 km depth. (B-D) Melting rates of different materials (in volume proportion per million years) above 100 km depth. The thick grey line is from Fig. 3B. Labels for lines in Panels B-C are same as those in Panel D. **Panels E-H**: Runs 13-15 with 50 km thick crust. (F) Fraction of asthenosphere above 90 km depth. (F-H) Melting rates of different materials (in volume proportion per million years) above 100 km depth. The thick grey line is from

Fig. 3C. The horizontal plotting range is between -150 km and 250 km (see Fig. 5A). *Lith. M.- lithospheric mantle, Asthen. - Asthenosphere. V_E- extension rate.*

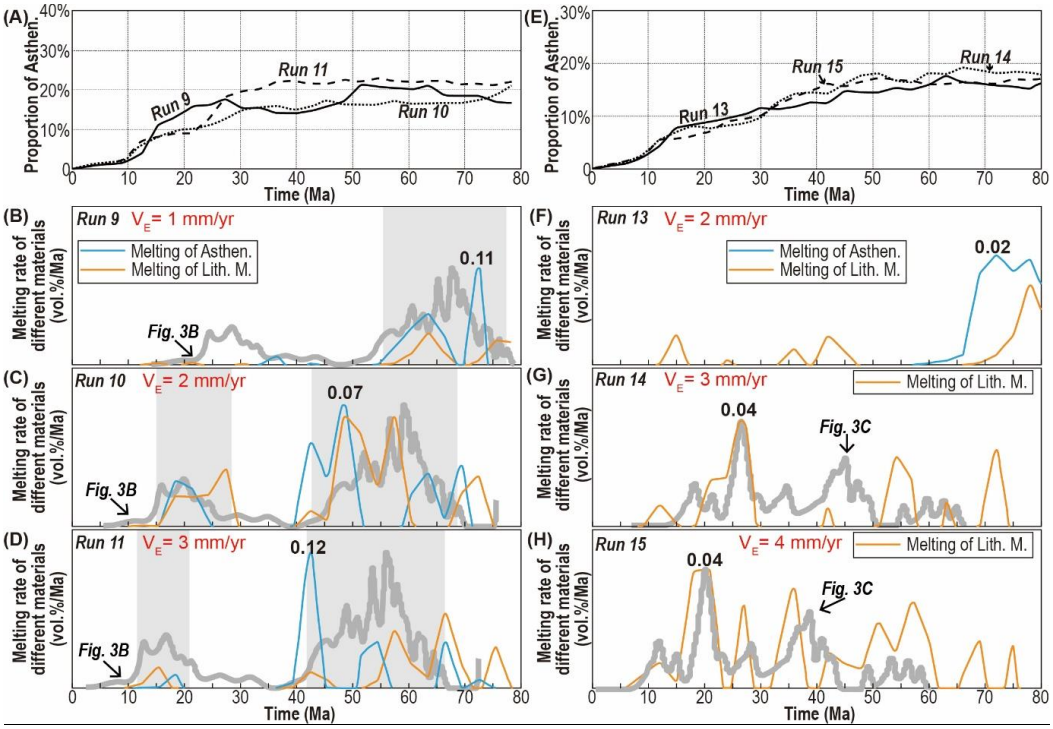

Fig. 9. Results of experimental runs with lithospheric extension.

Panels A-E: Runs 9-11 with 40 km thick crust. (A) Fraction of asthenosphere above 90 km depth. (B-D) Melting rates of different materials (in volume proportion per million years) above 100 km depth. The thick grey line is from Fig. 3B. Labels for lines in Panels B-C are same as those in Panel D. **Panels E-H**: Runs 13-15 with 50 km thick crust. (E) Fraction of asthenosphere above 90 km depth. (F-H) Melting rates of different materials (in volume proportion per million years) above 100 km depth. The thick grey line is from Fig. 3C. The horizontal plotting range is between 250 km and 50 km to the left of the extensional center (or subsidence center of the surface) (Fig. 10). Note that melting in regions away from the locus of extension is largely depressed. *Lith. M.- lithospheric mantle, Asthen. - Asthenosphere. V_E- extension rate.*

The initial crustal thickness does not obviously affect the general pattern of lithospheric replacement. ~50-150 km wide lithosphere is replaced by a

mushroom- shaped upwelling composed of metasome and/or asthenospheric materials.

In regions close to the vertical weak zone, after 80 Ma the newly accreted materials form ~20-40 % of the lithosphere (Fig. 8A and E). Overall melting is dominated by mantle melting (Fig. 8 B-D and 8F-H). Crustal melting in the runs with 50 km thick crust is clearly reduced (Fig.8F-H).

In regions away from the initially pre-existing vertical weak zone, former asthenosphere material only comprises ~20% of the regions shallower than 90 km (Fig. 9A and 9E). Again, melting behavior is depressed compared to the conditions shown in Fig. 6. Reduced melting is due to: 1) that crust is thinned during extension (Fig. 10), with associated enhanced cooling toward the Moho; and 2) the intensive melting (>10 %) during diapiric asthenospheric upwelling (Fig. 10) consumes heat, so the intruded asthenosphere is cooler than temperatures achieved during large-scale convective erosion and reworking (Fig. 7E and 10D).

Extension-induced lithospheric replacement

Run 15 is taken as a type-example for lithospheric modifications during extension.

As the lithosphere extends, asthenosphere and metasome material intrudes upwards utilizing a pre-existing vertical weak zone (Fig. 10B). This mushroom shaped upwelling leads to a locally elevated temperature structure.

Upwelling mantle materials experience ~10-20% melting (Fig. 10B) and they locally heat the lower crust to melting point at ~10 Ma (Fig. 8H).

During subsequent extension, an increase is noted in the width of mantle upwelling and the lateral extent of melting (Fig. 10C-D). After ~30 Ma, the shallow mantle gradually cools and convection ceases (Fig. 10C). Subsequent deeper mantle convection reworks the still ductile lowermost lithosphere and modifies the shape of intruded mantle materials (Fig. 10D). By ~80 Ma, the 1300℃ potential temperature contours have recovered to >80 km depths.

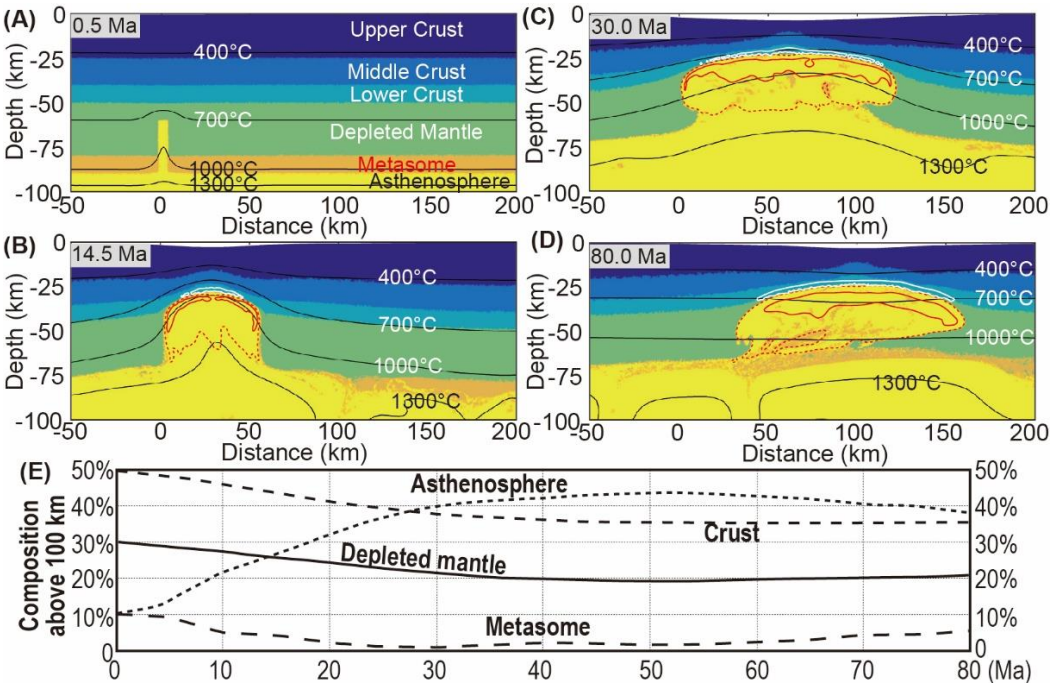

Fig.10. Lithospheric extension along a pre-existing vertical weak zone (Run 15).

(A) Initial conditions of this run (see more details in Fig. 5) (B) During lithospheric extension, asthenosphere and/or metasome material rises along the localized weak zone. These rising materials undergo de-compression melting. (C) The volume of intruded materials grows, while further upwelling of mantle is resisted by the presence of overlying crust. The lower crust is stretched to locally disappear. (D) In the following evolution, the melting center migrates with the locus of extension. The shape of the upwelling structure evolves to a 'mushroom'-like form similar to that observed in seismic records (compare to Fig. 4). (E) Volume fractions of different materials above 100 km depth. Note that pockets of metasome material are entrained into later upwelling where they can experience further decompression melting (also see Panels C-D). *White lines mark the range of crustal melting. Red dashed lines are contours of mantle with depletion >10%. Red solid lines are contours of mantle with depletion >20%.*

5. Discussion

5.1 Convective erosion driven by a Rayleigh-Taylor-type gravity instability

Although most initial asthenospheric upwelling occurs close to the ends of depleted mantle layer in Runs 1-8, the side boundary conditions themselves do not drive interface disturbances. The initial diapirs do not occur exactly along the left/right boundary (the Insect panel in Fig. 7B). Instead, they rise because the overlying material is stretched towards the sinking centers. This is a frequent characteristic of Rayleigh-Taylor type gravity instabilities (cf. [*Conrad et al.*, 1997]). Previous studies illustrate that when a non-linear viscosity is considered for the unstable layer, initial interface disturbances tend to focus at locations close to the edges of the layer [*Canright et al.*, 1993; *Harig et al.*, 2010; *Houseman et al.*, 1997]. Our experiments reproduce this behavior. They show that: 1) the initial downwelling and upwelling are separated due to the focusing of deformation during power-law creep (cf. [*Canright et al.*, 1993]); 2) Late-stage downwelling becomes more focused, while contemporaneous upwelling becomes more diffuse (Fig. 7E). The convective erosion mode seen here resembles a gravitational instability in a power-law creep material with a horizontal stress-free condition.

Unlike previous studies [*Gorczyk et al.*, 2012; *Harig et al.*, 2010] (also see discussion in Paper I), the gravitational instability at the base of relic lithosphere does not lead to large-scale lithospheric downwelling blobs because the post-delamination cratonic mantle initially retains its high strength ($>10^{21}$ Pa·s, Fig. 7) (cf. [*Djomani et al.*, 2001; *Lenardic and Moresi*, 1999; *Sleep*, 2003]). Depleted mantle can only be separated from the base of the lithosphere in relatively small amounts (Fig. 7). During this process >80 % of depleted mantle remains relatively unaffected by convective erosion, with only ~10-20 % mixing with asthenosphere (Fig. 6A and 7F). Because the depleted mantle is assumed to be lack water [*Sleep*, 2003], melting would primarily occur in the water-enriched and less-refractory asthenosphere. This scenario is consistent with the observation that asthenospheric

material is found to dominate the <80 Ma post-destruction basaltic magmas on the ENCC [*Zhang et al., 2008; Zheng et al., 2001*].

5.2. The role in melting of a pre-existing cratonic metasome MLDL

The earliest ca. 190-155 Ma magmas on the ENCC primarily sourced a relatively cool, hydrous, mantle component with a composition consistent with the proposed metasomatic mantle layer (*metasome*) at ~80-100 km depths with a composition like that of exhumed water-rich MARID xenoliths [*Dawson et al., 1977*; *Menzies et al.*, 1993; *Sweeney et al.*, 1993; *Xu*, 2001]. In our preferred scenario (Fig. 2), this geochemically-implied metasomatic layer is proposed to be the critical weak layer that led to lower keel delamination (the topic of Paper I). Only after delamination, could relatively shallow melting on-cratonic magmatism occur. This proposition is supported by studies of seismic images and numerical modelling. See paper I for further details on the potential origin of a metasomatic MLD-linked metasome layer.

5.3. Onset and distribution patterns of on-craton magmas

On-craton magmatism occurred ~20 Ma earlier on the Northern ENCC than on its southern portions (Fig. 3). Between ca. 150-100 Ma (Fig. 11), three magmatic belts can be identified on the ENCC. These three belts appear to have been active for similar time scales, and are separated by a region free of magmatism (Belt IV) in the central ENCC throughout ca. 150-100 Ma (Fig 11). Magmatism of Belts I and III did not migrate across the region, while the magmatic center of Belt I travelled eastwards after ca. 130 Ma (Fig. 11F).

In our preferred scenario, the onset of magmatism on the ENCC (Fig. 3) is controlled by the sequence of the proceeding keel delamination. While geologically rapid, the delamination process itself can occur in jerks, with pulses of rapid delamination ending as a keel fragment breaks away (Fig. 2A and details in Paper I). This implies that the earlier onset of magmatism on the northern

regions (Fig. 3) may indicate earlier keel delamination beneath them.

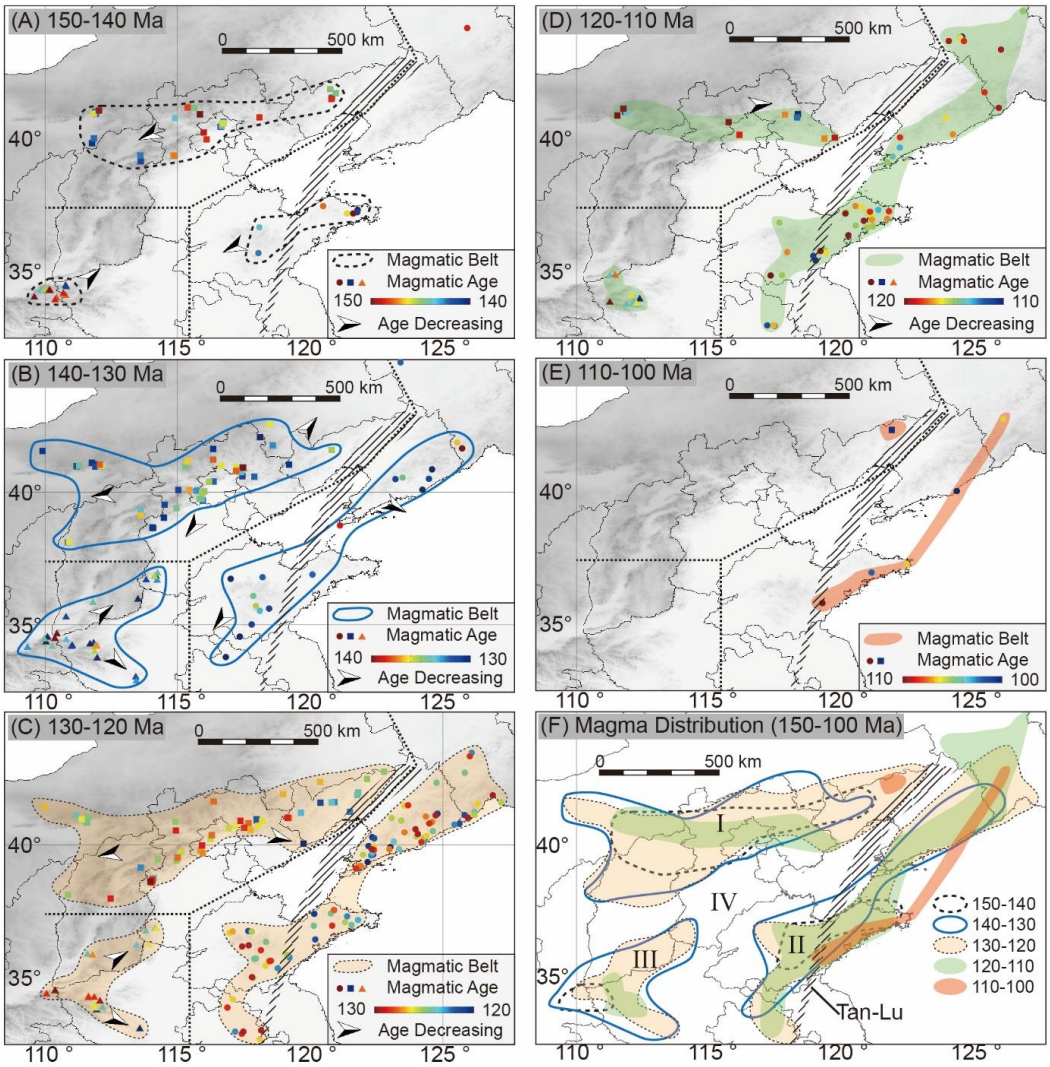

Fig. 11. Distribution of magmas on the ENCC during ca. 150-100 Ma.

Panels A-E: Distribution of magmas in 5 temporal snapshots. **Panel F:** A summary of data from Panels A-E. Three magmatic belts (I, II and III) can be identified (crudely divided by black dots in Panels A-E), their ranges expand after ca. 150 Ma, and peak between ca. 130 and 120 Ma. Belt IV is a magmatism free belt. Note that, after ca. 140 Ma: Belt I and III expanded towards the inner ENCC; Belt II expanded towards the northeast (in regions to the east of the northern Tan-Lu), and towards the southwest (in regions to west of the southern Tan-Lu). This is consistent with local crustal extension directions (Fig. 1B.) The data set of high resolution magmatic dating (534 dates in total) is based upon the work of [Zhang et al., 2014], with 64 recently published ages added to

their published data (Supplement II presents this data in tabular form). *Tan-Lu: the Tancheng-Lujiang Fault zone*.

After the delamination of lower keel, overall heating of the remaining lithosphere may explain the ca. 190-155 Ma magmatism in the northern regions with thick crust and weak lithospheric extension (Fig. 1B, 3A and 6G-I) [*Meng et al*., 2003]. In regions close to the Tan-Lu fault zone, delamination can have happened nearly coevally with the onset of lithospheric extension (ca. 160-150 Ma, [*He and Wang*, 2004; *Meng et al*., 2003]). Therefore, although these regions lacked thick crust, decompression melting during initial metasome/asthenosphere upwelling can have led to late first pulse magmatism at ca. 160-155 Ma (Fig. 3B and 8B-C).

Thereafter, mantle upwelling could lead to the second pulse of magmatism at ca. 135-115 Ma, in extension-free regions capped by thick crust (Fig. 6G-I) or in extensional regions that experienced focused thinning with associated asthenosphere intrusions into relic shallow cratonic lithosphere (Fig. 8B-C). In the former scenario, magmatism would gradually expand from the margins towards the inner craton (Fig. 7), while their distribution could still be concentrated in regions capped by thicker crust (i.e. the Belt I in Fig. 11). In the latter scenario, the area of magmatism grows as the region of focused intra- lithospheric upwelling expands, and the center of magmatism would move with the locus of lithospheric extension (Fig. 10). This latter scenario may help to explain the distribution of the magmatism in regions close to the Tan-Lu fault zone (Belt II in Fig. 11). Later (ca. 160 Ma) delamination with nearly coeval extension of lithosphere capped by thick crust may help to explain the nearly continuous ca. 160-120 Ma magmatism along the southwestern ENCC (Belt III in Fig. 11; also see Fig. 3C and 8G-H).

As noted above, limited melting should occur beneath extension-free regions capped by ~40 km thick crust (Fig. 6C-E). Even in scenarios with lithospheric

extension, melting is mostly absent in regions away from the extensional center (Fig. 9). In both situations, lower rates of mantle upwelling (Fig. 6A, 9 A and 9E) and thin or thinned crust results in a cooler lithospheric geotherm and reduced melting. In this interpretation, the magma-free Belt IV in Fig. 11 formed because this region was initially capped by relatively thin crust (i.e. <40 km), and it lay far from extensional centers, i.e. the Tan-Lu fault zone.

5.4. Implications for the origin of on-cratonic magmas

Initial on-cratonic magmas are primarily felsic in composition as by-products of lower crustal melting [*Wu et al.*, 2005; *Xu et al.*, 2009]. According to the studies of zircon saturation temperature, the Jurassic (ca. 190-155 Ma) granitic magmas (~750 ˚C) in Liaodong are ~50- 100 ˚C cooler than those with Cretaceous ages (ca. 135-115 Ma) [*Wu et al.*, 2007; *Xu et al.*, 2009]. This may indicate different triggers for crustal melting at these two stages, i.e. that fluids derived from subduction zones could have lowered the crustal solidus in Jurassic times [*Wu et al.*, 2007].

As noted above, we propose that the source material for the minor mafic magmas observed in the Jurassic was the preexisting metasomatic [*Menzies et al.*, 1993; *Xu*, 2001] intra-cratonic MLDL. The numerical experiments indicate that melting of this enriched layer can explain the Jurassic magmas. We suggest that 1) the ca. 190-155 Ma magmatism was triggered by underplating of MLDL-derived melts; and 2) the 135-115 Ma magmatism was created by shallower (~60-80 km deep) melting associated with upwelling during reworking of the asthenosphere, residual fragments of MLDL, and relic cratonic lithosphere.

190-155 Ma magmatism: crustal melting triggered by underplating

In the numerical experiments (Fig. 6-10), the first melting pulse is primarily due to deep (>80 km deep) melting of metasome MLDL and/or asthenosphere, in apparent contradiction to observations that most of the ca. 190-155 Ma magmas are primarily felsic in composition, indicating an origin related to crustal melting

[*Wu et al.*, 2005; *Xu et al.*, 2009]. This inconsistency highlights a key over-simplification in our numerical model, namely that it does not simulate the upward migration of melts that could lead to intruded mafic melts at the base of the crust. The accumulation of hot mafic melts at the base of the crust (*cf.* [*Bryan and Ferrari*, 2013]) could trigger minor melting of lower crust (with solidus of ~1050 ˚C, at ~50 km deep, Panel A in Fig. A1), with the crustal melts being recorded as the Jurassic granites.

As in arc magmatism [*Wu et al.*, 2007], the melts of deep low-degree melting of the metasome+ asthenosphere can also be rich in water that lowers the solidus of crust. Therefore, the underplating origin may help to explain the low saturation temperature of zircons in the Jurassic granites [*Wu et al.*, 2007]. Because the metasome MLDL contains higher proportions of volatiles than asthenosphere, its melting products may also more easily overcome the crustal buoyancy filter and be expressed as the observed minor amounts of ca. 190-155 Ma mafic magmas [*Xu*, 2001; *Xu et al.*, 2009].

135-115 Ma magmatism: melting related to upwelling

The numerical experiments imply that the 135-115 Ma magmatism on the ENCC was induced by even shallower upwelling of asthenosphere and residual metasome (Fig. 6- 10).

Due to the low partition coefficients of volatiles (cf. [*Aubaud et al.*, 2004]), most of the volatile content in the original metasoma MLDL and asthenosphere would have been lost during the ca. 190-155 Ma low-degree melting stage. Thus, products of shallower melting during ca. 135-115 Ma should not release as much water to lower the solidus of overlying crust. This is consistent with the Cretaceous granites having a higher zircon temperature than that of the Jurassic granites [*Wu et al.*, 2007].

As asthenosphere rises to <60 km that allowing higher degrees of melting (Fig. 7E and 10C), its contribution in magmatic source may increase (Fig. 6, 8 and9),

consistent with observations on mafic magmas younger than ca. 160 Ma [*Xu*, 2001; *Xu et al.*, 2009]. Note that, during this second pulse of melting, the asthenosphere is still not the only mantle material that melts (Fig. 6, 8 and 9). Metasome material also melts when entrained into later upwellings (Fig. 10E and 12). This may have contributed to the water-rich mantle source of the ~120 Ma basaltic lavas close to the Tan-Lu fault zone [*Xia et al.*, 2013].

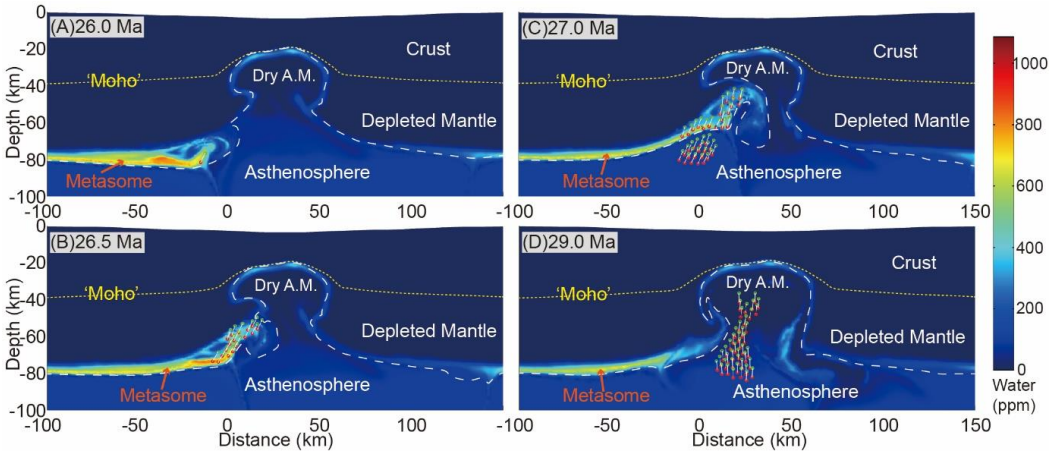

Fig. 12. The metasome MLDL as a potential water-rich source for Cretaceous (ca. 120 Ma) basalts on the ENCC.

Plots are made for the materials' water content (weight proportion in parts per million, ppm) of Run 10 (Table. 2). (A) If cool enough, metasome material can remain locally stable at depths below 80 km deep. (B) Metasome material is entrained into the upwelling asthenosphere, experiences decompression melting and releases water that can enhance melting of adjacent asthenosphere, in particular. (C) Upwelling asthenosphere also starts to melt. (D) Mixture of asthenosphere and metasome material becomes a primary magma source.

In these models, a second-pulse of crustal melting only occurs in the experiments with 50 km thick crust and no lithospheric extension (Fig. 6, 8 and 9). The lower initial Moho temperature in experiments with thinner initial crust does not favor crustal melting.

In scenarios without extension, the slow ascent of asthenosphere during

convective erosion gradually heats up the surrounding lithosphere. The asthenosphere itself cools down, experiences low-degree (~5%) melting, and loses most of its heat through conduction (Fig. 7). When the Moho temperature is hot enough (here, in the scenario with 50 km thick crust), lower crustal melting can occur. The melting material at this stage is composed of lower crust, ancient relic mantle and asthenosphere.

In scenarios with extension, more rapidly rising asthenosphere loses significant heat by large-degree (>10 %) decompression melting. In addition, the thinner crust induced by stretching cools faster, leading to a cooler Moho. Therefore, direct crustal melting does not occur. As noted above, the absence of crustal melting at times of potential underplating of mafic magmas at the Moho is due to limitations in our current numerical method.

5.5. How was the inhomogeneous lithospheric mantle created?

In previous studies, syn-cratonic destruction lithospheric extension and the existing of localized trans-lithospheric weaknesses (e.g. the Tan-Lu fault zone) are suggested to be important in creating the inhomogeneous mantle beneath the modern ENCC [*Hao et al.*, 2013; *Menzies et al*, 2007; *Xu et al.*, 2002; *Yuan et al.*, 1996]. Our results generally support this suggestion.

During lithospheric extension, the trans-lithospheric weak zone can allow ascent of asthenosphere+ metasome material (Fig. 10). Rising material often assumes a crude ‘mushroom-like’ form like those revealed in seismic studies (Fig. 4). The upwelling mantle material is predicted to release ~10-20 % (volume percent) mafic melts, which may lead to melt underplating and re-thickening of the mafic lower crustal layer [*Thybo et al.*, 2009; *Thybo and Artemieva*, 2013]. Compared with intermediate-felsic rocks, underplating mafic melts have a higher P wave velocity [*Christensen and Mooney*, 1995; *Gao et al.*, 1998]. This appears to be consistent with seismic studies [*Hao et al.*, 2013; *Xu et al.*, 2002], as the mushroom anomalies are typically underlain by high velocity anomalies within the

overlying crust (Fig. 4B-C). The results are also consistent with the observations that the lower crustal thickness in extensional regions appears to be noticeably thicker (~10 km) than the thicknesses beneath extension-free inner cratonic areas (<5 km) [*Deng et al.*, 2013; *Gao et al.*, 1998; *Xia et al.*, 2017].

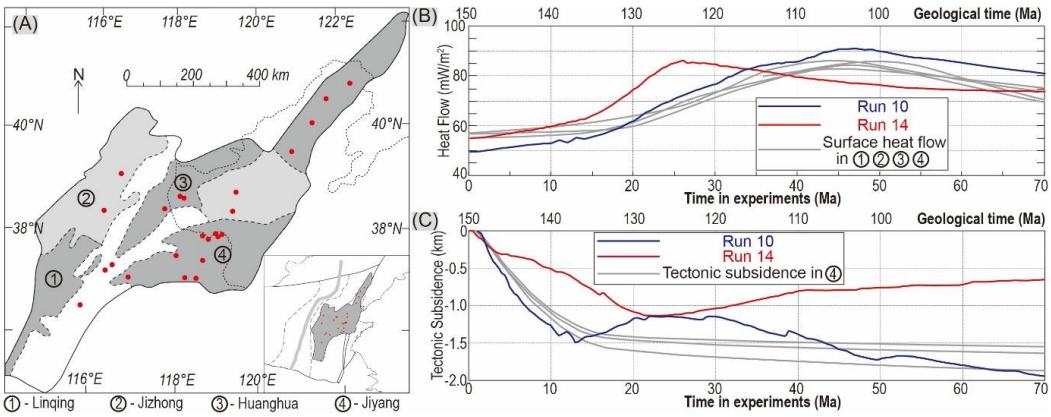

Fig. 13. Comparison between numerical experimental results and the geologic/geophysical record preserved in rift-basins.

(A) Locations for wells (red dots) that provide data for reconstructions of surface heat flow. ①-④ are names for syn-destruction rift-basins. (B) Comparison between numerical experimental results and reconstructions of surface heat flow (gray lines, [*Qiu et al.*, 2016]). (C) Comparison between numerical experimental results and reconstructions of tectonic subsidence (gray lines, [*He and Wang*, 2004]).

The evolution of surface heat flow and tectonic subsidence in the numerical results is also crudely consistent with the geologic record above mushroom-shaped velocity anomalies (Fig. 13). Scenarios with an initial 40 km thick crust appear to better match the crude observations.

Convective erosion in regions without strong lithospheric extension can also help to explain the petrological and geochemical heterogeneity of the ENCC mantle (Fig. 7E and F). According to the modelling results, the local replacement rate is predicated to be ~10-20 % (Fig. 6A, 6F and 7F). Because newly accreted material has experienced ~5-10 % partial melting, its solidus can remain lower

than that of dry, refractory relic cratonic mantle that once experienced > 30% melting ([*Lee et al.*, 2011]). As a consequence, post-destruction magmas can preferentially sample newly emplaced mantle [*Hong et al.*, 2012; *Xu* 2001; *Xu et al*., 2009].

6. Conclusions

In this paper, we explored the second post-keel-delamination stage of a two-stage craton destruction model, examining its implications for the recent evolution of the ENCC. In the proposed model, 1) the lower keel (below ~80-100 km) rapidly delaminates along an intra-cratonic weak layer within 20-10 Ma; and 2) after keel delamination along an 80-100 km deep MLDL, the relic lithosphere and MLDL material come into contact with hotter asthenosphere. The MLDL material heats up and undergoes partial melting, while the relic reworked lithosphere and intruding asthenosphere and MLDL material become more heterogeneous during a post-delamination evolution (80-60 Ma) that is dominated by lithospheric reworking involving convective-erosion and/or lithospheric-extension. Our conclusions are:

(1) The 190-155 Ma 'cold' felsic magmas on the ENCC are suggested to be produced by the crustal underplating of water-rich melts that derived from the melting of a possible mixture of enriched metasome layer +/- asthenosphere at >80 km depths. Subsequent 135-115 Ma magmatism is due to shallower mantle upwelling that develops during progressive convective erosion and lithospheric extension.

(2) The distribution of magmas is strongly shaped by the initial distribution of thicker (i.e. 50 km) crust and of trans-lithospheric weak zones. In regions capped by ~50 km thick crust, e.g. the northern margin of the ENCC, two pulses of magmatism occur during convective erosion of the relic lithosphere. In regions close to trans-lithospheric weaknesses (e.g. the Tan-Lu fault zone), multiple pulses

of magmatism happen during pulses(?) of lithospheric extension. In regions capped by thin/thinned crust (<40 km thick) that does not undergo extension, syn-destruction magmatism is rare.

(3) Lithosphere-scale faults or localized weak zones help to initiate sub-lithospheric mantle upwelling at depth. Their presence can lead to the extension-linked creation of seismic 'mushroom' anomalies found close to the Tan-Lu fault zone.

(4) The petrological and geochemical heterogeneity of the modern ENCC mantle is due to both lithospheric extension and convective erosion, which have led to ~10-30 % ancient cratonic mantle being replaced by asthenosphere + residues to melting of metasome MLDL.

Acknowledgements

This work was supported by the Chinese Academy of Sciences (Grant No. XDB18000000), the State Oceanography Bureau (Grant No. GASI -GEOGE-02) and the National Natural Science Foundation of China (Grant No. 41688103). We thank the Guangzhou Institute of Geochemistry, Chinese Academy of Sciences and Royal Holloway for supporting this Ph.D. work. We thank an anonymous reviewer for suggestions that led to a major restructuring of this paper. We thank Norm Sleep for giving us suggestions on the potential formation mechanism for the metasome/MLDL and for his constructive suggestions on modifying the paper. We thank Dr. Bing Xia and Fan Yang for helping us to modify the paper. We note that there are no data sharing issues since all the numerical information is provided in the figures& movies produced by solving the equations in the appendixes of the companion paper with initial& boundary conditions and parameters given in the paper.

Appendix:

This appendix describes the additional algorithms used here for numerical experiments that were not presented in the appendix of Paper I.

Density

Material density depends on temperature, pressure, depletion, and water dependent [*Djomani et al.*, 2001; *Richard et al.*, 2009; *Schutt et al.*, 2006; *Turcotte et al.*, 2014]:

$$\rho = \left(\left(1 - f + f\frac{\rho_{0molten}}{\rho_{0solid}} - \beta H \right) exp\left[-\int_{T_0}^{T_F} \alpha\left(P = P_0, T\right) dT + \int_{P_0}^{P_F} \frac{dP}{k} \right] \right) \quad \text{(A1)}$$

where the thermal expansion coefficient $\alpha = a_1 + a_2 T + a_3 T^{-2}$, ρ_{0solid} and $\rho_{0molten}$ (2.9g/cm^3 for mantle and 2.7/cm^3 for crust) are solid density and melt density at room temperature (T_0 =20℃) and pressure (P_0=0.1 Mpa), k is bulk modulus, T_F and P_F are temperature and pressure during calculation, f is depletion, H is water content in terms of weight fraction, and β is a coefficient expressing the linear dependency of the density on water content (0.025 wt.% H_2O^{-1}, cf. [*Richard et al.*, 2009])

Effective viscosity

The effective viscosity μ_{eff} is calculated in the form of [*Moresi et al.*, 2003], considering contributions from diffusion and dislocation creep, elasticity and plasticity:

$$\mu_{eff} = S \cdot \left[{\eta_{dis}}^{-1} + {\eta_{dif}}^{-1} + \left(\Delta t G\right)^{-1} + \Gamma_{II}/\Gamma_0 \right]^{-1} \quad \text{(A2)}$$

where η_{dis} is viscosity in dislocation creep, η_{dif} is viscosity in diffusion creep, Δt is time step during calculation, G is shear modulus, Γ_0 is the yielding plastic potential (Equation A3), Γ_{II} is the square root of the second invariant of deviatoric stress, and S is the strain weakening coefficient (see the Appendix of paper I).

$$\Gamma_0 = P\sin(\varphi) + c\cos(\varphi) \quad \text{(A3)}$$

where P is pressure, c is yielding cohesion and φ is friction angle.

Γ_0 in Equation A2 is 0 when $\Gamma_{II} < \Gamma_0$. If yielding occurs $\Gamma_{II} \geq \Gamma_0$, the effective viscosity on the yielding point is calculated by:

$$\mu_{eff} = \Gamma_0 / \Gamma_{II} \qquad \text{(A4)}$$

Mantle and Crustal Melting

We use the method in paper I to determine melting regions. Parameters of crustal melting, e.g. the solidus at room temperature and pressure T_0^m, the solidus's dependence on degree of melting $\left(\partial T^m / \partial f\right)_P$, the solidus's dependence on pressure $\left(\partial T^m / \partial P\right)_f$, are crudely estimated by numerically fitting experimental results for melting of amphibolite (Fig. A1A [*López et al.*, 2001]).

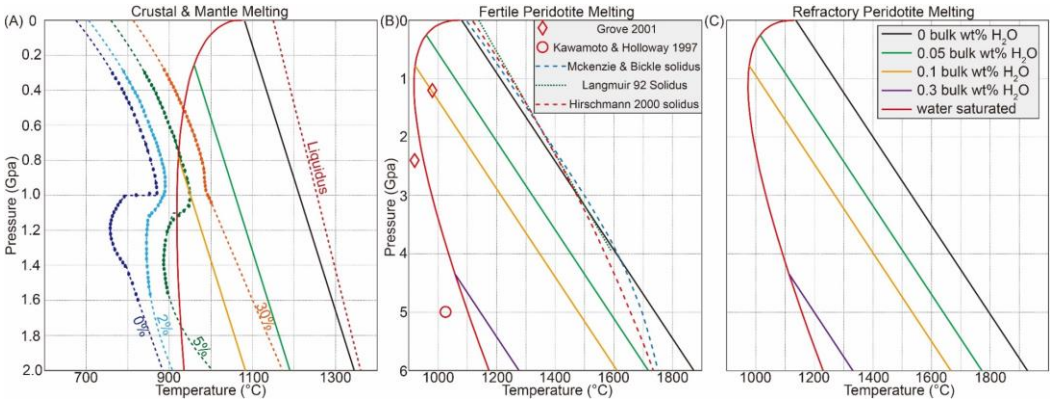

Fig. A1. Solidus in numerical experiments.

(A) Crustal solidus. Dots in panel A are the measured solidus for amphibolite with varying degrees of depletion [*López et al.*, 2001]. 2% means that amphibolite has experienced 2 % melt extraction. Dashed lines are the numerically fitted solidus used in modelling. Solid lines are mantle solidus from Panel B. (B) Asthenospheric/metasome material (fertile mantle) solidus. (C) Lithospheric mantle (depleted mantle) solidus. The effect of dissolved water on the solidus is linear and bounded by the saturation of water in the melt [*Katz et al.*, 2003]. "0.05 bulk wt. %" refers to the water content used for calculating the solidus.

Dehydration process

Potential dehydration of water-rich materials (e.g. asthenosphere and metasome) is only crudely considered following the approach of [*Gerya et al.*, 2011]. A 1wt% water content is set to be the maximum solubility for each material. When melting happens, new water tracers are added to track the evolution of water content. These tracers are advected every time step in a Lagrangian form. Their horizontal velocities are interpolated from the element they belong to, and their vertical velocities are set to be 10cm/yr (Fig. 12). Water in a tracer will be released to the material it encounters if this material's water content is lower than 1wt%. Once all water is removed from a tracer, it is deleted.

References:

Andrés-Martínez, M., J. P. Morgan, M. Pérez-Gussinyé, and L. Rüpke (2015), A new free-surface stabilization algorithm for geodynamical modelling: Theory and numerical tests, *Physics of the Earth and Planetary Interiors*, *246*, 41-51.

Aubaud, C., E. H. Hauri, and M. M. Hirschmann (2004), Hydrogen partition coefficients between nominally anhydrous minerals and basaltic melts, *Geophys Res Lett*, *31*(20), doi:Artn L2061110.1029/2004gl021341

Bird, P. (1979), Continental Delamination and the Colorado Plateau, *J Geophys Res*, *84*(Nb13), 7561-7571.

Brune, S., C. Heine, M. Perez-Gussinye, and S. V. Sobolev (2014), Rift migration explains continental margin asymmetry and crustal hyper-extension, Nature communications, 5, 4014, doi:10.1038/ncomms5014.

Bryan, S. E., and L. Ferrari (2013), Large igneous provinces and silicic large igneous provinces: Progress in our understanding over the last 25 years, *Bulletin of the Geological Society of America*, *125*(7-8), 1053-1078.

Canright, D., and S. Morris (1993), Buoyant Instability of a Viscous Film over a Passive Fluid, *Journal of Fluid Mechanics*, *255*, 349-372, doi: 10.1017/S0022112093002514.

Chen, L., M. M. Jiang, J. H. Yang, Z. G. Wei, C. Z. Liu, and Y. Ling (2014), Presence of an intralithospheric discontinuity in the central and western North China Craton: Implications for destruction of the craton, *Geology*, *42*(3), 223-226, doi:10.1130/G35010.1.

Conrad, C. P., and P. Molnar (1997), The growth of Rayleigh-Taylor-type instabilities in the lithosphere for various rheological and density structures, *Geophysical Journal International*, *129*(1), 95-112, doi: 10.1111/j.1365-246X.1997.tb00939.x.

Christensen, N. I., and W. D. Mooney (1995), Seismic velocity structure and composition of the continental crust: A global view, Journal of Geophysical Research: Solid Earth, 100(B6), 9761-9788, doi:10.1029/95jb00259.

Dawson, and J. V. Smith (1977), The MARID (mica-amphibole-rutile-ilmenite-diopside)

suite of xenoliths in kimberlite, *Geochimica et Cosmochimica Acta*, *41*(2), 309IN9311-9310IN11323.

Deng, Y. F., W. M. Fan, Z. J. Zhang, and J. Badal (2013), Geophysical evidence on segmentation of the Tancheng-Lujiang fault and its implications on the lithosphere evolution in East China, *Journal of Asian Earth Sciences*, *78*, 263-276, doi:10.1016/j.jseaes.2012.11.006.

Djomani, Y. H. P., S. Y. O'Reilly, W. L. Griffin, and P. Morgan (2001), The density structure of subcontinental lithosphere through time, *Earth and Planetary Science Letters*, *184*(3-4), 605-621.

Gao, S., T. C. Luo, B. R. Zhang, H. F. Zhang, Y. W. Han, Z. D. Zhao, and Y. K. Hu (1998), Chemical composition of the continental crust as revealed by studies in East China, *Geochimica Et Cosmochimica Acta*, *62*(11), 1959-1975, doi: 10.1016/S0016-7037(98)00121-5.

Gao, S., R. L. Rudnick, H. L. Yuan, X. M. Liu, Y. S. Liu, W. L. Xu, W. L. Ling, J. Ayers, X. C. Wang, and Q. H. Wang (2004), Recycling lower continental crust in the North China craton, *Nature*, *432*(7019), 892-897, doi:10.1038/nature03162.

Gerya, T. V., J. A. D. Connolly, D. A. Yuen, W. Gorczyk, and A. M. Capel (2006), Seismic implications of mantle wedge plumes, *Physics of the Earth and Planetary Interiors*, *156*(1-2), 59-74, doi:10.1016/j.pepi.2006.02.005.

Gerya, T. V., and F. I. Meilick (2011), Geodynamic regimes of subduction under an active margin: effects of rheological weakening by fluids and melts, *Journal of Metamorphic Geology*, *29*(1), 7-31, doi:10.1111/j.1525-1314.2010.00904.x.

Gerya, T. V., and D. A. Yuen (2003), Rayleigh–Taylor instabilities from hydration and melting propel ‘cold plumes’ at subduction zones, *Earth and Planetary Science Letters*, *212*(1), 47-62.

Gleason, G. C., and J. Tullis (1995), A flow law for dislocation creep of quartz aggregates determined with the molten salt cell, Tectonophysics, 247(1), 1-23.

Gorczyk, W., B. Hobbs, and T. Gerya (2012), Initiation of Rayleigh-Taylor instabilities in

intra-cratonic settings, *Tectonophysics*, *514*, 146-155, doi:10.1016/j.tecto.2011.10.016.

Griffin, W. L., S. Y. O'Reilly, J. C. Afonso, and G. C. Begg (2009), The Composition and Evolution of Lithospheric Mantle: a Re-evaluation and its Tectonic Implications, *Journal of Petrology*, *50*(7), 1185-1204, doi:10.1093/petrology/egn033.

Griffin, W. L., Z. Andi, S. Y. O'Reilly, and C. G. Ryan (1998), Phanerozoic evolution of the lithosphere beneath the Sino-Korean Craton, *Mantle Dynamics and Plate Interactions in East Asia*, *27*, 107-126.

Hao, T. Y., Q. Y. You, L. H. Liu, C. C. Lv, Y. Xu, Z. W. Li, C. L. Zhao, Y. P. Zheng, C. G. Liu, and G. Z. Han (2013), Joint land-sea seismic survey and research on the deep structures of the Bohai Sea areas, *Acta Oceanologica Sinica*, *32*(12), 13-24, doi:10.1007/s13131-013-0383-4.

Harig, C., P. Molnar, and G. A. Houseman (2010), Lithospheric thinning and localization of deformation during Rayleigh-Taylor instability with nonlinear rheology and implications for intracontinental magmatism, *J Geophys Res-Sol Ea*, *115*(B2), doi: 10.1029/2009jb006422.

Hasenclever, J. (2010), Modeling Mantle Flow and Melting Processes at Mid-Ocean Ridges and Subduction Zones — Development and Application of Numerical Models. *Ph.D. Dissertation*, Hamburg University.URL: http://ediss.sub.uni-hamburg.de/volltexte/2010/4873/.

Hasenclever, J., J. P. Morgan, M. Hort, and L. H. Rupke (2011), 2D and 3D numerical models on compositionally buoyant diapirs in the mantle wedge, *Earth and Planetary Science Letters*, *311*(1-2), 53-68, doi:10.1016/j.epsl.2011.08.043.

He, L. J. (2014), Numerical modeling of convective erosion and peridotite-melt interaction in big mantle wedge: Implications for the destruction of the North China Craton, *J Geophys Res-Sol Ea*, *119*(4), 3662-3677, doi:10.1002/2013JB010657.

He, L., and J. Wang (2004), Tectono‐thermal modelling of sedimentary basins with episodic extension and inversion, a case history of the Jiyang Basin, North China, *Basin Res*, *16*(4), 587–599.

Hirschmann, M. M., C. Aubaud, and A. C. Withers (2005), Storage capacity of H 2 O in nominally anhydrous minerals in the upper mantle, *Earth and Planetary Science Letters*, *236*(1), 167-181.

Hirth, G. and Kohlstedt, D., (2004). Rheology of the Upper Mantle and the Mantle Wedge: A View from the Experimentalists, in Inside the Subduction Factory (ed J. Eiler), American Geophysical Union, Washington, D. C., doi: 10.1029/138GM06.

Hong, L.-B., Y.-G. Xu, Z.-Y. Ren, Y.-S. Kuang, Y.-L. Zhang, J. Li, F.-Y. Wang, and H. Zhang (2012), Petrology, geochemistry and Re–Os isotopes of peridotite xenoliths from Yantai, Shandong Province: Evidence for Phanerozoic lithospheric mantle beneath eastern North China Craton, *Lithos*, *155*, 256-271.

Houseman, G. A., and P. Molnar (1997), Gravitational (Rayleigh-Taylor) instability of a layer with non-linear viscosity and convective thinning of continental lithosphere, *Geophysical Journal International*, *128*(1), 125-150, doi: 10.1111/j.1365-246X.1997.tb04075.x.

Jiang, G., X. Tang, S. Rao, P. Gao, L. Zhang, P. Zhao, and S. Hu (2016), High-quality heat flow determination from the crystalline basement of the south-east margin of North China Craton, J Asian Earth Sci, 118, 1-10.

Karato, S. I., T. Olugboji, and J. Park (2015), Mechanisms and geologic significance of the mid-lithosphere discontinuity in the continents, *Nature Geoscience*, *8*(7), 509-514, doi:10.1038/NGEO2462.

Katz, R. F., M. Spiegelman, and C. H. Langmuir (2003), A new parameterization of hydrous mantle melting, Geochem Geophy Geosy, 4(9), doi: 10.1029/2002gc000433.

Kay, R. W., and S. M. Kay (1993), Delamination and Delamination Magmatism, *Tectonophysics*, *219*(1-3), 177-189, doi: 10.1016/0040-1951(93)90295-U.

Kinck, J. J., E. S. Husebye, and F. R. Larsson (1993), The Moho depth distribution in Fennoscandia and the regional tectonic evolution from Archean to Permian times, *Precambrian Research*, 64(1-4), 23-51.

Korenaga, J., and S. I. Karato (2008), A new analysis of experimental data on olivine

rheology, Journal of Geophysical Research: Solid Earth, 113(B2), doi: 10.1029/2007JB005100.

Lenardic, A., and L.- N. Moresi (1999), Some thoughts on the stability of cratonic lithosphere: Effects of buoyancy and viscosity, *Journal of Geophysical Research: Solid Earth*, 104(B6), 12747-12758.

Lee, C.-T. A., P. Luffi, and E. J. Chin (2011), Building and destroying continental mantle, *Annual Review of Earth and Planetary Sciences*, *39*, 59-90.

Liao, J., and T. Gerya (2014), Influence of lithospheric mantle stratification on craton extension: Insight from two-dimensional thermo-mechanical modeling, *Tectonophysics*, *631*, 50-64, doi:10.1016/j.tecto.2014.01.020.

Liao, J., Q. Wang, T. Gerya, and M. D. Ballmer (2017), Modeling Craton Destruction by Hydration‐Induced Weakening of the Upper Mantle, *Journal of Geophysical Research: Solid Earth*, *122*(9), 7449-7466.

Lin, G., Y. Zhang, F. Guo, Y. J. Wang, and W. M. Fan (2005), Numerical modelling of lithosphere evolution in the North China Block: Thermal versus tectonic thinning, *Journal of Geodynamics*, *40*(1), 92-103, doi:10.1016/j.jog.2005.07.011.

Liu. L, J. Morgan, Y. Xu, and M. Menzies (2016), Numerical Modelling of the Destruction of the Eastern North China Craton, paper presented at AGU Fall Meeting Abstracts, abstract #T11B-2624.

López, S., and A. Castro (2001), Determination of the fluid–absent solidus and supersolidus phase relationships of MORB-derived amphibolites in the range 4–14 kbar, American Mineralogist, 86(11-12), 1396-1403.

Meng, Q.-R. (2003), What drove late Mesozoic extension of the northern China–Mongolia tract?, *Tectonophysics*, *369*(3), 155-174.

Menzies, W. Fan, and M. Zhang (1993), Palaeozoic and Cenozoic lithoprobes and the loss of> 120 km of Archaean lithosphere, Sino-Korean craton, China, *Geological Society, London, Special Publications*, *76*(1), 71-81.

Menzies, M., Y. G. Xu, H. F. Zhang, and W. M. Fan (2007), Integration of geology,

geophysics and geochemistry: A key to understanding the North China Craton, *Lithos*, *96*(1-2), 1-21, doi:10.1016/j.lithos.2006.09.008.

Moresi, L., F. Dufour, and H. B. Muhlhaus (2003), A Lagrangian integration point finite element method for large deformation modeling of viscoelastic geomaterials, *Journal of Computational Physics*, *184*(2), 476-497, doi: 10.1016/S0021-9991(02)00031-1.

Morgan, J. P. (2001), Thermodynamics of pressure release melting of a veined plum pudding mantle, *Geochem Geophy Geosy*, *2*(4), doi: 10.1029/2000GC000049.

Niu, Y. (2005), Generation and evolution of basaltic magmas: some basic concepts and a new view on the origin of Mesozoic–Cenozoic basaltic volcanism in eastern China, *Geological Journal of China Universities*, *11*(1), 9-46.

Pollitz, F. F., C. Wicks, and W. Thatcher (2001), Mantle flow beneath a continental strike-slip fault: postseismic deformation after the 1999 Hector Mine earthquake, *Science*, *293*(5536), 1814-1818, doi:10.1126/science.1061361.

Qiu, N. S., Y. H. Zuo, W. Xu, W. Z. Li, J. Chang, and C. Q. Zhu (2016), Meso-Cenozoic Lithosphere Thinning in the Eastern North China Craton: Evidence from Thermal History of the Bohai Bay Basin, North China, *J Geol*, *124*(2), 195-219, doi:10.1086/684830.

Rapp, R. P., and E. B. Watson (1995), Dehydration melting of metabasalt at 8–32 kbar: implications for continental growth and crust-mantle recycling, *Journal of Petrology*, *36*(4), 891-931.

Richard, G. C., and D. Bercovici (2009), Water-induced convection in the Earth's mantle transition zone, *J Geophys Res-Sol Ea*, *114*(B1), doi:10.1029/2008jb005734.

Rutter, E., and K. Brodie (2004), Experimental grain size-sensitive flow of hot-pressed Brazilian quartz aggregates, Journal of Structural Geology, 26(11), 2011-2023.

Rybacki, E., and G. Dresen (2004), Deformation mechanism maps for feldspar rocks, Tectonophysics, 382(3), 173-187.

Schutt, D. L., and C. E. Lesher (2006), Effects of melt depletion on the density and seismic velocity of garnet and spinel lherzolite, *J Geophys Res-Sol Ea*, *111*(B5), doi:

10.1029/2003jb002950.

Selway, K., H. Ford, and P. Kelemen (2015), The seismic mid-lithosphere discontinuity, *Earth and Planetary Science Letters*, *414*, 45-57, doi:10.1016/j.epsl.2014.12.029.

Sleep, N. H. (2003), Survival of Archean cratonal lithosphere, *J Geophys Res-Sol Ea*, *108*(B6), doi: 10.1029/2001jb000169.

Sweeney, R., A. Thompson, and P. Ulmer (1993), Phase relations of a natural MARID composition and implications for MARID genesis, lithospheric melting and mantle metasomatism, *Contrib Mineral Petr*, *115*(2), 225-241.

Thybo, H., and I. M. Artemieva (2013), Moho and magmatic underplating in continental lithosphere, *Tectonophysics*, *609*(1), 605-619.

Thybo, H., and C. A. Nielsen (2009), Magma-compensated crustal thinning in continental rift zones, *Nature*, *457*(7231), 873-876, doi:10.1038/nature07688.

Turcotte, D. L., and G. Schubert (2014), *Geodynamics*, Cambridge University Press, 623 pp.

Wang, Z. S., T. M. Kusky, and F. A. Capitanio (2016), Lithosphere thinning induced by slab penetration into a hydrous mantle transition zone, *Geophysical Research Letters*, *43*(22), 11567-11577, doi:10.1002/2016GL071186.

Wenker, S., and C. Beaumont (2017), Can metasomatic weakening result in the rifting of cratons?, *Tectonophysics*, 0040-1951, doi: 10.1016/j.tecto.2017.06.013.

Wilks, K. R., and N. L. Carter (1990), Rheology of some continental lower crustal rocks, Tectonophysics, 182(1), 57-77.

Wu, F.Y., X. H. Li, J. H. Yang, Y. F. Zheng (2007), Discussions on the petrogenesis of granites (*in Chinese*), *ACTA PETROLOGICA SINICA*, 10.3969/j.issn.1000-0569.2007.06.001.

Wu, F. Y., J. H. Yang, S. A. Wilde, and X. O. Zhang (2005), Geochronology, petrogenesis and tectonic implications of Jurassic granites in the Liaodong Peninsula, NE China, *Chem Geol*, *221*(1-2), 127-156, doi:10.1016/j.chemgeo.2005.04.010.

Xia, B., H. Thybo, and I. M. Artemieva (2017), Seismic crustal structure of the North

China Craton and surrounding area: Synthesis and analysis, *J Geophys Res-Sol Ea*, *122*(7), 5181-5207, doi:10.1002/2016JB013848.

Xia, Q. K., J. Liu, S. C. Liu, I. Kovacs, M. Feng, and L. Dang (2013), High water content in Mesozoic primitive basalts of the North China Craton and implications on the destruction of cratonic mantle lithosphere, *Earth and Planetary Science Letters*, *361*, 85-97, doi:10.1016/j.epsl.2012.11.024.

Xu, P. F., F. T. Liu, K. Ye, Q. C. Wang, B. L. Cong, and H. Chen (2002), Flake tectonics in the Sulu orogen in eastern China as revealed by seismic tomography, *Geophysical Research Letters*, *29*(10), doi: 10.1029/2001gl014185.

Xu, Y. G. (2001), Thermo-tectonic destruction of the archaean lithospheric keel beneath the Sino-Korean Craton in China: Evidence, timing and mechanism, *Phys Chem Earth Pt A*, *26*(9-10), 747-757, doi: 10.1016/S1464-1895(01)00124-7.

Xu, Y. G., H. Y. Li, C. J. Pang, and B. He (2009), On the timing and duration of the destruction of the North China Craton, *Chinese Science Bulletin*, *54*(19), 3379-3396, doi:10.1007/s11434-009-0346-5.

Yang, J., L. Zhao, B. J. Kaus, G. Lu, K. Wang, and R. Zhu (2017), Slab-triggered wet upwellings produce large volumes of melt: Insights into the destruction of the North China Craton, *Tectonophysics*, doi: 10.1016/j.tecto.2017.04.009.

Youssof, M., H. Thybo, I. M. Artemieva, and A. Levander (2013), Moho depth and crustal composition in Southern Africa, *Tectonophysics*, 609, 267-287.

Yuan (1996), Velocity structure of the Qinling lithosphere and mushroom cloud model. Science in China (Series D), 39 (1996), pp. 233-244.

Zhai, M.- G. and M. Santosh (2011), The early Precambrian odyssey of the North China Craton: a synoptic overview, *Gondwana Research*, 20(1), 6-25.

Zhang, H. F., S. L. Goldstein, X. H. Zhou, M. Sun, J. P. Zheng, and Y. Cai (2008), Evolution of subcontinental lithospheric mantle beneath eastern China: Re-Os isotopic evidence from mantle xenoliths in Paleozoic kimberlites and Mesozoic basalts, *Contributions to Mineralogy and Petrology*, *155*(3), 271-293, doi:10.1007/s00410-007-

0241-5.

Zhang, S. H., Y. Zhao, G. A. Davis, H. Ye, and F. Wu (2014), Temporal and spatial variations of Mesozoic magmatism and deformation in the North China Craton: Implications for lithospheric thinning and decratonization, *Earth-Science Reviews*, *131*, 49-87, doi:10.1016/j.earscirev.2013.12.004.

Zheng, J. P., S. Y. O'Reilly, W. L. Griffin, F. X. Lu, M. Zhang, and N. J. Pearson (2001), Relict refractory mantle beneath the eastern North China block: significance for lithosphere evolution, *Lithos*, *57*(1), 43-66, doi: 10.1016/S0024-4937(00)00073-6.

Zhu, Y. Xu, G. Zhu, H. Zhang, Q. Xia, and T. Zheng (2012a), Destruction of the north China Craton, *Science China Earth Sciences*, *55*(10), 1565-1587.

Zhu, G., D. Z. Jiang, B. L. Zhang, and Y. Chen (2012b), Destruction of the eastern North China Craton in a backarc setting: Evidence from crustal deformation kinematics, *Gondwana Research*, *22*(1), 86-103, doi:10.1016/j.gr.2011.08.005.

Zhu, G., M. L. Niu, C. L. Xie, and Y. S. Wang (2010), Sinistral to Normal Faulting along the Tan-Lu Fault Zone: Evidence for Geodynamic Switching of the East China Continental Margin, *J Geol*, *118*(3), 277-293, doi:10.1086/651540.

Supporting Information

Journal of Geophysical Research Solid Earth

Supporting Information for

Craton Destruction Part II: Evolution of Cratonic Lithosphere after a Rapid Keel Delamination Event

Liang Liu[1, 2, 3], Jason P. Morgan[1,4], Yigang Xu[2], Martin Menzies[1, 2]

[1] *Department of Earth Sciences, Royal Holloway University of London, Egham, TW20 0EX, United Kingdom.*

[2] *State Key Laboratory of Isotope Geochemistry, Guangzhou Institute of Geochemistry, Chinese Academy of Sciences, Guangzhou 510640, China.*

[3] *College of Earth Sciences, University of Chinese Academy of Sciences, Beijing, 100049, China.*

[4] *Department of Earth & Planetary Sciences, Harvard University, Cambridge, MA, USA.*

Contents of this file

Additional Supporting Information (Files uploaded separately)

Introduction

This supporting information provides a general overview of:

- Summary of results for runs not being presented in the main text.

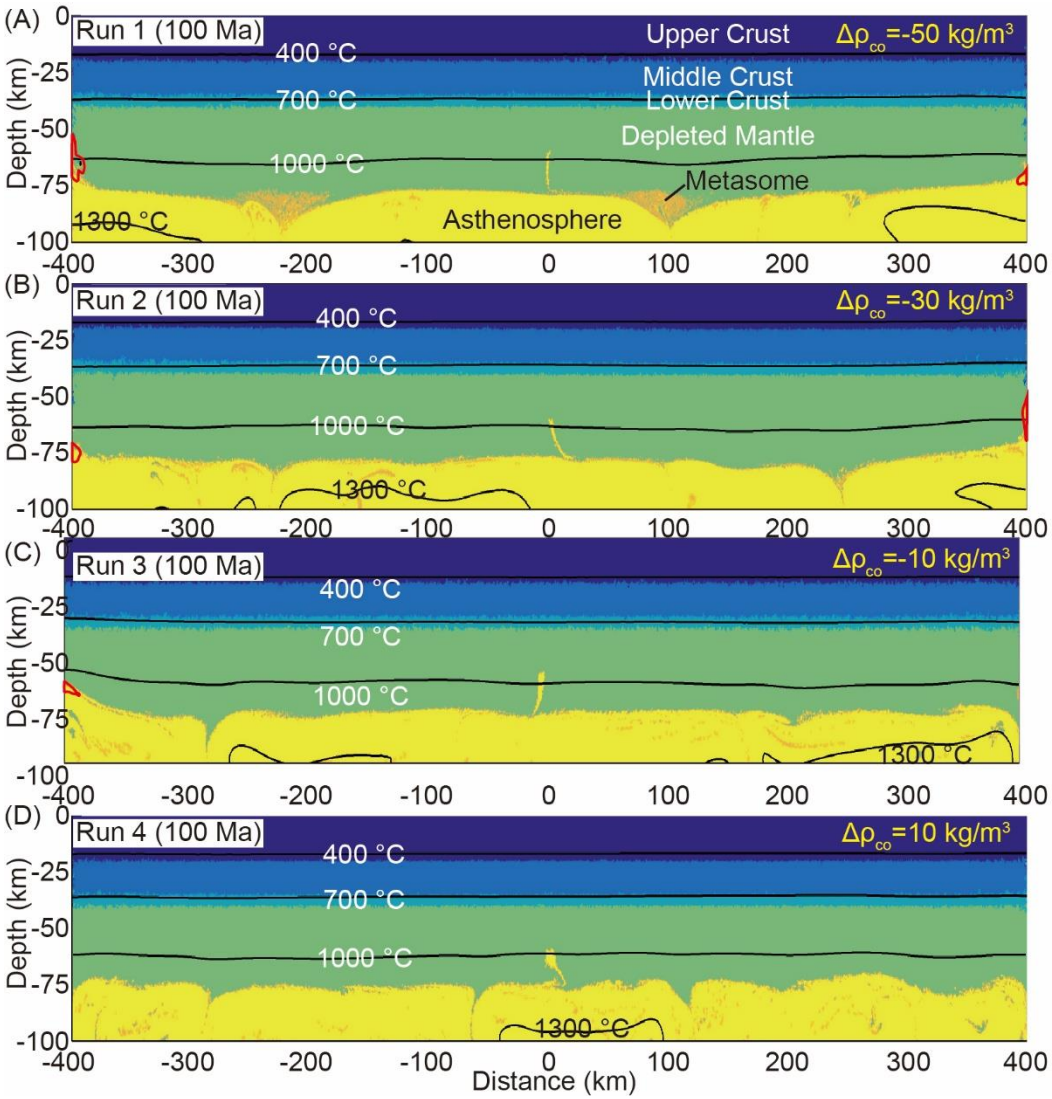

Figure S1. Results of convective erosion modelling (40 km-crust scenarios, Runs 1-4) at 100 Ma.

The metasome can still remain when asthenosphere has a higher compositional density. Note that, because the metasome material is assumed to have a weak rheology (see Tab. 1), it can mix with asthenosphere easily during small-scale convection. Red lines mark the contours of mantle melting (with depletion >0.05). Δρco- the compositional density difference between lithospheric mantle and asthenosphere.

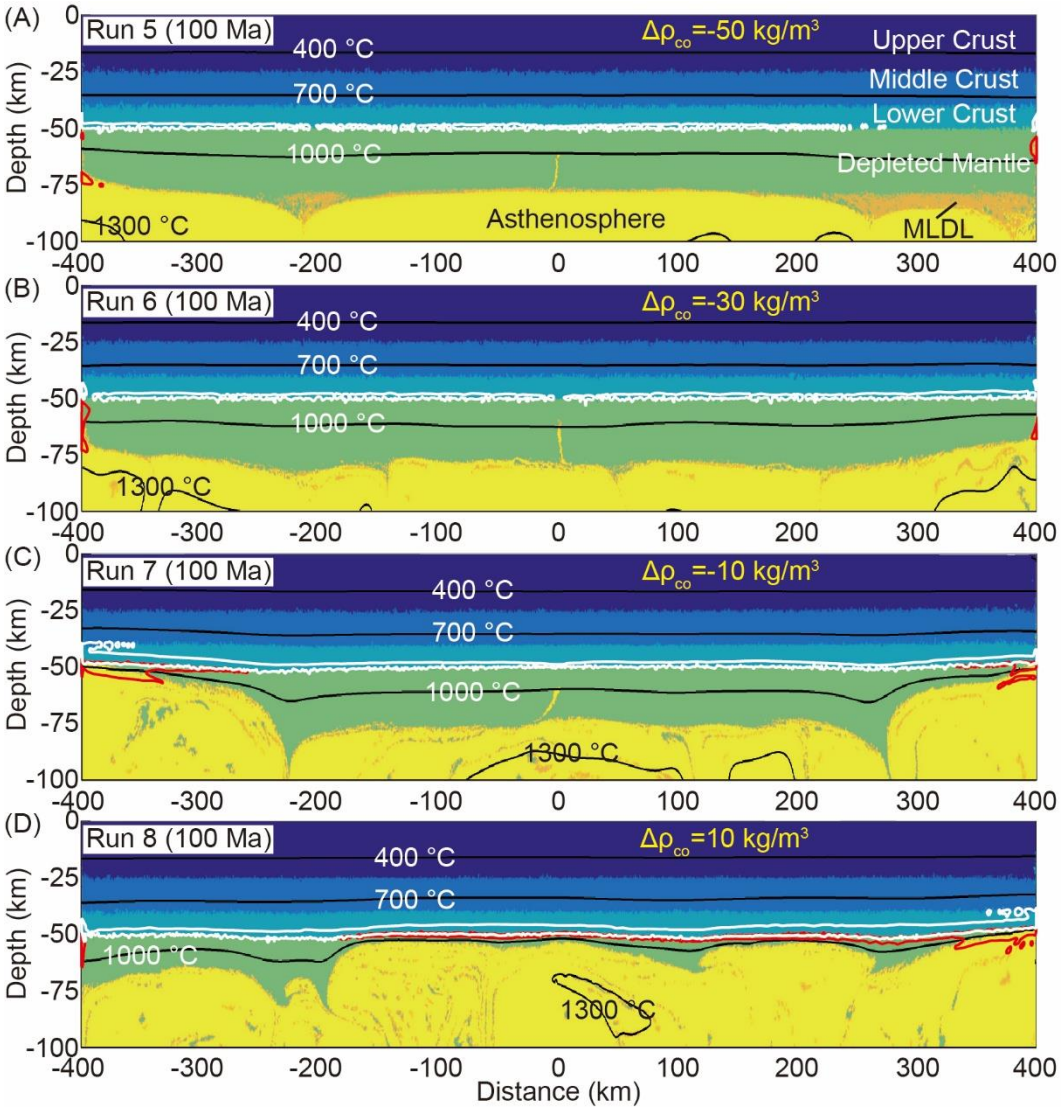

Figure S2. Results of convective erosion modelling (50 km-crust scenarios, Runs 5-8) at 100 Ma.

White lines mark the contours of crustal melting. Other plotting rules are same to Fig. S1.

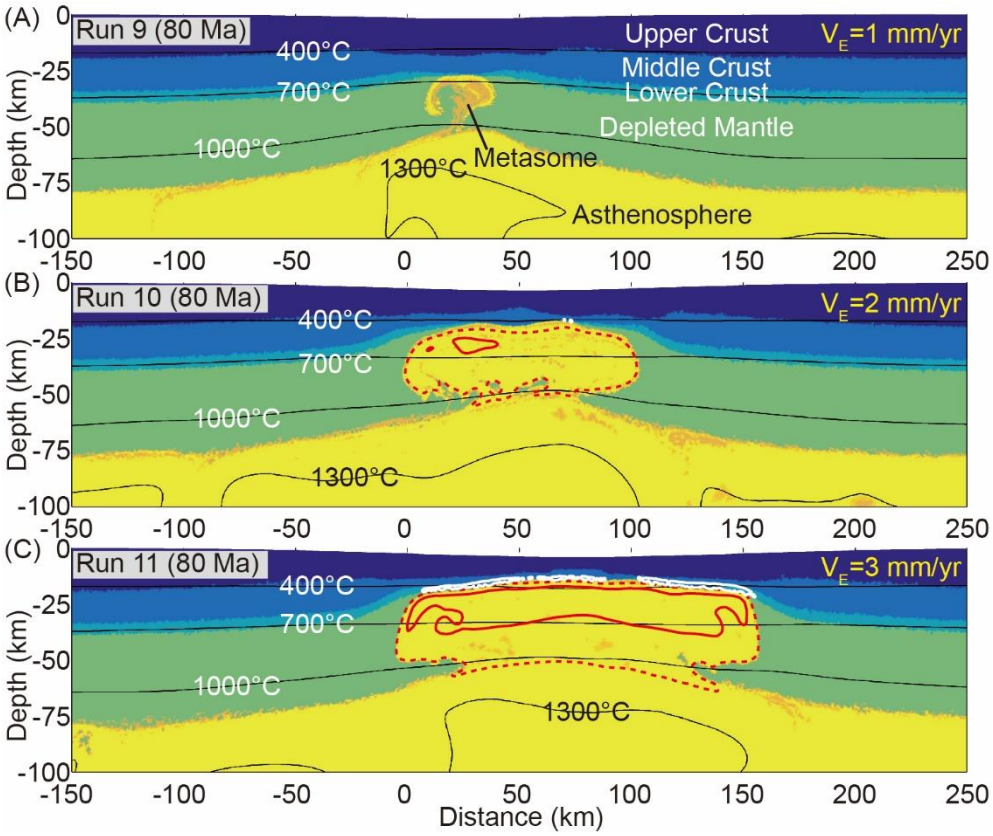

Figure S3. Results of extensional modelling (40 km-crust scenario, Runs 9-11) at 80 Ma.

(A) Small portions of metasome material infiltrate the lithosphere without notable melting. (B) ~100 km wide lithosphere is replaced by upwelling asthenosphere. This process creates ~200 km wide surface subsidence and crustal thinning (to ~25 km thick). Melting is apparent in the asthenosphere and/or the metasome. (C) Asthenosphere can rise to ~15 km and lithosphere is replaced by asthenosphere over a zone >150 km wide. Melting occurs at ~10 Ma after extension starts, and peaks at ~30 Ma later.

White lines mark the range of crustal melting. Red dashed lines are contours of mantle melting with depletion >0.1. Red solid lines are contours of mantle melting with depletion >0.2 (These two values can only be arrived during the rapid asthenosphere upwelling driven by extension). Meaning for the metasome melting records are same to those in Fig. S1. VE- extension speed.

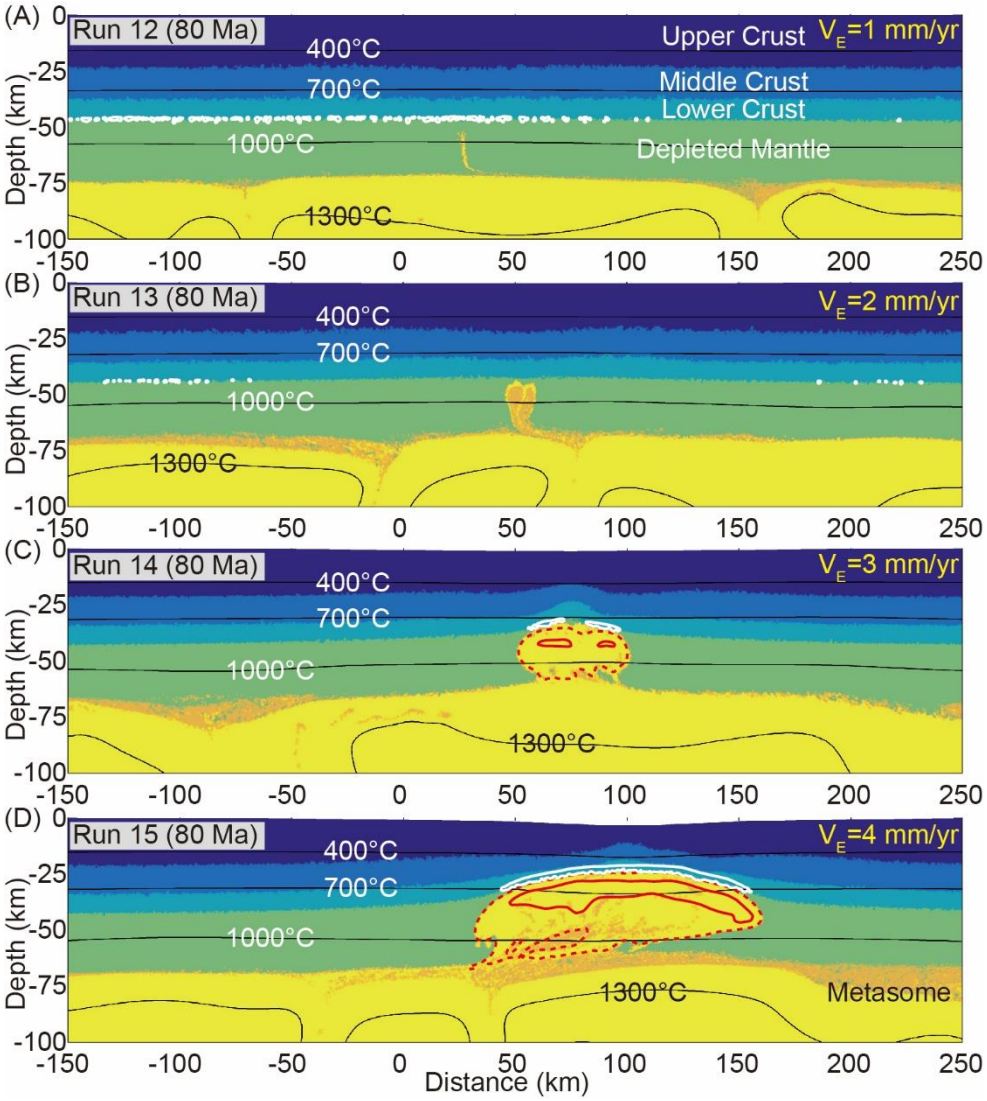

Figure S4. Result of extension modelling (50 km-crust scenarios) at 80 Ma.

(A-B) lithosphere is homogeneously thinned and lower crustal melting occurs at ~60-70 Ma. (C) ~50 km wide lithosphere is replaced by asthenosphere. (D) ~100 km wide lithosphere is replaced by asthenosphere. In Panels (C-D), there is a lack of mantle or crust melting during the first 10-20 Ma. The melting peak appears at ~20-30 Ma after melting begins. Contours are same to those in Fig. S3. VE- extension speed.

Data Set S1. Summary of the zircon U-Pb and ^{40}Ar-^{39}Ar dating results for the Cretaceous on-ENCC magmatism.

This data set is built based on the work of [Zhang et al., 2014], with 64 recently published ages also added.

Movie SV1. Records of Run 4 (see Tab. 2). Material Phase: see captions on the first frame of this video.

Movie SV2. Records of Run 8 (see Tab. 2). Material Phase: see captions on the first frame of this video.

Movie SV3. Records of Run 12 (see Tab. 2). Material Phase: see captions on the first frame of this video.

Movie SV4. Records of Run 15 (see Tab. 2). Material Phase: see captions on the first frame of this video.

Movie SV5. Temperature evolution of Run 4. White lines with an arrow mark the directions and speed of local flow. The maximum speed is 10-8.5 m/s. While contours are temperature contours (top-down): 400 ˚C, 700 ˚C, 1000 ˚C and 1300 ˚C.

Movie SV6. Temperature evolution of Run 8. Plot conventions are same to SV5.

Movie SV7. Temperature evolution of Run 12. Plot conventions are same to SV5.

Movie SV8. Temperature evolution of Run 15. Plot conventions are same to SV5.

Movie SV9. Temperature evolution of the delamination experiment. White lines with an arrow mark the directions and speed of local flow. The maximum speed is 10-8 m/s. While contours are temperature contours (top-down): 400 ˚C, 700 ˚C, 1000 ˚C and 1300 ˚C.

Rock Type	Age (Ma)	Method	Ref.
granodiorite	148±1	LA-ICP-MS	[*Guo et al.*, 2012]
monzogranite	142±1	SHRIMP	[*Guo et al.*, 2012]
granodiorite	142±1	LA-ICP-MS	[*Guo et al.*, 2012]
granite	140±4	SIMS	[*Meng et al.*, 2014]
granite	145±1	SIMS	[*Meng et al.*, 2014]
granite	142±2	SIMS	[*Meng et al.*, 2014]
andesite	147.6±1.6	^{40}Ar-^{39}Ar	[*Davis et al.*, 2001]
granitoid pluton	141±2	TIMS	[*Davis et al.*, 2001]
granitoid pluton	142±2	TIMS	[*Davis et al.*, 2001]
granitoid pluton	143±3	TIMS	[*Davis et al.*, 2001]
granitoid pluton	143±3	TIMS	[*Davis et al.*, 2001]
high-Mg adakite	144±9	SHRIMP	[*Gao et al.*, 2004]
granite	144.7±2.7	SHRIMP	[*Deng et al.*, 2004]
granite	144±2	SHRIMP	[*Liu et al.*, 2010b]
biotite quartz monzonite	146.2±1.4	TIMS	[*Mao et al.*, 2003]
granodioritic porphyry	146.2±3.9	TIMS	[*Mao et al.*, 2003]
quartz monzonite	147.6±1.6	TIMS	[*Mao et al.*, 2003]
lava-tuff	147±2	LA-ICP-MS	[*Zhang et al.*, 2009b]
tuff	142±1	LA-ICP-MS	[*Zhang et al.*, 2009b]
andesite	147±2	LA-ICP-MS	[*Zhang et al.*, 2009b]
dacite	143±4	LA-ICP-MS	[*Zhang et al.*, 2008c]
granite	145.6±1.6	TIMS	[*Wang and Li*, 2008]
granite	142.5±1.8	TIMS	[*Wang and Li*, 2008]
dioritic porphyry	143±2	LA-ICP-MS	[*Gao et al.*, 2013]
dioritic porphyry	142±2	LA-ICP-MS	[*Gao et al.*, 2011]
andesite	141±1	LA-ICP-MS	[*Gao et al.*, 2011]
andesite	148.3±3.0	^{40}Ar-^{39}Ar	[*Li et al.*, 2001]
dioritic porphyry	147±2	LA-ICP-MS	[*Yang et al.*, 2006c]
mafic dyke	144±2	SHRIMP	[*Liu et al.*, 2008]
mafic dyke	143±2	SHRIMP	[*Liu et al.*, 2008]
granite	149±5	LA-ICP-MS	[*Zhang et al.*, 2010]
granite	141±3	LA-ICP-MS	[*Zhang et al.*, 2010]
granite	146±4	LA-ICP-MS	[*Zhang et al.*, 2010]
granite	147±3	LA-ICP-MS	[*Zhang et al.*, 2010]
garnet-bearing granite	142±3	SHRIMP	[*Guo et al.*, 2005]
monzogranite	142±3	SHRIMP	[*Mao et al.*, 2005]
porphyritic granite	145±4	LA-ICP-MS	[*Jiao et al.*, 2010]
porphyritic granite	144±3	LA-ICP-MS	[*Jiao et al.*, 2010]
diorite	148±2	LA-ICP-MS	[*Zhang et al.*, 2008b]
k-feldspar granitic porphyry	148±1	LA-ICP-MS	[*Hu et al.*, 2011]

quartz diorite	149±1	LA-ICP-MS	[*Hu et al.*, 2011]
quartz diorite	149±1	LA-ICP-MS	[*Hu et al.*, 2011]
quartz diorite	150±1	LA-ICP-MS	[*Hu et al.*, 2011]
quartz monzonite	149±1	LA-ICP-MS	[*Hu et al.*, 2011]
monzogranite	146±1	LA-ICP-MS	[*Zhu et al.*, 2008]
granitic porphyry	141±1	LA-ICP-MS	[*Zhu et al.*, 2008]
granite	142±3	SHRIMP	[*Wang et al.*, 2010a]
monzogranitic porphyry	148±2	SHRIMP	[*Li et al.*, 2013b]
syenogranitic porphyry	148±2	SHRIMP	[*Li et al.*, 2013b]
granodioritic porphyry	142±2	SHRIMP	[*Li et al.*, 2013b]
monzogranite	150±1	LA-ICP-MS	[*Wang et al.*, 2011b]
porphyritic monzogranite	149±2	SHRIMP	[*Wang et al.*, 2011b]
volcanic rock	147.8±0.3	^{40}Ar-^{39}Ar	[*Wang et al.*, 2002]
andesite	145.6	LA-ICP-MS	[*Gao et al.*, 2012]
Diorite porphyry	144.1±1.2	LA–ICP–MS	[*Dong et al.*, 2013]
Diorite porphyry	146.2±1.8	LA–ICP–MS	[*Dong et al.*, 2013]
biotite monzogranite	142±3	SHRIMP	[*Mao et al.*, 2010]
Granite	141±1	SHRIMP	[*Shi et al.*, 2009]
Biotite Granite	143±3	SHRIMP	[*Shi et al.*, 2009]
Granite	145±2	SHRIMP	[*Shi et al.*, 2009]
Granite	144±2	SHRIMP	[*Shi et al.*, 2009]
Granite porphyry	142.1±2.0	LA-ICP-MS	[*Zhang et al.*, 2015]
Granite porphyry	141.0±1.6	LA-ICP-MS	[*Zhang et al.*, 2015]
K-feldspar Granite	140.4±1.4	LA-ICP-MS	[*Wang et al.*, 2013b]
rhyolitic tuff	131±2	LA-ICP-MS	[*Zhang et al.*, 2014]
granite	131±1	SIMS	[*He*, 2010]
monzogranite	140±1	LA-ICP-MS	[*Guo et al.*, 2012]
monzogranite	138±1	LA-ICP-MS	[*Guo et al.*, 2012]
monzogranite	136±4	TIMS	[*Davis and Darby*, 2010]
basalt	135.5±1.3	^{40}Ar-^{39}Ar	[*Davis and Darby*, 2010]
basalt	132.6±2.4	^{40}Ar-^{39}Ar	[*Davis and Darby*, 2010]
granite	131±1	SIMS	[*Meng et al.*, 2014]
granite	132±2	LA-ICP-MS	[*Guo et al.*, 2012]
quartz syenite porphyry	138±2	LA-ICP-MS	[*Zhang et al.*, 2014]
quartz diorite	133±1	LA-ICP-MS	[*Zhang et al.*, 2014]
granodiorite	138±1	LA-ICP-MS	[*Zhang et al.*, 2014]
monzogranite	137±1	LA-ICP-MS	[*Jiao et al.*, 2013]
porphyritic granite	133±1	LA-ICP-MS	[*Jiao et al.*, 2013]
granitoid pluton	131.7±1.5	TIMS	[*Davis et al.*, 2001]
granitoid pluton	130.0±1.5	TIMS	[*Davis et al.*, 2001]
rhyolitic welded tuff	130.8±0.5	^{40}Ar-^{39}Ar	[*Cope*, 2003]

amygdaoidal andesite	134±1	SHRIMP	[*Niu et al.*, 2004]
rhyolite	135±2	SHRIMP	[*Liu et al.*, 2003]
rhyolite	135.3±1.4	^{40}Ar-^{39}Ar	[*Ji et al.*, 2004]
tuff	130.7±0.4	^{40}Ar-^{39}Ar	[*He et al.*, 2006a]
granite	138±2	SHRIMP	[*Liu et al.*, 2010b]
K-feldspar granite	138.5±1.3	TIMS	[*Mao et al.*, 2003]
quartz monzonite	138.5±1.2	TIMS	[*Mao et al.*, 2003]
tuff	137±7	LA-ICP-MS	[*Zhang et al.*, 2009b]
dacite	139±3	LA-ICP-MS	[*Zhang et al.*, 2008c]
dacite	139±3	LA-ICP-MS	[*Zhang et al.*, 2008c]
dacite	140±3	LA-ICP-MS	[*Zhang et al.*, 2008c]
dacite	136±1	LA-ICP-MS	[*Zhang et al.*, 2008c]
rhyolite	132±2	LA-ICP-MS	[*Zhang et al.*, 2005b]
rhyolitic tuff	135±2	LA-ICP-MS	[*Zhang et al.*, 2005b]
tuffaceous rhyolite	136±2	LA-ICP-MS	[*Zhang et al.*, 2005b]
basaltic andesite	131±4	LA-ICP-MS	[*Zhang et al.*, 2005c]
rhyolite	136±2	LA-ICP-MS	[*Zhang et al.*, 2005c]
welded tuff	140±2	LA-ICP-MS	[*Zhang et al.*, 2005c]
acid tuff-lava	143±1	LA-ICP-MS	[*Zhang et al.*, 2005c]
dacite	132±1	LA-ICP-MS	[*Zhang et al.*, 2005a]
dacitic volcanic breccia lava	130±2	LA-ICP-MS	[*Zhang et al.*, 2005a]
granite	135±5	TIMS	[*Li et al.*, 2004]
monzogranite	132±5	TIMS	[*Li et al.*, 2004]
granodiorite	131±1	LA-ICP-MS	[*Wu et al.*, 2005a]
gneissic monzogranite	131±2	LA-ICP-MS	[*Wu et al.*, 2005b]
diabase dyke	139±2	LA-ICP-MS	[*Yang et al.*, 2007b]
rhyolite	135±1	SHRIMP	[*Shen et al.*, 2011]
andesite	132±5	LA-ICP-MS	[*Shen et al.*, 2011]
amphibole gabbro	132±2	LA-ICP-MS	[*Pei et al.*, 2011b]
dolerite	137±3	LA-ICP-MS	[*Pei et al.*, 2011b]
gabbro	134±7	SHRIMP	[*Pei et al.*, 2011b]
granite	139±2	LA-ICP-MS	[*Zhang et al.*, 2014]
quartz diorite	134±5	SHRIMP	[*Liu et al.*, 2010a]
quartz diorite	140±3	SHRIMP	[*Liu et al.*, 2010a]
aubergine rhyolite	133.8±4.7	SHRIMP	[*Yuan et al.*, 2006]
dacite	137.1±4.5	SHRIMP	[*Yuan et al.*, 2006]
granodiorite	131±2	LA-ICP-MS	[*Li et al.*, 2013a]
quartz diorite dyke	131±2	LA-ICP-MS	[*Li et al.*, 2013a]
andesitic breccia tuff	131±2	SHRIMP	[*Xu and Yang*, 2012]
granite	140±2	SHRIMP	[*Niu et al.*, 2011]
granodiorite	135.2±3.8	^{40}Ar-^{39}Ar	[*Davis et al.*, 2001]

granitoid pluton	138.2±1.5	TIMS	[*Davis et al.*, 2001]
granitoid pluton	136±2	TIMS	[*Davis et al.*, 2001]
granodiorite	132±2	LA-ICP-MS	[*Sun et al.*, 2010]
granodiorite	133±1	SIMS	[*Sun et al.*, 2010]
mafic enclave	134±2	LA-ICP-MS	[*Sun et al.*, 2010]
mafic enclave	134±1	SIMS	[*Sun et al.*, 2010]
quartz monzodiorite	132±3	LA-ICP-MS	[*Sun et al.*, 2010]
porphyritic granodiorite	134±2	LA-ICP-MS	[*Sun et al.*, 2010]
porphyritic granodiorite	130±1	SIMS	[*Sun et al.*, 2010]
quartz monzodiorite	134±1	SIMS	[*Sun et al.*, 2010]
porphyritic granodiorite	132±1	SIMS	[*Sun et al.*, 2010]
dioritic dyke	136±1	TIMS	[*Wang et al.*, 2011d]
deformed diorite	135±1	TIMS	[*Wang et al.*, 2011d]
syenodiorite	132±1	LA-ICP-MS	[*Lan et al.*, 2011]
diorite	132±2	SHRIMP	[*Xu et al.*, 2007]
pyroxene diorite	132.8±0.3	^{40}Ar-^{39}Ar	[*Xu et al.*, 2004a]
gabbro-diorite	134±2	SHRIMP	[*Yang et al.*, 2008a]
gabbro	131±2	SHRIMP	[*Yang et al.*, 2005]
norite-diorite	131±5	LA-ICP-MS	[*Yang et al.*, 2006b]
pyroxene diorite	135±2	LA-ICP-MS	[*Yang et al.*, 2006b]
biotite diorite	133±4	LA-ICP-MS	[*Yang et al.*, 2006b]
andesitic volcanic rocks	136±1	LA-ICP-MS	[*Zhu et al.*, 2010]
granite	133±3	LA-ICP-MS	[*Zhang et al.*, 2010]
quartz monzonite	131±3	LA-ICP-MS	[*Li et al.*, 2013a]
dioritic porphyry	134±1	LA-ICP-MS	[*Li et al.*, 2013a]
granodiorite	132±9	LA-ICP-MS	[*Qi et al.*, 2011]
hornblende gabbro	131±1	LA-ICP-MS	[*Wang et al.*, 2011a]
syenite	132±2	SHRIMP	[*Chen et al.*, 2008]
monzonite	132±1	SHRIMP	[*Chen et al.*, 2008]
gabbroic diorite	132±2	SHRIMP	[*Chen et al.*, 2008]
monzodiorite	133±2	SHRIMP	[*Chen et al.*, 2008]
syenite	138±1	LA-ICP-MS	[*Xiao et al.*, 2007]
trachyte porphyry	132±2	SHRIMP	[*Yang et al.*, 2009]
syenite	135±3	SHRIMP	[*Zhou and Chen*, 2006]
quartz monzonite	134±2	LA-ICP-MS	[*Ying et al.*, 2011]
granite	138±3	SHRIMP	[*Mao et al.*, 2005]
biotite granite	131±1	SHRIMP	[*Mao et al.*, 2005]
granitic porphyry	136±2	SHRIMP	[*Mao et al.*, 2005]
k-feldspar granitic porphyry	131±1	LA-ICP-MS	[*Hu et al.*, 2011]
k-feldspar granitic porphyry	132±1	LA-ICP-MS	[*Hu et al.*, 2011]
monzogranite	133±1	LA-ICP-MS	[*Zhou et al.*, 2008]

monzogranite	132±1	LA-ICP-MS	[*Zhou et al.*, 2008]
granite	132±1	LA-ICP-MS	[*Hu et al.*, 2012]
granitic porphyry	131±1	SHRIMP	[*Zhao et al.*, 2010]
granite	138±3	SHRIMP	[*Wang et al.*, 2010a]
monzogranite	134±1	LA-ICP-MS	[*Guo et al.*, 2009]
monzogranite	135±2	LA-ICP-MS	[*Guo et al.*, 2009]
monzogranite	133±2	LA-ICP-MS	[*Wang et al.*, 2011b]
dioritic porphyry	131±3	SHRIMP	[*Xu et al.*, 2004b]
quartz dioritic porphyry	131±1	LA-ICP-MS	[*Yang et al.*, 2008c]
trachyandesite	133±1	LA-ICP-MS	[*Pei et al.*, 2008]
biotite monzogranite	131±1	LA-ICP-MS	[*Gao et al.*, 2014b]
biotite monzogranite	138±3	SHRIMP	[*Mao et al.*, 2010]
biotite granite	132±2	SHRIMP	[*Mao et al.*, 2010]
Granite	131±1	SHRIMP	[*Mao et al.*, 2010]
granite porphyry	136±2	SHRIMP	[*Mao et al.*, 2010]
granite porphyry	134±1	SHRIMP	[*Mao et al.*, 2010]
granite porphyry	131±1	SHRIMP	[*Mao et al.*, 2010]
Porphyritic granite	134.4±1.0	LA-ICP-MS	[*Zhang et al.*, 2015]
Quartz monzonite	135.0±1.0	LA-ICP-MS	[*Zhang et al.*, 2015]
Porphyritic granite	138.7±1.1	LA-ICP-MS	[*Zhang et al.*, 2015]
Porphyritic quartz monzonite	134.6±1.1	LA-ICP-MS	[*Zhang et al.*, 2015]
Monzonite	132.2±1.7	LA-ICP-MS	[*Zhang et al.*, 2015]
Graniteporphyry	131.2±0.9	LA-ICP-MS	[*Zhang et al.*, 2015]
biotite monzogranite	133.7±1.4	LA-ICP-MS	[*Zhao et al.*, 2012]
granodiorite	132.9±2.2	LA-ICP-MS	[*Zhao et al.*, 2012]
rhyolite	128±1	LA-ICP-MS	[*Zhang et al.*, 2014]
volcanic rocks	125.7±0.6	^{40}Ar-^{39}Ar	[*Davis and Darby*, 2010]
volcanic rocks	125.8±0.6	^{40}Ar-^{39}Ar	[*Davis and Darby*, 2010]
volcanic rocks	125.5±0.7	^{40}Ar-^{39}Ar	[*Davis and Darby*, 2010]
volcanic rocks	127.2±1.0	^{40}Ar-^{39}Ar	[*Davis and Darby*, 2010]
volcanic rocks	125.2±0.7	^{40}Ar-^{39}Ar	[*Davis and Darby*, 2010]
granite	124.7±0.6	^{40}Ar-^{39}Ar	[*Davis and Darby*, 2010]
dioritic porphyrite	124±2	LA-ICP-MS	[*Zhang et al.*, 2014]
andesite porphyrite	128±1	LA-ICP-MS	[*Zhang et al.*, 2014]
granite	129±1	LA-ICP-MS	[*Jiao et al.*, 2013]
perlitic glassy tuff	127.2±1.5	^{40}Ar-^{39}Ar	[*Davis et al.*, 2001]
diorite	125.8±1.3	^{40}Ar-^{39}Ar	[*Davis et al.*, 2001]
trachyte	122.5±5.5	^{40}Ar-^{39}Ar	[*Davis et al.*, 2001]
granitoid pluton	127±2	TIMS	[*Davis et al.*, 2001]
granitoid pluton	127.0±1.5	TIMS	[*Davis et al.*, 2001]
granitoid pluton	128.5±1.5	TIMS	[*Davis et al.*, 2001]

granitoid pluton	128.8±1.5	TIMS	[*Davis et al.*, 2001]
biotite tuff	127.4±1.0	^{40}Ar-^{39}Ar	[*Cope*, 2003]
rhyolite	122±2	SHRIMP	[*Niu et al.*, 2004]
ignimbrite	129±1	SHRIMP	[*Niu et al.*, 2004]
congomeratic crystal-lithic tuff	126±3	SHRIMP	[*Niu et al.*, 2004]
basaltic andesite	126.1±0.4	^{40}Ar-^{39}Ar	[*Chen et al.*, 2005]
sub-volcanic rocks	122.1±2.6	^{40}Ar-^{39}Ar	[*Chen et al.*, 2005]
tuff	125±2	SHRIMP	[*Chen et al.*, 2005]
volcanic ash	120.1±0.5	^{40}Ar-^{39}Ar	[*He et al.*, 2004]
volcanic ash	124±4	SHRIMP	[*He et al.*, 2004]
tuff	120.1±0.4	^{40}Ar-^{39}Ar	[*He et al.*, 2004]
tuff	123.0±1.4	^{40}Ar-^{39}Ar	[*He et al.*, 2006b]
tuff	123.3±1.3	^{40}Ar-^{39}Ar	[*He et al.*, 2006b]
tuff	129.0±1.3	^{40}Ar-^{39}Ar	[*He et al.*, 2006a]
mylonitic diorite	128±3	SHRIMP	[*Wang et al.*, 2010b]
syenite	120±1	LA-ICP-MS	[*Yang et al.*, 2008c]
alkali rhyolite	120±1	LA-ICP-MS	[*Yang et al.*, 2008c]
porphyritic syenite	129±1	LA-ICP-MS	[*Yang et al.*, 2008c]
syenite	130±1	LA-ICP-MS	[*Yang et al.*, 2008c]
porphyritic syenite	130±1	LA-ICP-MS	[*Yang et al.*, 2008c]
alkali amphibole granite	129±1	LA-ICP-MS	[*Yang et al.*, 2008c]
mafic dyke	125±4	LA-ICP-MS	[*Wu et al.*, 2006]
monzogranite	123±3	LA-ICP-MS	[*Wu et al.*, 2006]
dioritic porphyry	126±2	SHRIMP	[*Luo et al.*, 2001]
granitic porphyry	124±1	SHRIMP	[*Luo et al.*, 2001]
dioritic porphyry	125±1	SHRIMP	[*Luo et al.*, 2001]
biotite granite	124±1	SHRIMP	[*Luo et al.*, 2001]
dacite	130±1	LA-ICP-MS	[*Yang et al.*, 2006a]
rhyolite	126±1	LA-ICP-MS	[*Yang et al.*, 2006a]
acid tuff	130±1	LA-ICP-MS	[*Zhang et al.*, 2005b]
acid tuff	129±1	LA-ICP-MS	[*Zhang et al.*, 2005b]
dacite	129±2	LA-ICP-MS	[*Zhang et al.*, 2005b]
basaltic andesite	130±3	LA-ICP-MS	[*Zhang et al.*, 2005c]
high-Mg adakite	126±1	LA-ICP-MS	[*Huang et al.*, 2007]
granite	129±2	LA-ICP-MS	[*Wang et al.*, 2012]
granite	129±3	TIMS	[*Wei et al.*, 2003]
granite dyke	128±2	LA-ICP-MS	[*Wu et al.*, 2005a]
dioritic enclave	120±1	LA-ICP-MS	[*Wu et al.*, 2005a]
dioritic enclave	121±2	LA-ICP-MS	[*Wu et al.*, 2005a]
dioritic enclave	121±3	LA-ICP-MS	[*Wu et al.*, 2005a]
monzogranite	121±1	LA-ICP-MS	[*Wu et al.*, 2005a]

quartz diorite	124±3	LA-ICP-MS	[*Wu et al.*, 2005a]
diabase	128±1	LA-ICP-MS	[*Wu et al.*, 2005a]
porphyritic granite	125±3	SHRIMP	[*Wu et al.*, 2005b]
granitic porphyry	125±4	SHRIMP	[*Wu et al.*, 2005b]
foliated dioritic dyke	125±2	SHRIMP	[*Wu et al.*, 2005b]
undeformed dioritic dyke	121±4	SHRIMP	[*Wu et al.*, 2005b]
fine-grained monzogranite	128±5	LA-ICP-MS	[*Wu et al.*, 2005b]
monzogranite	120±4	LA-ICP-MS	[*Wu et al.*, 2005b]
gneissic granidiorite	122±2	LA-ICP-MS	[*Wu et al.*, 2005b]
fine-grained monzogranite dyke	124±5	LA-ICP-MS	[*Wu et al.*, 2005b]
fine-grained monzogranite	122±6	LA-ICP-MS	[*Wu et al.*, 2005b]
porphyritic granite	129±2	LA-ICP-MS	[*Wu et al.*, 2005b]
quartz diorite	127±4	LA-ICP-MS	[*Wu et al.*, 2005b]
granodiorite	121±2	LA-ICP-MS	[*Wu et al.*, 2005b]
fine-grained monzogranite	122±2	LA-ICP-MS	[*Wu et al.*, 2005b]
syenogranite	126±2	LA-ICP-MS	[*Wu et al.*, 2005b]
diabase dyke	126±4	LA-ICP-MS	[*Wu et al.*, 2005b]
porphyritic monzogranite	130±3	LA-ICP-MS	[*Wu et al.*, 2005b]
monzogranite	121±2	LA-ICP-MS	[*Wu et al.*, 2005b]
monzogranitic porphyrite	128±2	LA-ICP-MS	[*Wu et al.*, 2005b]
porphyritic monzogranite	124±2	LA-ICP-MS	[*Wu et al.*, 2005b]
monzonite	127±1	LA-ICP-MS	[*Wu et al.*, 2005b]
quartz monzonite	128±2	LA-ICP-MS	[*Wu et al.*, 2005b]
porphyritic granodiorite	127±5	LA-ICP-MS	[*Wu et al.*, 2005b]
porphyritic monzogranite	120±2	LA-ICP-MS	[*Wu et al.*, 2005b]
porphyritic granodiorite	128±3	LA-ICP-MS	[*Wu et al.*, 2005b]
diorite	120±2	TIMS	[*Wu et al.*, 2005b]
alkali feldspar granite	130±2	TIMS	[*Wu et al.*, 2005b]
porphyritic granodiorite	125.8±0.7	TIMS	[*Wu et al.*, 2005b]
syenogranite	121.1±0.6	TIMS	[*Wu et al.*, 2005b]
alkaline granite	130.0±0.9	TIMS	[*Wu et al.*, 2005b]
monzogranite	129±1	LA-ICP-MS	[*Meng et al.*, 2013]
hornblende biotite monzogranite	126±1	LA-ICP-MS	[*Meng et al.*, 2013]
grbbro	127±1	LA-ICP-MS	[*Meng et al.*, 2013]
biotite monzogranite	123±1	LA-ICP-MS	[*Meng et al.*, 2013]
biotite monzogranite	124±3	LA-ICP-MS	[*Ji et al.*, 2009]
gneissic granite	122±2	LA-ICP-MS	[*Guo et al.*, 2004a]
gneissic granite	125±2	TIMS	[*Guo et al.*, 2004a]
porphyritic granite	129±2	LA-ICP-MS	[*Guo et al.*, 2004a]
monzogranitic dyke	124±5	LA-ICP-MS	[*Guo et al.*, 2004a]
monzogranitic dyke	120±4	TIMS	[*Guo et al.*, 2004a]

monzogranite	122±6	LA-ICP-MS	[*Guo et al.*, 2004a]
Andesite	126±6	SHRIMP	[*Liu et al.*, 2011]
rhyolite	126±3	LA-ICP-MS	[*Liu et al.*, 2011]
gabbro	126±4	SHRIMP	[*Miao et al.*, 2010]
olivine websterite	130±2	LA-ICP-MS	[*Pei et al.*, 2011b]
amphibole gabbro-diorite	129±5	SHRIMP	[*Pei et al.*, 2011b]
alkali feldspar granite	123±3	TIMS	[*Wu et al.*, 2002]
gabbro	129±1	TIMS	[*Wu et al.*, 2011]
monzogranite	124±4	TIMS	[*Wu et al.*, 2011]
alkali feldspar granite	125±4	SHRIMP	[*Wu et al.*, 2011]
quartz monzogranite	123±2	SHRIMP	[*Wu et al.*, 2011]
alkali feldspar granite	127±3	SHRIMP	[*Wu et al.*, 2011]
monzogranite	126±1	LA-ICP-MS	[*Pei et al.*, 2011a]
syenogranite	130±1	LA-ICP-MS	[*Pei et al.*, 2011a]
granodiorite	127±1	LA-ICP-MS	[*Pei et al.*, 2011a]
granitic porphyrite	127±1	LA-ICP-MS	[*Pei et al.*, 2011a]
syenogranite	125±1	LA-ICP-MS	[*Pei et al.*, 2011a]
alkali feldspar granite	123±1	LA-ICP-MS	[*Pei et al.*, 2011a]
syenogranite	123±1	LA-ICP-MS	[*Pei et al.*, 2011a]
syenogranite	122±1	LA-ICP-MS	[*Pei et al.*, 2011a]
granodiorite	123±1	LA-ICP-MS	[*Pei et al.*, 2011a]
alkali feldspar granite	122±2	LA-ICP-MS	[*QIN*, 2010]
alkali feldspar granite	125±2	LA-ICP-MS	[*QIN*, 2010]
alkali feldspar granite	124±2	LA-ICP-MS	[*QIN*, 2010]
granodiorite	125±3	SHRIMP	[*Liu*, 2010]
quartz diorite	126±2	LA-ICP-MS	[*Liu et al.*, 2012a]
granodiorite	125±2	LA-ICP-MS	[*Liu et al.*, 2012a]
porphyritic granite	126±2	LA-ICP-MS	[*Liu et al.*, 2012a]
quartz monzonite	127±3	SHRIMP	[*Chen et al.*, 2005]
monzonite	129±3	SHRIMP	[*Chen et al.*, 2005]
mafic microgranular enclave	126±3	SHRIMP	[*Chen et al.*, 2007]
granodiorite	130.7±1.4	SHRIMP	[*Cai et al.*, 2005]
dacite	130±5	LA-ICP-MS	[*Yuan et al.*, 2006]
porphyritic monzogranite	130±2	LA-ICP-MS	[*Li et al.*, 2013a]
quartz diorite dyke	130±1	LA-ICP-MS	[*Li et al.*, 2013a]
dacite (Baiqi Formation)	126±3	SHRIMP	[*Wang et al.*, 2006a]
granitoid pluton	128.4±1.5	TIMS	[*Davis et al.*, 2001]
porphyritic granodiorite	130±1	SIMS	[*Sun et al.*, 2010]
quartz syenite	129±1	LA-ICP-MS	[*Lan et al.*, 2011]
aegirine-augite syenite	130±2	LA-ICP-MS	[*Lan et al.*, 2011]
hornblende syenite	130±1	LA-ICP-MS	[*Lan et al.*, 2011]

monzonite	130±1	LA-ICP-MS	[*Lan et al.*, 2011]
quartz monzonite	130±1	LA-ICP-MS	[*Lan et al.*, 2013]
potash-rich volcanic rocks	124.3±0.6	^{40}Ar-^{39}Ar	[*Qiu et al.*, 2002]
gabbro	127±2	SHRIMP	[*Xu et al.*, 2007]
diorite	126±3	SHRIMP	[*Xu et al.*, 2007]
porphyritic diorite	130±2	SHRIMP	[*Xu et al.*, 2007]
diorite	129±3	SHRIMP	[*Xu et al.*, 2007]
syenodioritic porphyry	124.9±0.2	^{40}Ar-^{39}Ar	[*Xu et al.*, 2004a]
granodioritic porphyry	124.4±0.3	^{40}Ar-^{39}Ar	[*Xu et al.*, 2004a]
granodioritic porphyry	124.9±0.2	^{40}Ar-^{39}Ar	[*Xu et al.*, 2004a]
gabbro-diorite	129±1	SHRIMP	[*Yang et al.*, 2008b]
gabbro	127±2	SHRIMP	[*Yang et al.*, 2005]
dioritic ore	129±4	SHRIMP	[*Li et al.*, 2011]
porphyritic diorite	129±1	LA-ICP-MS	[*Wang et al.*, 2011c]
porphyritic diorite	128±1	LA-ICP-MS	[*Wang et al.*, 2011c]
andesitic volcanic rocks	122±1	LA-ICP-MS	[*Zhu et al.*, 2010]
andesitic volcanic rocks	128±2	LA-ICP-MS	[*Ling et al.*, 2009]
quartz monzodiorite	129±1	SHRIMP	[*Liu et al.*, 2013]
monzonite dyke	123±1	SHRIMP	[*Liu et al.*, 2013]
basaltic volcanic rocks	129±2	SHRIMP	[*Zhang et al.*, 2008a]
basaltic volcanic rocks	129.9±1.7	^{40}Ar-^{39}Ar	[*Zhang et al.*, 2008a]
monzogranite	125±3	SHRIMP	[*Goss et al.*, 2010]
monzogranite	125±3	SHRIMP	[*Goss et al.*, 2010]
quartz monzonite	121±8	LA-ICP-MS	[*Zhang et al.*, 2010]
porphyritic granodiorite	128±2	SHRIMP	[*Wang et al.*, 1998]
porphyritic granodiorite	126±2	SHRIMP	[*Wang et al.*, 1998]
granodiorite	130±3	SHRIMP	[*Wang et al.*, 1998]
granodiorite	129±3	SHRIMP	[*Wang et al.*, 1998]
monzogranite	128±6	SHRIMP	[*Wang et al.*, 1998]
doleritic porphyry	125±2	LA-ICP-MS	[*Liu et al.*, 2009a]
doleritic porphyry	127±2	LA-ICP-MS	[*Liu et al.*, 2009a]
doleritic porphyry	123±2	LA-ICP-MS	[*Liu et al.*, 2009a]
doleritic porphyry	124±2	LA-ICP-MS	[*Liu et al.*, 2009a]
doleritic porphyry	125±1	LA-ICP-MS	[*Liu et al.*, 2009a]
andesitic basalt	122.0±1.5	^{40}Ar-^{39}Ar	[*KUANG et al.*, 2012]
andesitic basalt	122.0±1.8	^{40}Ar-^{39}Ar	[*KUANG et al.*, 2012]
granite dyke	123±5	SHRIMP	[*Zhang et al.*, 2007]
hornblende monzonite	123±4	TIMS	[*Zhou et al.*, 2003]
pyroxene monzonite	126±3	TIMS	[*Zhou et al.*, 2003]
rhyolite	128±2	LA-ICP-MS	[*Ling et al.*, 2007]
rhyolite	128±2	LA-ICP-MS	[*Ling et al.*, 2007]

trachyandesite	124±1	LA-ICP-MS	[*Liu et al.*, 2009b]
rhyolite	122±1	LA-ICP-MS	[*Zhu et al.*, 2010]
Trachyandesite	124±1	LA-ICP-MS	[*Zhu et al.*, 2010]
trachyte	124±1	LA-ICP-MS	[*Zhu et al.*, 2010]
trachyte	122±2	LA-ICP-MS	[*Zhu et al.*, 2010]
quartz monzonite	127±1	LA-ICP-MS	[*Li et al.*, 2013a]
diorite	125±1	LA-ICP-MS	[*Li et al.*, 2013a]
monzonite	127±3	LA-ICP-MS	[*Ying et al.*, 2007]
trachyandesite	125±7	SHRIMP	[*Yang et al.*, 2009]
gabbro	125±5	SHRIMP	[*Wang et al.*, 2006b]
diorite	127±1	SHRIMP	[*Peng et al.*, 2004]
diorite	126±1	SHRIMP	[*Peng et al.*, 2004]
dioritic porphyry	124.9±0.3	^{40}Ar-^{39}Ar	[*Xu et al.*, 2004a]
hornblende diorite	127.7±0.3	^{40}Ar-^{39}Ar	[*Xu et al.*, 2004a]
hornblende diorite	127.1±0.1	^{40}Ar-^{39}Ar	[*Xu et al.*, 2004a]
diorite	125±1	LA-ICP-MS	[*Xu et al.*, 2009]
quartz monzonite	128±1	LA-ICP-MS	[*Ying et al.*, 2011]
gabbro	123±2	SHRIMP	[*Wang et al.*, 2013a]
diorite	126±2	SHRIMP	[*Wang et al.*, 2013a]
monzonite	130±2	LA-ICP-MS	[*Ying et al.*, 2011]
biotite monzogranite	127±1	SHRIMP	[*Mao et al.*, 2005]
granite	129±1	LA-ICP-MS	[*Xiao et al.*, 2012]
granite	129±2	LA-ICP-MS	[*Xiao et al.*, 2012]
granite	128±2	LA-ICP-MS	[*Xiao et al.*, 2012]
monzogranite	121±1	LA-ICP-MS	[*Zhou et al.*, 2008]
diabase	129±2	SHRIMP	[*Zhao et al.*, 2010]
granodiorite	126.9±0.2	^{40}Ar-^{39}Ar	[*Xu et al.*, 2004a]
granodiorite	130±3	SHRIMP	[*JIN et al.*, 2003]
dioritic porphyry	127±1	LA-ICP-MS	[*Yang et al.*, 2008b]
hornblende dioritic porphyry	127±1	LA-ICP-MS	[*Yang et al.*, 2008b]
monzodioritic porphyry	129±2	LA-ICP-MS	[*Yang et al.*, 2008b]
granodiorite	130±2	SHRIMP	[*Yang et al.*, 2010]
syenogranite	129±5	LA-ICP-MS	[*Yang et al.*, 2010]
syenogranite	130±3	LA-ICP-MS	[*Yang et al.*, 2010]
porphyry granodiorites	123±4	SHRIMP	[*Liu et al.*, 2012b]
trachydacite	129±2	LA-ICP-MS	[*Pei et al.*, 2008]
quartz monzonite	128±1	LA-ICP-MS	[*Fu et al.*, 2012]
syenogranite	125±2	LA-ICP-MS	[*Gao et al.*, 2014b]
monzonite	122±2	LA-ICP-MS	[*Gao et al.*, 2014b]
lamprophyre	126.7±2	K–Ar	[*Guo et al.*, 2004b]
lamprophyre	122.2±1.8	K–Ar	[*Guo et al.*, 2004b]

lamprophyre	126.0±2.0	K–Ar	[*Guo et al.*, 2004b]
lamprophyre	123.5±2.3	K–Ar	[*Guo et al.*, 2004b]
gabbro	127.5±2.2	SIMS	[*Huang et al.*, 2012]
gabbro	122±2	SIMS	[*Huang et al.*, 2012]
diorite porphyry	124.0±1.2	LA-ICP-MS	[*Li et al.*, 2015]
diorite porphyry	129.0±2.8	LA-ICP-MS	[*Li et al.*, 2015]
quartz diorite porphyry	131.8±1.7	LA-ICP-MS	[*Li et al.*, 2015]
syenodiorite	129.3±3.2	LA-ICP-MS	[*Li et al.*, 2015]
syenite porphyry	128.7±2.0	LA-ICP-MS	[*Li et al.*, 2015]
lamprophyre	120.8±1.8	LA-ICP-MS	[*Ma et al.*, 2014]
lamprophyre	121.6±1.7	LA-ICP-MS	[*Ma et al.*, 2014]
lamprophyre	120.6±2.9	LA-ICP-MS	[*Ma et al.*, 2014]
Biotite monzogranite	127±1	SHRIMP	[*Mao et al.*, 2010]
graniticdyke	130±2	SHRIMP	[*Mao et al.*, 2010]
dolerite dyke	129±2	SHRIMP	[*Mao et al.*, 2010]
Granite porphyry	130.0±1.2	LA-ICP-MS	[*Zhang et al.*, 2015]
Granite porphyry	123.2±1.5	LA-ICP-MS	[*Zhang et al.*, 2015]
biotite monzogranite	130.6±1.4	LA-ICP-MS	[*Zhao et al.*, 2012]
monzogranite	114±1	LA-ICP-MS	[*Guo et al.*, 2012]
volcanic rocks	119.2±0.6	^{40}Ar-^{39}Ar	[*Davis and Darby*, 2010]
granite	119±2	TIMS	[*Davis and Darby*, 2010]
granite	112±2	TIMS	[*Davis and Darby*, 2010]
granitoid pluton	119±2	TIMS	[*Davis et al.*, 2001]
granitoid pluton	118.0±1.5	TIMS	[*Davis et al.*, 2001]
granitoid pluton	119±2	TIMS	[*Davis et al.*, 2001]
granitoid pluton	117±3	TIMS	[*Davis et al.*, 2001]
granitoid pluton	113±2	TIMS	[*Davis et al.*, 2001]
granitoid pluton	111±4	TIMS	[*Davis et al.*, 2001]
alkali-feldpar granite	117±1	LA-ICP-MS	[*Yang et al.*, 2008c]
alkali amphibole granite	118±1	LA-ICP-MS	[*Yang et al.*, 2008c]
alkali rhyolite	119±1	LA-ICP-MS	[*Yang et al.*, 2008c]
granite	115±1	LA-ICP-MS	[*Wang et al.*, 2012]
undeformed dioritic dyke	117±7	SHRIMP	[*Wu et al.*, 2005b]
porphyritic monzogranite	118±3	LA-ICP-MS	[*Wu et al.*, 2005b]
deformed mafic dyke	113.9±1.6	LA-ICP-MS	[*Yang et al.*, 2007a]
biotite granite	113±2	SHRIMP	[*Ji et al.*, 2009]
granite dyke	116±2	LA-ICP-MS	[*Liu et al.*, 2011]
trachyte	118±2	LA-ICP-MS	[*Sui and Chen*, 2012]
granodiorite	119±2	LA-ICP-MS	[*Zhang et al.*, 2003]
quartz diorite	116±1	LA-ICP-MS	[*Zhang et al.*, 2003]
monzogranite	119±2	LA-ICP-MS	[*Wu et al.*, 2011]

monzogranite	114±2	LA-ICP-MS	[*Wu et al.*, 2011]
diorite	119±2	LA-ICP-MS	[*QIN*, 2010]
potash-rich volcanic rocks	114.8±0.6	^{40}Ar-^{39}Ar	[*Qiu et al.*, 2002]
potash-rich volcanic rocks	117.8±0.6	^{40}Ar-^{39}Ar	[*Qiu et al.*, 2002]
potash-rich volcanic rocks	117.0±0.6	^{40}Ar-^{39}Ar	[*Qiu et al.*, 2002]
potash-rich volcanic rocks	118.2±0.6	^{40}Ar-^{39}Ar	[*Qiu et al.*, 2002]
lamprophyre	119.6±0.7	^{40}Ar-^{39}Ar	[*Qiu et al.*, 2002]
biotite pyroxenite	115.1±1.1	^{40}Ar-^{39}Ar	[*Lin et al.*, 1996]
quartz monzonite	115.1±0.3	^{40}Ar-^{39}Ar	[*Lin et al.*, 1996]
basalt dyke	116.8±0.7	^{40}Ar-^{39}Ar	[*Zhang et al.*, 2008a]
basalt dyke	110.6±1.0	^{40}Ar-^{39}Ar	[*Zhang et al.*, 2008a]
volcanic rock	115.2±3.9	^{40}Ar-^{39}Ar	[*Zhang et al.*, 2008a]
basalt dyke	117.1±0.8	^{40}Ar-^{39}Ar	[*Zhang et al.*, 2008a]
basalt dyke	119.2±0.6	^{40}Ar-^{39}Ar	[*Zhang et al.*, 2008a]
volcanic rock	111.0±0.8	^{40}Ar-^{39}Ar	[*Zhang et al.*, 2008a]
volcanic rock	110.4±1.6	^{40}Ar-^{39}Ar	[*Zhang et al.*, 2008a]
monzogranite	118±1	SHRIMP	[*Goss et al.*, 2010]
syenogranite	117±1	SHRIMP	[*Goss et al.*, 2010]
monzogranite	116±2	SHRIMP	[*Goss et al.*, 2010]
monzonite enclave	116±1	SHRIMP	[*Goss et al.*, 2010]
monzogranite	113±2	SHRIMP	[*Goss et al.*, 2010]
granite	111±2	LA-ICP-MS	[*Zhang et al.*, 2010]
feldspar porphyry dyke	120±2	SHRIMP	[*Wang et al.*, 1998]
pyroxene diorite	114.5±0.8	TIMS	[*Guo et al.*, 2005]
porphyritic alkali feldspar granite	114±1	TIMS	[*Guo et al.*, 2005]
porphyritic alkali feldspar granite	113±1	SHRIMP	[*Guo et al.*, 2005]
gabbro-diorite	113±2	LA-ICP-MS	[*Hu et al.*, 2007]
granite	119±1	LA-ICP-MS	[*Li et al.*, 2012]
granite	120±1	LA-ICP-MS	[*Li et al.*, 2012]
mafic enclave	119±1	LA-ICP-MS	[*Li et al.*, 2012]
olivine basalt	114.9±0.6	^{40}Ar-^{39}Ar	[*KUANG et al.*, 2012]
andesitic basalt	119.3±0.5	^{40}Ar-^{39}Ar	[*KUANG et al.*, 2012]
andesitic basalt	113.0±1.3	^{40}Ar-^{39}Ar	[*KUANG et al.*, 2012]
granite dyke	116±3	SHRIMP	[*Zhang et al.*, 2007]
granite	116.9±0.7	^{40}Ar-^{39}Ar	[*Zhang et al.*, 2007]
granite	118±3	SHRIMP	[*Zhang et al.*, 2007]
granite	116.8±1.4	^{40}Ar-^{39}Ar	[*Zhang et al.*, 2007]
granite	113±3	SHRIMP	[*Zhang et al.*, 2007]
granite	116±4	TIMS	[*Zhou et al.*, 2003]
monzogranite	115±1	TIMS	[*Zhou et al.*, 2003]
monzogranite	115±2	SHRIMP	[*Zhang and Zhang*, 2007]

monzonitic porphyry	114±2	LA-ICP-MS	[*Tan et al.*, 2008]
dioritic porphyry	116±1	LA-ICP-MS	[*Tan et al.*, 2008]
trachydacite	119±1	LA-ICP-MS	[*Zhu et al.*, 2010]
rhyolite	120±1	LA-ICP-MS	[*Zhu et al.*, 2010]
trachyte	117±1	LA-ICP-MS	[*Zhu et al.*, 2010]
Trachyandesite	120±1	LA-ICP-MS	[*Zhu et al.*, 2010]
trachyandesite	118±2	LA-ICP-MS	[*Zhu et al.*, 2010]
trachyte	116±1	LA-ICP-MS	[*Zhu et al.*, 2010]
quartz dioritic porphyry	118±2	SHRIMP	[*Yang et al.*, 2004]
granitic porphyry	112±1	SHRIMP	[*Ye et al.*, 2006]
alkali-feldspar granite	115±2	SHRIMP	[*Ye et al.*, 2008]
granitic porphyry	114±1	LA-ICP-MS	[*Dai et al.*, 2009]
granitic porphyry	117±1	LA-ICP-MS	[*Dai et al.*, 2009]
monzogranite	112±2	LA-ICP-MS	[*Yang et al.*, 2010]
granodiorite	118±1	SIMS	[*Liu et al.*, 2012b]
granodiorite	115±1	SIMS	[*Liu et al.*, 2012b]
granodiorite	118±3	LA-ICP-MS	[*Liu et al.*, 2012b]
granite	112±1	SIMS	[*Liu et al.*, 2012b]
mafic dyke	111.8±0.6	^{40}Ar-^{39}Ar	[*Liu et al.*, 2012b]
rhyolite (Yingcheng Formation)	116±2	SHRIMP	[*Zhang et al.*, 2009a]
rhyolite (Yingcheng Formation)	115.2±0.4	SHRIMP	[*Zhang et al.*, 2009a]
rhyolite (Yingcheng Formation)	117±2	SHRIMP	[*Zhang et al.*, 2009a]
rhyolite (Yingcheng Formation)	116±3	SHRIMP	[*Zhang et al.*, 2009a]
basalt (Yingcheng Formation)	110±2	SHRIMP	[*Zhang et al.*, 2009a]
basaltic trachyandesite	118±6	LA-ICP-MS	[*Pei et al.*, 2008]
basaltic trachyandesite	118±1	K-Ar	[*Pei et al.*, 2008]
trachyandesite	116±1	LA-ICP-MS	[*Pei et al.*, 2008]
basaltic andesite	114±4	LA-ICP-MS	[*Pei et al.*, 2008]
rhyolite	119±1	LA-ICP-MS	[*Pei et al.*, 2008]
basaltic trachyandesite	110±16	LA-ICP-MS	[*Pei et al.*, 2008]
diorite	116±1	LA-ICP-MS	[*Cai et al.*, 2013]
pyroxene diorite	117±1	LA-ICP-MS	[*Cai et al.*, 2013]
biotite monzogranite	115±1	LA-ICP-MS	[*Gao et al.*, 2014b]
biotite monzogranite	117±1	LA-ICP-MS	[*Gao et al.*, 2014b]
biotite monzogranite	115±1	LA-ICP-MS	[*Gao et al.*, 2014b]
biotite monzogranite	120±1	LA-ICP-MS	[*Gao et al.*, 2014b]
syenogranite	115±2	LA-ICP-MS	[*Gao et al.*, 2014a]
monzonite porphyry	114±2	LA-ICP-MS	[*Tan et al.*, 2008]
diorite porphyry	116±1 Ma	LA-ICP-MS	[*Tan et al.*, 2008]
granite	115±2	SHRIMP	[*Mao et al.*, 2010]
dioritedyke	117±3	SHRIMP	[*Mao et al.*, 2010]

Syenogranite porphyry	112±1	SHRIMP	[*Mao et al.*, 2010]
biotite gabbro	114.9±2.4	LA–ICP-MS	[*Tang et al.*, 2014]
quartz monzonite	115.2±2.4	LA–ICP-MS	[*Tang et al.*, 2014]
K-feldspar granite	118.1±2.8	LA–ICP-MS	[*Tang et al.*, 2014]
basalt	106.1±0.8	^{40}Ar-^{39}Ar	[*Yang and Li*, 2008]
andesite	106±3	LA-ICP-MS	[*Liu et al.*, 2011]
syenogranite	108±1	LA-ICP-MS	[*Wu et al.*, 2011]
latite andesite	109.9±0.6	^{40}Ar-^{39}Ar	[*Qiu et al.*, 2001]
trachytic rhyolite	108.2±0.6	^{40}Ar-^{39}Ar	[*Qiu et al.*, 2001]
basalt dyke	106.7±0.9	^{40}Ar-^{39}Ar	[*Zhang et al.*, 2008a]
porphyritic alkali feldspar granite	108±2	TIMS	[*Guo et al.*, 2005]

Data Set S1. Summary of the zircon U-Pb and ^{40}Ar-^{39}Ar dating results for the Cretaceous on-ENCC magmatism.

This data set is built based on the work of [Zhang et al., 2014], with 64 recently published ages also added.

References:

Cai, J. H., G. H. Yan, B. L. Mu, K. X. Reng, B. Song, and F. T. Li (2005), Zircon U-Pb age, Sr-Nd-Pb isotopic compositions and trace element of Fangshan complex in Beijing and their petrogenesis significance., *Acta Petrologica Sinica*, *21*(3), 776-788.

Cai, Y. C., H. R. Fan, M. Santosh, X. Liu, F. F. Hu, K. F. Yang, T. G. Lan, Y. H. Yang, and Y. S. Liu (2013), Evolution of the lithospheric mantle beneath the southeastern North China Craton: Constraints from mafic dikes in the Jiaobei terrain, *Gondwana Research*, *24*(2), 601-621, doi:10.1016/j.gr.2012.11.013.

Chen, B., W. Tian, B. M. Jahn, and Z. C. Chen (2008), Zircon SHRIMP U-Pb ages and in-situ Hf isotopic analysis for the Mesozoic intrusions in South Taihang, North China craton: Evidence for hybridization between mantle-derived magmas and crustal components, *Lithos*, *102*(1-2), 118-137, doi:10.1016/j.lithos.2007.06.012.

Chen, B., W. Tian, M. G. Zhai, and Y. Arakawa (2005), Zircon U-Pb geochronology and geochemistry of the Mesozoic magmatism in the Taihang Mountains and other places of the North China craton, with implications for petrogenesis and geodynamic setting., *Acta Petrologica Sinica*, *21*(1), 13-24.

Chen, Z. C., B. Chen, and W. Tian (2007), Hf isotopic compositions and geological significance; a case study of Mesozoic batholiths and mafic enclaves in North Taihang, *Acta Petrologica Sinica*, *23*(2), 295-306.

Cope, T. D. (2003), Sedimentary evolution of the Yanshan fold-thrust belt, Northeast China (Doctoral dissertation, Stanford University).

Dai, B. Z., S. Y. Jiang, and X. L. Wang (2009), Petrogenesis of the granitic porphyry related to the giant molybdenum deposit in Donggou, Henan province, China: Constraints from petrogeochemistry, zircon U-Pb chronology and Sr-Nd-Hf isotopes., *Acta Petrologica Sinica*, *25*(11), 2889-2901.

Davis, G. A., and B. J. Darby (2010), Early Cretaceous overprinting of the Mesozoic Daqing Shan fold-and-thrust belt by the Hohhot metamorphic core complex, Inner Mongolia, China, *Geoscience Frontiers*, *1*(1), 1-20.

Davis, G. A., Z. Yadong, W. Cong, B. J. Darby, Z. Changhou, and G. Gehrels (2001), Mesozoic tectonic evolution of the Yanshan fold and thrust belt, with emphasis on Hebei and Liaoning provinces, northern China, *Memoirs-Geological Society of America*, 171-198.

Deng, J. F., S. G. Su, X. X. Mo, G. C. Zhao, Q. H. Xiao, and G. Y. Ji (2004), The sequence of magmatic-tectonic events and orogenic processes of the Yanshan Belt, North China, *Acta Geol Sin-Engl*, *78*(1), 260-266.

Dong, G. C., M. Santosh, S. R. Li, J. F. Shen, X. X. Mo, S. Scott, K. Qu, and X. Wang (2013), Mesozoic magmatism and metallogenesis associated with the destruction of the North China Craton: Evidence from U-Pb geochronology and stable isotope geochemistry of the Mujicun porphyry Cu-Mo deposit, *Ore Geology Reviews*, *53*, 434-445, doi:10.1016/j.oregeorev.2013.02.006.

Fu, L. B., J. H. Wei, T. M. Kusky, H. Y. Chen, J. Tan, Y. J. Li, W. J. Shi, C. Chen, and S. Q. Zhao (2012), The Cretaceous Duimiangou adakite-like intrusion from the Chifeng region, northern North China Craton: Crustal contamination of basaltic magma in an intracontinental extensional

environment, *Lithos*, *134*, 273-288, doi:10.1016/j.lithos.2012.01.007.

Gao, R. Wei, Z. Hou, G. Ma, R. Zhao, Z. Chen, J. Wu, Y. Peng, and M. Gao (2011), Mujicun porphyry copper mineralization: response to Mesozoic thinning of lithosphere in North China Craton, *Mineral Deposits*, *30*(5), 891-902.

Gao, S., R. L. Rudnick, H. L. Yuan, X. M. Liu, Y. S. Liu, W. L. Xu, W. L. Ling, J. Ayers, X. C. Wang, and Q. H. Wang (2004), Recycling lower continental crust in the North China craton, *Nature*, *432*(7019), 892-897, doi:10.1038/nature03162.

Gao, X. Y., T. P. Zhao, Z. W. Bao, and A. Y. Yang (2014a), Petrogenesis of the early Cretaceous intermediate and felsic intrusions at the southern margin of the North China Craton: Implications for crust-mantle interaction, *Lithos*, *206*, 65-78, doi:10.1016/j.lithos.2014.07.019.

Gao, X. Y., T. P. Zhao, and W. T. Chen (2014b), Petrogenesis of the early Cretaceous Funiushan granites on the southern margin of the North China Craton: Implications for the Mesozoic geological evolution, *Journal of Asian Earth Sciences*, *94*, 28-44, doi:10.1016/j.jseaes.2014.07.042.

Gao, Y. F., M. Santosh, Z. Q. Hou, R. H. Wei, G. X. Ma, Z. K. Chen, and J. L. Wu (2012), High Sr/Y magmas generated through crystal fractionation: Evidence from Mesozoic volcanic rocks in the northern Taihang orogen, North China Craton, *Gondwana Research*, *22*(1), 152-168, doi:10.1016/j.gr.2011.11.002.

Gao, Y. F., M. Santosh, R. H. Wei, G. X. Ma, Z. K. Chen, and J. L. Wu (2013), Origin of high Sr/Y magmas from the northern Taihang Mountains: Implications for Mesozoic porphyry copper mineralization in the North China Craton, *Journal of Asian Earth Sciences*, *78*, 143-159, doi:10.1016/j.jseaes.2012.10.040.

Goss, S. C., S. A. Wilde, F. Y. Wu, and J. H. Yang (2010), The age, isotopic signature and significance of the youngest Mesozoic granitoids in the Jiaodong Terrane, Shandong Province, North China Craton, *Lithos*, *120*(3-4), 309-326, doi:10.1016/j.lithos.2010.08.019.

Guo, B., L. M. Zhu, B. Li, H. J. Gong, and J. Q. Wang (2009), Zircon U-Pb age and Hf isotope composition of the Huashan and Heyu granite plutons at the southern margin of North China Craton: Implications for geodynamic setting, *Acta Petrologica Sinica*, *25*(2), 265-281.

Guo, C. L., F. Y. Wu, J. H. Yang, J. Q. Lin, and D. Y. Sun (2004a), The extensional setting of the Early Cretaceous magmatism in eastern China: example from the Yinmawanshan pluton in southern Liaodong Peninsula, *Acta Petrologica Sinica*, *20*(5), 1193-1204.

Guo, F., W. M. Fan, Y. J. Wang, and M. Zhang (2004b), Origin of early Cretaceous calc-alkaline lamprophyres from the Sulu orogen in eastern China: implications for enrichment processes beneath continental collisional belt, *Lithos*, *78*(3), 291-305, doi:10.1016/j.lithos.2004.05.001.

Guo, J. H., F. K. Chen, X. M. Zhang, W. Siebel, and M. G. Zhai (2005), Evolution of syn- to post-collisional magmatism from north Sulu UHP belt, eastern China: zircon U-Pb geochronology, *Acta Petrologica Sinica*, *21*(4), 1281-1301.

Guo, L., T. Wang, J. J. Zhang, J. Liu, G. W. Qi, and J. B. Li (2012), Evolution and time of formation of the Hohhot metamorphic core complex, North China: new structural and geochronologic evidence, *International Geology Review*, *54*(11), 1309-1331, doi:10.1080/00206814.2011.638438.

He, X. Wang, F. Jin, Z. Zhou, F. Wang, L. Yang, X. Ding, A. Boven, and R. Zhu (2006a), The 40Ar/39Ar dating of the early Jehol biota from Fengning, Hebei Province, northern China, *Geochemistry, Geophysics, Geosystems*, *7*(4), doi: 10.1029/2005GC001083.

He, X. Wang, Z. Zhou, F. Jin, F. Wang, L. Yang, X. Ding, A. Boven, and R. Zhu (2006b), 40Ar/39Ar dating of Lujiatun bed (Jehol Group) in Liaoning, northeastern China, *Geophysical Research Letters*, *33*(4), doi: 10.1029/2005GL025274.

He, H. Y., X. L. Wang, Z. H. Zhou, F. Wang, A. Boven, G. H. Shi, and R. X. Zhu (2004), Timing of the Jiufotang Formation (Jehol Group) in Liaoning, northeastern China, and its implications, *Geophysical Research Letters*, *31*(12), doi: 10.1029/2004gl019790.

He, Y. (2010), Coupling of Mesozoic shallow and deep tectonicmagma evolution in the middle segment of the northern margin of North China Plate [Ph. D. thesis]: Beijing, *Peking University (in Chinese with English abstract)*.

Hu, L. Jian-wei, and D. Xiao-dong (2011), LA-ICP-MS zircon U-Pb dating of granitoid intrusions related to iron-copper polymetallic deposits in Luonan-Lushi area of southern North China Craton and its geological implications, *Mineral Deposits*, *30*(6), 979-1001.

Hu, F. F., H. R. Fan, J. H. Yang, M. G. Zhai, L. W. Xie, Y. H. Yang, and X. M. Liu (2007), Petrogenesis of Gongjia gabbro-diorite in the Kunyushan area, Jiaodong peninsula: Constraints from petro-geochemistry, zircon U-Pb dating and Hf isotopes, *Acta Petrologica Sinica*, *23*(2), 369-380.

Hu, J., S. Y. Jiang, H. X. Zhao, Y. Shao, Z. Z. Zhang, E. Xiao, Y. F. Wang, B. Z. Dai, and H. Y. Li (2012), Geochemistry and petrogenesis of the Huashan granites and their implications for the Mesozoic tectonic settings in the Xiaoqinling gold mineralization belt, NW China, *Journal of Asian Earth Sciences*, *56*, 276-289, doi:10.1016/j.jseaes.2012.05.016.

Huang, H., S. Gao, Z. C. Hu, X. M. Liu, and H. L. Yuan (2007), Geochemistry of the high-Mg andesites at Zhangwu, western Liaoning: Implication for delamination of newly formed lower crust, *Sci China Ser D*, *50*(12), 1773-1786, doi:10.1007/s11430-007-0121-x.

Huang, X. L., J. W. Zhong, and Y. G. Xu (2012), Two tales of the continental lithospheric mantle prior to the destruction of the North China Craton: Insights from Early Cretaceous mafic intrusions in western Shandong, East China, *Geochimica Et Cosmochimica Acta*, *96*, 193-214, doi:10.1016/j.gca.2012.08.014.

Ji, M., J. L. Liu, L. Hu, H. M. Guan, G. Davis, and W. Zhang (2009), Zircon SHRIMP U-Pb age of Yinmawanshan and Zhaofang pluton in South Liaoning metamorphic core complex and its geological implications., *Acta Petrologica Sinica*, *25*(1), 173-181.

Ji, Q., S. Ji, Y. Cheng, H. You, and J. Lu (2004), The first fossil soft-shell eggs with embryos from Late Mesozoic Jehol Biota of western Liaoning, China, *ACTA GEOSCIENTIA SINICA.*, *25*(3; ISSU 82), 275-286.

Jiao, J., Z. Tang, Z. Qian, H. Yuan, H. Yan, T. Sun, G. Xu, and X. Li (2010), Metallogenic mechanism, magma source and zircon U-Pb age of Jinduicheng granitic porphyry, East Qinling, *Earth Science–Journal of China University of Geosciences*, *35*, 1011-1022.

Jiao, S. T., D. P. Yan, Q. Zhang, C. D. Li, B. Wan, and Z. H. Tian (2013), Zircon U-Pb age, geochemistry characteristics of Badaling granitoid complex and their geological significance, *Acta Petrologica Sinica*, *29*(3), 769-780.

Jin, W. Wang, Q. Gao, S. LIU, and Xiaochun (2003), Formation Time and Sources of the Huaiguang "Migmatitic Granodiorite" in Bengbu, Anhui Province: Evidence from SHRIMP Zircon U-Pb Geochronology, *Acta Geosicientia Sinica*, 24(4; ISSU 77), 331-336.

Kuang, P. ChongJin, L. ZhenYu, H. LuBing, Z. YuTing, Q. HuaNing, and X. YiGang (2012), 40Ar-39Ar geochronology and geochemistry of mafic rocks from Qingshan Group, Jiaodong area: Implications for the destruction of the North China Craton, *Acta Petrologica Sinica*, *28*(4), 1073-1091.

Lan, T. G., H. R. Fan, F. F. Hu, A. G. Tomkins, K. F. Yang, and Y. S. Liu (2011), Multiple crust-mantle interactions for the destruction of the North China Craton: Geochemical and Sr-Nd-Pb-Hf isotopic evidence from the Longbaoshan alkaline complex, *Lithos*, *122*(1-2), 87-106, doi:10.1016/j.lithos.2010.12.001.

Lan, T. G., H. R. Fan, M. Santosh, F. F. Hu, K. F. Yang, Y. H. Yang, and Y. S. Liu (2013), Crust-mantle interaction beneath the Luxi Block, eastern North China Craton: Evidence from coexisting mantle- and crust-derived enclaves in a quartz monzonite pluton, *Lithos*, *177*, 1-16, doi:10.1016/j.lithos.2013.05.017.

Li, F. Lu, X. Li, Y. Zhou, S. Sun, J. Li, and D. Zhang (2001), Geochemical features and origin of volcanic rocks of Tiaojishan Formation in Western Hills of Beijing, *Acta Petrologica et Mineralogica (in Chinese)*, *20*(2), 123-133.

Li, H., K. Geng, Y. Li, and C. Zhuo (2011), Zircon SHRIMP U–Pb age of Tongjing gold deposit in Yinan County, Shandong and its geological significance, *Mineral Deposits*, *30*, 497-506.

Li, Q., M. Santosh, S. R. Li, and J. Q. Zhang (2015), Petrology, geochemistry and zircon U-Pb and Lu-Hf isotopes of the Cretaceous dykes in the central North China Craton: Implications for magma genesis and gold metallogeny, *Ore Geology Reviews*, *67*, 57-77, doi:10.1016/j.oregeorev.2014.11.015.

Li, S. R., M. Santosh, H. F. Zhang, J. F. Shen, G. C. Dong, J. Z. Wang, and J. Q. Zhang (2013a), Inhomogeneous lithospheric thinning in the central North China Craton: Zircon U-Pb and S-He-Ar isotopic record from magmatism and metallogeny in the Taihang Mountains, *Gondwana Research*, *23*(1), 141-160, doi:10.1016/j.gr.2012.02.006.

Li, T. G., G. Wu, Y. C. Chen, Z. Y. Li, X. S. Yang, and C. J. Qiao (2013b), Geochronology, geochemistry and petrogenesis of the Yinjiagou complex in western Henan Province, China., *Acta Petrologica Sinica*, *29*(1), 46-66.

Li, X. C., H. R. Fan, M. Santosh, F. F. Hu, K. F. Yang, T. G. Lan, Y. S. Liu, and Y. H. Yang (2012), An evolving magma chamber within extending lithosphere: An integrated geochemical, isotopic and zircon U-Pb geochronological study of the Gushan granite, eastern North China Craton, *Journal of Asian Earth Sciences*, *50*, 27-43, doi:10.1016/j.jseaes.2012.01.016.

Li, Y. G., M. G. Zhai, J. H. Yang, L. C. Miao, and H. Guan (2004), Gold mineralization age of the Anjiayingzi gold deposit in Chifeng County, Inner Mongolia and implications for Mesozoic metallogenic explosion in North China, *Sci China Ser D*, *47*(2), 115-121, doi:10.1360/02yd0418.

Lin, J., D. Tan, and Y. Jin (1996), 40Ar/39Ar ages of Mesozoic igneous activities in western Shandong, *Acta Petrologica et Mineralogica*, *15*(3), 213-220.

Ling, W. L., R. C. Duan, X. J. Xie, Y. Q. Zhang, J. B. Zhang, J. P. Cheng, X. M. Liu, and H. M. Yang (2009), Contrasting geochemistry of the Cretaceous volcanic suites in Shandong province and its implications for the Mesozoic lower crust delamination in the eastern North China craton, *Lithos*, *113*(3-4), 640-658, doi:10.1016/j.lithos.2009.07.001.

Ling, W. L., X. J. Xie, X. M. Liu, and J. P. Cheng (2007), Zircon U-Pb dating on the Mesozoic

volcanic suite from the Qingshan Group stratotype section in eastern Shandong Province and its tectonic significance, *Sci China Ser D*, *50*(6), 813-824, doi:10.1007/s11430-007-2065-6.

Liu (2010), Paleozoic-Early Mesozoic Magmatic Belts and Tectonic Significance in Siziwangqi Area, Inner Mongolia, *China University of Geosciences, Beijing (in Chinese with English abstract)*.

Liu, C. Li, Y. Mu, H. Sun, F. Huang, and J. Zheng (2010a), Zircon shrimp U–Pb age of Chiwawu granite complex and its implicatio in the northern Taihang Mountain, *Geol. Explor*, *46*, 0442-0447.

Liu, P. Li, and S. Tian (2003), SHRIMP U-Pb zircon age of Late Mesozoic tuff (lava) in Luanping basin, northern Hebei, and its implications, *Acta Petrol. Mineral*, *22*(3), 237-244.

Liu, Z. Ni, M. Zhai, Y. Shi, G. Yan, and J. Lu (2010b), Zircon SHRIMP U-Pb dating of granite in Chicheng country, Northern Hebei Province and its geological implication, *Journal of Mineralogy and Petrology*, *30*(2), 38-44.

Liu, Pengrui-Xiong, and Yuxin-Ma (2013), SHRIMP zircon U-Pb and molybdenite Re-Os age of the copper Polymetallic deposit in Zouping volcanic basin, Shandong Province, *Geological Bulletin of China*, *32*(0), 1621-1630.

Liu, J., Y. Zhao, X. M. Liu, Y. Wang, and X. W. Liu (2012a), Rapid exhumation of basement rocks along the northern margin of the North China craton in the early Jurassic: evidence from the Xiabancheng Basin, Yanshan Tectonic Belt, *Basin Research*, *24*(5), 544-558, doi:10.1111/j.1365-2117.2011.00538.x.

Liu, J. L., M. Ji, L. Shen, H. M. Guan, and G. A. Davis (2011), Early cretaceous extensional structures in the Liaodong Peninsula: Structural associations, geochronological constraints and regional tectonic implications, *Sci China Earth Sci*, *54*(6), 823-842, doi:10.1007/s11430-011-4189-y.

Liu, S., R. Z. Hu, S. Gao, C. X. Feng, L. Qi, H. Zhong, T. F. Xiao, Y. Q. Qi, T. Wang, and I. M. Coulson (2008), Zircon U-Pb geochronology and major, trace elemental and Sr-Nd-Pb isotopic geochemistry of mafic dykes in western Shandong Province, east China: Constrains on their petrogenesis and geodynamic significance, *Chemical Geology*, *255*(3-4), 329-345, doi:10.1016/j.chemgeo.2008.07.006.

Liu, S., R. Z. Hu, S. Gao, C. X. Feng, B. B. Yu, G. Y. Feng, Y. Q. Qi, T. Wang, and I. M. Coulson (2009a), Petrogenesis of Late Mesozoic mafic dykes in the Jiaodong Peninsula, eastern North China Craton and implications for the foundering of lower crust, *Lithos*, *113*(3-4), 621-639, doi:10.1016/j.lithos.2009.06.035.

Liu, S., R. Z. Hu, S. Gao, C. X. Feng, B. B. Yu, Y. Q. Qi, T. Wang, G. Y. Feng, and I. M. Coulson (2009b), Zircon U-Pb age, geochemistry and Sr-Nd-Pb isotopic compositions of adakitic volcanic rocks from Jiaodong, Shandong Province, Eastern China: Constraints on petrogenesis and implications, *Journal of Asian Earth Sciences*, *35*(5), 445-458, doi:10.1016/j.jseaes.2009.02.008.

Liu, S. A., S. G. Li, S. S. Guo, Z. H. Hou, and Y. S. He (2012b), The Cretaceous adakitic-basaltic-granitic magma sequence on south-eastern margin of the North China Craton: Implications for lithospheric thinning mechanism, *Lithos*, *134*, 163-178, doi:10.1016/j.lithos.2011.12.015.

Luo, Z., L. Miao, K. Guan, Y. Qiu, Y. Qiu, N. McNaughton, and D. Groves (2001), SHRIMP U–Pb zircon age of magmatic rock in Paishanlou gold mine district, Fuxin, Liaoning Province, China, *Geochimica*, *30*(5), 483-490.

Ma, L., S.-Y. Jiang, A. W. Hofmann, B.-Z. Dai, M.-L. Hou, K.-D. Zhao, L.-H. Chen, J.-W. Li, and

Y.-H. Jiang (2014), Lithospheric and asthenospheric sources of lamprophyres in the Jiaodong Peninsula: A consequence of rapid lithospheric thinning beneath the North China Craton?, *Geochimica et Cosmochimica Acta*, *124*, 250-271.

Mao, D. B., Z. H. Chen, C. T. Zhong, Y. C. Zuo, S. Shi, and X. D. Hu (2003), Studies on the geochronology and geochemical characteristics of Mesozoic intrusions in Beichagoumen area, northern Hebei province, *Acta Petrologica Sinica*, *19*(4), 661-674.

Mao, J. W., G. Q. Xie, F. Pirajno, H. S. Ye, Y. B. Wang, Y. F. Li, J. F. Xiang, and H. J. Zhao (2010), Late Jurassic-Early Cretaceous granitoid magmatism in Eastern Qinling, central-eastern China: SHRIMP zircon U-Pb ages and tectonic implications, *Australian Journal of Earth Sciences*, *57*(1), 51-78, doi:10.1080/08120090903416203.

Mao, J. W., G. Q. Xie, Z. H. Zhang, X. F. Li, Y. T. Wang, C. Q. Zhang, and Y. F. Li (2005), Mesozoic large-scale metallogenic pulses in North China and corresponding geodynamic settings, *Acta Petrologica Sinica*, *21*(1), 169-188.

Meng, E., F. L. Liu, J. R. Shi, and J. Cai (2013), Zircon U-Pb chronology, geochemistry of the previously "Pre-Sinian" intrusive rocks in Dandong area of southeastern Liaoning Province, and its tectonic implications, *Acta Petrologica Sinica*, *29*(2), 421-436.

Meng, Q. P., Y. K. He, W. Zhang, R. G. Zheng, C. Xu, Z. Y. Zhang, and T. R. Wu (2014), Time constraints on the inversion of the tectonic regime in the northern margin of the North China Craton: Evidence from the Daqingshan granites, *Journal of Asian Earth Sciences*, *79*, 246-259, doi:10.1016/j.jseaes.2013.09.032.

Miao, L. C., F. Q. Zhang, D. Y. Liu, Y. R. Shi, and X. Q. HangQiang (2010), Zircon SHRIMP U-Pb dating for gabbro at Chaotiehe in the Haicheng area, eastern Liaoning, *Chinese Science Bulletin*, *55*(4-5), 403-410, doi:10.1007/s11434-009-0404-z.

Niu, B. G., Z. J. He, B. Song, J. S. Ren, and L. W. Xiao (2004), SHRIMP geochronology of volcanics of the Zhangjiakou and Yixian Formations, northern Hebei Province, with a discussion on the age of the Xing'anling group of the Great Hinggan Mountains and volcanic strata of the southeastern coastal area of China, *Acta Geol Sin-Engl*, *78*(6), 1214-1228.

Niu, X. L., B. Chen, and X. Ma (2011), Petrogenesis of the Dengzhazi A-type pluton from the Taihang-Yanshan Mesozoic orogenic belts, North China Craton, *Journal of Asian Earth Sciences*, *41*(2), 133-146, doi:10.1016/j.jseaes.2011.01.008.

Pei, W. Xu, D. Yang, W. Ji, Y. Yu, and X. Zhang (2008), Mesozoic volcanic rocks in the southern Songliao basin: zircon U–Pb ages and their constraints on the nature of basin basement, *Earth Science*, *33*(5), 603-617.

Pei, F. P., W. L. Xu, D. B. Yang, Y. Yu, E. Meng, and Q. G. Zhao (2011a), Petrogenesis of late Mesozoic granitoids in southern Jilin province, northeastern China: Geochronological, geochemical, and Sr-Nd-Pb isotopic evidence, *Lithos*, *125*(1-2), 27-39, doi:10.1016/j.lithos.2011.01.004.

Pei, F. P., W. L. Xu, D. B. Yang, Y. Yu, W. Wang, and Q. G. Zhao (2011b), Geochronology and geochemistry of Mesozoic mafic-ultramafic complexes in the southern Liaoning and southern Jilin provinces, NE China: Constraints on the spatial extent of destruction of the North China Craton, *Journal of Asian Earth Sciences*, *40*(2), 636-650, doi:10.1016/j.jseaes.2010.10.015.

Peng, WangYJ, and G. FanWm (2004), sHRImP zircon U- Pb

geochronologyofthedioritesforsouthern Taihang mountainsinthenorthchinainteriorandits petrogenesis, *Acta Petrologicasinica*, *20*(5), 1253-1262.

Qi, X. U. Hongbo, and J. Zhang (2011), Geochemistry,Geochronology and Geological Significance of Gufengshan Granodiorite in Linfen Grabben Basin, *Geological Review*, *57*(4), 565-573.

QIN (2010), A study on the tectonic environment of the Mesozoic granitoid in Laoling area, southern Jilin Provnice.

Qiu, J., D. Wang, C.-H. Lo, and H. Liu (2001), 40Ar-39Ar Dating for volcanic rocks of Qingshan Formation in Jiaolai basin, eastern Shandong province: A case study of the Fenlingshan volcanic apparatus in Wulian County, *Geological Journal of China Universities*, *7*(3), 351-355.

Qiu, J., X. Xu, and C.-H. Lo (2002), Potash-rich volcanic rocks and lamprophyres in western Shandong Province: 40Ar-39Ar dating and source tracing, *Chinese Science Bulletin*, *47*(2), 91-96..

Shen, L., J. L. Liu, L. Hu, M. Ji, H. M. Guan, and G. A. Davis (2011), The Dayingzi detachment fault system in Liaodong Peninsula and its regional tectonic significance, *Sci China Earth Sci*, *54*(10), 1469-1483, doi:10.1007/s11430-011-4202-5.

Shi, Y. R., X. T. Zhao, Y. S. Ma, D. G. Hu, Q. S. Liu, Z. H. Wu, Y. Y. Zhao, and D. Y. Liu (2009), Late Jurassic-Early Cretaceous Plutonism in the Northern Part of the Precambrian North China Craton: SHRIMP Zircon U-Pb Dating of Diorites and Granites from the Yunmengshan Geopark, Beijing, *Acta Geol Sin-Engl*, *83*(2), 310-320, doi:10.1111/j.1755-6724.2009.00033.x.

Sui, Z., and Y. Chen (2012), Petrogenesis of volcanic rocks from Sankeyushu formation in Southern Jilin: Evidences from zircon U–Pb ages and Hf isotopes, *Geoscience*, *26*, 627-634.

Sun, J. F., J. H. Yang, F. Y. Wu, X. H. Li, Y. H. Yang, L. W. Xie, and S. A. Wilde (2010), Magma mixing controlling the origin of the Early Cretaceous Fangshan granitic pluton, North China Craton In situ U-Pb age and Sr-, Nd-, Hf- and O-isotope evidence, *Lithos*, *120*(3-4), 421-438, doi:10.1016/j.lithos.2010.09.002.

Tan, J., J. H. Wei, L. L. Guo, K. Q. Zhang, C. L. Yao, J. P. Lu, and H. M. Li (2008), LA-ICP-MS zircon U-Pb dating and phenocryst EPMA of dikes, Guocheng, Jiaodong Peninsula: Implications for North China Craton lithosphere evolution, *Sci China Ser D*, *51*(10), 1483-1500, doi:10.1007/s11430-008-0079-3.

Tang, H. Y., J. P. Zheng, C. M. Yu, X. Q. Ping, and H. W. Ren (2014), Multistage crust-mantle interactions during the destruction of the North China Craton: Age and composition of the Early Cretaceous intrusions in the Jiaodong Peninsula, *Lithos*, *190*, 52-70, doi:10.1016/j.lithos.2013.12.002.

Wang, Z.-l. Chen, B.-l. Chen, F.-x. Dong, H.-d. Zhang, F. Han, and Y. Zhou (2013a), Chronology and geochemistry on Mesozoic diorite from the Xi'anli iron ore area in Pingshun, Shanxi Province, *Rock and Mineral Analysis*, *32*, 131-144.

Wang, W. Liu, S. Wang, and W. Song (2002), 40Ar/39Ar and K/Ar dating on the volcanic rocks in the Songliao basin, NE China: constraints on stratigraphy and basin dynamics, *International Journal of Earth Sciences*, *91*(2), 331-340.

Wang, X. U. Wen-Liang, and F. Wang (2011a), Petrogenesis of the Early Cretaceous Xi'anli Hornblende-Gabbros from the Southern Taihang Mountains: Evidence from Zircon U-Pb Geochronology, Hf Isotope and Whole-Rock Geochemistry, *Earth Sci-J China Univ Geosci, 36(3), 471-482.*

Wang, H. Ye, A. Ye, Y. Sun, Y. Li, and C. Zhang (2010a), Zircon SHRIMP U-Pb ages and their significances of the Wenyu and Niangniangshan granitic plutons in the Xiaoqinling area, central China, *Chinese Journal of Geology*, *45*(1), 167-180.

Wang, L. G., Y. M. Qiu, N. J. McNaughton, D. I. Groves, Z. K. Luo, J. Z. Huang, L. C. Miao, and Y. K. Liu (1998), Constraints on crustal evolution and gold metallogeny in the Northwestern Jiaodong Peninsula, China, from SHRIMP U-Pb zircon studies of granitoids, *Ore Geology Reviews*, *13*(1-5), 275-291, doi: 10.1016/S0169-1368(97)00022-X.

Wang, T., L. Guo, Y. D. Zheng, T. Donskaya, D. Gladkochub, L. S. Zeng, J. B. Li, Y. B. Wang, and A. Mazukabzov (2012), Timing and processes of late Mesozoic mid-lower-crustal extension in continental NE Asia and implications for the tectonic setting of the destruction of the North China Craton: Mainly constrained by zircon U-Pb ages from metamorphic core complexes, *Lithos*, *154*, 315-345, doi:10.1016/j.lithos.2012.07.020.

Wang, X. C., Y. S. Liu, and X. M. Liu (2006a), Mesozoic adakites in the Lingqiu Basin of the central North China Craton: Partial melting of underplated basaltic lower crust, *Geochemical Journal*, *40*(5), 447-461, doi: 10.2343/geochemj.40.447.

Wang, X. L., S. Y. Jiang, B. Z. Dai, and J. Kern (2013b), Lithospheric thinning and reworking of Late Archean juvenile crust on the southern margin of the North China Craton: evidence from the Longwangzhuang Paleoproterozoic A-type granites and their surrounding Cretaceous adakite-like granites, *Geological Journal*, *48*(5), 498-515, doi:10.1002/gj.2464.

Wang, X. X., T. Wang, Q. J. Qi, and S. Li (2011b), Temporal-spatial variations, origin and their tectonic significance of the Late Mesozoic granites in the Qinling, Central China., *Acta Petrologica Sinica*, *27*(6), 1573-1593.

Wang, Y., H. Fan, F. Hu, Y. Lan, P. Jiao, and S. Wang (2011c), Zircon U–Pb ages and geochemistry of elements and isotopes of the diorite from Tongjing, Yinan, western Shandong province, *Acta Petrol. Mineral*, *30*, 553-566.

Wang, Y., J. Han, J. Li, Z.-x. Ouyang, Y. Tong, and K. Hou (2010b), Age, petrogenesis and geological significance of the deformed granitoids in the Louzidian metamorphic core complex, southern Chifeng, InnerMongolia: Evidence from zircon U-Pb dates and Hf isotopes, *Acta Petrol Et Mineral*, *29*, 763-778.

Wang, Y., and H. M. Li (2008), Initial formation and mesozoic tectonic exhumation of an intracontinental tectonic belt of the northern part of the Taihang Mountain Belt, eastern Asia, *J Geol*, *116*(2), 155-172, doi:10.1086/529153.

Wang, Y., L. Y. Zhou, and J. Y. Li (2011d), Intracontinental superimposed tectonics-A case study in the Western Hills of Beijing, eastern China, *Geological Society of America Bulletin*, *123*(5-6), 1033-1055, doi:10.1130/B30257.1.

Wang, Y. J., W. M. Fan, H. F. Zhang, and T. P. Peng (2006b), Early Cretaceous gabbroic rocks from the Taihang Mountains: Implications for a paleosubduction-related lithospheric mantle beneath the central North China Craton, *Lithos*, *86*(3-4), 281-302, doi:10.1016/j.lithos.2005.07.001.

Wei, J., C. Liu, Z. Li, and Y. Zhao (2003), U-Pb, Rb-Sr isotopic dating of the diagenesis and mineralization of gold deposits in the Dandong area, *ACTA GEOLOGICA SINICA-CHINESE EDITION-*, *77*(1), 113-119.

Wu, J. Yang, and X. Liu (2005a), Geochronological framework of the Mesozoic granitic

magmatism in the Liaodong Peninsula, Northeast China, *Geological Journal of China Universities*, *11*(3), 305-317.

Wu, F. Y., J. Q. Lin, S. A. Wilde, X. O. Zhang, and J. H. Yang (2005b), Nature and significance of the Early Cretaceous giant igneous event in eastern China, *Earth and Planetary Science Letters*, *233*(1-2), 103-119, doi:10.1016/j.epsl.2005.02.019.

Wu, F. Y., D. Y. Sun, W. C. Ge, Y. B. Zhang, M. L. Grant, S. A. Wilde, and B. M. Jahn (2011), Geochronology of the Phanerozoic granitoids in northeastern China, *Journal of Asian Earth Sciences*, *41*(1), 1-30, doi:10.1016/j.jseaes.2010.11.014.

Wu, F. Y., D. Y. Sun, H. M. Li, B. M. Jahn, and S. Wilde (2002), A-type granites in northeastern China: age and geochemical constraints on their petrogenesis, *Chemical Geology*, *187*(1-2), 143-173, doi: 10.1016/S0009-2541(02)00018-9.

Wu, F. Y., J. H. Yang, Y. B. Zhang, and X. M. Liu (2006), Emplacement ages of the Mesozoic granites in southeastern part of the Western Liaoning Province., *Acta Petrologica Sinica*, *22*(2), 315-325.

Xiao, R. Zhanli, and Q. Jiangfeng (2007), Geochemistry and zircon LA-ICP MS U-Pb dating of the Zijinshan alkaline complex in the Linxian County, Shanxi Province: Geological Implication, *Geological Review*, *53*(3), 433-440.

Xiao, E., J. Hu, Z. Z. Zhang, B. Z. Dai, Y. F. Wang, and H. Y. Li (2012), Petrogeochemistry, zircon U-Pb dating and Lu-Hf isotopic compositions of the Haoping and Jinshanmiao granites from the Huashan complex batholith in eastern Qinling Orogen, *Acta Petrologica Sinica*, *28*(12), 4031-4046.

Xu, Y. DeBin, P. Fuping, and Y. Yang (2009), Petrogenesis of Fushan high-Mg-# diorites from the southern Taihang Mts. in the central North China Craton: Resulting from interaction of peridotite-melt derived from partial melting of delaminated lower continental crust, *Acta Petrologica Sinica*, *25*(8), 1947-1961.

Xu, D. Wang, Q. Wang, F. Pei, and J. Lin (2004a), 40Ar/39Ar dating of hornblende and biotite in Mesozoic intrusive complex from the North China Block: Constraints on the time of lithospheric thinning, *Geochimica*, *33*(3), 221-231.

Xu, and L. Yang (2012), SHRIMP U-Pb Dating and Its Geological Implications for Zircon in the Tiaojishan Group Volcanic Rocks of the Shenxian Mountain in the Taihang Aera, *Bulletin of Mineralogy Petrology & Geochemistry*, *31*(3), 257-260.

Xu, W. L., Q. H. Wang, X. C. Liu, D. Y. Wang, and J. H. Guo (2004b), Chronology and sources of mesozoic intrusive complexes in the Xuzhou-Huainan Region, central China: Constraints from SHRIMP zircon U-Pb dating, *Acta Geol Sin-Engl*, *78*(1), 96-106.

Xu, Y. G., X. Y. Wu, Z. Y. Luo, J. L. Ma, X. L. Huang, and L. W. Xie (2007), Zircon hf isotope compositions of middle Jurassic-Early Cretaceous intrusions in Shandong Province and its implications, *Acta Petrologica Sinica*, *23*(2), 307-316.

Yang, F. Wu, J. Shao, L. Xie, and X. Liu (2006a), In situ U–Pb dating and Hf isotopic analyses of zircons from volcanic rocks of the Houcheng and Zhangjiakou Formations in the Zhang-Xuan area, Northeast China, *Earth Science*, *31*(1), 71-80.

Yang, W.-L. Xu, D.-B. Yang, C.-C. Liu, X.-M. Liu, and Z.-C. Hu (2006b), Petrogenesis of the Mesozoic high-Mg diorites in west Shandong: evidence from chronology and petro-geochemistry, *Earth Science*, *31*(1), 81-92.

Yang, W.-l. Xu, D.-b. Yang, C. Liu, and X. Liu (2005), Chronology of the Jinan gabbro in Western Shandong: evidence from LA-ICP-MS zircon U-Pb dating, *Acta Geoscientia Sinica*, *26*(4), 321.

Yang, C. H., W. L. Xu, D. B. Yang, W. Wang, W. D. Wang, and J. M. Liu (2008a), Petrogenesis of Shangyu gabbro-diorites in western Shandong: Geochronological and geochemical evidence, *Sci China Ser D*, *51*(4), 481-492, doi:10.1007/s11430-008-0029-0.

Yang, D., W. Xu, D. Wang, Q. Wang, and F. Pei (2004), SHRIMP zircon U–Pb dating of the Quli quartz diorite porphyry, Sanmenxia city, Henan, and its geological significance, *Chinese Geology*, *31*(4), 379-383.

Yang, D. B., W. L. Xu, F. P. Pei, Q. H. Wang, and S. Gao (2008b), Chronology and Pb isotope compositions of Early Cretaceous adakitic rocks in Xuzhou-Huaibei area, central China: Constraints on magma sources and tectonic evolution in the eastern North China Craton, *Acta Petrologica Sinica*, *24*(8), 1745-1758.

Yang, D. B., W. L. Xu, Q. H. Wang, and F. P. Pei (2010), Chronology and geochemistry of Mesozoic granitoids in the Bengbu area, central China: Constraints on the tectonic evolution of the eastern North China Craton, *Lithos*, *114*(1-2), 200-216, doi:10.1016/j.lithos.2009.08.009.

Yang, J.-H., F.-Y. Wu, S.-L. Chung, C.-H. Lo, S. A. Wilde, and G. A. Davis (2007a), Rapid exhumation and cooling of the Liaonan metamorphic core complex: Inferences from 40Ar/39Ar thermochronology and implications for Late Mesozoic extension in the eastern North China Craton, *Geological Society of America Bulletin*, *119*(11-12), 1405-1414.

Yang, J. H., J. F. Sun, F. Chen, S. A. Wilde, and F. Y. Wu (2007b), Sources and petrogenesis of late triassic dolerite dikes in the liaodong peninsula: Implications for post-collisional lithosphere thinning of the eastern North China Craton, *Journal of Petrology*, *48*(10), 1973-1997, doi: 10.1093/petrology/egm046.

Yang, J. H., F. Y. Wu, J. A. Shao, S. A. Wilde, L. W. Xie, and X. M. Liu (2006c), Constraints on the timing of uplift of the Yanshan Fold and Thrust Belt, North China, *Earth and Planetary Science Letters*, *246*(3-4), 336-352, doi:10.1016/j.epsl.2006.04.029.

Yang, J. H., F. Y. Wu, S. A. Wilde, F. Chen, X. M. Liu, and L. W. Xie (2008c), Petrogenesis of an alkali Syenite-Granite-Rhyolite suite in the Yanshan Fold and Thrust Belt, Eastern North China Craton: Geochronological, geochemical and Nd-Sr-Hf isotopic evidence for lithospheric thinning, *Journal of Petrology*, *49*(2), 315-351, doi:10.1093/petrology/egm083.

Yang, W., and S. G. Li (2008), Geochronology and geochemistry of the Mesozoic volcanic rocks in Western Liaoning: Implications for lithospheric thinning of the North China Craton, *Lithos*, *102*(1-2), 88-117, doi:10.1016/j.lithos.2007.09.018.

Yang, X. K., H. X. Chao, N. I. Volkova, M. L. Zheng, and W. H. Yao (2009), Geochemistry and SHRIMP geochronology of alkaline rocks of the Zijinshan massif in the eastern Ordos basin, China, *Russian Geology and Geophysics*, *50*(9), 751-762, doi:10.1016/j.rgg.2009.08.002.

Ye, J. Mao, L. I. Yongfeng, B. Guo, C. Zhang, J. Liu, Q. Yan, Beijing, Beijing, and Beijing (2006), SHRIMP Zircon U-Pb and Molybdenite Re-Os Dating for the Superlarge Donggou Porphyry Mo Deposit in East Qinling,China,and Its Geological Implication, *Acta Geologica Sinica*, *80*(7), 1078-1088.

Ye, H., J. Mao, L. Xu, J. Gao, G. Xie, X. Li, and C. He (2008), SHRIMP zircon U-Pb dating and geochemistry of the Taishanmiao aluminous A-type granite in western Henan Province, *Geological*

Review, *54*(5), 699-711.

Ying, J. F., H. F. Zhang, M. Sun, Y. J. Tang, X. H. Zhou, and X. M. Liu (2007), Petrology and geochemistry of Zijinshan alkaline intrusive complex in Shanxi Province, western North China Craton: Implication for magma mixing of different sources in an extensional regime, *Lithos*, *98*(1-4), 45-66, doi:10.1016/j.lithos.2007.02.001.

Ying, J. F., H. F. Zhang, and Y. J. Tang (2011), Crust-mantle interaction in the central North China Craton during the Mesozoic: Evidence from zircon U-Pb chronology, Hf isotope and geochemistry of syenitic-monzonitic intrusions from Shanxi province, *Lithos*, *125*(1-2), 449-462, doi:10.1016/j.lithos.2011.03.004.

Yuan, H. L., X. M. Liu, Y. S. Liu, S. Gao, and W. L. Ling (2006), Geochemistry and U-Pb zircon geochronology of Late-Mesozoic lavas from Xishan, Beijing, *Sci China Ser D*, *49*(1), 50-67, doi:10.1007/s11430-004-0009-y.

Zhang, L. Jinliang, Z. Tian, D. Shuwen, and Y. Jiayin (2008a), Cretaceous to Paleocene tectono—sedimentary evolution of the Jiaolai Basin and the contiguous areas of the Shandong Peninsula (nor th China) and its geodynamic implications, *Acta Geologica Sinica*, *82*(9), 1229-1257.

Zhang, J. Li, T. Zhang, and J. Yuan (2007), Late Mesozoic kinematic history of the Muping-Jimo fault zone in Jiaodong Peninsula, Shandong Province, east China, *Geological Review*, *53*(3), 289-300.

Zhang, W. Li, D. Zhao, Y. Cao, X. Xie, H. Zhang, S. Peng, and H. Li (2008b), U-Pb age of the Lianhuagou intrusive rocks in Luonan County, Shaanxi province and its geological implications, *Acta Geoscientica Sinica*, *6*.

Zhang, X. Liu, S. Gao, L. Zhang, Z. Li, F. Yang, and X. Wang (2005a), Redefinition of the Zhangjiakou Formation in Lingyuan, western Liaoning and its significance–constraints from laser ICP-MS zircon U–Pb ages, *Geol Bull China*, *24*(2), 110-117.

Zhang, X. Liu, Y. Zhang, H. Yuan, and Z. Hu (2005b), Zircon U-Pb ages and significance of bottom and top beds of Zhangjiakou Formation in Liaoning and Hebei provinces, *Earth Science*, *30*(4), 387-401.

Zhang, H. Yuan, Z. Hu, X. Liu, and C. Diwu (2005c), U-Pb zircon dating of the Mesozoic volcanic strata in Luanping of North Hebei and its significance, *Earth Sci*, *30*(6), 707-720.

Zhang, F. Q., X. G. Cheng, H. L. Chen, C. W. Dong, X. Yu, J. Xiao, Y. Xu, Y. M. Pang, and P. Shu (2009a), Zircon chronological and geochemical constraints on the Late Mesozoic volcanic events in the southeastern margin of the Songliao Basin, NE China., *Acta Petrologica Sinica*, *25*(1), 39-54.

Zhang, H., M. X. Wang, and X. M. Liu (2008c), LA-ICP-MS dating of Zhangjiakou Formation volcanic rocks in the Zhangjiakou region and its geological significance, *Prog Nat Sci*, *18*(8), 975-981, doi:10.1016/j.pnsc.2008.01.028.

Zhang, H., Z. L. Wei, X. M. Liu, and D. Li (2009b), Constraints on the age of the Tuchengzi Formation by LA-ICP-MS dating in northern Hebei-western Liaoning, China, *Sci China Ser D*, *52*(4), 461-470, doi:10.1007/s11430-009-0052-9.

Zhang, J., Z. F. Zhao, Y. F. Zheng, and M. N. Dai (2010), Postcollisional magmatism: Geochemical constraints on the petrogenesis of Mesozoic granitoids in the Sulu orogen, China, *Lithos*, *119*(3-4), 512-536, doi:10.1016/j.lithos.2010.08.005.

Zhang, J. Q., S. R. Li, M. Santosh, Q. Li, S. D. Niu, Z. D. Li, X. G. Zhang, and L. B. Jia (2015), Timing and origin of Mesozoic magmatism and metallogeny in the Wutai-Hengshan region: Implications for destruction of the North China Craton, *Journal of Asian Earth Sciences*, *113*, 677-694, doi:10.1016/j.jseaes.2015.05.004.

Zhang, S. H., Y. Zhao, G. A. Davis, H. Ye, and F. Wu (2014), Temporal and spatial variations of Mesozoic magmatism and deformation in the North China Craton: Implications for lithospheric thinning and decratonization, *Earth-Science Reviews*, *131*, 49-87, doi:10.1016/j.earscirev.2013.12.004.

Zhang, T., and Y. Zhang (2007), Geochronological sequence of Mesozoic intrusive magmatism in Jiaodong Peninsula and its tectonic constraints, *Geological Journal of China Universities*, *13*(2), 323-336.

Zhang, X. O., P. A. Cawood, S. A. Wilde, R. Q. Liu, H. L. Song, W. Li, and L. W. Snee (2003), Geology and timing of mineralization at the Cangshang gold deposit, north-western Jiaodong Peninsula, China, *Mineralium Deposita*, *38*(2), 141-153, doi:10.1007/s00126-002-0290-7.

Zhao, H., J. Mao, H. Ye, G. Xie, and Z. Yang (2010), Geochronology and geochemistry of the alkaline granite porphyry and diabase dikes in Huanglongpu area of Shanxi Province: Petrogenesis and implications for tectonic environment, *Geology of China*, *37*, 12-27.

Zhao, H. X., S. Y. Jiang, H. E. Frimmel, B. Z. Dai, and L. Ma (2012), Geochemistry, geochronology and Sr-Nd-Hf isotopes of two Mesozoic granitoids in the Xiaoqinling gold district: Implication for large-scale lithospheric thinning in the North China Craton, *Chemical Geology*, *294*, 173-189, doi:10.1016/j.chemgeo.2011.11.030.

Zhou, H. S., C. Q. Ma, C. Zhang, L. Chen, J. Y. Zhang, and Z. B. She (2008), Yanshanian aluminous A-type granitoids in the Chunshui of Biyang, south margin of North China Craton: Implications from petrology, geochronology and geochemistry, *Acta Petrologica Sinica*, *24*(1), 49-64.

Zhou, J., Y. Zheng, and Z. Zhao (2003), Zircon U–Pb dating on Mesozoic granitoids at Wulian, Shangdong province, *Geological Journal of China Universities*, *9*(2), 185-194.

Zhou, L., and B. Chen (2006), Petrogenesis and significance of the Hongshan syenitic pluton, South Taihang : zircon SHRIMP U-Pb age, chemical compositions and Sr-Nd isotopes, *Progress in Natural Science*, *16*(2), 192-200.

Zhu, G., M. L. Niu, C. L. Xie, and Y. S. Wang (2010), Sinistral to Normal Faulting along the Tan-Lu Fault Zone: Evidence for Geodynamic Switching of the East China Continental Margin, *J Geol*, *118*(3), 277-293, doi:10.1086/651540.

Zhu, L., G. Zhang, B. Guo, and B. Li (2008), U–Pb (LA-ICP-MS) zircon dating for the large Jinduicheng porphyry Mo deposit in the East Qinling, China, and its metallogenetic geodynamical setting, *Acta Geologica Sinica*, *82*(2), 204-220.

1

Chapter 5. Evidence for Cratonic Keel Graveyards in the Mantle Transition Zone.

Liang Liu, Jason P. Morgan, Yigang Xu and Martin Menzies. This manuscript has been submitted to *Terra Nova*.

Authors contribution

J. P. Morgan Proposed the idea for this work. L. Liu performed this work under the primary supervision of J. P. Morgan. L. Liu and J. P. Morgan collected the geological, geochemical and geophysical observations in this paper. L. Liu and J. P. Morgan designed the numerical experiments. L. Liu, J. P. Morgan and Y-G Xu discussed the implications from numerical experiments. L. Liu wrote the manuscript in collaboration with J. P. Morgan, M. Menzies and Y-G Xu.

Evidence for Cratonic Keel Graveyards in the Mantle Transition Zone

Liang Liu[1, 2, 3], Jason P. Morgan[1], Yigang Xu[2] and Martin Menzies[1, 2]

[1] *Department of Earth Sciences, Royal Holloway University of London, Egham, TW200EX, United Kingdom.*

[2] *State Key Laboratory of Isotope Geochemistry, Guangzhou Institute of Geochemistry, Chinese Academy of Sciences, Guangzhou 510640, China.*

[3] *University of Chinese Academy of Sciences, Beijing, 100049, China.*

Corresponding author: leonliu4geo@gmail.com

Corresponding author: J. Morgan, Jason.Morgan@rhul.ac.uk

Abstract:

In at least two places, beneath former locations of the eastern North China Craton and western Wyoming Craton, the mantle transition zone has high seismic wavespeed anomalies that lack a direct connection to recently subducted slabs. The conventional interpretation for these anomalies has been that they are due to stagnant slabs introduced by subduction. Here we show further seismic evidence that supports Xu and Zhao's recent hypothesis that these high wavespeed anomalies may be due to the presence of delaminated cratonic "keel" fragments, fragments that now are relatively stagnant within the transition zone. We also explore the evolution of numerical experiments of a geodynamic model *that* can reproduce the scenario inferred from seismic wavespeed observations when the lower cratonic keel delaminates along a metasomatized and weak ~80-100km-deep Mid-Lithosphere Discontinuity Layer. This mode of recycling of cratonic lithospheric keel fragments into the convecting mantle has geochemical implications as the mechanism to create a long-hypothesized geochemical source component in OIB and MORB.

1. Introduction

Subduction zones are regions where cold, seismically fast slabs sink into the mantle. The first order correlation between subduction and regionally fast seismic wavespeeds was noticed in early studies of global seismic tomography (Creager and Jordan, 1984, Dziewonski, 1984). Later it was recognized that subduction zones often contain accumulations of fast wavespeed anomalies at 500-1000 km depths. These are widely known as 'slab graveyards', and have been well-documented at Pacific and American subduction zones (cf. (Fukao and Obayashi, 2013, Sigloch, 2011)). Here we propose that *some* high wavespeed anomalies in the transition zone that have been presumed to be slab graveyards may in fact be 'keel graveyards' that reflect a strikingly different geodynamic process, namely the delamination and sinking of the lowermost (i.e. >80km-deep) portions of the lithospheric keel to an Archean craton. We review recent seismic evidence documenting that this event happened beneath the two best-known examples of recent Archean keel destruction, the Eastern North China Craton (ENCC) and the Western Wyoming Craton (WWC). We also discuss numerical experiments that further explore a potential cratonic lithospheric failure mechanism that can lead to this geological phenomenon. These experiments explore the geodynamical behavior when the seismically recognized Mid-Lithosphere Discontinuity (MLD) is actually a weak, metasomatically-derived Mid-Lithosphere Discontinuity Layer (MLDL). In this situation, we find that the cratonic lithosphere is typically stable and strong as long as the edges of regions with an interbedded cratonic MLDL abut into cool and strong mantle. Under the exceptional conditions when an intracratonic MLDL comes in close (~10-20km) proximity to weak asthenosphere, then the lower craton can delaminate in a mode that these numerical experiments show to be consistent with the seismic structures found in the transition zones beneath North China and North America.

If true, this hypothesis would have significant implications for the process by which cratons are destroyed, the proper interpretation of high seismic wavespeed anomalies within the transition zone, and the geodynamic process by which cratonic material is recycled to become a detectable geochemical component within the convecting mantle.

78

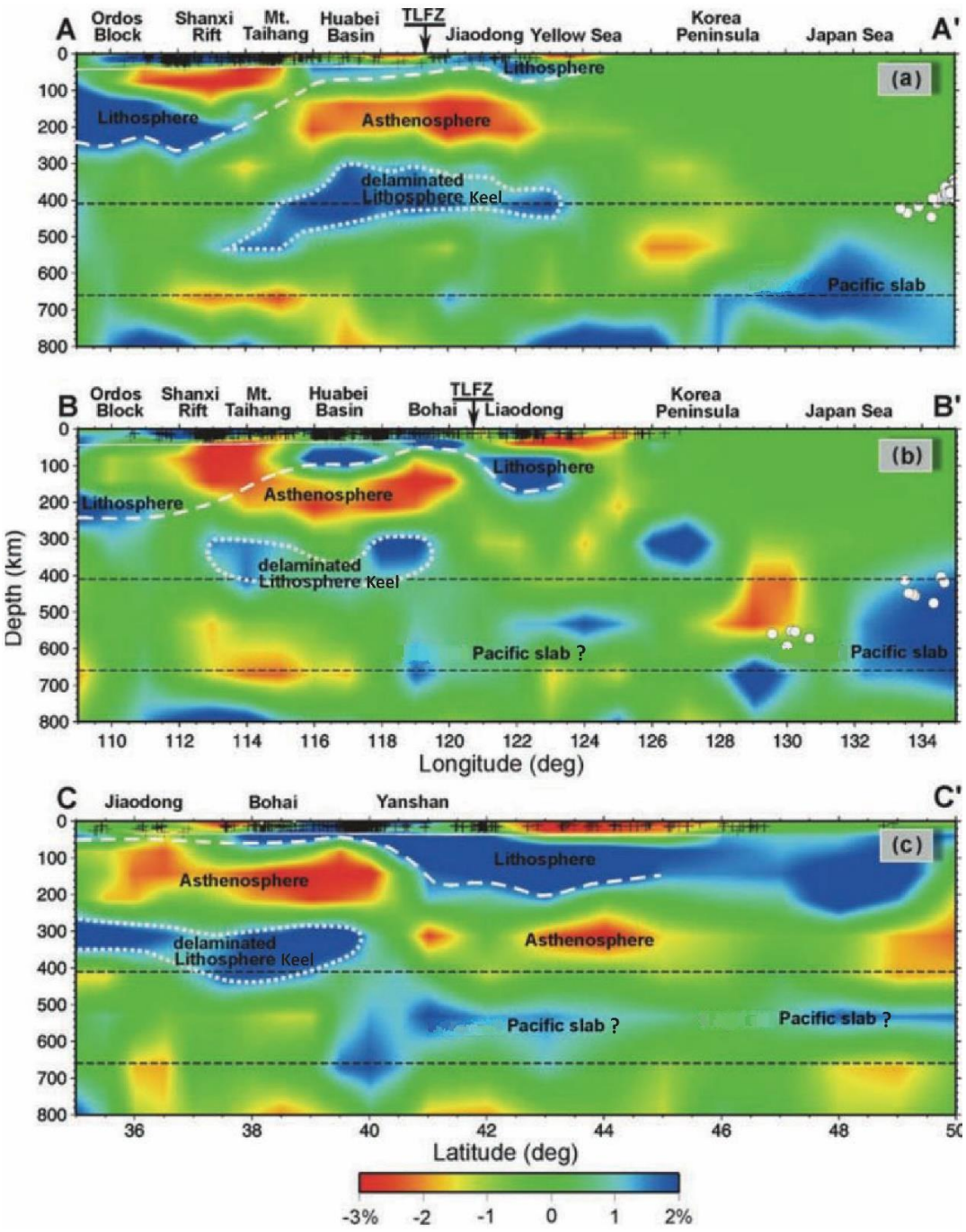

79

80 **Figure 1. Vertical cross-sections of P-wave velocity image beneath the Eastern North China**
81 **Craton (ENCC).**
82 (A) Cross-section along 37˚ N with longitude marked beneath cross-section B. (B) Cross-section along
83 39˚ N with longitude marked beneath. (C) Cross-section along 119˚ E with latitude marked beneath.
84 The present-day 80-100km lithosphere of the ENCC is found to be underlain by ~100km thick high
85 wavespeed anomalies. These anomalies appear to lack of direct connections to any nearby seismically
86 active subducting slabs in the upper mantle. Figure modified from ((Xu and Zhao, 2009)).

2. High wavespeed anomalies in the transition zone

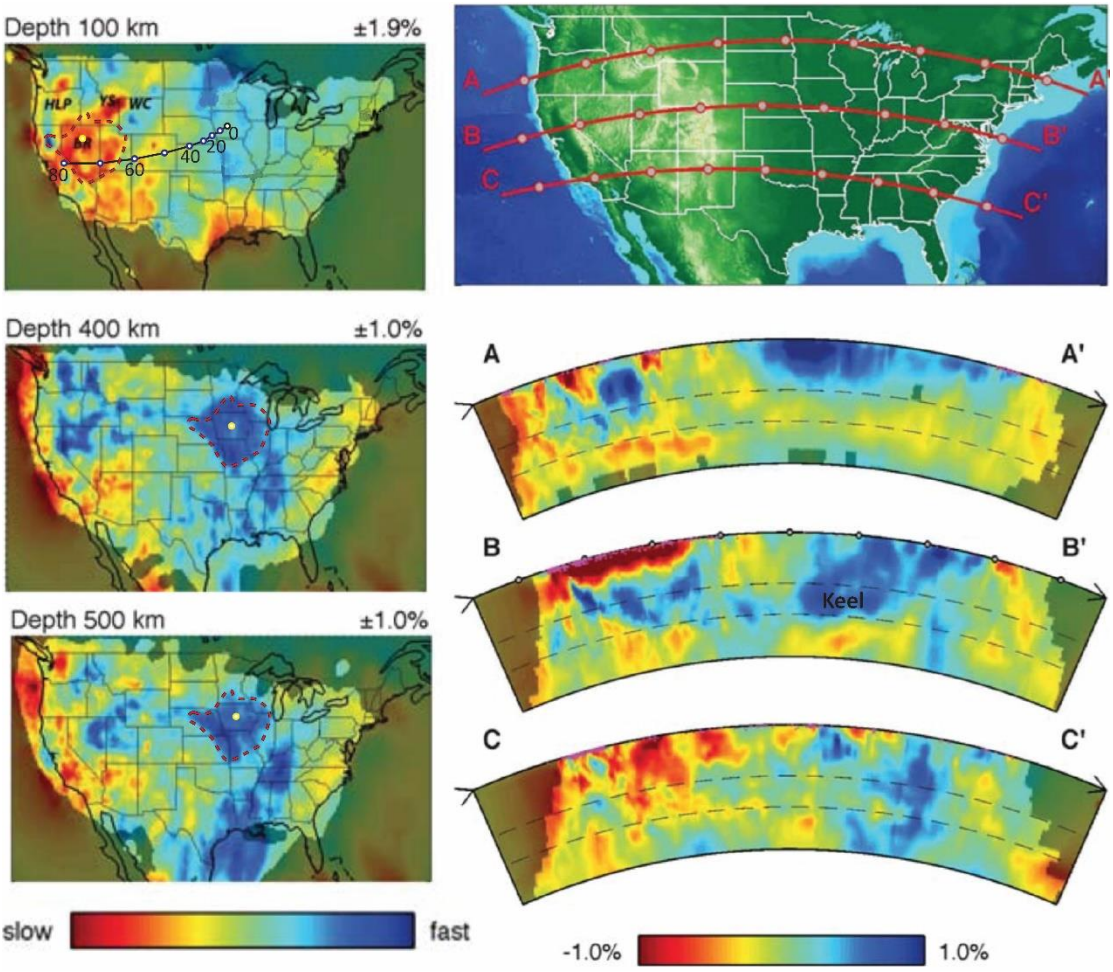

Figure 2. Seismic observation implying keel delamination.

Left hand side panels: lateral variations in P-wave velocity at 100, 400 and 500 km depth in the mantle beneath the continental United States from Burdick et al. (2017) (Burdick, et al., 2017). The black line with dots and ages (in Myr) in the 100km slide shows Morgan's (1983) reconstruction where the surface of N. America would have overlain the center of the high wavespeed anomaly now beneath Iowa. The shape of the present-day Basin & Range/W. Wyoming Craton slow wavespeed anomaly (red-dashed line) in the 100km cross-section appears be similar to the shape of the present-day high wavespeed anomalies (red-dashed lines) in the 400km and 500km cross-sections beneath Iowa that we propose to be the sunken former keel to the Western Wyoming Craton. *Abbreviations in the 100km cross-section:* HLP- High Lava Plains, YS- Yellowstone, BR- Basin and Range, WC- Wyoming Craton. ***Right hand side panels***: vertical cross sections A, B, C to depths of 1000km. Dashed lines mark 410km and 660km depths. Figure modified from Burdick et al., 2017 (Burdick, et al., 2017).

Seismic evidence for keel delamination was first noted by Xu and Zhao (Xu and Zhao, 2009), who invoked this process beneath the ENCC to explain the existence of high-wavespeed transition zone anomalies that: (a) lie above presumed slab-related wavespeed anomalies, and (b) lie beneath unusually thin (~80-100km) lithosphere of the present-day ENCC (Figure. 1). Both seismic features can be explained by the keel delamination hypothesis, with the 'hole' left by removal of the keel being the cause of anomalously thin lithosphere, while the sunken keel fragments create a high-wavespeed anomaly in the transition zone.

Recent USArray-based tomographic images beneath N. America appear to show another example of this phenomena (Burdick, et al., 2017). Beneath Iowa in the Central United States, there is a high wavespeed anomaly in the transition zone that appears to be disconnected from its nearby overlying craton root and underlying subduction-related anomalies (Figure. 2). Plate motion reconstructions (Morgan, 1983) imply that, at the time of the onset of the Laramide orogeny, this region underlay the present-day WWC and Basin and Range (Fig. 2). WWC keel delamination at the onset of the Laramide Orogeny would explain a similar link between past keel delamination, the post-delamination tectonics and thinned lithosphere in the region where delamination occurred, and present-day high wavespeed anomalies in the transition zone caused by sunken former keel mantle. Similarly, a layer of relic shallow lithospheric mantle appears to survive after non-cratonic delamination events such as that proposed to have recently happened beneath the Canadian Cordillera (Bao et al., 2014). After keel delamination there, ~1Ga 'old lithospheric mantle' mantle xenoliths were exhumed, carried in post-delamination asthenosphere-sourced magmas (Francis *et al.*, 2010; Peslier *et al.*, 2000).

3. Geodynamic Setting for Numerical Experiments on Keel Delamination

To further investigate the geodynamic processes that trigger and allow the delamination of cratonic keel fragments, we have recently been investigating keel delamination through numerical experiments (Liu, et al., 2018a;2018b). These delamination experiments often lead to sunken keel fragments similar in size and depth to the above seismic observations. Here, keel delamination (*cf.* (Menzies, et al., 1993, Xu, 2001)) is proposed to take place along a weak

and spatially significant Mid-Lithospheric Discontinuity (*cf.* (Selway, et al., 2015)) Layer (MLDL) that lies within the cratonic lithosphere in the ~80-100 km depth range as shown in Figure 3A-3C. Our preferred hypothesis for the origin of the MLDL is that it is a metasomatized layer rich in weak water-rich minerals in the depth range proposed for enhanced metasomatism of cratonic lithosphere (*cf.* Griffin et al., 2003; Sodoudi et al., 2013). Metasomatic minerals, e.g. mica and/amphibole, are found in mantle xenoliths in the ENCC, the WWC, and South African craton (Downes et al., 2004; Dudás, 1991; Gao et al., 2002; Griffin et al., 2004; Lu et al., 1991; Tang et al., 2013). These xenoliths are named MARID xenoliths, being composed of **M**ica (>50 vol.%), **A**mphibole (~25 vol.%), **R**utile, **I**lmenite, and **D**iopside (Dawson et al., 1977). At 80-100 km depths, amphibole (Getsinger et al., 2014) and mica (Kirby et al., 1987) appear to be weaker than wet olivine (Hirth et al., 2004). Amphibole, in particular, is only stable at p-T conditions shallower than ~100km (*cf*. Sweeney et al*.,* 1993), and the depth when it can become stable is consistent with the observed lower depth-limit to the seismically-inferred MLDL. Top-side seismic reflection techniques suggest the topside wavespeed reduction in this layer is associated with a relatively sharp (<5km thick) depth-interval, and a total layer thickness of ~10-25km (Karen Fischer, personal communication, December 2017). Receiver function and SS-precursor-inferred layer thicknesses are consistent with a ~10km-thick MLDL, but have much cruder vertical resolution. For example, Sp receiver functions are consistent with inferred MLDL thickness in the western US of 15-30km (Lekic and Fischer, 2014), while SS-precursor measurements only constrain the 'reflector' to be a 'sharp discontinuity with an average velocity contrast of 5±1.5% occurring over <14km' (Tharimena et al., 2017). In what follows, we will usually assume that the main weak region of the MLDL is 10km thick.

We propose that the lower cratonic keel in metasomatized regions is typically denser than ambient asthenosphere, so that, if the rare conditions arise where it can delaminate, then it will do so and sink into deeper mantle (Liu et al., 2018a). In the following experiments, the compositional keel density below the MLDL is assumed to be 3340 kg/m^3, e.g. denser than overlying more highly depleted peridotite (3310 kg/m^3), but still compositionally more buoyant than adjacent more fertile asthenosphere (3360 kg/m^3). Overall, the cratonic keel will be denser

than surrounding asthenosphere due to its significantly cooler temperature.

Delamination of continental mantle lithosphere was first proposed decades ago (*cf*. Bird, 1979; Kay et al., 1993; Menzies et al., 1993). It was originally proposed, with delamination occurring within the lower crust or Moho, for the recent uplift of the Colorado Plateau [*Bird*, 1979], and has been recently invoked to explain non-cratonic lithosphere delamination beneath the Canadian Cordilliera (Bao et al., 2014). However, after keel removal events, former cratonic regions appear to retain fragments of relic lithospheric mantle to depths of ~80-100 km (*cf*. Liu et al., 2018a; Hansen et al., 2015; Hopper et al., 2014; Wu et al., 2014; Zhang et al., 2008; Zheng et al., 2001; Zhu et al., 2012). This is directly documented by the presence of shallow (<~80 km), but not deep (>~80 km), Archaean mantle xenoliths in later magmatism (Menzies et al., 1993; Xu, 2001; Zheng et al., 2001). We interpret this as strong observation evidence that shallow lithospheric mantle relics persist after cratonic keel removal events.

After it was recognized that there was strong petrological evidence that the North China Craton had lost its cratonic keel (Menzies et al., 1993), many conceptual and numerical models were proposed to thin a keel, most related to convective erosion (e.g. keel yielding during orogenic events (Conrad et al., 1997; Gorczyk et al., 2012; Houseman et al., 1981); keel weakening by long term keel refertilization (Foley, 2008; O'Reilly et al., 2013; Tang et al., 2013), keel weakening by more rapid volitile incorporation from nearby subducting slabs (He, 2014; Niu, 2005; Wang et al., 2016; Wenker et al., 2017; Zhao, 2004). A critical discussion of these previous models and their apparent limitations to explain key observations on the ENCC and the WCC is given in Liu et al. (2018a; 2018b). Here we focus instead on exploring geodynamic model results that seem consistent with the above seismic evidence favoring keel delamination along a weak MLDL.

4. Numerical Methods

The experiments use a Lagrangian thermomechanical Finite Element approach with remeshing whenever elements become too-distorted. A modified version of 2-D Lagrangian finite element code, "m2tri_trunk" (Hasenclever, 2010) based on the approaches used in

187 "MILAMIN" (Dabrowski, et al., 2008), is used. This version includes a free surface boundary
188 condition (Andrés-Martínez et al., 2015). Tracer particles are added for tracking different
189 material properties. The 2-D experimental domain is subdivided using an adaptive triangle
190 mesh generator that keeps high resolution across material boundaries and interfaces, e.g. slabs
191 and keels (see Appendix). The thermomechanical code solves for heat transport and
192 elastoviscoplastic deformation in crust and mantle rocks. Parameters for the experiments
193 shown below are listed in Tables 1-2.
194

	A.M.	*L.M.1*	*L.M.2*	*L.M.3*	*L.M.4*	*C.*	*W.L.*
A_{dis} ($Pa^{-n}\cdot s^{-1}$)	$10^{-15.05}$	$4.85\cdot10^{-17}$	$4.85\cdot10^{-17}$	$4.85\cdot10^{-17}$	$3.0\cdot10^{-22}$	$1.4\cdot10^{-21.2}$	$10^{-15.4}$
n_{dis}	3.5	3.5	3.5	3.5	3.5	4.2	3
E_{dis} ($kJ\cdot mol^{-1}$)	480	535	535	535	540	445	356
V_{dis} ($cm^3\cdot mol^{-1}$)	8	8	8	8	8	8	8
A_{dif} ($Pa^{-n}\cdot s^{-1}$)	$10^{-8.65}$	$10^{-8.65}$	$10^{-8.65}$	$10^{-8.65}$	$10^{-8.65}$	$5.13\cdot10^{-11}$	$10^{-13.3}$
n_{dif}	1	1	1	1	1	1	1
E_{dif} ($kJ\cdot mol^{-1}$)	335	375	375	375	375	201	170
V_{dif} ($cm^3\cdot mol^{-1}$)	4	4	4	4	4	4	4
Shear Modulus (GPa)	74	74	74	74	74	40	74
Cohesion (MPa)	20	20	20	20	20	20	20
Friction Angle(°)	30 ($\gamma = 0$)→15 ($\gamma > 1.5$)						
Heat Conductivity K ($Wm^{-1}\cdot K^{-1}$)	3.3	3.3	3.3	3.3	3.3	2.5	3.3
Radiogenic heat production ($\mu W\cdot m^{-3}$)	0.033	0.033	0.033	0.033	0.033	1	0.33
Heat Capacity ($J\cdot kg^{-1}K^{-1}$)	1200	1200	1200	1200	1200	1200	1200
Reference Density ρ_0 ($kg\cdot m^{-3}$)	3360	3310	3340	3310	3310	2800	3320
$a_1(10^{-4})$	0.2697	0.27165	0.27165	0.27014	0.27768	0.27014	0.2697
$a_2(10^{-8}\ K^{-1})$	1.0192	1.04971	1.04971	1.05945	0.95451	1.05945	1.0192
$a_3\ (K^2)$	-0.1282	-0.15031	-0.15031	-0.1243	-0.12404	-0.1243	-0.1282
Bulk Modulus k (Gpa^{-1})	134	129	129	130	128	63	134

195

Tab. 1. Parameters for the numerical experiments shown in Figures 3,4, and 5.

Dislocation and diffusion viscosities are calculated with $\eta = 1/2\, A^{-1/n} \dot{\varepsilon}_{II}^{1/n-1} \exp\left((E + P \cdot V)/nRT\right)$, where η is viscosity, $\dot{\varepsilon}$ is the second invariant of strain rate, A is a pre-exponential constant, E is the activation energy, R is the universal gas constant, T is temperature, P is pressure, V is the activation volume, and ρ_0 is the reference density for different materials. Thermal expansion is temperature and pressure dependent $\alpha = \alpha_0 + \alpha_1 T + \alpha_2 T^{-2}$, where a_1, a_2, a_3 are constants (Djomani, et al., 2001, O'Reilly and Griffin, 2006). γ is the second invariant of finite strain.

Subscript "dis" refers to parameters for dislocation creep while "dif" is for diffusion creep. Notations for abbreviations: A.M. - asthenospheric mantle, L.M.1 - the upper part of cratonic lithospheric mantle, L.M.2- the lower part of cratonic lithospheric mantle (the keel), L.M.3, non-cratonic continental lithospheric mantle, L.M.4, oceanic lithospheric mantle, W.L. - the weak layer, C. - crust.

	Dislocation Rheology	*Diffusion Rheology*
A.M.	Wet olivine (Hirth and Kohlstedt, 2004)	Wet olivine (Hirth and Kohlstedt, 2004)
L.M.1-3	Dry olivine (Hirth and Kohlstedt, 1996)	Dry olivine (Hirth and Kohlstedt, 2004)
L.M.4	Dry olivine (Karato and Wu, 1993)	Wet olivine (Hirth and Kohlstedt, 2004)
C.	Pikwitonei granulite (Wilks and Carter, 1990)	Anorthite-quartz aggregates (Xiao, et al., 2002)
Other parameters are picked up from (Brune, et al., 2014)		

Tab. 2. References for the rheological parameters used for different materials in this calculation.

Abbreviations as in Tab. 1.

4.1. Temperature

For computational simplicity, temperature is treated as a potential temperature. The thermal calculation includes the effects of thermal diffusion, thermal convection, radioactive heating and shear heating (viscous dissipation) (Equation 1).

Temperature is determined from an equation governing energy conservation:

$$\rho C_p \frac{\partial T}{\partial t} = \frac{\partial}{\partial x}\left(K \frac{\partial T}{\partial x} \right) + \frac{\partial}{\partial z}\left(K \frac{\partial T}{\partial z} \right) + H \quad (1)$$

where ρ is density, C_p is heat capacity, t is time, K is thermal conductivity, and H is the volumetric heat production rate (including both radioactive heating and viscous dissipation). Note that the advection of heat is included in the Lagrangian mesh deformation.

4.2. Elastoviscoplastic Deformation

The different materials used in the model are treated as incompressible materials with use of the Boussinesq Approximation (*cf*. Turcotte and Schubert, 2014). Tracer particles are used to track seven different compositional materials (e.g. upper crust, asthenosphere, etc.). See Figure A1 for the definitions of each possible material type. Each material type is associated with a specific rheology that is potentially p, T, strain-rate, accumulated strain, and plastic yield-stress dependent. Table 1 gives the values assumed for the experiments. The number of tracer particles within each element ranges between 7 and 25. Viscosity is calculated at every integration point with the material type determined from the closest tracer particle within the element. Density is also uniform within each element with a value determined as the average of the density of the tracer particles within the element.

For each tracer particle, density is temperature and pressure dependent (Equations 7-8) (Djomani, et al., 2001, Schutt and Lesher, 2006). Each material rheology can include elastic, viscous, and plastic effects. Yielding and plastic flow

behavior are calculated using the method described by Moresi et al. (Moresi, et al., 2003).

Elastoviscoplastic deformation is described using the equations for force equilibrium (2-3) and mass conservation (4):

$$\frac{\partial}{\partial x}\left(\eta_{VEP}\left(\frac{4}{3}\frac{\partial u}{\partial x}-\frac{2}{3}\frac{\partial v}{\partial z}\right)\right)+\frac{\partial}{\partial z}\left(\eta_{VEP}\left(\frac{\partial u}{\partial x}+\frac{\partial v}{\partial z}\right)\right)-\frac{\partial P}{\partial x}=f_x+F_x^{e,t} \quad (2)$$

$$\frac{\partial}{\partial z}\left(\eta_{VEP}\left(\frac{4}{3}\frac{\partial v}{\partial z}-\frac{2}{3}\frac{\partial u}{\partial x}\right)\right)+\frac{\partial}{\partial z}\left(\eta_{VEP}\left(\frac{\partial u}{\partial x}+\frac{\partial v}{\partial z}\right)\right)-\frac{\partial P}{\partial y}=\rho g+f_y+F_y^{e,t} \quad (3)$$

$$\frac{\partial u}{\partial x}+\frac{\partial v}{\partial z}=-\frac{P}{\kappa} \quad (4)$$

where the effective viscosity $\eta_{VEP}=1/\left(1/\eta+1/G\Delta t\right)$, η is viscosity, G is elastic shear modulus, and Δt is the time step. In these equations u and v refer to horizontal and vertical velocity components, P is the dynamic pressure, g is the acceleration of gravity, and κ is the penalty term used for ensuring incompressibility with κ being 10^6 times the maximum effective viscosity (η_{VEP}) (Hasenclever, 2010). $F_i^{e,t}$ is the internal elastic stress (Moresi, et al., 2003) that can be advected by material flow. This behavior is described as

$$F_i^{e,t}=-\left(\eta_{VEP}/\mu\Delta\mathrm{t}\right)\left(\partial\tau_{ii}^{old\,J}/\partial x_i+\partial\tau_{ii}^{old\,J}/\partial x_j\right) \quad (5)$$

where $\tau_{ii}^{old\,J}$ is the Jaumann-rotated stress of the previous time (Kaus, et al., 2010), given by:

$$\tau_{ij}^{old\,J}=\tau_{ij}^{old}+\left(\omega_{ik}^{old}\tau_{ki}^{old}-\tau_{ik}^{old}\omega_{ki}^{old}\right)\Delta t \quad (6)$$

where τ_{ij}^{old} is the is the deviatoric stress from the previous time step, $\omega_{ij}=1/2\left(\partial u_i/\partial x_j-\partial u_j/\partial x_i\right)$.

The equation of state for density is:

$$\rho = \rho_0 \, exp\left[-\int_{T_0}^{T_F} \alpha\left(P = P_0, T\right) dT + \int_{P_0}^{P_F} \frac{dP}{k} \right] \tag{7}$$

$$\alpha = \alpha_0 + \alpha_1 T + \alpha_2 T^{-2} \tag{8}$$

where ρ_0 is the reference density, α is the temperature dependent thermal expansion coefficient at $T_0 = 20^{\circ}C$, P_0 is atmospheric pressure, k is the bulk modulus (assumed to be constant), and T_F and P_F are the temperature (in Kelvin) and pressure. (Details of the remeshing algorithm and the initial and boundary conditions for each experiment are given in the Appendix, and the code algorithms are further discussed in Liu et al., 2018a.)

Here we will present three type-example numerical experiments. The first is the 'typical' state of a cratonic keel, in which no delamination takes place even over billions of years (see Figure 3 and Supplementary Video SV1). This is the situation that arises if the edges to MLDLs are cold, strong, mantle lithosphere. The second and third experiments are situations in which an edge of a MLDL has become exposed so that it lies within ~20km of warm asthenospheric mantle. In the second experiment (see Figure 4 and Supplementary Video SV2) this edge forms near the onset of nearby subduction beneath the edge of a thinned back-arc, several hundred kilometers from the edge of a craton, as has been proposed (Isozaki, et al., 2010) to have been the situation when cratonic keel delamination began beneath the Eastern North China Craton, while in the third case the edge forms in the absence of nearby subduction (see Figure 5 and Supplementary Video SV5). In both of these latter cases, cratonic keel delamination commences within ~1-10Ma after the MLDL 'exposure' event, and follows a similar delamination history that only stops when keel-tearing along the MLDL reaches an internal edge of the MLDL.

5. Numerical Results

5.1. Craton Keel Stability

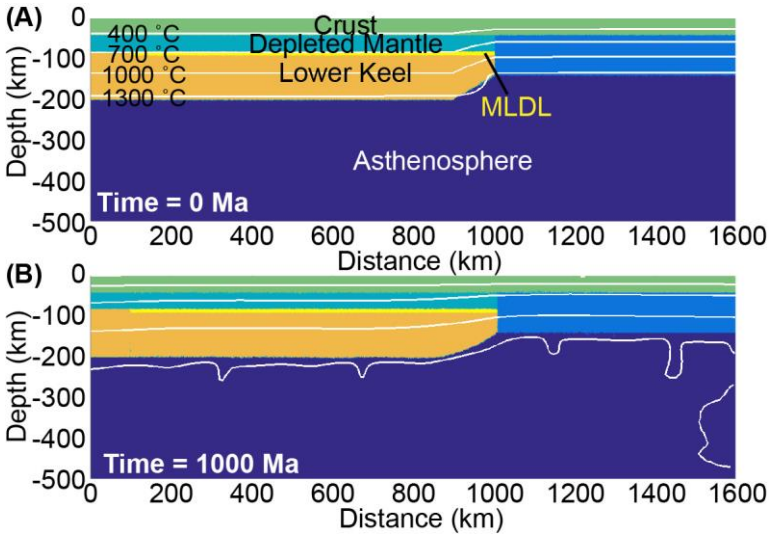

Figure 3. A numerical experiment illustrating the typical stability of a craton's keel as long as its MLDL's ends terminate within cool, strong mantle.

(A) Initial conditions. Note the preexistence of a weaker MLDL that extends over the cratonic keel region. In these panels, white lines with numbers show potential temperature isotherms. (B) Results after 1 Ga of evolution. No keel tearing is observed. The same plot conventions are used as in panel A.

Cratonic keel-removal is a rare geological phenomenon. Any keel delamination mechanism that could explain how keel-removal happened in the ENCC and the WWC must first be able to explain the longevity of stable cratons. In this type-example experiment, the MLDL channel ends within strong (~10^{22} Pa·s) surrounding mantle, which we propose to be the typical state for intracratonic MLDLs. The lithosphere near the MLDL is 140 km thick, and its relatively cool geotherm implies that the mantle adjacent to the MLDL has >10^{22} Pa·s viscosity. A gradual lithospheric thickness change close to cratonic edges is consistent with seismic observations (*cf. Begg et al.*, 2009). When the MLDL ends in lithosphere that is ~140km thick – 40-km thicker than in the following experiments – then intracratonic keel delamination does not occur over the 1Ga model timespan of the numerical experiment, as seen by the 1 Ga snapshot at the end of the experiment

(Figure 3), and in the supplementary video SV1. After 1Gyr of model time, the shape of the keel margin has become smoother. But the MLDL's shape change is hardly distinguishable (see Figure 3B), and the keel has remained stable. Liu et al. (2018a) used a semi-analytical model to further explore craton tearing along a weak MLDL, and showed that that this type of craton keel is anticipated to stably persist as long as the MLDL ends within ~10^{23} Pa-s mantle. The mechanical reason for this is that the MLDL cannot fail by tearing until weak mantle can reach and fill the void created by the growing tear.

5.2. Intracratonic Keel Delamination With Far-Field Subduction

In the type-example experiment shown in Figure 4 and Supplementary Video SV4, delamination and tearing of the cratonic keel happens along the weaker, spatially discontinuous, ~80-km-deep MLDL (Figure 4C). Keel delamination propagates only as far as the MLDL exists, stopping at the internal edge to this weak metasomatism-linked layer (see Figure 4D-E). As it delaminates and sinks, the keel breaks into ~300 km × 110 km fragments. Some of its overlying MLDL is dragged down by the sinking keel fragments (see Figure 4D-F). Keel fragments quickly sink through the low viscosity, buoyant, asthenosphere, then slow and tend to stagnate within the underlying higher-viscosity mantle transition zone (see Figure 4E-F). Here the mantle viscosity is assumed to rapidly increase due to phase changes (*cf.* Helffrich and Wood, 2001). The net density contrast of the keel could also diminish due to compositional and phase-change-linked reasons (*cf.* Griffin, et al., 2009, Lee, 2003), and the possible lower potential temperature of this zone (Morgan, et al., 2013, Morgan, et al., 1995). However, these additional complexities are not included in the experiment shown in Figure 4. Liu et al. (2018a) analyze the factors controlling the rate of this process in greater detail; here we only care that it is relatively fast, and that it leads to the type of transition zone structures shown in Figure 4.

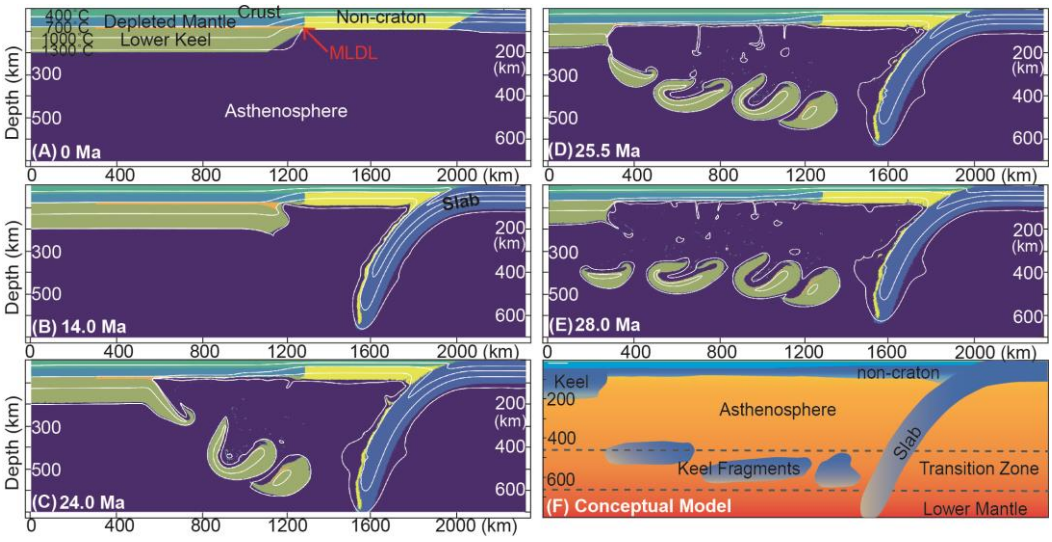

Figure 4. A numerical experiment illustrating the process of intracratonic keel delamination along a weak MLDL in the presence of far-field subduction.

(A) Initial conditions. Note the preexistence of a weaker MLDL that extends over the cratonic keel region that will eventually delaminate. (B) Keel delamination starts as subduction begins on the other side of a recently thinned region adjacent to the craton. The cratonic keel decouples from its overlying lithosphere by progressive tearing along an intra-cratonic weak layer. (C-D) During delamination, the keel maintains a roughly ~300 km horizontal integrity before it fragments. Keel fragments rapidly sink beneath the low viscosity and relatively buoyant asthenosphere to stagnate within the underlying mantle transition zone. (E) The episode of keel delamination stops where the intra-cratonic weaker layer ends. The subducting slab continues to sink deeper than its adjacent keel fragments. (F) The final snapshot of this evolution redrawn in 'cartoon form' as a conceptual model that highlights the tectonic structures present beneath the lithosphere. In these panels, white lines with numbers show potential temperature isotherms.

5.3. Intracratonic Keel Delamination Without Far-Field Subduction

Finally, we demonstrate that thinned lithosphere near a MLDL edge, not the onset of far-field subduction, is the key factor to trigger an intracratonic keel delamination event. In the type-example experiment shown in Figure 5 and Supplementary Video SV3 the far-field subduction condition is removed. Without nearby regional subduction, the onset of keel delamination is slower than in the

scenario considered in Figure 4. This occurs because far-field subduction induces more vigorous flow in the asthenosphere near the keel's edge that weakens its power-law-creep-dependent viscosity. Nonetheless, the basic pattern of keel delamination closely resembles that shown in Figure 4. As in the scenario shown in Figure 4, keel delamination only occurs when weaker surrounding asthenosphere can easily flow into the MLDL to fill the void left by keel tearing and delamination (see Figure 5C). Again, keel delamination propagates only as far as the MLDL exists, stopping at the internal edge to this weak metasomatism-linked layer (see Figure 5D-E). As it delaminates and sinks, the keel again breaks into ~300 km × 110 km fragments.

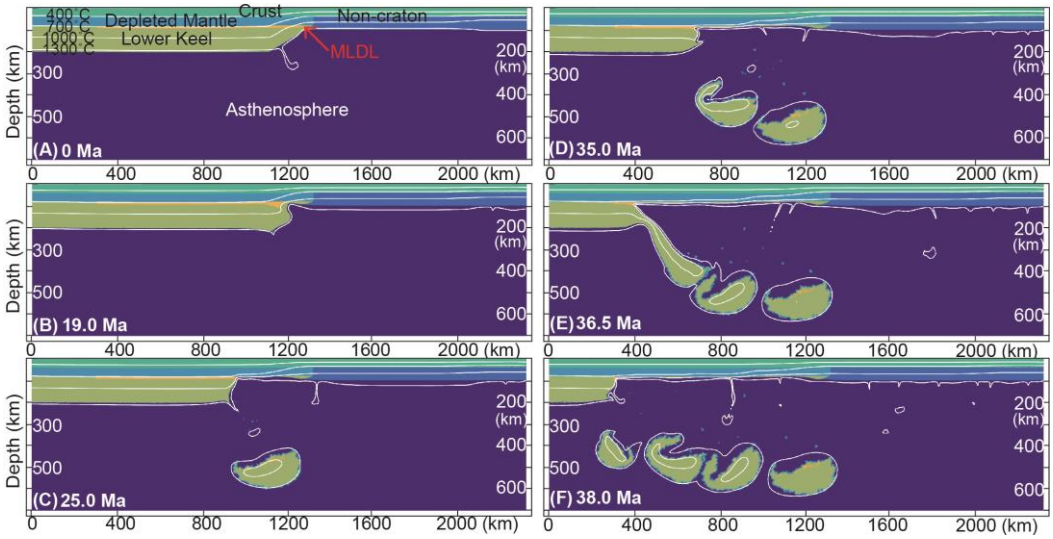

Figure 5. A numerical experiment illustrating the process of intracratonic keel delamination along a weak MLDL in the absence of far-field subduction.

(A) Initial conditions. Note the preexistence of a weaker MLDL that extends over the cratonic keel region that will eventually delaminate. (B-F) Evolution of the keel delamination process. This numerical experiment has essentially the same behavior as the experiment shown in Figure 4, except that keel delamination initiates and proceeds at a somewhat slower rate because the mantle wedge flow induced by the far-field subduction process in the run in Figure 4 further weakens the asthenosphere due to its power-law

creep rheology. The mesh resolution below 300 km deep is set to be 40 km, and therefore the boundary of the delaminated fragments is not as clear as that in Figure 4.

In this scenario, the spatial scale of the above keel delamination events is limited to regions where the intermittent MLDL existed. Delamination stops at internal edges to the MLDL. In general, cratonic keels are stable unless their edge is thinned to the point where there is an 'easy' flow-connection between the asthenosphere and a widespread MLDL. Oceanic slabs naturally tend to subduct deeper than delaminated keel fragments (see Figure 4F), in this example they ultimately subduct into the lower mantle. The geodynamic snapshot shown in Figure 4E-4F juxtaposes (a) destroyed craton (b) remaining craton, and (c) geodynamically stagnant "exotic" keel material that tends to persist within the mantle transition zone.

6. Implications of Keel Delamination

The numerical realization of this scenario provides a simple explanation for features noted by Xu and Zhao (2009) in their seismic imaging beneath northern China (see Fig. 1B and Fig. 1D-E). It would imply that these high wavespeed anomalies are due to the presence of delaminated keel fragments, while the overlying former cratonic lithosphere is anomalously thin, hence prone to later tectonic and magmatic disturbances linked to melting of underlying asthenosphere, and reworking and stretching of the now much thinner, weaker lithosphere.

After delamination, keel fragments should tend to persist within the mantle transition zone. Their initially cooler temperature and high relative strength only permit their slow conductive reheating, which allows them to remain relatively cold for ~100-200 Myr. Even after they warm until their temperature anomaly disappears, they could retain a fast seismic wavespeed if their bulk composition

(Griffin, et al., 2009, Ita and Stixrude, 1992, Lee, 2003) is anomalously fast in comparison to ‘normal’ non-cratonic mantle. Once reheated, keel material could again return to being relatively buoyant. It would then rise to at least the base of a potentially even more buoyant plume-fed asthenosphere (Morgan, et al., 2013, Morgan, et al., 1995), at which point this geochemical mantle component (McKenzie and O'Nions, 1983) could mix into the source region for OIB and MORB volcanism. Isotopic and geochemical anomalies found in oceanic basalts in the Southern Mid-Atlantic Ridge (Class and Le Roex, 2006, Schwindrofska, et al., 2016) suggest the participation of recycled (metasomatic) continental lithospheric materials (Weiss, et al., 2016) in their magma sources -- note that this region was formerly overlain by S. Gondwana cratons. Former ‘continental lithospheric mantle’ has also been proposed to be a type component for an isotopic flavor sampled in ocean island basalts (McKenzie and O'Nions, 1983). ‘Recycled continental lithosphere’ materials would be introduced into the transition zone by older keel delamination events similar to those documented here, providing a straightforward geodynamical mechanism to create the source of the curious geochemical anomalies found along the present-day Southern Mid-Atlantic Ridge (Class and Le Roex, 2006, Schwindrofska, et al., 2016).

7. Conclusions

Xu and Zhao (2009) proposed that the seismic structure beneath the Eastern North China Craton was evidence for intracratonic keel delamination from its overlying keelless craton. We agree with this interpretation, and present seismic evidence supporting that a similar cratonic keel delamination event occurred in the Western Wyoming Craton, and further note that Bao et al. (2014) found evidence implying an analogous non-cratonic lithosphere delamination event beneath the Canadian Cordillera. This geodynamic mode of intracratonic keel delamination naturally arises in numerical experiments that investigate keel delamination along

a weak Mid-Lithosphere Discontinuity Layer (MLDL) that arises because conditions for lithospheric mantle metasomatism are favored at ~80-100km depths within cratonic lithosphere. At these depths, p-T conditions make water-rich MARID (mica and amphibole-dominated) assemblages stable, so that upward-migrating metasomatic melts will tend to freeze and react in this depth-interval of cratonic lithosphere, thereby forming the mechanically weak MARID mineralogy seen in mantle xenoliths from cratonic lithosphere (Dawson et al., 1977). In normal circumstances, cratonic lithosphere has numerous cool intracratonic regions where the intermittent MLDL is not present, and the lateral edges of the MLDL are places with relatively cool and strong mantle. In this case, a cratonic keel can remain stable for >1Ga, despite the presence of a laterally discontinuous MLDL. In contrast, if a rare geological event is able to bring the MLDL to within ~20km from warm, weak asthenosphere, then the cratonic keel will rapidly tear and delaminate along the MLDL within ~3-10Ma, with ~100km x 300km-sized keel fragments rapidly sinking to the base of the asthenosphere. This spatial pattern agrees with Xu and Zhao (2009)'s suggestion for the origin of non-subduction-related seismic structures seen in the mantle transition zone beneath the present keelless East North China Craton, and similar structures related to keel delamination from the Western Wyoming Craton presently seen beneath Iowa, North America. Recycled cratonic lithosphere materials would be introduced into the transition zone by older keel delamination events similar to those documented here, thereby creating a geochemical 'continental lithosphere' component proposed to exist within the convecting mantle.

Appendix: Initial Conditions, Boundary Conditions, and Meshing and Remeshing in the Numerical Experiments

Initial conditions and boundary conditions.

The computational domain is a 3900km wide × 1500 km deep box (see Figure A1). A free surface boundary condition is applied along the top boundary following the approach of Andrés-Martínez, et al. (2015). Free slip boundary conditions are used for the left, right and bottom boundaries. Potential temperature is set to be 0˚C at the top boundary, and 1350˚C at the base of the computational box. A 1-D steady-state conductive thermal profile (Turcotte and Schubert, 2014) with 40 km crust and the horizontally varying lithospheric thickness profile shown in Figure A1 is interpolated for the cratonic continental part (initial craton thickness taken to be 200km) and the non-cratonic continental part (initial lithosphere thickness taken to be 100km) to create the initial temperature field. A 1-D half-space cooling solution after 40 Myr of cooling is used to describe the initial temperatures of the oceanic subregion to depths of 200 km. The initial temperature distribution in the transitions between cratonic continental and non-cratonic continental sub-regions, and between oceanic and non-cratonic continental sub-regions are linear averages between their surrounding subregions as shown in Figure A1.

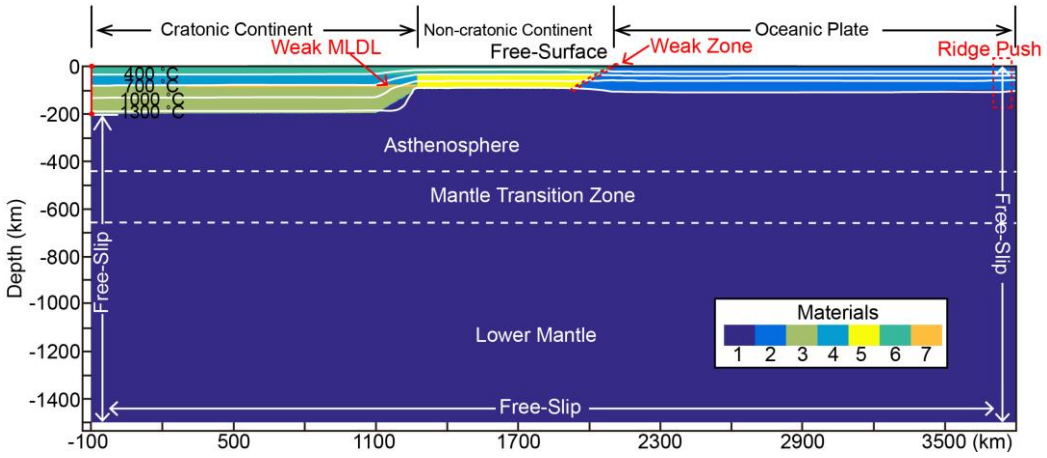

Figure A1. Initial conditions.

The computational domain is 3900 km wide × 1500 km deep. White lines with temperatures are isotherms. The mantle transition zone and lower mantle materials share similar parameters with the asthenosphere (see Tab. A1) except for activation volumes: V_{dis} = 11 $cm^3 \cdot mol^{-1}$ and V_{diff} = 6 $cm^3 \cdot mol^{-1}$ for the transition zone, V_{dis} = 14 $cm^3 \cdot mol^{-1}$ and V_{diff} = 10 $cm^3 \cdot mol^{-1}$ for the lower mantle (abbreviations in Tab. A1).

To force subduction, a leftwards 2×10^{-9} m/s (~6 cm/yr) velocity is applied to a 20km wide × 100 km deep oceanic plate region (see the red dashed rectangle in Figure A1 for scale) throughout the experiment. A weak zone (10^{19} Pa·s) is added between the oceanic plate and the non-cratonic continental plate to promote decoupling along this predetermined weak interface. The thickness of this weak-zone is set to be that of two small elements (~9 km), and this weak region stops at -200 km to crudely simulate the effects of a pressure-limit to the presence of weaker alteration minerals such as serpentine (Rüpke, et al., 2004) above the surface of subducting slabs. Here these rather ad-hoc conditions are only used to force growing slab subduction-influenced flow along the right-hand edge of non-cratonic material, and to highlight the differing spatial patterns of keel and slab sinking. In other experiments that did not include a forced subduction boundary condition, keel delamination follows a similar spatial evolution to that shown in Figure 3. In all models that we have explored to date, keel delamination will only start when the lithosphere adjacent to the craton is thinned as shown in Figure A1 (Liu, et al., 2016).

Meshing and Re-meshing

The computational domain is a mesh of triangular elements that is built using an adaptive mesh generation algorithm that makes element sizes be relatively small (~4.5 km) when near internal boundaries between different materials (see Equations A1-4). Element sizes are made to be 10 times larger than this (~40 km)

in regions far from internal material interfaces, while at transitional distances, element size is linearly interpolated between these two end-member values. This approach guarantees relatively high resolution along material interfaces and within thin material layers during a calculation. We find that material interfaces remain well-tracked even when high velocities occur due to the effects of slab subduction and keel tearing and sinking (see Figure A2). Because we use a Lagrangian approach in which straight-sided element vertices advect with material flow, some elements can become heavily distorted in regions of strong shear. A new equant-element mesh is regenerated by re-meshing whenever elements are deemed to be 'too-distorted' (This is defined to be when any interior angle of an element is larger than 170° or smaller than 7°, or any mesh quality factor Q is smaller than 0.2, see Equation A1). In Run 1, the Lagrangian approach is only used for the portion with temperature >1150°C; a semi- Lagrangian approach [*Hasenclever*, 2010] is used for the remaining deeper portion (the more ductile asthenosphere) in order to minimize computational time. Equations A2-A4 are used to define the preferred element size *R* as a function of distance *r* from an internal boundary interface.

$$Q = \left(L_2 + L_3 - L_1\right)(L_1 + L_3 - L_2)(L_1 + L_2 - L_3)\big/(L_1 L_2 L_3) \tag{A1}$$

where L_1, L_2 and L_3 are the side lengths of the triangular element.

$$L_0 = R_2 \ when \ r \ > 4.75 \cdot R_2 \tag{A2}$$

$$L_0 = \frac{r}{3.75 \cdot R_2}(R_2 - R_1) + R_1 \ when \ R_1 < r \le 4.75 \cdot R_2 \tag{A3}$$

$$L_0 = R_1 \ when \ r <= R_1 \tag{A4}$$

where L0 is the characteristic element size used for a certain set of coordinates, r is distance between center of "spring bar" connecting element vertexes [*Persson et al.*, 2004] to its closest reference point (RP) sampled along an interphase boundary. R1 is the smallest element size (here 4.45 km), and R2 is the largest size (44.32 km). The adaptive algorithm first samples reference points (RPs) on the interfaces between different material types using the MATLAB function

‘tricontour’. It then determines how far the center of each spring bar is from its nearest RP, and assigns a preferred length size R to the center of each spring bar. This mesh-size information is used to generate a new relatively equant mesh of triangles using a finite-element-reformulated version of the DISTMESH algorithm [Persson et al., 2004] done by Taramón et al. (2017). The last step is to interpolate the current variable fields onto the new mesh.

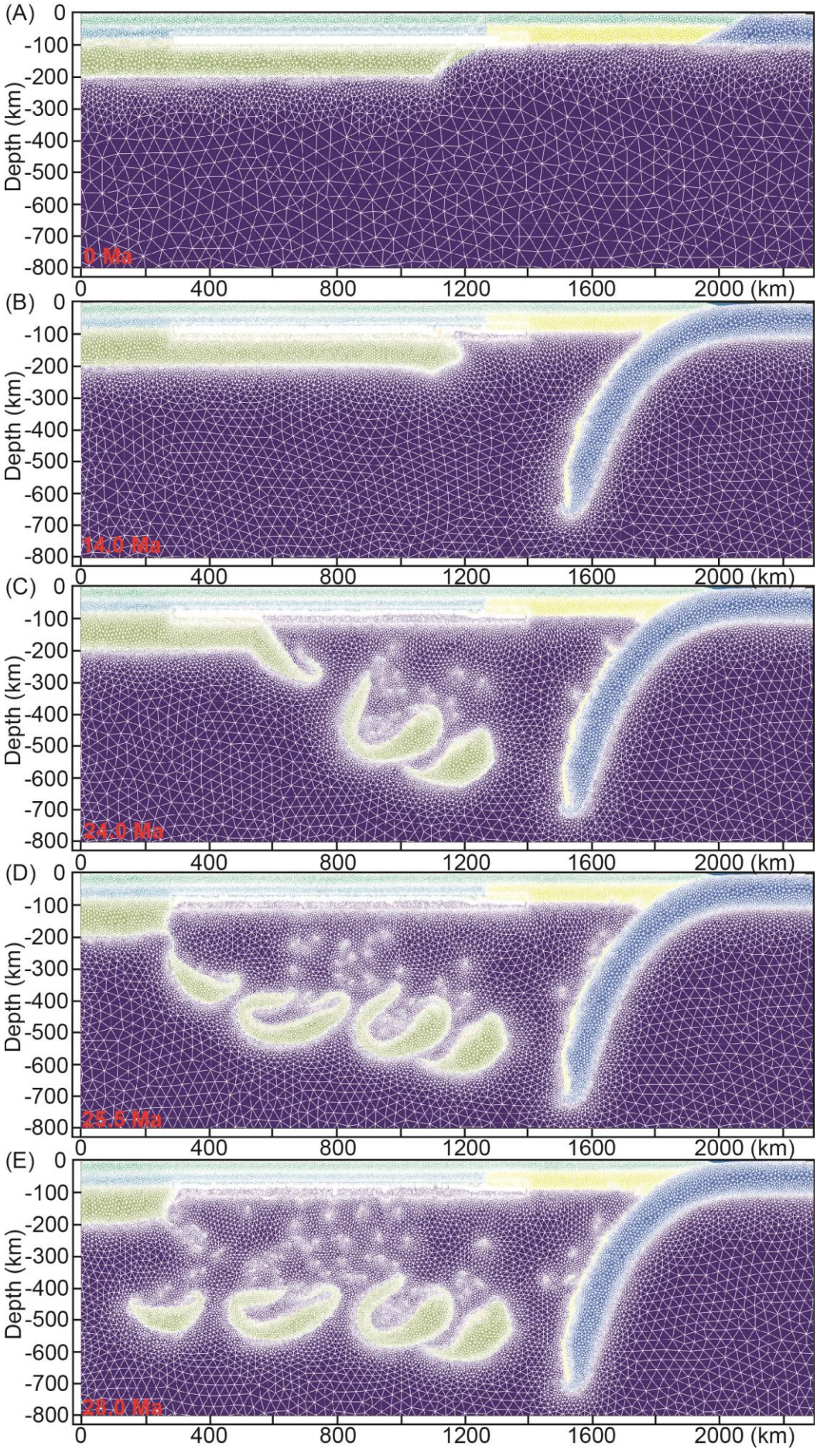
(A)
(B)
(C)
(D)
(E)
Depth (km)
0
-100
-200
-300
-400
-500
-600
-700
-800
0 Ma
14.0 Ma
24.0 Ma
25.5 Ma
28.0 Ma
0
400
800
1200
1600
2000 (km)

Figure A2. Material phase plot with meshes.

The triangular meshes (in white) are plotted on the material phase field. Same plot conventions as in Figure 4. Element sizes are relatively small (~4 km) when near internal boundaries between different materials. Element sizes are made to be 10 times larger than this (~40 km) in regions far from internal material interfaces, while at transitional distances, element size is linearly interpolated between these two end-member values.

References:

Andrés-Martínez, M., Morgan, J.P., Pérez-Gussinyé, M. and Rüpke, L., 2015. A new free-surface stabilization algorithm for geodynamical modelling: Theory and numerical tests. *Physics of the Earth and Planetary Interiors*, **246**, 41-51.

Bao, X., Eaton, D.W. and Guest, B., 2014. Plateau uplift in western Canada caused by lithospheric delamination along a craton edge *Nature Geoscience*, **7**, 830.

Begg, G., Griffin, W., Natapov, L., et al., 2009. The lithospheric architecture of Africa: Seismic tomography, mantle petrology, and tectonic evolution *Geosphere*, **5**, 23-50.

Brune, S., Heine, C., Perez-Gussinye, M. and Sobolev, S.V., 2014. Rift migration explains continental margin asymmetry and crustal hyper-extension. *Nat Comm.*, **5**, 4014, 10.1038/ncomms5014.

Burdick, S., Vernon, F.L., Martynov, V., et al., 2017. Model Update May 2016: Upper‐Mantle Heterogeneity beneath North America from Travel‐Time Tomography with Global and USArray Data. *Seismological Research Letters*, **88**, 319-325.

Class, C. and Le Roex, A.P., 2006. Continental material in the shallow oceanic mantle—How does it get there? *Geology*, **34**, 129-132.

Conrad, C.P. and Molnar, P., 1997. The growth of Rayleigh–Taylor-type instabilities in the lithosphere for various rheological and density structures *Geophysical Journal International*, **129**, 95-112.

Creager, K.C. and Jordan, T.H., 1984. Slab penetration into the lower mantle. *Journal of Geophysical Research: Solid Earth*, **89**, 3031-3049.

Dabrowski, M., Krotkiewski, M. and Schmid, D.W., 2008. MILAMIN: MATLAB-based finite element method solver for large problems. *Geochemistry Geophysics Geosystems*, **9**, 10.1029/2007GC001719.

Dawson and Smith, J., 1988. Metasomatised and veined upper-mantle xenoliths from Pello Hill, Tanzania: evidence for anomalously-light mantle beneath the Tanzanian sector of the East African Rift Valley. *Contributions to Mineralogy and Petrology*, **100**, 510-527.

Djomani, Y.H.P., O'Reilly, S.Y., Griffin, W.L. and Morgan, P., 2001. The density structure of subcontinental lithosphere through time. *Earth and Planetary Science Letters*, **184**, 605-621.

Downes, H., Macdonald, R., Upton, B.G., et al., 2004. Ultramafic xenoliths from the Bearpaw Mountains, Montana, USA: Evidence for multiple metasomatic events in the lithospheric mantle beneath the Wyoming craton *Journal of Petrology*, **45**, 1631-1662.

Dudás, F.Ö., 1991. Geochemistry of igneous rocks from the Crazy Mountains, Montana, and tectonic models for the Montana alkalic province *Journal of Geophysical Research: Solid Earth*, **96**, 13261-13277.

Dziewonski, A.M., 1984. Mapping the lower mantle: determination of lateral heterogeneity in P velocity up to degree and order 6. *Journal of Geophysical Research: Solid Earth*, **89**, 5929-5952.

Foley, S.F., 2008. Rejuvenation and erosion of the cratonic lithosphere *Nature Geoscience*, **1**, 503.

Francis, D., Minarik, W., Proenza, Y. and Shi, L., 2010. An overview of the Canadian Cordilleran lithospheric mantle *Canadian Journal of Earth Sciences*, **47**, 353-368.

Fukao, Y. and Obayashi, M., 2013. Subducted slabs stagnant above, penetrating through, and trapped below the 660 km discontinuity. *Journal of Geophysical Research: Solid Earth*, **118**, 5920-5938.

Gao, S., Rudnick, R.L., Carlson, R.W., et al., 2002. Re–Os evidence for replacement of ancient mantle lithosphere beneath the North China craton *Earth and Planetary Science Letters*, **198**, 307-322.

Gorczyk, W., Hobbs, B. and Gerya, T., 2012. Initiation of Rayleigh–Taylor instabilities in intra-cratonic settings *Tectonophysics*, **514**, 146-155.

Griffin, O'Reilly, S.Y., Afonso, J.C. and Begg, G.C., 2009. The Composition and Evolution of Lithospheric Mantle: a Re-evaluation and its Tectonic Implications. *Journal of Petrology*, **50**, 1185-1204.

Griffin, W., O'Reilly, S.Y., Doyle, B., et al., 2004. Lithosphere mapping beneath the North American plate *Lithos*, **77**, 873-922.

Griffin, W., O'Reilly, S.Y., Natapov, L. and Ryan, C., 2003. The evolution of lithospheric mantle beneath the Kalahari Craton and its margins *Lithos*, **71**, 215-241.

Hansen, S.M., Dueker, K. and Schmandt, B., 2015. Thermal classification of lithospheric discontinuities beneath USArray *Earth and Planetary Science Letters*, **431**, 36-47.

Hasenclever, J., 2010. Modeling Mantle Flow and Melting Processes at Mid-Ocean Ridges and Subduction Zones — Development and Application of Numerical Models. *Ph.D. Dissertation*, Hamburg University.URL: http://ediss.sub.uni-hamburg.de/volltexte/2010/4873/.Helffrich, G.R. and Wood, B.J., 2001. The Earth's mantle. *Nature*, **412**, 501-507.

He, L., 2014. Numerical modeling of convective erosion and peridotite-melt interaction in big mantle wedge: Implications for the destruction of the North China Craton *Journal of Geophysical Research: Solid Earth*, **119**, 3662-3677.

Hopper, E., Ford, H.A., Fischer, K.M., et al., 2014. The lithosphere–asthenosphere boundary and the tectonic and magmatic history of the northwestern United States *Earth and Planetary Science Letters*, **402**, 69-81.

Houseman, G.A., McKenzie, D.P. and Molnar, P., 1981. Convective instability of a thickened boundary layer and its relevance for the thermal evolution of continental

convergent belts *Journal of Geophysical Research: Solid Earth*, **86**, 6115-6132.

Hirth, G. and Kohlstedt, D., 2004. Rheology of the Upper Mantle and the Mantle Wedge: A View from the Experimentalists, in Inside the Subduction Factory (ed J. Eiler), American Geophysical Union, Washington, D. C.. 10.1029/138GM06.

Hirth, G. and Kohlstedt, D.L., 1996. Water in the oceanic upper mantle: implications for rheology, melt extraction and the evolution of the lithosphere. *Earth and Planetary Science Letters*, **144**, 93-108.

Isozaki, Y., Aoki, K., Nakama, T. and Yanai, S., 2010. New insight into a subduction-related orogen: a reappraisal of the geotectonic framework and evolution of the Japanese Islands. *Gondwana Research*, **18**, 82-105.

Ita, J. and Stixrude, L., 1992. Petrology, elasticity, and composition of the mantle transition zone. *Journal of Geophysical Research: Solid Earth*, **97**, 6849-6866.

Karato, S.-I. and Wu, P., 1993. Rheology of the upper mantle: A synthesis. *Science*, **260**, 771-778.

Kaus, B.J.P., Muhlhaus, H. and May, D.A., 2010. A stabilization algorithm for geodynamic numerical simulations with a free surface. *Physics of the Earth and Planetary Interiors*, **181**, 12-20.

Lee, C.T.A., 2003. Compositional variation of density and seismic velocities in natural peridotites at STP conditions: Implications for seismic imaging of compositional heterogeneities in the upper mantle. *Journal of Geophysical Research: Solid Earth*, **108**, 10.1029/2003JB002413.

Lekić, V. and Fischer, K.M., 2014. Contrasting lithospheric signatures across the western United States revealed by Sp receiver functions *Earth and Planetary Science Letters*, **402**, 90-98.

Liu, L., Morgan, J.P., Xu, Y. and Menzies, M., 2018a. Craton Destruction Part I: Cratonic Keel Delamination along a weak Mid-Lithospheric Discontinuity layer, *in press, Journal of Geophysical Research: Solid Earth,* doi: 10.1029/2017JB015372.

Liu, L., Morgan, J.P., Xu, Y. and Menzies, M., 2018b. Craton Destruction Part II: Evolution of Cratonic Lithosphere after a Rapid Keel Delamination Event*, in press, Journal of Geophysical Research: Solid Earth,* doi: 10.1029/2017JB015374.

Lu, F., Han, Z., Zheng, J. and Ren, Y., 1991. Characteristics of Paleozoic mantle-lithosphere in Fuxian, Liaoning province *Geological Science and Technology Information*, **10**, 20.

McKenzie, D. and O'Nions, R., 1983. Mantle reservoirs and ocean island basalts. *Nature*, **301**, 229-231.

Menzies, Fan, W. and Zhang, M., 1993. Palaeozoic and Cenozoic lithoprobes and the loss of > 120 km of Archaean lithosphere, Sino-Korean craton, China. *Geological Society,*

London, Special Publications, **76**, 71-81.

Moresi, L., Dufour, F. and Mühlhaus, H.-B., 2003. A Lagrangian integration point finite element method for large deformation modeling of viscoelastic geomaterials. *Journal of Computational Physics*, **184**, 476-497.

Morgan, J., Hasenclever, J. and Shi, C., 2013. New observational and experimental evidence for a plume-fed asthenosphere boundary layer in mantle convection. *Earth and Planetary Science Letters*, **366**, 99-111.

Morgan, J., Morgan, W.J., Zhang, Y.S. and Smith, W.H., 1995. Observational hints for a plume‐fed, suboceanic asthenosphere and its role in mantle convection. *Journal of Geophysical Research: Solid Earth*, **100**, 12753-12767.

Morgan, W.J., 1983. Hotspot tracks and the early rifting of the Atlantic. *Tectonophysics*, **94**, 123-139.

Niu, Y., 2005. Generation and evolution of basaltic magmas: some basic concepts and a new view on the origin of Mesozoic–Cenozoic basaltic volcanism in eastern China *Geological Journal of China Universities*, **11**, 9-46.

O'Reilly, S.Y. and Griffin, W., 2013. Mantle metasomatism. In: *Metasomatism and the chemical transformation of rock*. Springer.

O'Reilly, S. and Griffin, W., 2006. Imaging global chemical and thermal heterogeneity in the subcontinental lithospheric mantle with garnets and xenoliths: Geophysical implications. *Tectonophysics*, **416**, 289-309.

Peslier, A.H., Reisberg, L., Ludden, J. and Francis, D., 2000. Os isotopic systematics in mantle xenoliths; age constraints on the Canadian Cordillera lithosphere *Chemical Geology*, **166**, 85-101.

Ros, E., Pérez‐Gussinyé, M., Araújo, M., Thoaldo Romeiro, M., Andrés‐Martínez, M. and Morgan, J.P., 2017. Lower Crustal Strength Controls on Melting and Serpentinization at Magma‐Poor Margins: Potential Implications for the South Atlantic. *Geochemistry, Geophysics, Geosystems,* 10.1002/2017GC007212.

Rüpke, L.H., Morgan, J.P., Hort, M. and Connolly, J.A., 2004. Serpentine and the subduction zone water cycle. *Earth and Planetary Science Letters*, **223**, 17-34.

Schutt, D.L. and Lesher, C.E., 2006. Effects of melt depletion on the density and seismic velocity of garnet and spinel lherzolite. *Journal of Geophysical Research-Solid Earth*, **111**, 10.1029/2003JB002950.

Schwindrofska, A., Hoernle, K., Hauff, F., et al., 2016. Origin of enriched components in the South Atlantic: Evidence from 40 Ma geochemical zonation of the Discovery Seamounts. *Earth and Planetary Science Letters*, **441**, 167-177.

Selway, K., Ford, H. and Kelemen, P., 2015. The seismic mid-lithosphere discontinuity. *Earth and Planetary Science Letters*, **414**, 45-57.

Shinevar, W.J., Behn, M.D. and Hirth, G., 2015. Compositional dependence of lower crustal viscosity. *Geophysical Research Letters*, **42**, 8333-8340.

Sigloch, K., 2011. Mantle provinces under North America from multifrequency P wave tomography. *Geochemistry, Geophysics, Geosystems*, **12**, 10.1029/2010GC003421.

Sodoudi, F., Yuan, X., Kind, R., et al., 2013. Seismic evidence for stratification in composition and anisotropic fabric within the thick lithosphere of Kalahari Craton *Geochemistry, Geophysics, Geosystems*, **14**, 5393-5412.

Sweeney, R.J., Thompson, A.B. and Ulmer, P., 1993. Phase relations of a natural MARID composition and implications for MARID genesis, lithospheric melting and mantle metasomatism *Contributions to Mineralogy & Petrology*, **115**, 225-241.

Tang, Y.-J., Zhang, H.-F., Ying, J.-F. and Su, B.-X., 2013. Widespread refertilization of cratonic and circum-cratonic lithospheric mantle *Earth-Science Reviews*, **118**, 45-68.

Tasaka, M., Hiraga, T. and Zimmerman, M.E., 2013. Influence of mineral fraction on the rheological properties of forsterite+ enstatite during grain‐size‐sensitive creep: 2. Deformation experiments. *Journal of Geophysical Research: Solid Earth*, **118**, 3991-4012

J. M. Taramón, J. P. Morgan, C. Shi, J. Hasenclever, Generation of unstructured meshes in 2-D, 3-D, and spherical geometries with embedded high resolution sub-regions, arXiv:1711.06333 (https://arxiv.org/abs/1711.06333).

Tharimena, S., Rychert, C. and Harmon, N., 2017. A unified continental thickness from seismology and diamonds suggests a melt-defined plate *Science*, **357**, 580-583.

Taramón, J. M., J. P. Morgan, C. Shi, J. Hasenclever (2017), Generation of unstructured meshes in 2-D, 3-D, and spherical geometries with embedded high resolution sub-regions; arXiv: 1711.06333.

Turcotte, D.L. and Schubert, G., 2014. *Geodynamics*. Cambridge University Press, 623 pp.

Wang, Z., Kusky, T.M. and Capitanio, F.A., 2016. Lithosphere thinning induced by slab penetration into a hydrous mantle transition zone *Geophysical Research Letters*, **43**.

Weiss, Y., Class, C., Goldstein, S.L. and Hanyu, T., 2016. Key new pieces of the HIMU puzzle from olivines and diamond inclusions. *Nature, 10.1038/nature19113*.

Wenker, S. and Beaumont, C., 2017. Can metasomatic weakening result in the rifting of cratons? *Tectonophysics*.

Wilks, K.R. and Carter, N.L., 1990. Rheology of some continental lower crustal rocks. *Tectonophysics*, **182**, 57-77.

Wu, F., Xu, Y., Zhu, R. and Zhang, G., 2014. Thinning and destruction of the cratonic lithosphere: A global perspective *Science China Earth Sciences*, **57**, 2878-2890.

Xiao, X., Wirth, R. and Dresen, G., 2002. Diffusion creep of anorthite‐quartz aggregates.

Journal of Geophysical Research: Solid Earth, **107**, 10.1029/2001JB000789.

Xu, 2001. Thermo-tectonic destruction of the archaean lithospheric keel beneath the Sino-Korean Craton in China: Evidence, timing and mechanism. *Physics and Chemistry of the Earth Part a-Solid Earth and Geodesy*, **26**, 747-757.

Xu and Zhao, D., 2009. Upper-mantle velocity structure beneath the North China Craton: implications for lithospheric thinning. *Geophysical Journal International*, **177**, 1279-1283.

Zhang, H.-F., Goldstein, S.L., Zhou, X.-H., et al., 2008. Evolution of subcontinental lithospheric mantle beneath eastern China: Re–Os isotopic evidence from mantle xenoliths in Paleozoic kimberlites and Mesozoic basalts *Contributions to Mineralogy and Petrology*, **155**, 271-293.

Zhao, D., 2004. Global tomographic images of mantle plumes and subducting slabs: insight into deep Earth dynamics *Physics of the Earth and Planetary Interiors*, **146**, 3-34.

Zheng, J., O'Reilly, S.Y., Griffin, W., et al., 2001. Relict refractory mantle beneath the eastern North China block: significance for lithosphere evolution *Lithos*, **57**, 43-66.

Zhu, R., Xu, Y., Zhu, G., et al., 2012. Destruction of the North China craton *Science China Earth Sciences*, **55**, 1565-1587.

Chapter 6: Conclusions Remarks

1) The destruction of the Eastern North China Craton (ENCC) appears to be accompanied by (or preceded by) the failing process of one cratonic basin (North China Cratonic Basin, NCCB) in the Mesozoic times (ca. 200-160 Ma).

2) The long-term subsidence history of the NCCB may indicate that the ENCC used to bear a dense keel bottom before craton destruction in the Mesozoic times (ca. 180- 160 Ma).

3) The dense cratonic keel can possibly have been produced during the long-term evolution of the NCC as an ‘edged’ or ‘isolated’ craton; while the keel removal process during the ENCC destruction may have led to the partly reversion of the NCCB upon the ENCC.

4) We propose an intra-cratonic keel delamination model inspired by observations of geologically recent delamination events beneath the eastern North China Craton (ENCC) and western Wyoming Craton (WWC).

5) Keel delamination along a water rich or MARID bearing MLDL can explain the geologically implied keel removal speeds observed on the western Wyoming Craton in North America and the eastern North China Craton in China.

6) Cratonic keel delamination appears to be independent of the weak intra-cratonic layer’s density; delamination still occurs when the MLDL’s net density is lower than that of keel and asthenosphere.

7) Seismologists may have imaged sunken cratonic keel fragments associated with geologically recent keel delamination beneath the eastern North China Craton and western Wyoming Craton, and maybe even a recent ‘hanging’ keel fragment at the westerns edge of the remaining Wyoming Craton that is the cause of the fast-vertical seismic anomaly known colloquially as the ‘Idaho Drip’ (Schmand and Humphries, 2011).

8) Old water in the form of pre-delamination (>>200 Ma) cratonic metasomes (mica-amphibole-rutile-ilmenite-diopside) is crucial in initiating craton

delamination - the first step in craton destruction. Young water linked to relatively recent (<<150Ma) Pacific subduction is less crucial.

9) Lithospheric faults or localized weak zones help to initiate sub-lithospheric mantle upwelling at depth. Their presence can lead to the extension-linked creation of seismic "mushroom" anomalies that are underlain by thickened lower crust.

10) MLDL reactivation can explain the volumetrically minor ca. 180-160 magmatic pulse; while post-delamination convective erosion leads to the intensive ca. 160-110Ma pulse at the margins of the ENCC. Lithospheric extension induces focused crustal melting close to trans-lithospheric weakness.

11) After keel removal, the role of the paleo-Pacific subduction became more evident, in inducing the ca. 140-100 Ma extensional episode, and later (<<150Ma) tectonism and magmatism.